

Electronic Thesis and Dissertation Repository

8-22-2019 10:00 AM

Dynamic mechanostimulation of live cells during real-time microscopy

Daniel Lorusso, *The University of Western Ontario*

Supervisor: Dixon, S. Jeffrey, *The University of Western Ontario*

Co-Supervisor: Holdsworth, David W., *The University of Western Ontario*

A thesis submitted in partial fulfillment of the requirements for the Doctor of Philosophy degree in Physiology and Pharmacology

© Daniel Lorusso 2019

Follow this and additional works at: <https://ir.lib.uwo.ca/etd>



Part of the [Other Medical Sciences Commons](#)

Recommended Citation

Lorusso, Daniel, "Dynamic mechanostimulation of live cells during real-time microscopy" (2019).
Electronic Thesis and Dissertation Repository. 6480.
<https://ir.lib.uwo.ca/etd/6480>

This Dissertation/Thesis is brought to you for free and open access by Scholarship@Western. It has been accepted for inclusion in Electronic Thesis and Dissertation Repository by an authorized administrator of Scholarship@Western. For more information, please contact wlsadmin@uwo.ca.

Abstract

Our body's functioning depends on the ability of cells to sense and react to their local mechanical environment; this process is known as mechanotransduction. Despite the importance of understanding how cells interact with mechanical stimuli, the specific mechanisms governing such processes have yet to be elucidated. Using microscopy to detect the early responses of living cells to mechanical loads and forces would be a critical step towards further understanding cellular mechanotransduction. Dynamic and high-frequency cyclical loads are relevant to human physiology and disease. Yet, modern microscopy systems are not capable of delivering the appropriate mechanical stimuli to live cell cultures. To address this deficiency, we developed a suite of mechanostimulation platforms that provide precise and relevant loads and forces to cell cultures during simultaneous microscopic analysis. We developed a motion-control system capable of precisely delivering vibrations to live cells during real-time microscopy. Using this system, we found that vibration of osteoblastic cells does not elicit acute elevation of cytosolic free calcium, but did desensitize responses to later stimulation with extracellular ATP. We next developed and validated a technique for the practical fabrication of microfluidic channels. In contrast to the effect of vibration, osteoblastic cells were found to respond to changes in fluid shear stress with transient elevation in the concentration of cytosolic free calcium. Lastly, we developed a system to apply disturbed fluid flow to live cells during real-time imaging. This system was used to demonstrate changes in the concentration of cytosolic free calcium in human endothelial cells exposed to laminar and disturbed flow. Our findings indicate that different forms of mechanical stimuli activate distinct signaling pathways in cells. Moreover, these new technologies will facilitate investigations of the signaling pathways activated by

dynamic mechanical stimulation of a variety of cell types, in particular those of the skeletal and vascular systems.

Keywords

Mechanotransduction, Mechanical loading, Mechanostimulation, Microscopy, Real-time monitoring, Calcium imaging, Fluorescence microscopy, Fluid shear stress, Vibration, Acceleration, Microfluidics, Polydimethylsiloxane, Micro-milling, Computer-aided design, Computer-aided manufacturing, Computational fluid dynamics, Osteoblasts, Osteoclasts, ATP, P2 receptors, Purinergic signaling, Vascular endothelial cells, Disturbed flow, Wall shear stress, Oscillatory shear index, Transverse wall shear stress, Laminar flow, Micro-particle imaging velocimetry, Particle tracking, Silicone, Lab-on-a-chip, Oscillatory shear stress

Summary for Lay Audience

Our bodies have the capability to respond and adapt to mechanical loads and forces. Cells, the functional units of our body, have the machinery responsible for sensing and responding to these forces. For example, during physical activity such as running, the cells in our bones sense the repeated force applied to the body, and can signal to strengthen the bone tissue if necessary. Indeed, over time, increases or decreases in physical activity can strengthen or weaken our bones, respectively. In general, physical forces play an important role in the regular healthy function of the human body, and also in the development of many serious diseases, including bone disorders like osteoporosis and vascular diseases like atherosclerosis. Therefore, it is important to understand the processes by which cells carry out these functions. However, these processes have been difficult to study for many reasons. For one, there are several different kinds of forces that can interact with cells, including shear stress due to fluid flow and acceleration due to vibration. Another reason is that it is technically challenging to observe the immediate changes in cell activity when a specific force is applied.

In this thesis, we describe the development of new technologies that will allow scientists to study the early responses of living cells to the application of controlled physical forces. The first study describes a tool that allows scientists to vibrate cells back-and-forth hundreds of times per second, while only moving them less than the width of a human hair. The second study describes a tool that allows scientists to easily and affordably flow fluid over cells in a controlled way. The final study describes a tool that allows scientists to apply fluid flow to cells in a way similar to that seen in diseased blood vessels. These tools are all integrated with existing microscopes and cellular-imaging techniques. Our findings indicate that

vibration and fluid flow activate different biological control systems within the interior of the cell. Further studies using these devices may aid in the development of new medical treatments for diseases like osteoporosis and atherosclerosis.

Co-Authorship Statement

Chapter 2 was adapted from an original research article titled “Vibration of osteoblastic cells using a novel motion-control platform does not acutely alter cytosolic calcium, but desensitizes subsequent responses to extracellular ATP”. This paper is currently in revision for the *Journal of Cellular Physiology*. The manuscript was authored by Daniel Lorusso, Hristo N. Nikolov, David W. Holdsworth and S. Jeffrey Dixon. As the primary author of the manuscript, I was responsible for the experimental design; design of the device; development and refinement of the methods for device fabrication, device calibration, particle tracking, and imaging; collection of experimental data; performance of data analysis; statistics; interpretation of the results; and manuscript preparation. Hristo Nikolov contributed to development of the device. David Holdsworth and Jeffrey Dixon formed the study concept; contributed to device and study design, development of the device, cell experiments, imaging techniques, and interpretation of results; as well as provided editorial and infrastructure support.

Chapter 3 was adapted from an original research article titled “Practical fabrication of microfluidic platforms for live-cell microscopy”, which was originally published in the peer-reviewed journal of *Biomedical Microdevices* (*Biomed Microdevices* 18:78, 2016). It is reproduced here with permission from Springer Nature (Appendix C). The manuscript was authored by Daniel Lorusso, Hristo N. Nikolov, Jaques S. Milner, Noelle M. Ochtony, Stephen M. Sims, S. Jeffrey Dixon, and David W. Holdsworth. As the primary author of the manuscript, I was responsible for the experimental design; design of the microfluidic device; development and refinement of the methods for microfluidic device fabrication, microfluidic cell culture, particle tracking, finite element modeling, and calcium imaging; collection of

experimental data; performance data analysis; statistics; interpretation of the results; and manuscript preparation. Hristo Nikolov contributed to development of device fabrication methods, and machined the molds for microfluidic chip casting. Jaques Milner provided expertise in fluid mechanics and performed computational fluid dynamics calculations. Noelle Ochtony provided assistance in cell culture and cell experiments. Stephen Sims and Jeffrey Dixon provided guidance in cell experiments and imaging techniques, as well as infrastructure for cell culture and imaging experiments. David Holdsworth formed the study concept, contributed to study design, development of methods for device fabrication and particle tracking, aided in interpretation of results, as well as provided editorial and infrastructure support.

Chapter 4 is an original research article titled “A microfluidic system for real-time microscopic imaging of endothelial cell responses to laminar and disturbed fluid flow”, in preparation for submission. The manuscript was co-authored by Daniel Lorusso, Kayla Soon, Ethan Sacoransky, Hristo N. Nikolov, John R. de Bruyn, J. Geoffrey Pickering, S. Jeffrey Dixon, David W. Holdsworth and Tamie L. Poepping. As the primary author, I was responsible for study design, device design, device fabrication, data collection and analysis, cell culture, cell experiments, and manuscript preparation. Kayla Soon contributed to device fabrication and PIV data acquisition, Ethan Sacoransky contributed to PIV data analysis, Hristo Nikolov contributed to the design process and milled the micro-device molds. John R. de Bruyn contributed to micro-PIV system implementation, Geoffrey Pickering and Jeffrey Dixon contributed to developing the rationale and understanding the biological significance, as well as financial, and infrastructure support for cell and imaging experiments. David Holdsworth and Tamie Poepping formed the study concept, contributed to the study design

and rationale, contributed to data analysis techniques, and provided editorial and infrastructure support.

Acknowledgments

Supervisors and principle investigators David W. Holdsworth and S. Jeffrey Dixon are thanked for their scientific guidance and editorial input throughout my thesis project.

Tamie L. Poepping and Stephen M. Sims are thanked for their scientific input, manuscript assistance, and infrastructure support.

Hristo Nikolov, Chris. Norley, Steve Pollmann, and Tom Chmiel are thanked for their scientific and technical input and efforts towards my research. They and the remainder of the Holdsworth group, and Robarts Imaging are thanked for their scientific and technical input. Matthew Teeter, and Maria Drangova are also thanked for their scientific advice.

Evaline Warmels and Nicholas Park are thanked for their contributions to CAD modeling of the microfluidic device dish holder and vibration system.

Ryan Beach, Brandon Kim, Alexey Pereverzev, Tom Chrones, and Matt Grol are thanked for their work to aid in cell culture and cell experiments, as well as for their advice and assistance in laboratory management. Ryan Beach contributed to osteoclast and eGFP-actin cell preparations, and osteoclast experiments in Chapter 2. Garth Blackler, Tom Appleton, and the Appleton lab are thanked for their accommodation in sharing of lab space and supplies. I also acknowledge the Skeletal Biology Laboratories. Cheryle Seguin and the Seguin lab, as well as Doug Hamilton and the Hamilton lab are also thanked for their sharing of lab space, equipment, and supplies. I also thank Mike Kovach and colleagues from Horiba-PTI for their generous infrastructure support, providing the fluorescence monitoring equipment used throughout these studies.

I am also grateful to Hao Yin, Emma Prescott, Geoff Pickering, and Caroline O'Neil for their assistance and contributions to endothelial cell culture protocols and supplies.

Yuki Bao and Mona Hassanzedah are thanked for their assistance and effort in data processing in MatLab in Chapter 4; their hard work is appreciated. Mona also aided in early work, including drawing of the disturbed flow device.

I thank Nica Borradaile for her contributions as the Graduate Studies Representative for Physiology and Pharmacology on my thesis advisory committee. I also thank Lina Dagnino and the rest of my advisory committee (Jeff Dixon, Stephen Sims, and David Holdsworth) for their guidance and scientific input.

I also acknowledge my sincere appreciation to The University of Western Ontario, Robarts Research Institute, The Bone and Joint Institute, The Canadian Institutes of Health Research, and the Ontario government for their generous financial and infrastructure support.

Table of Contents

Abstract.....	ii
Summary for Lay Audience.....	iv
Co-Authorship Statement.....	vi
Acknowledgments.....	ix
Table of Contents.....	xi
List of Tables.....	xv
List of Figures.....	xvi
List of Appendices.....	xix
List of Abbreviations.....	xx
Chapter 1.....	1
1 Introduction.....	1
1.1 Chapter summary.....	2
1.2 Overview of mechanotransduction research.....	4
1.3 Mechanical stimuli relevant to mechanotransduction.....	6
1.3.1 Tensile stress and strain.....	9
1.3.2 Fluid shear stress and fluid flow.....	11
1.3.3 Acceleration and vibration.....	14
1.4 Mechanotransduction.....	20
1.4.1 Cellular mechanisms.....	20
1.4.2 Biological roles and significance of mechanotransduction.....	32
1.5 Bone.....	32
1.5.1 Bone biology and mechanotransduction.....	32
1.5.2 Mechanically related bone diseases and dysfunctions.....	35
1.6 Vasculature.....	37

1.6.1	Vascular biology and mechanotransduction	37
1.6.2	Mechanical vascular disease and dysfunction	39
1.7	Methods to study mechanotransduction.....	42
1.7.1	Vibration	42
1.7.2	Fluid flow and microfluidics.....	45
1.7.3	Particle image velocimetry	47
1.8	Rationale and objectives	48
1.9	References.....	52
Chapter 2.....		69
2	Vibration of osteoblastic cells using a novel motion-control platform does not acutely alter cytosolic calcium, but desensitizes subsequent responses to extracellular ATP .	69
2.1	Chapter summary	70
2.2	Introduction.....	71
2.3	Materials and methods	73
2.3.1	Motion control platform for horizontal vibration of live cells during microscopy	73
2.3.2	Characterization of motion using high-speed imaging and micro-particle tracking	77
2.3.3	Culture and transfection of osteoblastic cell lines	79
2.3.4	Isolation and culture of rat osteoclasts.....	79
2.3.5	Spectrofluorometric measurement of $[Ca^{2+}]_i$	80
2.3.6	Microspectrofluorimetry and fluorescence ratio imaging of $[Ca^{2+}]_i$	81
2.3.7	Fluorescence imaging of actin dynamics and time-lapse phase-contrast microscopy	82
2.3.8	Statistical analyses	83
2.4	Results.....	83
2.4.1	Accuracy and precision of the motion-control platform.....	83
2.4.2	Assessment of fluid motion using microscope-based particle tracking....	91

2.4.3	LMHF vibration of live UMR-106 rat osteoblast-like cells while monitoring $[Ca^{2+}]_i$ using microspectrofluorimetry	94
2.4.4	LMHF vibration of live MC3T3-E1 murine osteoblast-like cells while monitoring $[Ca^{2+}]_i$ by fluorescence ratio imaging	97
2.4.5	Cell morphology and actin dynamics in cells exposed to LMHF vibration	105
2.5	Discussion.....	108
2.5.1	Novel motion-control platform for application of vibrational stimuli....	108
2.5.2	Vibration of osteoblastic cells does not acutely alter cytosolic calcium	111
2.5.3	Vibration of osteoblastic cells desensitizes subsequent responses to extracellular ATP	114
2.6	References.....	117
Chapter 3.....		123
3	Practical fabrication of microfluidic platforms for live-cell microscopy.....	123
3.1	Chapter summary	124
3.2	Introduction.....	124
3.3	Methods.....	126
3.3.1	Microfluidic device fabrication.....	126
3.3.2	Measurement of channel dimensions.....	129
3.3.3	Computational fluid dynamics.....	129
3.3.4	Particle image velocimetry	130
3.3.5	Cell culture and imaging.....	131
3.4	Results.....	133
3.4.1	Device measurements	133
3.4.2	Computational fluid dynamics.....	133
3.4.3	Particle velocimetry	137
3.4.4	Validation of biocompatibility & $[Ca^{2+}]_i$ imaging	137
3.5	Discussion & conclusions	140

3.6	References.....	145
Chapter 4..... 147		
4	A microfluidic system for real-time microscopic imaging of endothelial cell responses to laminar and disturbed fluid flow.....	147
4.1	Chapter summary.....	148
4.2	Introduction.....	149
4.3	Methods.....	152
4.3.1	Microfluidic device fabrication.....	152
4.3.2	Micro-particle image velocimetry.....	154
4.3.3	Micro-PIV data processing and analysis.....	157
4.3.4	Cell culture and live-cell imaging.....	159
4.4	Results.....	160
4.4.1	Laminar flow characterization measurements.....	160
4.4.1	Disturbed flow analysis.....	162
4.4.2	Imaging $[Ca^{2+}]_i$ during disturbed flow.....	172
4.5	Discussion & conclusions.....	177
4.6	References.....	182
Chapter 5..... 187		
5	General discussion & conclusions.....	187
5.1	Summary & future directions.....	188
5.2	General significance.....	192
5.3	Limitations of the research and suggestions for future studies.....	194
5.4	Concluding remarks.....	198
5.5	References.....	199
Appendices..... 201		
Curriculum Vitae..... 218		

List of Tables

Table 2.1 Peak accelerations recorded using the on-board accelerometer or optical tracking at various nominal frequencies and accelerations.....	86
Table 2.2 Peak accelerations recorded using the on-board accelerometer or optical tracking at various nominal frequencies and accelerations.....	90
Table 3.1 Precision of micro-channel height and width dimensions.....	134

List of Figures

Figure 1.1 Waveform of an impulse load.	8
Figure 1.2 Average common carotid flow waveform.	8
Figure 1.3 Physical strain due to stretching.	10
Figure 1.4 Shear stress is a function of viscosity and the velocity gradient.	12
Figure 1.5 Shear stress due to blood flow in a vessel cross section.	15
Figure 1.6 Relationship of acceleration to velocity and displacement during simple harmonic oscillations.	16
Figure 1.7 Schematic showing timeline of the molecular mechanisms involved in mechanotransduction.	21
Figure 1.8 P2 receptor signaling pathways.	27
Figure 1.9 Mechanobiology of bone: lacunar-canalicular fluid flow.	34
Figure 1.10 Hemodynamics and endothelial cell related vascular disease.	40
Figure 1.11 Vibration of live cells <i>in vitro</i>	43
Figure 2.1 The motion-control platform mounted on an inverted microscope.	75
Figure 2.2 Accelerations monitored using on-board accelerometer.	85
Figure 2.3 Direct observation of vibrational displacement with optical particle tracking.	89
Figure 2.4 Tracking of fixed and unfixed particles to evaluate the possibility of flow between the fluid and the culture dish.	93
Figure 2.5 LMHF vibration of rat osteoblastic cells while monitoring $[Ca^{2+}]_i$ by microspectrofluorimetry.	96

Figure 2.6 LMHF vibration of murine osteoblastic cells during real-time fluorescence ratio imaging of $[Ca^{2+}]_i$	99
Figure 2.7 Spectrofluorimetric measurement of ATP-induced elevation of $[Ca^{2+}]_i$ in MC3T3-E1 cells suspended in Ca^{2+} -containing and Ca^{2+} -free buffer.....	102
Figure 2.8 Spectrofluorometric measurement of ATP-induced elevation of $[Ca^{2+}]_i$ in MC3T3-E1 cells following depletion of intracellular Ca^{2+} stores.....	104
Figure 2.9 Magnitude of the peak elevation of $[Ca^{2+}]_i$ induced by ATP in MC3T3-E1 cells pretreated with vibration or sham.	106
Figure 2.10 Magnitude of the peak elevation of $[Ca^{2+}]_i$ induced by ATP in MC3T3-E1 cells pretreated with vibration or sham, with non-responding cells excluded.....	107
Figure 2.11 Live-cell imaging of actin dynamics showed no acute changes in actin distribution induced by vibration.	109
Figure 3.1 Microfluidic device fabrication.	127
Figure 3.2 A 3D visualization of the computational fluid dynamics (CFD)-generated velocity profiles and derived wall shear rates.....	136
Figure 3.3 High-speed imaging of micro-particle flow within microfluidic channels.	138
Figure 3.4 Peak-velocity from CFD and PIV over a range of steady flow rates.....	139
Figure 3.5 Osteoblast-like cells imaged inside a prototype microfluidic channel.....	141
Figure 3.6 Device compatibility with live-cell fluorescence imaging of cytosolic free calcium.....	143
Figure 4.1 Microfluidic device design and fabrication.	153
Figure 4.2 Imaging of micro-particles and resultant velocity vector fields.	156
Figure 4.3 Laminar flow characterization plots from micro-PIV.....	164

Figure 4.4 Wall shear stress resulting from laminar flow in the microfluidic device.	166
Figure 4.5 Wall shear stress as a function of flow rate over a range of channel positions.....	168
Figure 4.6 WSS vector maps were combined to generate x-y positional quiver plots.	169
Figure 4.7 2D colour-encoded maps of wall shear stress metrics derived from micro-PIV during disturbed flow in the microfluidic device.	171
Figure 4.8 Repeatability of disturbed flow metrics determined by micro-PIV.	174
Figure 4.9 $[Ca^{2+}]_i$ imaging in VECs during disturbed flow.	176

List of Appendices

Appendix A: Legends for movie files.....	201
Appendix B: Animal use protocol	203
Appendix C: Copyright permissions.....	204

List of Abbreviations

2D	Two-dimensional
3D	Three-dimensional
<i>a</i>	Acceleration
A	Area
AA	Arachidonic acid
AM	Acetoxymethyl ester
ANCOVA	Analysis of covariance
ANOVA	Analysis of variance
ATP	Adenosine triphosphate
[Ca ²⁺] _i	Intracellular free calcium concentration
CAD	Computer-aided design
CAM	Computer-aided manufacturing
CaM	Calmodulin
CFD	Computational fluid dynamics
CFL	Courant-Friedrichs-Lewy
CM	Centimetre
sCMOS	Scientific complementary metal–oxide–semiconductor
CNC	Computer numerical control
CO ₂	Carbon dioxide
COX	Cyclooxygenase
D	Displacement
DAG	Diacylglycerol
ECM	Extracellular matrix
EGFP	Enhanced green fluorescent protein
EGTA	Ethylene glycol-bis(β-aminoethyl ether)-N,N,N',N'-tetraacetic acid
EGM-2	Endothelial Growth Medium-2
ELWD	Extra-long working distance
eNOS	Endothelial nitric oxide synthase
ENT1	Equilibrative nucleoside transporter 1
ER	Endoplasmic reticulum

f	Frequency
FBS	Fetal bovine serum
FN	Fibronectin
FPS	Frames per second
<i>g</i>	Standard acceleration due to gravity
g	Grams
GPCR	G-protein coupled receptor
h	Hours
HAEC	Human aortic endothelial cell
HCO ₃ ⁻	Bicarbonate
HEPES	4-(2-hydroxyethyl)-1-piperazineethanesulfonic acid
HUVEC	Human umbilical vein endothelial cell
Hz	Hertz
ID	Inner diameter
IP ₃	Inositol 1,4,5-trisphosphate
kHz	Kilohertz
L	Litre
LINC	Linker of nucleoskeleton and cytoskeleton
LMHF	Low magnitude high frequency
m	Metre
MEM	Minimum essential media
min	Minute
mL	Millilitre
mm	Millimetre
mM	Millimolar
mOsm	Milliosmole
ms	Millisecond
N	Newtons
NA	Numerical aperture
NFAT	Nuclear factor of activated T cells
nm	Nanometre
NO	Nitric oxide

Ω	Ohm
OD	Outer diameter
OSI	Oscillatory shear index
OPG	osteoprotegerin
Pa	Pascals
PBS	Phosphate buffered saline
PDMS	Polydimethylsiloxane
PGE ₂	Prostaglandin E ₂
PIV	Particle image velocimetry
PLA ₂	Phospholipase A ₂
PLC	Phospholipase C
RANKL	Receptor activator of nuclear factor κ B ligand
Re	Reynolds number
RFI	Relative fluorescence intensity
RPM	Revolutions per minute
s	Seconds
SAC	Stretch activated ion channel
SD	Standard deviation
SE	Standard error
SEM	Standard error of the mean
τ	Shear stress
t	Time
T	Period
TAWSS	Time-averaged wall shear stress
TLWSS	Transverse to laminar wall shear stress
TransWSS	Transverse wall shear stress
TRPV4	Transient Receptor Potential Cation Channel Subfamily V Member 4
μ	Viscosity coefficient
μ g	Micrograms
μ L	Microlitre
μ m	Micrometres
μ M	Micromolar

UV	Ultraviolet
v	Velocity
VEC	Vascular endothelial cell
VEGF	Vascular endothelial growth factor
Vib	Vibrated
ω	Angular frequency
W	Watt
WBV	Whole body vibration
WSS	Wall shear stress
Nd:YLF	Neodymium-doped yttrium lithium fluoride

Chapter 1

Introduction

1.1 Chapter summary

Cells and tissues can convert physical information from their local mechanical environment into biochemical signals through the process known as mechanotransduction. Physical forces acting on cells and tissues include strain (e.g. due to stretching), acceleration (e.g. during vibration), and fluid shear stress (due to flow of extracellular fluid). Mechanotransduction is thought to be ubiquitous in life on earth and organisms have developed sophisticated and sometimes specialized mechanisms with which to process these various types of mechanical signals. In some cases, mammalian cells detect a strain, which is then amplified by release of ATP into the extracellular fluid, which in turn signals through cell-surface purinergic receptors, initiating transient elevation in the concentration of cytosolic free calcium. Change in cytosolic free calcium levels then leads to a cascade of downstream signaling events, affecting cell fate and phenotype through the modulation of transcription, translation, and protein activity. The immediate and transient nature of such signals makes real-time monitoring of cellular responses to mechanical signals imperative for understanding these phenomena.

Many previous studies of mechanotransduction have investigated its roles in the musculoskeletal and circulatory systems. In the case of the musculoskeletal system, mechanical stimulation with vibration and fluid flow has been implicated in bone health, as anabolic signals fundamental to adequate bone strength. When this signaling is perturbed or otherwise disrupted, inadequate remodeling leads to a deficiency in bone mass that is diagnosed in humans as osteoporosis. In the case of the vasculature,

endothelial cells that line blood vessels are mechanically sensitive. They respond to the fluid shear stress caused by blood flow and require this stimulus to maintain a healthy phenotype. If hemodynamics are perturbed, which occurs naturally in certain geometries of the vasculature (e.g. at bifurcations), then endothelial dysfunction may occur. This pathological inflammatory signaling leads to disease states like atherosclerosis.

Research tools exist to study cellular mechanotransduction. In the case of fluid shear stress, flow chambers allow the study of cells responding to changes in fluid flow.

Microfluidics have allowed more relevant micro-scale geometries, which has increased the impact of these studies. However barriers to entry into this field remain high for many labs, as custom devices usually require complex and expensive methods of fabrication.

Custom devices are also required to study real-time cell responses to dynamic mechanical stimuli such as vibration and disturbed fluid flow. Most vibration studies are performed with whole-body vibration devices, where an entire animal is vibrated. Devices exist to study the response of cells to vibration, but they are not readily compatible with real-time monitoring. Similarly with respect to disturbed flow, although the potential impact on cells has been known for decades, there are few systems available to study the immediate effect in real time.

It is perhaps unsurprising that the ability for cells and tissues to respond to their physical surroundings is so essential. More surprising however, may be that relative to other sensory-transduction processes, the scientific understanding of mechanotransduction is comparatively incomplete; it is for this reason that we contribute to the science surrounding mechanotransduction. Therefore, the overall objective of this thesis is to

develop a suite of instruments for the dynamic mechanostimulation of live cells, integrated with real-time microscopy.

In this introductory chapter, we discuss the context for mechanotransduction research, including, the forces we deem most relevant to biology, mechanotransduction mechanisms that have been identified in the literature, tissues in which mechanotransduction is known to be highly important, and the methods commonly used to study the early events of mechanotransduction in cells and tissues. Lastly, we address the specific aims and objectives of this thesis.

1.2 Overview of mechanotransduction research

The importance of mechanotransduction in biology is difficult to overstate – this is exemplified by its key role in human physiology. The evolutionary development of mechanosensation is understood to have a common ancestor phylogenetically preceding multicellular organisms. Mechanosensation, the sensitivity of biological systems to mechanical stimulation, is thought to be ubiquitous in nature among all 3 domains of life (Kloda and Martinac, 2002). Mechanosensitive proteins show homology between kingdoms (Martinac, 2001). Examples of these are stretch-activated ion channels, which are described in prokaryotes (Blount et al., 1996), archaea (Kloda and Martinac, 2001; Le Dain et al., 1998) and eukaryotes (Guharay and Sachs, 1984). This ubiquity among all phylogenetic domains underscores the importance for life to have this ability of interacting with the physical environment.

Although the ability of organisms to interact with their mechanical environment is intuitive to humans (i.e. understanding the sense of touch is innate), formal scientific inquiry into mechanobiology (aside from that relating to somatosensation of the nervous system) likely began with Julius Wolff. His work “Law of Transformation of the Bone” described the propensity of bone to change its shape as a result of loading (Wolff, 2010a; Wolff, 2010b; Wolff, 2011; Wolff et al., 1986). Since recognition that mechanical loading is essential to the physiology of the skeleton, the same has been realized for other tissues (Wall et al., 2017), including but not limited to skeletal muscle (Huxley and Hanson, 1954), cardiac muscle (Abraham et al., 2016; Katz, 2002; McCormick and Tzima, 2016; Takahashi et al., 2013), blood vessels (Ando and Yamamoto, 2009; Berk, 2008; Davies, 1995; Davies et al., 1995; Papaioannou and Stefanadis, 2005), the kidneys (Nauli et al., 2003; Nauli and Zhou, 2004; Raghavan and Weisz, 2016; Weinbaum et al., 2010), and the lungs (Alevriadou et al., 2017; Liu et al., 1999; Mahto et al., 2014).

Various forms of mechanical loading of all these tissues converge on a few key modes of mechanical stimulation. While forces applied to tissues and cells may differ in their presentation, cells can only respond to these stimuli through a limited number of fundamental mechanisms. Here, we suggest that many mechanotransductive phenomena are the result of strains arising through one or more of the following mechanical stimuli: tensile stress and strain, fluid shear stress, and acceleration.

1.3 Mechanical stimuli relevant to mechanotransduction

There are multiple relevant forms of mechanical stimulation (Janmey and McCulloch, 2007; Scott et al., 2008), including tensile strain (stretching) (Reed et al., 2014), acceleration (e.g. vibration) (Zhou et al., 2014b), and fluid shear stress (Macek Jilkova et al., 2014). The literature reveals that these are currently being investigated in multiple systems and, at the moment, it is not entirely known which types of forces and stimuli are the most relevant to each specific cell type. In nature, the effects of these forces are difficult to isolate as they often act simultaneously, and may have multiple effects on cell signaling. In this thesis, we attempted to isolate each stimulus, as a reductive approach may be key to parsing their individual effects, and for identifying how best to manipulate them in the future for medical interventions.

In determining which parameters of mechanical stimuli are most relevant, the literature cites the dynamic nature and the magnitude of the resulting strain as being key attributes. A static mechanical stimulus is one that does not vary in magnitude or direction over time, whereas a dynamic stimulus may change in magnitude and/or direction over time. It has recently been postulated that the most relevant stimuli in cellular mechanotransduction are highly dynamic in nature. Although mechanotransduction has been investigated for some time, the relevance of dynamic, high frequency stimuli has been recognized much more recently (Michel, 1988; Weinbaum et al., 1994).

The biological relevance of high-frequency stimuli may not be immediately obvious when one considers typical loading scenarios (e.g. walking at a rate of 1 Hz). However, this can be explained by the fact that it is the range of frequencies that are actually transmitted through the body (Seidel et al., 2001), not the rate of the initial loading, which is significant. In the example of the musculoskeletal system, the natural resonance of human bone dictates the range of frequencies transmitted through that tissue. Human bone has been found to transmit frequencies of approximately 100 Hz (Benirschke et al., 1993), with more recent research showing transmissibility up to 20 Hz (Meusch and Rahmatalla, 2014) (Fig. 1.1). Thus, there is a range of frequencies that could be of interest in bone as well as other tissues.

The dynamic nature of mechanostimulation is also important in other tissues, such as the vasculature. The human heart beats approximately once every second, pumping blood throughout our vessels, which applies a fluid shear stress to the vascular endothelium. Examining an archetypal blood flow waveform (Figure 1.2) of the carotid artery reveals a flow rate that is temporally variable and contains high frequency components in the tens of Hz. Interestingly, it is not entirely dissimilar in appearance to the impulse waveforms of loaded bone seen in Figure 1.1. This similarity in dynamic loading may play a role in the cellular mechanotransductive mechanisms used to respond and adapt to these stimuli.

In this thesis, we focused on vibration and fluid shear stress in bone cells (osteoblasts and osteoclasts) as well as vascular endothelial cells. However, the tools developed in these studies were designed to be applicable to many different cell models. Strains due to tensile stresses were not directly addressed in these studies. However, tensile stress and

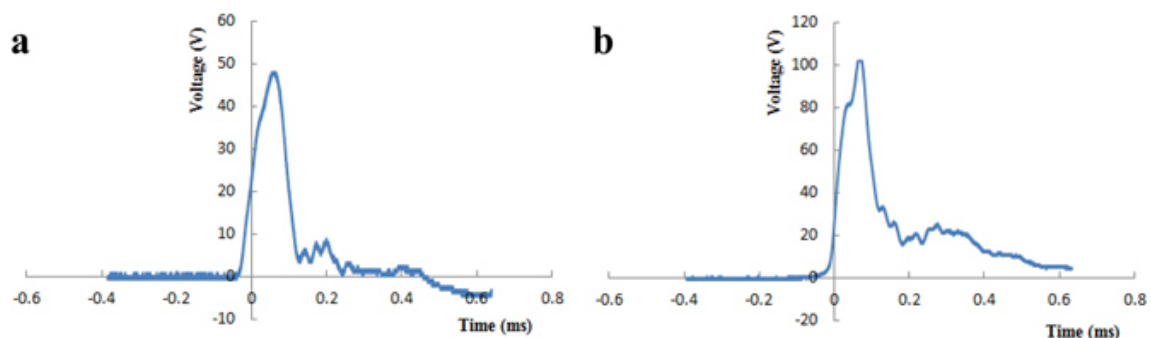


Figure 1.1 Waveform of an impulse load. Rabbits with femoral implants were loaded by dropping an impact mass, with a load of either 500 N (a) or 1000 N (b). Impulse loads were detected with a pressure sensor, resulting in a voltage, representative of the impact force, over time. Impulse loading results in a rapid peak load, and subsequent lower magnitude but high frequency ringing. This image is taken from (Diao et al., 2017), and reproduced under the terms of the Attributions 4.0 International (CC BY 4.0) license.

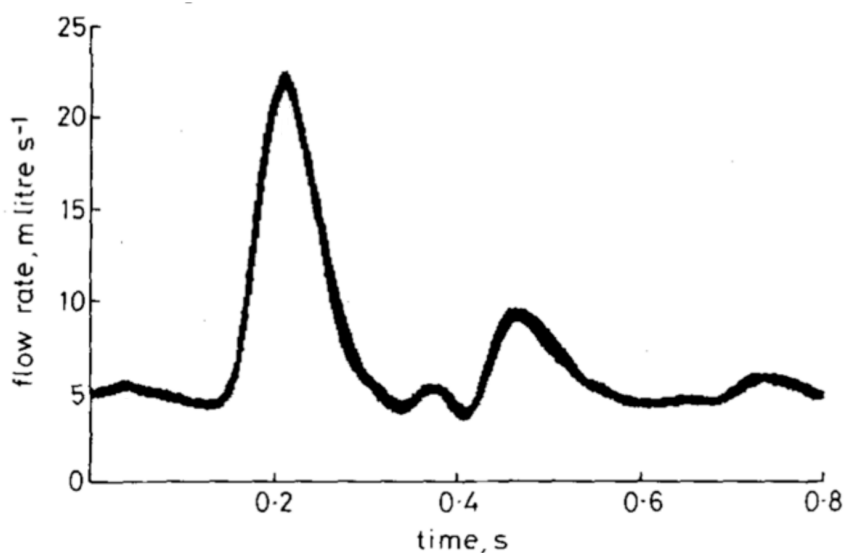


Figure 1.2 Average common carotid flow waveform. Two thousand repetitions of carotid flow simulated by a pump for the production of physiological flow waveforms. This arterial waveform displays the dynamic and time-dependent nature of blood flow rate within an artery. Reproduced with permission from (Holdsworth et al., 1991).

strain are addressed below, due to their relevance to and interconnectedness with the other modes of mechanical stimulation.

1.3.1 Tensile stress and strain

Strain (ε) is the measure of deformation (i.e. change in dimensions) caused by the application of an external force when stretching an object (Callister, 2001). It is defined as equal to the change in length (ΔL) of an object divided by the original length (L_0) of the object (Fig 1.3):

$$\varepsilon = \frac{\Delta L}{L_0}$$

Therefore, strain is a unitless dimension. Straining an object by stretching is achieved by applying a tensile force to the object. The stress (σ) imparted upon an object is equal to the force (F , in Newtons) that is used to stretch the object, divided by the cross-sectional area of the object (A , in square meters):

$$\sigma = \frac{F}{A}$$

The magnitude of strain experienced by a particular object at a fixed force is determined by the elasticity of the material that makes up the object, which is expressed as Young's modulus (Y). The Young's modulus (Pa) of a given material is equivalent to the stress divided by the strain, within the elastic region of an object's deformation (i.e. the region of strain values within which the object returns to its original shape after cessation of the applied force), and is given by:

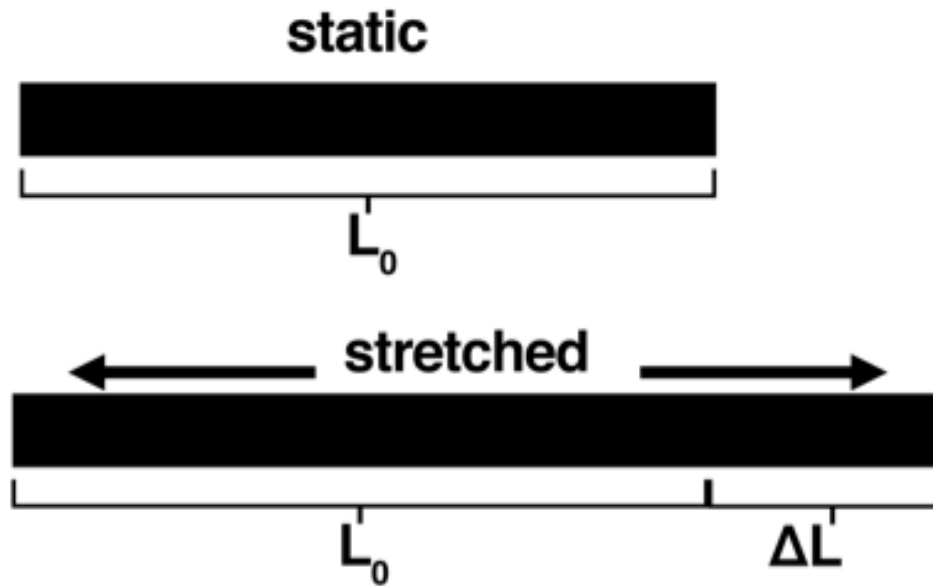


Figure 1.3 Physical strain due to stretching. As a tensile force is applied to the object, it changes its length and is strained. The degree of deformation is proportional to the material properties, defined by the Young's modulus, and the tensile stress (F/A).

$$Y = \frac{\sigma}{\varepsilon}$$

This system is governed by Hooke's Law, which states that, within this elastic region, the stress is directly proportional to the strain and the elastic modulus of the object.

Rearranging the Young's modulus gives us Hooke's Law:

$$\sigma = Y \cdot \varepsilon$$

Strain deformation is relevant in many human tissues, including both the skeleton (Yu et al., 2015) and the vasculature (Back et al., 2013). When a material, such as bone or blood vessel is stretched, the cells that adhere to the strained matrix are also deformed (Miller, 2017).

1.3.2 Fluid shear stress and fluid flow

Wall shear stress (WSS) due to fluid flow is the force generated when a viscous fluid flows over a surface (Cengel and Cimbala, 2018). When we consider the factors contributing to the shear stress (τ) generated by a fluid flowing along a surface, we are primarily concerned with a few factors of the system, including: the velocity of the fluid, the geometry of the fluid container, and the fluid's characteristics (i.e. viscosity and density). To understand the concept of shear stress, we can imagine a fluid-filled container with an overlying plate (Fig. 1.4). If we apply a force to the plate to slide it across the fluid surface, the layer of fluid in contact with the plate will move with the

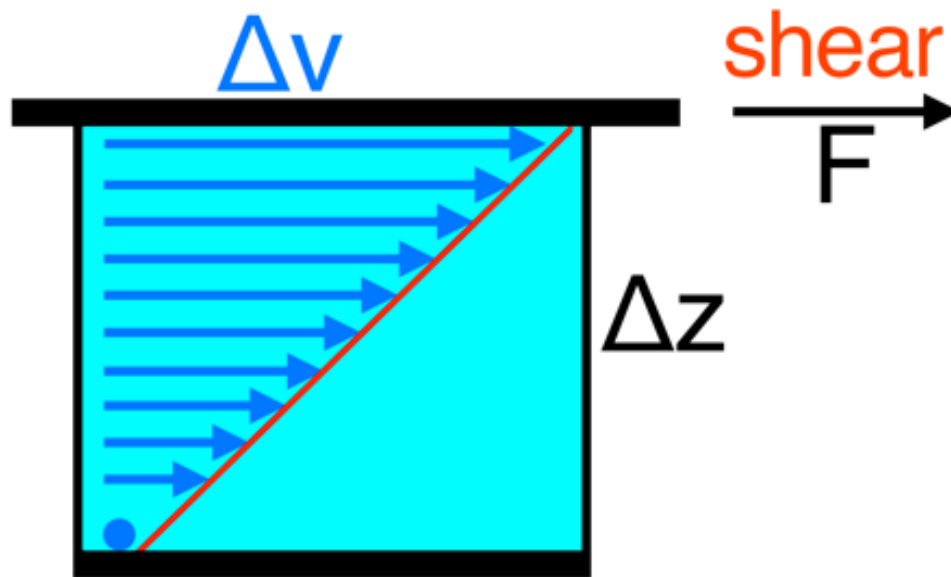


Figure 1.4 Shear stress is a function of viscosity and the velocity gradient. As the upper plate is moved along the surface at a velocity, it drags the fluid in contact with it due to viscosity. The stress caused by the interaction of the viscous fluid with the moving plate is shear stress and is equal to the slope of the change in velocity (v) over the change per increment in height (Δz).

plate. This is a no-slip fluid boundary condition that occurs due to viscous forces, where micro-scale interactions of the fluid's molecules with the plate have macro-scale effects on fluid behaviour. This viscous drag is proportional to the viscosity coefficient of the fluid (μ), which relates to the ratio of shear stress (F/A) applied to the velocity gradient ($\Delta v/\Delta z$) generated according to Newton's equation as:

$$\mu = \frac{F/A}{\Delta v/\Delta z}$$

$$\therefore \frac{F}{A} = \mu \frac{\Delta v}{\Delta z}$$

where F is force (N/m^2), A is area in m^2 , Δv is the difference in velocity (m/s), and Δz is the increment in height (m). The viscosity coefficient is therefore reported in units of $\text{Pa}\cdot\text{s}$, and is the coefficient of proportionality between the shear stress applied and the resulting velocity gradient, with increasing viscosity coefficient indicating higher shear stress for the same velocity gradient. Water (at 20°C) for example, has a viscosity of $1.0016 \text{ mPa}\cdot\text{s}$.

As the top lamina moves, these viscous forces will also interact within the fluid itself, and it will drag the lamina beneath it, and so on. This creates a velocity gradient within the fluid. As the velocity gradient reaches the bottom of the container, the final lamina of fluid in contact with the wall will have zero velocity. This is the same no-slip condition as observed at the wall of the moving plate. Shear stress is generated as a result of this velocity gradient, both between fluid laminae, and at the boundary between the fluid and the walls.

The linear velocity gradient is a simplification, and its true nature will depend upon the geometry of the flow container. For example, flow in a pipe (Fig. 1.5) has a maximal velocity of two-fold greater than that of the mean velocity. The maximal velocity occurs farthest from the effect of viscous drag on the walls, and therefore at the 3D-centre (centreline, and central plane) of the pipe. Shear stress at the wall can be calculated by evaluating the shear stress where height is equal to zero:

$$\tau = \mu \left. \frac{\Delta v}{\Delta z} \right|_{z=0}$$

Wall shear stress is an important parameter of fluid flow in biological systems. It is the quantity by which physiological responses to flow are evaluated. It is hypothesized to be a key force that cells detect in order to respond to flow in their local environment.

1.3.3 Acceleration and vibration

When an object in motion translates its position in space it is described as being displaced (Halliday et al., 2005). Displacement (D) in one dimension is calculated as:

$$D = \Delta x = x_1 - x_0$$

The rate of change of an object's displacement over time is expressed as the object's velocity (v), which is defined as:

$$v = dD/dt$$

Acceleration (a) is then defined as the rate of change of velocity over time (Fig. 1.6):

$$a = dv/dt$$

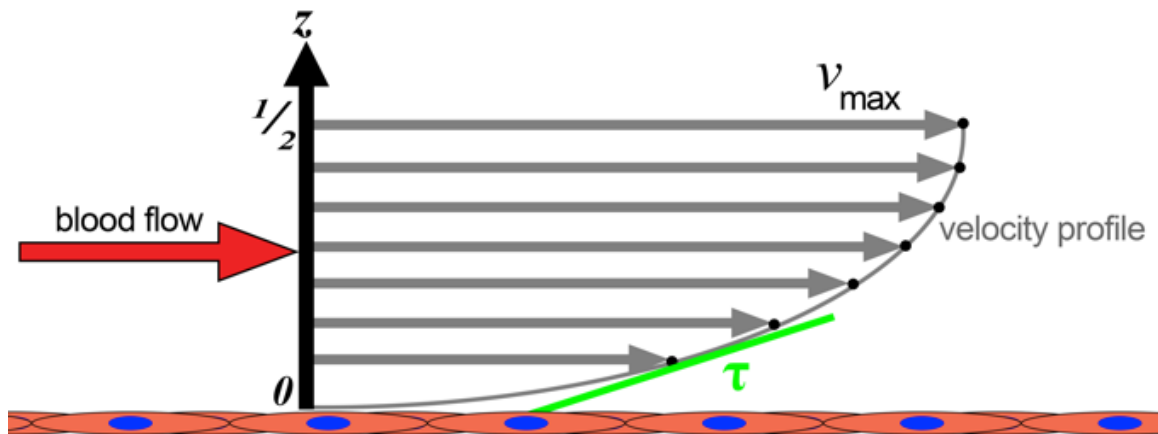


Figure 1.5 Shear stress due to blood flow in a vessel cross section. As fluid is pumped through a blood vessel, a velocity gradient is formed relative to the geometry of the vessel. The maximal velocity occurs at the centre of the vessel, and reaches zero at the vessel wall (no-slip). The vessel wall is lined by vascular endothelial cells, which are sheared by the flow of blood. The shear stress (τ) is equal to the viscosity multiplied by the velocity gradient (i.e. the slope of the velocity profile). Fluid flow also commonly occurs within in bone, for example, shearing osteocytes lining the lacunar-canalicular network.

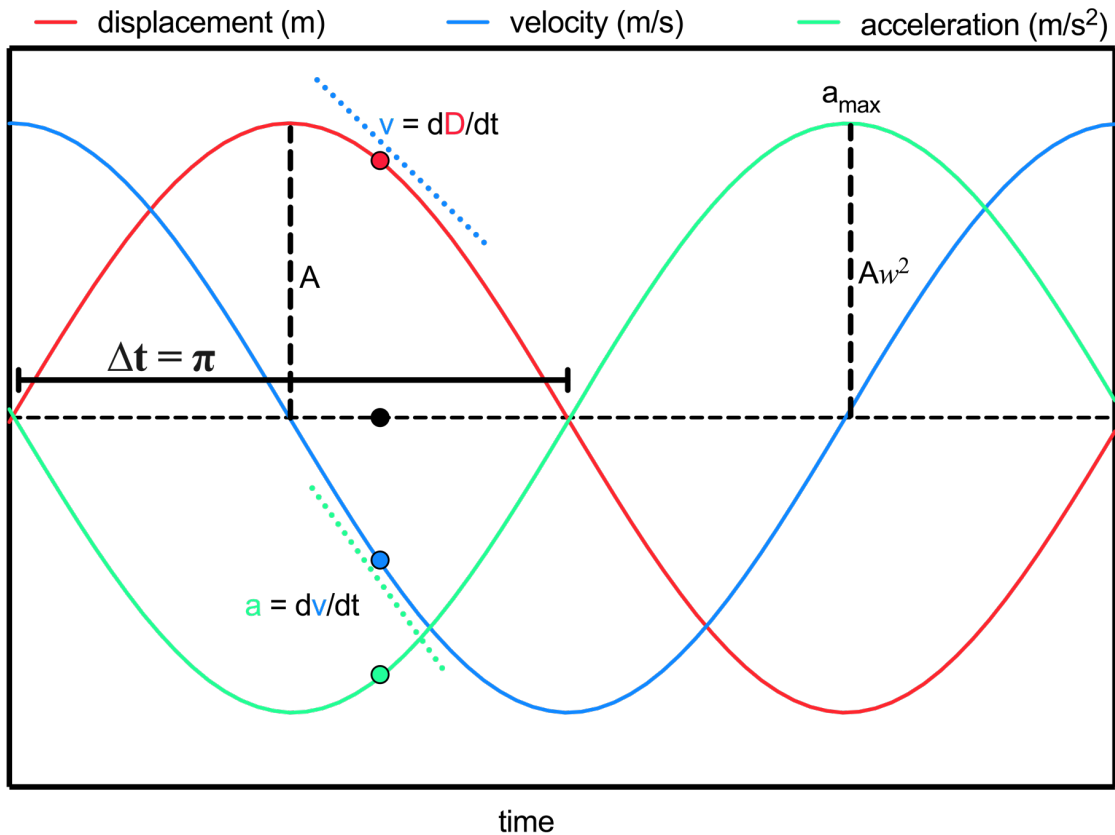


Figure 1.6 Relationship of acceleration to velocity and displacement during simple harmonic oscillations. As an object moves, its motion is described by a displacement (D , m), which is the difference between the object's starting and ending position. Velocity (v , m/s) is the rate of change of displacement (first derivative, dotted blue tangent) as a function of time. The rate of change of velocity (second derivative of displacement, dotted green tangent) is acceleration (a , m/s²). In simple harmonic oscillations, an object's motion is sinusoidal. Sinusoids are characterized by their frequency (f) and amplitude (A). Frequency is the inverse of the period ($T = 2\pi = 1/f$) and is the rate of cycles per unit time in Hz. Amplitude is the maximal distance from sinusoidal peak to baseline. Frequency, amplitude, and peak acceleration are all defined by the expression $a_{\text{peak}} = A(2\pi f)^2$. Dotted black line indicates sinusoidal baseline.

Dynamic accelerations (i.e. those that vary over time) can take many forms, the most fundamental being sinusoidal oscillations. Oscillating sinusoidal motion (y) described as a function of time takes the form of:

$$y = A \sin(\omega t)$$

where A is the amplitude (in meters), ω is the angular frequency of the motion over time (in radians per second), and t is time (in seconds). As we know that the first derivative of motion is velocity, we can describe the rate of change of sinusoidal motion as:

$$v = A \omega \cos(\omega t)$$

The rate of change of velocity can then be described as the acceleration by:

$$a = -A \omega^2 \sin(\omega t)$$

We can also describe the angular frequency as:

$$\omega = \frac{2\pi}{T}$$

where T is the period of the oscillation, or the time required to complete a sinusoidal cycle (in seconds). The period is therefore equal to the inverse of frequency (cycles per second or Hz).

$$T = \frac{1}{f}$$

Thus angular frequency can also be expressed as:

$$\omega = 2\pi f$$

If we then replace angular frequency with this equivalent expression when describing the acceleration of a sinusoidal oscillation, we obtain:

$$a = -A (2\pi f)^2 \sin (2\pi f t)$$

The acceleration reaches its peak value when $\sin(2\pi ft)$ reaches its peak value and is equal to 1, therefore:

$$a_{peak} = A(2\pi f)^2$$

Thus, the peak acceleration, amplitude, and frequency of a simple harmonic oscillator are all related to one another by this expression.

Acceleration is relevant in biology in several forms. All organisms on earth experience gravity, which is the force that of attraction between two masses towards each other. Constant acceleration due to the force of gravity (g) is equal to $\sim 9.8 \text{ m/s}^2$ at the surface of the Earth. The force of gravity is relevant to biology, and influences organismal development and physiology (Morey-Holton, 2003). Less obvious, but still thought to be important, are dynamic oscillating accelerations experienced as vibrations. Vibrations are commonly experienced in the modern world and can be relevant when operating motor vehicles or using power tools (Cardinale and Pope, 2003; Cardinale and Wakeling, 2005; Ozkaya et al., 1994). Sometimes these vibrations are of relatively high magnitude (peak acceleration $>1 \text{ g}$) and may have adverse biological effects (Charles et al., 2018; Kwaku Essien et al., 2018; Nilsson et al., 2017; Shen and House, 2017). It has recently been

hypothesized that human tissues are sensitive to low magnitude (<1 g), high frequency (>15 Hz) vibrations, known as LMHF vibrations (Fritton et al., 1997; Rubin et al., 2001). Upon impulse loading, the skeleton is vibrated and experiences high-frequency signals determined by the tissue's material characteristics (Guo and Teo, 2005; Kiiski et al., 2008; Pope et al., 1997; Randall et al., 1997; Rubin et al., 2003). Additionally, different parts of the body appear to have different transmissibility, depending upon their distance from the vibrational source and the surrounding structures (Hu et al., 2015; Kiiski et al., 2008).

Not only are the immediate mechanisms that detect and transduce vibrational mechanical stimuli unclear, their longer-term biological effects are equally murky. Early studies of LMHF vibration and their effects on human tissues were mostly focused on the effects of whole-body vibration (WBV) on the musculoskeletal system. Some investigators reported that vibration had anabolic effects on bone and catabolic effects on adipose tissue (Judex et al., 2003; Rubin et al., 2001; Rubin et al., 2002; Rubin et al., 2007). As well, WBV showed promise as a potential non-pharmacological intervention for serious pathologies such as osteoporosis (Gilsanz et al., 2006; Judex et al., 2002; Rubin et al., 2001). However, these findings have been controversial as other investigators have been unable to confirm these anabolic effects (Cardinale and Pope, 2003; Castillo et al., 2006; Iwamoto et al., 2005; Lynch et al., 2010; Roelants et al., 2004), or the clinical efficacy of WBV in populations most at risk (Merriman and Jackson, 2009; Slatkowska et al., 2011). Additionally, some investigators have reported that LMHF vibrational exposure has negative, degenerative effects on the musculoskeletal system in mouse models (McCann

et al., 2017). This uncertainty makes it paramount to further understand the cellular mechanisms underlying the process of vibrational mechanotransduction.

1.4 Mechanotransduction

1.4.1 Cellular mechanisms

Mechanotransduction is the process by which cells sense and respond to mechanical stimuli. It is an essential process to human physiology, and organisms have developed sophisticated cellular mechanisms to sense mechanical loads and strains, and convert them to biochemical signals. These biochemical signals can then be amplified and processed by second messengers, eventually affecting cell behaviour. In Fig. 1.7, we present a schematic of the timeline for mechanotransductive signaling processes in mammalian cells. This summarizes our laboratory's view of these processes (references are provided in the following sections).

A tissue is loaded mechanically, and the force applied stresses the cell. The cell experiences strain, which is detected by an initial mechanosensor (e.g. integrins, primary cilia, ion channels). This signal is amplified by the rapid release of ATP into the extracellular fluid. This ATP then functions as an autocrine and paracrine signal, binding to P2 nucleotide receptors on the plasma membrane amplifying the initial signal. The P2 receptors then activate various intracellular signaling pathways including, in many cases, elevation of cytosolic free calcium. These signals lead to the production and release of secondary signaling molecules (e.g. nitric oxide and prostaglandins). Gene expression

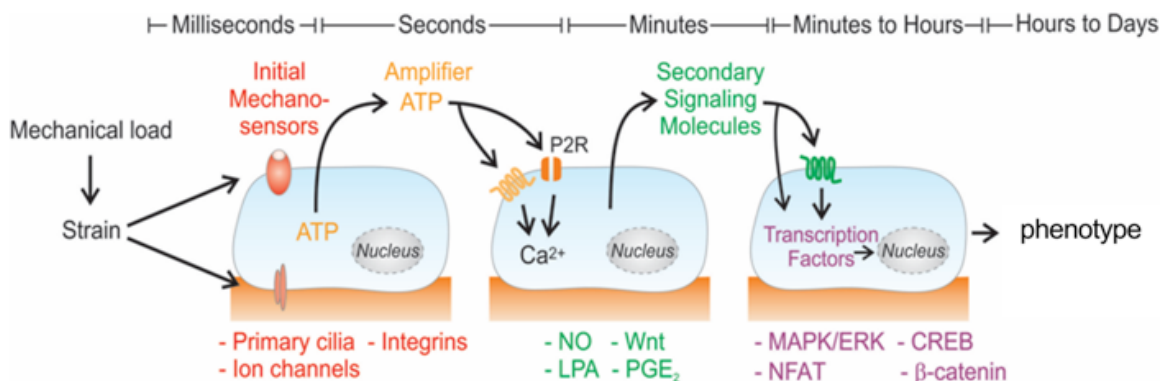


Figure 1.7 Schematic showing timeline of the molecular mechanisms involved in mechanotransduction. Following mechanical loading, the cell is stressed, imparting strain. The strain is detected by the initial mechanosensor. This leads to the release of extracellular ATP, often causing a transient elevation in cytosolic calcium levels. Further secondary signaling amplifies this response, leading to changes in transcription and eventually cell phenotype. The exact workings of these mechanisms remain unclear and likely vary depending on the nature of the mechanical load, the cell type, and its context. NO is nitric oxide, LPA is lysophosphatidic acid, PGE₂ is prostaglandin E₂, MAPK/ERK is the mitogen-activated protein kinases/extracellular signal-regulated kinases, NFAT is nuclear factor of activated T-cells, CREB is cAMP (cyclic AMP) response element-binding protein.

can then be altered by the activation of transcription factors (e.g. NFAT) that influence cell phenotype and fate.

1.4.1.1 Mechanosensors

The first step in the mechanotransduction signaling cascade involves sensation of the mechanical stimulus. As discussed above, mechanical stimuli can present in several different modes. Sensation of some of these mechanical stimuli is better understood than others. Below, we discuss a few of the candidate mechanosensors that have been proposed by others.

1.4.1.1.1 Stretch-activated channels

Stretch-activated ion channels (SACs) are transmembrane ion channels. More generally, they are referred to as mechanically sensitive ion channels. The basic function of these channels is to permit ion movement across the cell membrane. SACs play a role in the gating of many different ions, including Ca^{2+} , Na^+ , and K^+ . Here we focus on Ca^{2+} -permeable SACs and their relevance to mechanotransduction. As free- Ca^{2+} concentration ($[\text{Ca}^{2+}]$) is much greater in the extracellular space compared to the cytoplasm, functionally, their activation results in the elevation of cytosolic free- Ca^{2+} concentration ($[\text{Ca}^{2+}]_i$). They are part of a larger collection of Ca^{2+} entry channels (Deliot and Constantin, 2015), classified by their gating mechanisms, which include ligand-gated channels (e.g. P2X family) (Schmid and Evans, 2019), store-operated channels (e.g. Orai family) (Putney, 2018), and voltage-gated channels (Ca_v family) (Zamponi et al., 2015). Stretch-activated channels, as the name implies, are activated through stimulation with

mechanical stretch. The requirement of classification as a SAC is that the channel gates in response to mechanical stress – it does not imply physiological relevance (Sachs, 2010). Simply, a stress is applied to the cell membrane, stretching it. This strains the cell membrane, causing SACs within the membrane to open.

These channels are well known for their role in cardiac function (Reed et al., 2014), however they have also been implicated in cancer biology (Deliot and Constantin, 2015), among other pathologies. Piezo1 is a SAC that has been identified to play an important role in vascular mechanobiology (Murthy et al., 2017) and osteoblastogenesis (Sugimoto et al., 2017). TRPV4 has also been identified as a mechanosensor in mammalian cells. It is also a Ca^{2+} -permeable non-selective cation channel, known to play a role in the physiology of many tissues including the vasculature and the skeleton (Yin and Kuebler, 2010). Interestingly, although TRPV4 has been shown to be required for mechanotransduction in mesenchymal stem cells, it may not be sufficient alone. TRPV4 has been found to also co-localize with another proposed mechanosensor, the primary cilium (Corrigan et al., 2018). TRPV4 may not be directly activated by stretch, rather by ligand gating (Watanabe et al., 2003), however mechanical activation has been shown (Loukin et al., 2010).

1.4.1.1.2 Primary cilia

The primary cilium is a cellular structure that was previously hypothesized to be vestigial (Satir et al., 2010). It has more recently been implicated in playing an important, yet controversial role in cellular mechanotransduction (Delling et al., 2013; Delling et al., 2016). The primary cilium is similar to motile cilia in form, but not in function or

expression; it has a microtubular core structure but no motile function, and is found in nearly all cell types (Nguyen and Jacobs, 2013). Initial discoveries of primary-cilium-mediated mechanotransduction were made in the renal system, where primary cilia were found to not only sense fluid flow (Praetorius and Spring, 2001), but also to be essential for mechanotransduction (Praetorius and Spring, 2003).

The basic hypothesis of flow sensing by primary cilia is described as follows (Nag and Resnick, 2017). The cilium presents on the membrane of the cell. Extracellular fluid flows through the tissue (e.g. renal tubule, blood vessel, bone canaliculus) deflecting the primary cilium. This deflection strains a membrane protein (e.g. TRPV4) co-localized to the cilium. This initiates a downstream signaling cascade. The primary cilium is thought to orchestrate mechanotransduction through a Ca^{2+} -dependent mechanism. Studies have shown however that in canine kidney cells, the fluid shear sensing mechanism does not require primary cilia, but is mediated *via* ATP-dependent Ca^{2+} signaling (Rodat-Despoix et al., 2013). It has also been postulated that the primary cilium is localized near integrin-mediated cell-matrix attachments, providing a mechanism of membrane tension sufficient for mechanotransduction (Spasic and Jacobs, 2017).

1.4.1.1.3 Integrins

Integrins are membrane proteins that mediate cell-matrix attachment and also play a role in cell-cell attachments (Barczyk et al., 2010). They are a large family of dimeric proteins, and their subunit composition varies based on tissue expression. Generally, they bind large extracellular matrix (ECM) molecules such as collagen, fibronectin, vitronectin, and laminin, creating a link between the ECM and the cytoskeleton at sites

known as focal adhesion complexes. This anchoring role is important in cell adhesion, and is intimately related to the proposed mechanotransduction signaling function.

The classical integrin mechanotransduction mechanism is known as the tensegrity model (Ingber, 2008). It proposes that the cytoskeleton, due to its linkage to the ECM *via* integrins, is in constant homeostatic tension. Thus, when a mechanical stimulus arises, such as the stretch of the matrix to which the cell is attached, the tensile homeostasis is disrupted, which is sensed by integrin signaling complexes (Ingber, 1997). Upon application of force, the integrin changes conformation to stabilize its cell-matrix bond. Additionally, cytoskeletal proteins are recruited (e.g. talin) that can only bind to sites on integrin-related complexes (i.e. vinculin) exposed through stretching (Sun et al., 2016). Lastly, integrins are functionally related to SACs as they gate Piezo1 and TRPV4 in response to a force applied to the integrin (Ross et al., 2013).

Thus it is likely that these different mechanisms, along with those yet undiscovered, either vary in relevance based on cell type, or are part of a coordinated assembly of mechanotransduction complexes. Activation of these mechanosensors is the first step in the mechanotransductive cascade, followed by downstream biochemical signaling.

1.4.1.2 Downstream signaling

1.4.1.2.1 Nucleotides and cytosolic calcium signaling

Through the activation of mechanosensors, strain is transduced from a mechanical signal to a biochemical one. Cells release ATP in response to a myriad of mechanical stimuli, including fluid shear (Genetos et al., 2005) and vibration (Yamazaki et al., 2003). The

role of ATP release has been suggested as a mechanism to amplify downstream signaling cascades (e.g. Ca^{2+} signalling) (Suadicani et al., 2006). Beyond mechanotransduction, extracellular ATP has a vast range of biological effects, ranging from regulation of differentiation and proliferation, to more tissue-specific functions (e.g. vasodilation) (Volonte et al., 2006). ATP is considered to be an evolutionarily ancient signaling molecule, where aside from its metabolic function, likely has origins as an extracellular signal indicating danger to neighbouring cells (Burnstock and Verkhratsky, 2009). The exact mechanisms of ATP release from the cell are not clear. In recent studies, an exocytotic mechanism of ATP release in airway smooth muscle cells was identified (Takahara et al., 2014). Vesicular release has been observed in pre-synaptic neuron terminals and through ion channels in astroglia (P2X₇) (Pankratov et al., 2006). It has been suggested that, in urothelial cells at least, Pannexin 1 may mediate ATP release (Negoro et al., 2014). There have also been suggestions that ATP release is a fundamental response to membrane damage (Mikolajewicz et al., 2018).

Regardless of the mechanism, once ATP is released from the cell, it can interact with cell surface purinoceptors (Fig. 1.8). Purinergic signaling, although controversial following its initial proposition (Burnstock, 1972), is now accepted as a key mechanism in physiology and pathology (Burnstock, 2017). Purinoceptors are a large family of transmembrane receptors, whose subtypes include P1, P2Y, and P2X. Adenosine nucleoside transporters (e.g. ENT1) have also been proposed to play a role in modulating purinergic signaling (Pastor-Anglada and Perez-Torrás, 2018), but are not purinoceptors themselves. P1 receptors are G-protein coupled receptors (GPCRs) activated by extracellular adenosine. P2 receptors are subdivided into P2Y GPCRs and P2X ATP-

gated ion channels. Different receptor subtypes have distinct pharmacology. P2Y are more ligand promiscuous and are activated by both purine and pyrimidine nucleotides,

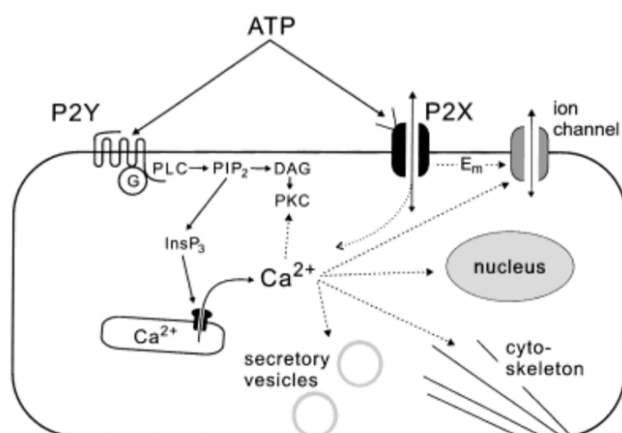


Figure 1.8 P2 receptor signaling pathways. Extracellular ATP signals through cell-surface P2 receptors to initiate the transient elevation of cytosolic free Ca²⁺. P2 receptors can either mediate release of Ca²⁺ from intracellular stores, or ion entry from the extracellular space. Reproduced with permission from (Dixon and Sims, 2000).

whereas P2X is more specific for ATP and its analogs (Ralevic and Burnstock, 1998). In mammals, the P2Y family is comprised of 8 subtypes, and the P2X family is comprised of 7 subtypes (Boeynaems et al., 2005; Erb et al., 2006). P2 expression is tissue dependent, however both P2Y and P2X are widely distributed, and both are present in the vasculature (Burnstock, 2016) and musculoskeletal systems (Orriss, 2015).

In many cases, activation of P2 receptors leads to downstream $[Ca^{2+}]_i$ signaling. In response to nucleotide binding, P2X channels open, allowing the entry of extracellular Ca^{2+} . Several P2Y receptors are coupled through G proteins to activation of phospholipase C (PLC). PLC activity generates inositol 1,4,5-trisphosphate (IP_3) and diacylglycerol (DAG). IP_3 then activates IP_3 receptors on the endoplasmic reticulum (ER), allowing flux of Ca^{2+} from the ER to the cytoplasm (Dixon and Sims, 2000). Therefore, elevation of cytosolic free Ca^{2+} can be due either to influx of extracellular Ca^{2+} or release of Ca^{2+} from intracellular stores.

Cytosolic Ca^{2+} is an important second messenger with functions ranging from life and death of the cell, and nearly everything else in between (Berridge et al., 1998). Cytosolic free Ca^{2+} (Ca^{2+}_i) is another example of an evolutionarily ancient signal, and plays an essential role in unicellular and multicellular organisms (Carafoli and Krebs, 2016). It is considered to be a master regulator of cell function and, as such, the cell has developed a sophisticated toolkit with which to manipulate this pathway (Berridge et al., 2000). In very simple terms, Ca^{2+}_i can be considered as a binary on/off switch. The cell, through great effort, sustains extremely low concentrations of cytosolic free Ca^{2+} (~100 nM) in the resting state. When activated, free Ca^{2+} may rise a full order of magnitude in concentration (to ~1 μ M). The fundamentals of the Ca^{2+} signaling toolkit are as follows:

1) a stimulus turns on the Ca^{2+} signaling cascade, 2) Ca^{2+} mobilizing signals increase $[\text{Ca}^{2+}]_i$, 3) Ca^{2+} -dependent signaling processes occur, and 4) cellular machinery restores $[\text{Ca}^{2+}]_i$ to the resting state. It should be noted that it is now recognized that Ca^{2+} signalling is not a simple on/off system, but an extremely complex spatiotemporal signal within cells (Berridge and Dupont, 1994). This underscores the potential importance of devices that would enable real-time Ca^{2+} imaging in live cells during – or immediately following – mechanical stimulation.

One of the best-known Ca^{2+} -dependent signaling molecules is calmodulin (CaM). It is a primary sensor of $[\text{Ca}^{2+}]_i$ and classically plays a role in the contraction of smooth muscle cells (Walsh, 1983). Its calcium sensing ability comes from its structure. It has four EF-hand domains, which are helix-loop-helix motifs that bind ionized Ca^{2+} (Gifford et al., 2007). CaMs function as Ca^{2+} sensors and activate proteins, often phosphatases and kinases, which are unable to interact with Ca^{2+} directly. These CaM-dependent proteins can then go on to regulate the activity of multiple effectors, influencing protein activity and gene expression.

The off reactions returning $[\text{Ca}^{2+}]_i$ to its basal levels are the last part of the toolkit. When calcium levels are sufficiently high, a variety of Ca^{2+} pumps and exchangers are activated, transporting Ca^{2+} out of the cytoplasm, and either back into intracellular stores or the extracellular space. This is a critical aspect of Ca^{2+} signalling, as extended levels of high $[\text{Ca}^{2+}]_i$ are destructive to the cell, eventually leading to apoptosis (Orrenius et al., 2003).

Ca^{2+} signaling is organized, not just through the exquisite control of baseline $[\text{Ca}^{2+}]_i$, but also through precise spatiotemporal dynamics. In terms of spatial control, $[\text{Ca}^{2+}]_i$ can occur as subcellular sparks or puffs depending on the source, and are constructed from fundamental events known as quarks or blips. Alternatively, $[\text{Ca}^{2+}]_i$ waves, constructed from elementary events, can be generated and range from subcellular, to whole cell, and even intercellular signals (Abu Khamidakh et al., 2013; Huo et al., 2010; Jing et al., 2013; Jorgensen et al., 1997). They are a product of positive feedback loops as neighbouring Ca^{2+} -sensitive receptors are activated by local elementary events. Temporally, $[\text{Ca}^{2+}]_i$ can be a cyclical signal persisting from seconds to hours. Since sustained signaling is harmful, it is rapidly switched on and off, and the frequency of these transients encodes information to the cell regarding function.

As previously stated, $[\text{Ca}^{2+}]_i$ is a master regulator of cell signaling, however it is not the only way cells mediate signaling from sensor to effector of a mechanotransduction pathway. Next we highlight some downstream Ca^{2+} -dependent and independent mechanisms of cellular mechanotransduction.

1.4.1.2.2 Other secondary mechanisms contributing to mechanotransduction

Following initiation of mechanotransductive signaling, a host of downstream signaling cascades can be activated, influencing cellular behaviour. The pathways that are involved will depend on the type of stimulus applied, the parameters of that stimulus, and the type of cell. Here we review selected secondary mechanisms that cells use to bridge the gap from stimulus to effector.

One mechanotransductive pathway in bone cells that has been characterized is the production of prostaglandin E₂ (PGE₂) induced by fluid shear stress following its detection by the primary cilium (Malone et al., 2007). PGE₂ is a mediator of inflammation, and as such, its production is a common target of anti-inflammatory drug intervention (Rao and Knaus, 2008). In bone cells, it stimulates osteoblastogenesis, as well as bone formation and resorption (Li et al., 2005). PGE₂ is a fatty-acid chain biosynthesized from arachidonic acid (AA) *via* cyclooxygenase (COX) enzyme activity (Park et al., 2006). The expression of COX-2 in bone cells is itself induced by fluid shear (Li et al., 2005). AA, the precursor to PGE₂, is cleaved from membrane phospholipids by the enzyme phospholipase A₂ (PLA₂). Certain PLA₂ isoforms are activated by elevation of [Ca²⁺]_i; however there are Ca²⁺-independent PLA₂s as well (e.g. iPLA₂β in bone) (Ramanadham et al., 2015). In kidney cells, this mechanotransduction pathway was found to be Ca²⁺-independent (Malone et al., 2007). However, others have shown that mechanically induced PGE₂ release from osteoblasts can occur by an ATP- and Ca²⁺-dependent mechanism (Genetos et al., 2005).

Another mechanotransduction pathway reported is the generation of nitric oxide (NO) in response to fluid shear stress. NO is a free radical gas that is also a signaling molecule (Bryan et al., 2009). In vascular endothelial cells, NO is generated in response to shear stress through induction of endothelial nitric oxide synthase (eNOS). Both Ca²⁺-dependent and -independent mechanisms can mediate the shear stress eNOS response. Following NOS activation, NO is produced, diffuses through the cell membrane, and activates guanylyl cyclase in neighbouring vascular smooth muscle cells (Sprague et al., 2010). This leads to vasodilation of the blood vessel. NO has also been implicated in

mediating the effects of mechanical loading on bone by enhancing formation and suppressing resorption (Bakker et al., 2001; Johnson et al., 1996).

1.4.2 Biological roles and significance of mechanotransduction

The aforementioned steps in the mechanotransduction pathway can often lead to changes in gene expression. For example, shear stress in vascular endothelial cells has been shown to regulate the expression of as many as 350 genes (Wragg et al., 2014). In bone, the family of transcription factors known as NFAT play an important role in osteoblast differentiation and the regulation of bone mass (Koga et al., 2005; Winslow et al., 2006). NFAT2 has been found to be activated in response to fluid shear stress through a Ca^{2+} -dependent/COX-2 mediated mechanism, thought to originate from $\beta 1$ integrins and P2 purinergic signaling (Celil Aydemir et al., 2010).

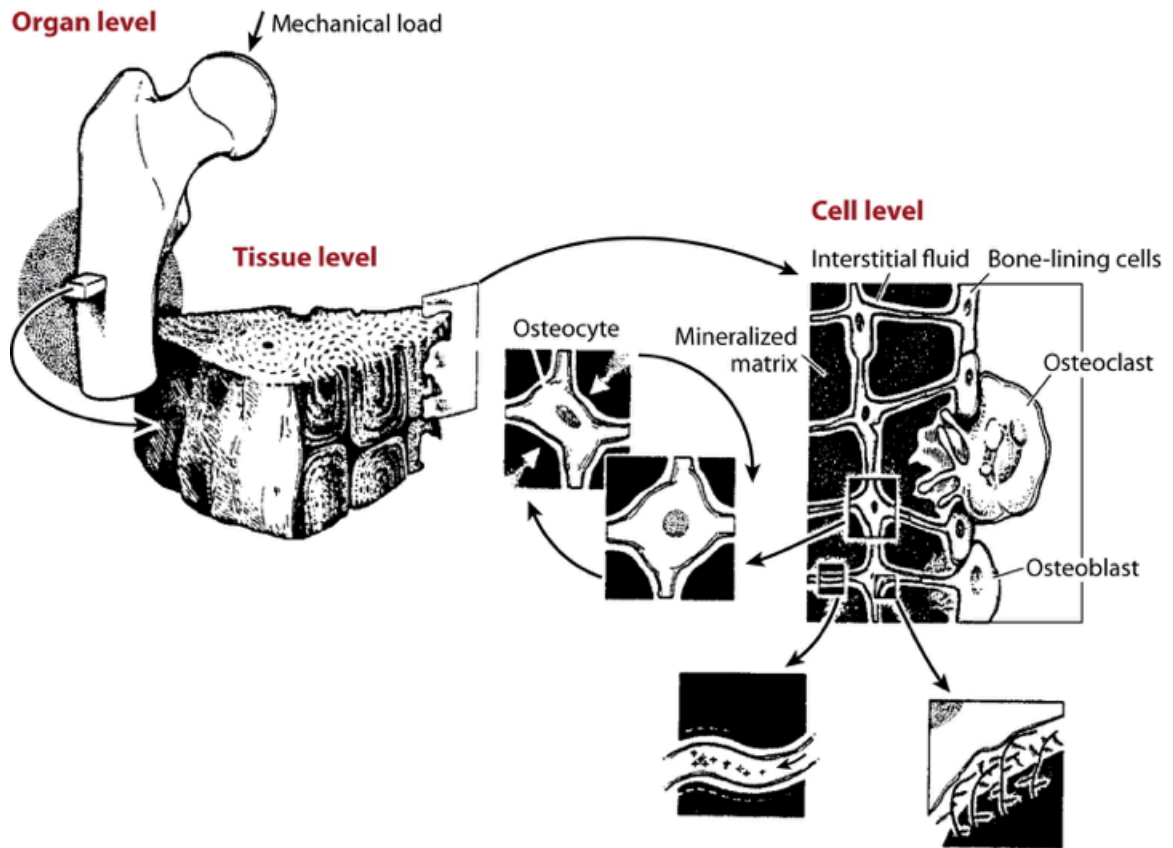
1.5 Bone

1.5.1 Bone biology and mechanotransduction

The skeleton is an organ system that has several roles in human physiology. It is often viewed as a static frame with only structural functions. Indeed, it plays an important role as the supporting system for the human body. However, we now know that bone is a dynamic organ that is constantly changing, with complex endocrine functions as well. Aside from its well-known function in mineral homeostasis (Fukumoto and Martin, 2009), bone influences glucose sensitivity and testosterone secretion (Guntur and Rosen, 2012).

The primary cells of bone are osteoblasts, osteocytes, and osteoclasts. The osteoblast is derived from the mesenchymal stem cell lineage. The osteoblast secretes matrix and then differentiates into either a bone lining cell or an osteocyte, or undergoes apoptosis. Osteocytes are terminally differentiated matrix-embedded cells. Bone is maintained and repaired through remodeling, an active process involving all the aforementioned bone cells in a cycle of resorption coupled with formation. Osteoclasts are the bone resorbing cells, while osteoblasts form new matrix to be mineralized, and then are embedded in the matrix and differentiate into osteocytes. These cell types work together to form the basic multicellular unit of bone remodeling. Mechanical stimulation is thought to be a major regulator of bone formation (Pead et al., 1988). Osteocytes, with their vast networks of intercellular connections through gap junctions, have been proposed to play an important role in sensing, transducing, and transmitting responses to mechanical stimuli (Bonewald, 2011; Robling et al., 2006).

Perhaps surprisingly, fluid flow is thought to be an important player in bone biology. An interstitial fluid occupies the porosities in bone surrounding osteocytes and their processes. These porosities are known as the lacunar-canalicular network, and are comprised of the spaces surrounding osteocyte cell bodies (lacunae) and the channels surrounding osteocyte processes (canaliculi). The interstitial fluid is important for tissue metabolism and cell communication, however, it is also thought to influence bone biology by flowing in response to the mechanical loading of bone (Fritton and Weinbaum, 2009). The basic hypothesis of lacunar-canalicular fluid flow is as follows (Fig. 1.9). A mechanical load is applied to the bone, deforming it slightly. This deformation causes fluid movement in the lacunar-canalicular network, mechanically



AR Fritton SP, Weinbaum S. 2009.
 Annu. Rev. Fluid Mech. 41:347–74

Figure 1.9 Mechanobiology of bone: lacunar-canalicular fluid flow. Upon loading of the bone, the tissue is deformed, and interstitial fluid is ejected in response. Interstitial fluid will then shear osteocytes within the bone matrix, initiating communication with nearby osteoblasts and osteoclasts regarding the nature of the shear stress. Reproduced with permission from (Fritton and Weinbaum, 2009)

stimulating osteocytes. The magnitude of fluid shear stress in bone is thought to range from approximately 1 to 3 Pa (Weinbaum et al., 1994). The cyclical nature of interstitial fluid flow is more difficult to assess, and is dependent on both the rate of loading, and the frequency of oscillations that result from each load. However, it has been established that frequencies in the tens of Hz are likely relevant (Malachanne et al., 2011).

The influence of mechanical forces in bone biology is pervasive (Klein-Nulend et al., 2005). Along with hormone levels, mechanical loading is a primary regulator of bone remodeling. This allows bones to adapt to their loading environment, strengthening bone in response to increases in mechanical loading. This strengthening of bone is mediated by depositing new bone (increasing the bone mass), and aligning remodeled bone in the axis of loading. The mechanical loads are also thought to orchestrate the coordination among the basic multicellular units of bone remodeling, where fields of high strain signal bone formation, and fields of low strain signal bone resorption.

1.5.2 Mechanically related bone diseases and dysfunctions

Due to the importance of mechanical signals in health, mechanotransduction gone awry will lead to pathology (Jalouk and Lammerding, 2009). The impact of skeletal disease on modern healthcare is under-recognized. Up to 33% of people on earth suffer from a musculoskeletal condition – many of which are mechanically related (Collaborators, 2017). Part of this under-representation in medicine is possibly due to the lack of options for intervention, a symptom of the lack of understanding of many basic mechanotransductive processes. Mechanically related bone disease can stem from insufficient or excessive loading, aberrant signaling, or genetic abnormalities. Disuse

osteoporosis is the loss of bone mass due to insufficient mechanical loading. This is known to occur during periods of extended micro-gravity (Bloomfield, 2006; Burger and Klein-Nulend, 1998) or prolonged bed rest (Abramson and Delagi, 1961; Takata and Yasui, 2001). During these periods of disuse, the skeleton detects the lack of mechanical stimulation and disassembles bone (Penley et al., 2002; Rogers et al., 1999). An estimated 1 to 2% of bone mass is lost for every month in micro-gravity (Ulbrich et al., 2014). The exact mechanisms for micro-gravity-induced bone loss are unclear, but there is evidence that micro-gravity increases osteoclast resorption, while simultaneously compromising osteoblast cellular integrity (Nabavi et al., 2011). Additionally, micro-gravity has been shown to disrupt bone cell function (Grimm et al., 2016).

Aberrant mechanotransductive signaling has been implicated in osteoarthritis, spondyloarthritis, osteo- and chondro-sarcoma, degenerative disk disease, and osteoporosis (Spyropoulou et al., 2015). Osteoporosis, a disease common in the elderly and characterized by low bone mass, has been heavily investigated for its links to mechanotransduction. Bone-cell differentiation from mesenchymal stem cells is coupled with mechanical loading, and ageing has been shown to reduce this responsiveness through an ERK1/2 pathway (Joiner et al., 2012). Additionally, aged osteoblasts show reduced calcium signaling, and dysregulated NO, PGE₂, and COX-2 signaling.

It is clear that mechanical loading is essential to the structural and functional properties of the human skeleton. In the following section, we introduce some basics of the vasculature; another organ system whose physiology and pathology is intimately coupled to mechanical loading.

1.6 Vasculature

1.6.1 Vascular biology and mechanotransduction

At a glance, the vasculature of the human body may appear to be little more than a passive network of pipes, mediating blood transport and therefore tissue oxygenation.

Indeed, if this were the only function of the vasculature, its significance to human health would still be overwhelming. However, the current understanding of vascular biology has advanced such that we know the role of the vasculature is that previously mentioned and much more (Conklin, 2014). Briefly, some of these less-known functions include, but are not limited to, inflammation, organ formation and regeneration, wound and fracture healing, and stem cell behaviour (Ramasamy, 2017; Ramasamy et al., 2015).

Simply described, the vascular system is comprised of the heart – the pump from which blood flow is generated; and the vasculature – the vessels that mediate the flow of blood throughout the body (Mohrman et al., 2018). The systemic vasculature is divided into arteries and veins – vessels that either deliver oxygen-rich blood to the body, or return oxygen-depleted blood to the heart, respectively. Beyond this distinction, vessels are further described by their size, ranging from large vessels up to 3 cm in diameter (e.g. aorta), to microvessels as small as 5 μm in diameter (e.g. capillaries). As we can imagine, this high-degree of variability within the vasculature results in a wide range of hemodynamic conditions and vascular function. The basic structure of a vessel can be described in three layers, the intima, media, and adventitia. Briefly, the intima is the inner layer of the vessel, describing the vessel wall comprised of vascular endothelial cells (VECs). These VECs line the inside of blood vessels and directly contact the flowing

blood. The media is the middle layer of the vessel; it is mainly composed of vascular smooth muscle cells (SMCs) in arteries, and connective tissues in veins. The adventitia is the outer layer of the vessel; it is mainly composed of the structural ECM proteins collagen and elastin (in arteries). The microvasculature has its own structure. For example, capillary bed microvessels have a wall that is one endothelial cell thick. This structure relates to their function in controlling the movement of molecules between blood and tissue.

Significant discoveries in the role of mechanical loads and forces in vascular physiology have been made over the decades. As mentioned previously in this chapter, the vessel maintains the ability to modulate its diameter in response to stress on the vessel wall through an NO-mediated signaling mechanism. This ability for the vasculature to self-regulate and optimize its resistance to flow – as the result of coordinated action between multiple cell types all converging within minutes (Gerlach et al., 1993) – is a truly profound example of mechanotransduction in human physiology.

VECs can discriminate between different forms of fluid flow. They are able to decrypt the information encoded into shear-stress stimuli over complex range of variables such as shear magnitude, direction, and time-dependent frequency. This capability is readily observed *in vivo*. This ability of VECs to discriminate between different flow paradigms has been established in the literature (Helmlinger et al., 1991). This situates blood flow dynamics as crucial to the physiology and dysfunction of VECs, a topic discussed in the following section.

1.6.2 Mechanical vascular disease and dysfunction

The impact of vascular disease on human health is staggering. It is a leading cause of death worldwide, and as many as 25% of deaths globally can be attributed to cardiovascular diseases (Mc Namara et al., 2019). One disease that carries a sizeable portion to blame for this burden is atherosclerosis, as the major global cause of morbidity and mortality (Rafieian-Kopaei et al., 2014). Atherosclerosis is a disease characterized by fatty inclusions in the intima and media of arteries, leading to hardening of the vessel, and eventually, clot formation and thrombosis. Atherosclerotic lesions manifest in predictable regions of complex flow (naturally occurring bends and bifurcations of the vasculature, Fig. 1.10a). This is indicative of the ability of VECs to discriminate between different types of flow. The susceptibility of VECs to atheroprone flow disturbances (deviations from the atheroprotective physiological pulsatile, uni-directional flow) is a major focus of vascular mechanotransduction researchers (Fig. 1.10b). It has been

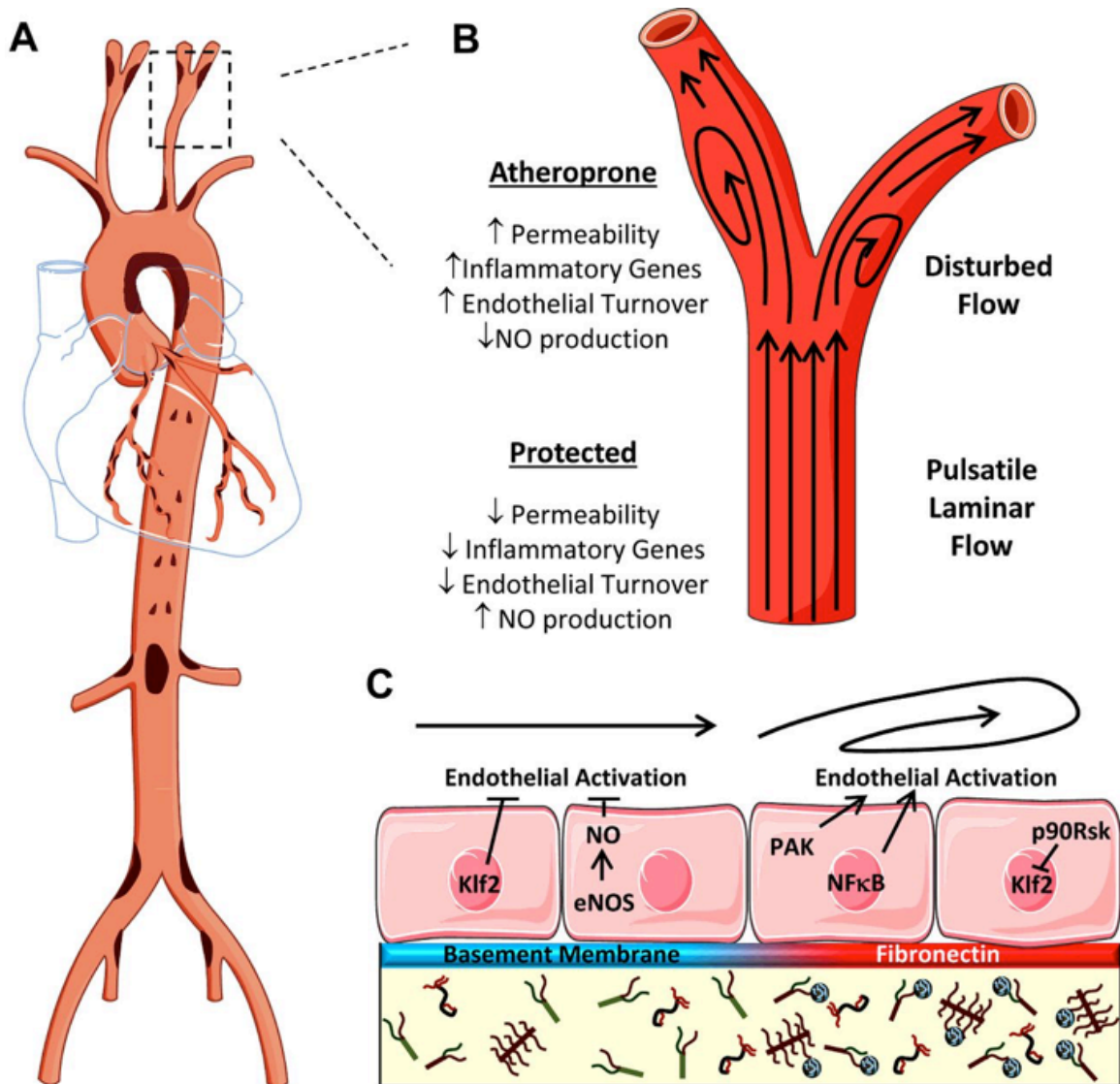


Figure 1.10 Hemodynamics and endothelial cell related vascular disease. a) Atheroprone regions (dark brown) in the arterial tree. b) Effects on the vasculature of atheroprone (disturbed) flow, and atheroprotective (uni-directional, pulsatile laminar) flow. c) Endothelial cell activation is inhibited by atheroprotective flow and induced by disturbed flow. Reproduced with permission from (Yurdagul et al., 2016).

suggested that this is due to an inability of cells to acclimate themselves to the constantly changing shear vectors (Hahn and Schwartz, 2009). Indeed, the behaviour of VECs in response to stimulation with disturbed flow *in vitro*, emulates the signaling changes seen in endothelial dysfunction (Zhou et al., 2014a). Endothelial cells have been shown to activate in response to disturbed flow (Fig. 1.10c). Endothelial activation and dysfunction are convergent mechanisms that both lead to vascular disease (Liao, 2013). Activated endothelial cells express cell-surface molecules associated with leukocyte adhesion, an important step in endothelial pathologies, which is initiated by flow disturbances (Gimbrone et al., 1997). Dysfunctional endothelial cells have inhibited NO signaling; a key protective factor for vascular health that is normally upregulated by atheroprotective flow. Despite the clear medical relevance, the earliest steps in endothelial responses to flow disturbances remain incompletely described, and this is due to a lack of technology.

The prevalence of mechanotransduction in physiology and pathology is clear, and researchers have probed this topic with great depth and breadth. However, gaps in the knowledge base still remain, especially in the nature of immediate, transient, mechanotransductive signalling. In the following section, we review some of the established tools to study mechanotransduction that have been reported in the literature.

1.7 Methods to study mechanotransduction

1.7.1 Vibration

As previously mentioned in this introductory section, the bulk of research into the physiological effects of vibration has been done with WBV. Though less prevalent, there has also been relevant work done investigating the responses of cultured cells to vibrational stimuli. A selection of these methods are discussed in this subsection.

The most common way to apply vibration stimuli to cells is with an electromagnetic shaker. This type of device works on the same fundamental premise as a speaker. A wound copper coil creates an electrical field, and when driven with current, creates a displacement to a permanent magnet (Fig. 1.11) (Michael Delaine-Smith et al., 2015). Most studies examine the long-term effects of vibration on cells, often evaluated by assaying changes in gene expression. Kim et al. found that mesenchymal stem cells chronically vibrated at 90 Hz and 0.3 g showed an increase in the expression of type 1 collagen, osteoprotegerin (OPG), and vascular endothelial growth factor (VEGF); however, this response was only found in 3D-cultures, and not observed in 2D-cultures (Kim et al., 2012). In another study, osteoblast-like cells MC3T3-E1 chronically vibrated over a range of accelerations at 40 Hz were found to increase their expression of Wnt10B and OPG, while decreasing their expression of sclerostin and RANKL (Hou et al., 2011).

Given the transient nature of $[Ca^{2+}]_i$, it is a difficult ion to measure reliably without a device integrated directly into the imaging system. Researchers have attempted to observe $[Ca^{2+}]_i$ immediately following vibration, and found that $[Ca^{2+}]_i$ was

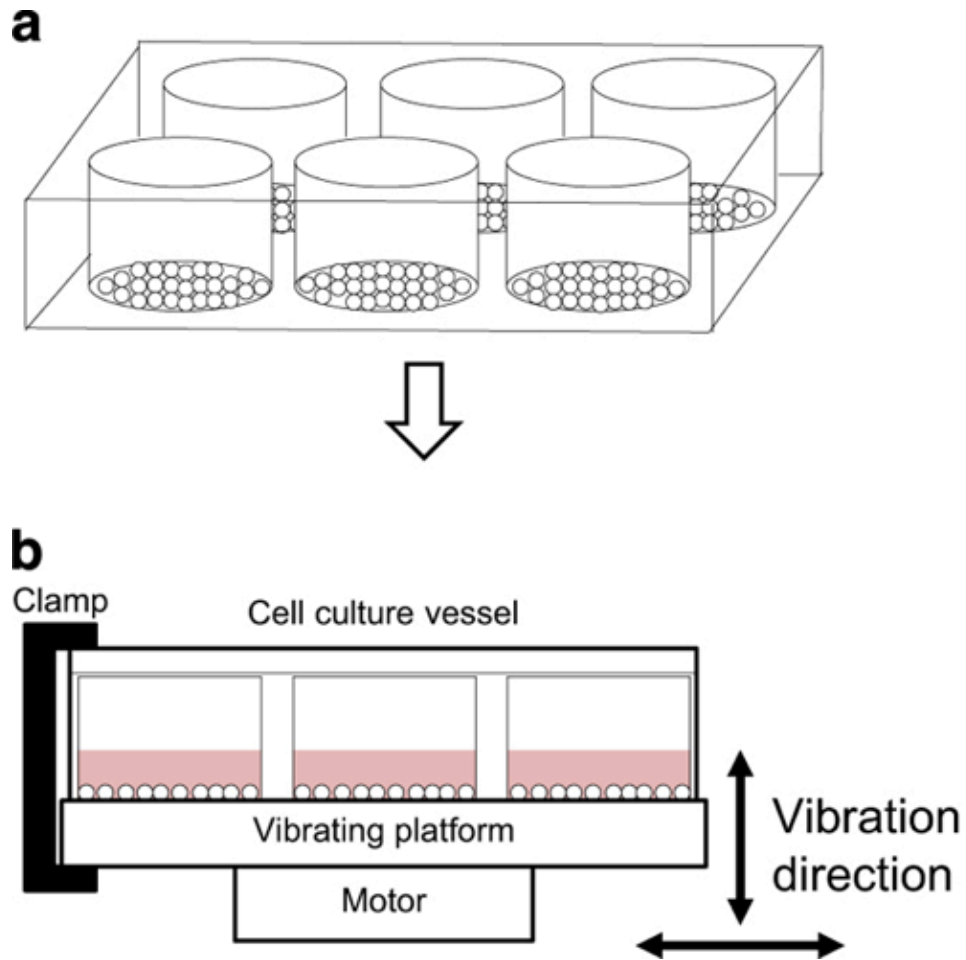


Figure 1.11 Vibration of live cells *in vitro*. Electromagnetic shakers are commonly employed by researchers to vibrate cell cultures. Cells are typically grown in wells, then transferred to the vibration device for experimentation. Vibration is usually delivered vertically, i.e. normal to the cell surface, however horizontal vibrations (parallel to the cell surface) are also possible. Minimal fluid shear is delivered using this method of vibration. Reproduced from (Michael Delaine-Smith et al., 2015) under CC BY-NC-ND 3.0 US license.

significantly increased in osteocyte-like cells vibrated for one hour at 90 Hz and 0.04 g (Wu et al., 2016). In this study, Wu et al. applied “vertical” vibrations (i.e. normal to the surface of the cell culture dish) to MLO-Y4 with an electromagnetic shaker. Their conclusion is suspect however. The use of non-ratiometric dye (like fluo-4 used in the referenced study) to evaluate $[Ca^{2+}]_i$ between different samples is troublesome as it does not account for parameters like cell thickness and unequal loading. Also, having to transfer cells from a vibration device to the microscope creates the opportunity for unintentional mechanical loading of cells during the transfer procedure. Interestingly though, they note that according to the finite element model of the cell they constructed, shear stress in general should provide higher magnitudes of deformation relative to the force applied when compared to vibration. Also, they indicated that, in their finite element model at least, cells might have resonant frequencies at 34, 86, 104, 149, and 163 Hz. This information could be useful, as vibrations at these magnitudes may have amplified deformations.

Another study claims to vibrate cells during imaging yields a $[Ca^{2+}]_i$ response at 220 Hz (Nishitani et al., 2015). In their experiment, the cell was not experiencing a vibrational displacement as could be interpreted; rather, it experienced a membrane strain. The investigators cyclically deformed the gelatinous membrane to which the cells are adhered with a vibrating rod. This stretches the gel, applying tensile strain on the cells.

Nanokicking is a relatively recently described type of vibrational stimulus that is so-named due to its ultra-low, nano-scale displacement. It uses the same concept as LMHF vibration, but at even lower magnitudes and even higher frequencies (Robertson et al., 2018). Nanokicking has already shown to be a potentially potent mechanical stimulus.

Recent studies have found 5 kHz of nanovibrational stimuli to significantly augment the expression of osteogenic factors (Pemberton et al., 2015).

1.7.2 Fluid flow and microfluidics

The cellular responses to fluid flow have been studied in depth the past quarter century. More remains to be discovered regarding these mechanisms, especially the earliest steps in the pathways. In the present subsection, we discuss a selection of methods for studying the responses of live-cells to fluid flow.

Many modern studies investigating the biological effects of fluid flow are done in microfluidics (Polacheck et al., 2013). Parallel plate and other flow chambers were most commonly used in the initial studies for imaging live-cells during flow (Alford et al., 2003; Hung et al., 1995; Nauman et al., 1999; Sirois et al., 1998; Yellowley et al., 1997). Both techniques have their advantages but traditional parallel plate flow chambers have become less common with the rise of microfluidics. Custom microfluidic devices can be designed and built rapidly. microfluidics due to their small volumes use fewer reagents and can therefore be cost-effective, and microfluidic geometries are relevant in scale to many physiological flow situations (e.g. microvasculature). Microfluidics can be fabricated by a variety of different methods. The method that is selected will depend on your application, technical skills, and available resources. Microfluidics can be incredibly difficult to manufacture and require enormous financial investment, but they can also be low-cost and accessible to non-engineers (Lorusso et al., 2016; Nguyen et al., 2018). Laminates, molding, 3D printing, and nanofabrication are the most common families of microfluidic fabrication methods (Gale et al., 2018). Not all microfluidics are compatible

with live cells. The construction material generally determines the biocompatibility. For biocompatibility, devices generally must be oxygen permeable, and cells must be able to adhere either naturally or with surface treatment. These are major reasons why PDMS has become so popular as a microfluidic construction material (Halldorsson et al., 2015).

While PDMS is certainly not the ideal material (Berthier et al., 2012), it has been useful in cellular studies for many years (Sia and Whitesides, 2003), and continues to provide value to biologists and microfluidic scientists.

Turbulence, as observed in the diseased vasculature (Ohyama et al., 2002), and models of the diseased vasculature (DiCarlo et al., 2019; Poepping et al., 2010), are not easily simulated in microfluidic environments. This is because turbulence is usually defined by a high-Reynolds number (Re) flow, a parameter that predicts the transition from laminar to turbulent flow and is characterized partly by the cross-sectional area of the flow channel. The geometric considerations of microfluidics imply very small cross-sections, resulting in very low Re . However it is possible to create flow that carries the characteristics of turbulence (i.e. non-laminar flow disturbances) (Liu et al., 2009; Wang et al., 2014) at low Re . Strategies can be employed to generate non-laminar flows in micro-scale fluidic geometries, and this has been achieved by various methods (Kumaran and Bandaru, 2016; Redford et al., 2005; Sousa et al., 2018; Wang et al., 2016). Non-laminar flow in microfluidics can either be generated by an active or passive mechanism. Active methods involve using some sort of transducer to influence the flow and can include acoustic, electric, thermal, and other mechanisms. Passive methods on the other-hand generally include designing the geometry of the channel in such a way as to promote non-laminarities. Some of these methods include barriers, twisting, zig-zagging, and

serpentine microfluidic structures (Lee et al., 2011). Active schemes are generally more effective, while passive schemes are generally simpler and easier to implement. Most implementations previously mentioned are for chemical and physical applications of non-laminar flows. Such devices fit for biological studies are rare, and when they do exist, are generally not compatible with real-time monitoring during flow stimulation (Tovar-Lopez et al., 2019). Due to this difficulty, most studies that employ non-steady flows typically utilize simple pulsatile and oscillating (low frequency) flow regimens (Chen et al., 2013; Corrigan et al., 2018; Tkachenko et al., 2009; Voyvodic et al., 2012).

1.7.3 Particle image velocimetry

Particle image velocimetry (PIV) is a technique used to experimentally measure the behaviour of a fluid in motion. Micro-PIV has been used extensively in both microfluidic device geometries (Ergin et al., 2018) and with difficult to predict, time-dependent (i.e. disturbed) flows (Westerweel et al., 2013). Micro-PIV is not the only method used to detect flow patterns experimentally, but it has become the dominant one reported in the literature. Hot wire anemometry and laser Doppler velocimetry are the two other most common measurement methods, though their use has waned in recent years due to the advantages of micro-PIV (Westerweel et al., 2013).

The fundamentals of the method are simple (Pitts and Fenech, 2013). The PIV fluid to be measured is seeded with tracer particles. The seeded PIV fluid is then pumped through the geometry of interest at a controlled rate. The particles in motion are imaged by a high-speed video camera. Each frame is then divided into small interrogation windows, which represent a cluster of particles that is identified and centroided. Frame-by-frame

software then uses cross-correlation to determine the displacement (dx) of each cluster centroid between frames. Given the time-scale (dt) between frames one can then determine the velocity (dx/dt) of each centroid for that period. These measurements are done per unit area, such that the velocity vectors are calculated as a discretized field over the imaging region.

As fluid itself has no discrete visual landmarks at the micro-scale, the PIV fluid is seeded with fiducial marker beads. These fiducial markers are intended to be visual markers that recapitulate the flow of the fluid itself, acting as a proxy. As such, they must be sufficiently small that the markers themselves neither behave differently from the fluid, nor affect the flow of the fluid by their presence (van Overbrüggen et al., 2016).

Therefore, in micro-scale geometries, micro-particles are used, and are detected with microscope optics. In situations of high-velocity flow, higher frame rates must be used to faithfully capture the particle motion. As frame rate increases, exposure necessarily decreases, resulting in a lower ratio of signal to noise. If the signal becomes too difficult to detect, methods are available to improve the imaging performance. Seeding with fluorescent tracer particles, and illuminating them with the appropriate light source (i.e. a laser), is one solution to this problem. With a laser-based PIV system, one can increase the level of signal as compared with illumination by broad wavelength light sources.

1.8 Rationale and objectives

The molecular signaling pathways governing the cellular processes of mechanotransduction are not fully understood. Specifically, the earliest cellular steps of these mechanotransduction pathways are the least studied. One of the reasons for this

knowledge gap is that these molecular signals are transient and, to be characterized, must be observed in real-time. Modern imaging systems, while powerful, do not have the capability to provide the relevant mechanical stimuli.

To address this deficiency in mechanotransduction research, we developed systems for dynamic mechanical stimulation of live cells, that were integrated with existing microscopy and imaging devices. These platform technologies are modular for compatibility with several different imaging systems and modalities. In this thesis, I present approaches in cell physiology, real-time microscopy, and device engineering that were combined to accomplish these goals. The specific aims and hypotheses for each chapter containing original research were as follows.

Objective 1

Aim 1: Development and validation of a system for high-frequency vibration of live cells during real-time microscopy.

Hypothesis 1: A novel, integrated system could be developed for real-time microscopy of live cells during high-frequency low-magnitude vibration. This technology enabled, for the first time, the dynamic mechanostimulation of live cells with high-frequency (up to 500 Hz) vibrations (up to 1 g peak acceleration) during concurrent real-time microscopy. Utilization of this system allowed investigation of the immediate reactions of cells to such stimuli. In response to the high-frequency vibrational stimulation of osteoblast-like cells, a lack of $[Ca^{2+}]_i$ transients were observed, but a desensitization to exogenous ATP.

Objective 2

Aim 2: Development and validation of a microfluidics fabrication technique for devices compatible with live-cell microscopy; and

Hypothesis 2: A microfluidics fabrication technique geared towards non-specialists could be developed that allows for the production of leak-proof polydimethylsiloxane devices compatible with live-cell microscopy. Using a replica molding technique, we generated microfluidic devices and tested them for reproducibility and biocompatibility. The flow characteristics of this chamber were modeled using computational fluid dynamics and validated using experimental micro-particle imaging velocimetry. The compatibility of the device with live cell cultures, and $[Ca^{2+}]_i$ imaging systems was also verified.

Objective 3

Aim 3: Development and validation of a system to study the real-time responses of live cells to disturbed fluid flow.

Hypothesis 3: A device could be developed to deliver disturbed fluid flow to live-cells during real-time microscopy. Disturbed flow environments, like those seen in the recirculation zones around atherosclerotic plaques, are thought to be a major role in the disease's progression. This technology will enable the application of varying, yet precisely controlled, non-laminar disturbed flow to cells during real-time imaging, allowing the observation of immediate mechanotransductive responses. This device will enable the further understanding of how cells respond to these different flow paradigms

This proposal is a multi-faceted investigation into a complex biological problem that has yet to be sufficiently addressed due to technical barriers. By overcoming these barriers through the development techniques to monitor live-cells with real-time microscopy during dynamic mechanostimulation, we can pave the way towards better understanding of the mechanisms underlying mechanotransduction; a highly-conserved biological process with considerable significance in several fields of study, including human physiology.

1.9 References

- Abraham DM, Davis RT, 3rd, Warren CM, Mao L, Wolska BM, Solaro RJ, Rockman HA. 2016. beta-Arrestin mediates the Frank-Starling mechanism of cardiac contractility. *Proceedings of the National Academy of Sciences of the United States of America* 113(50):14426-14431.
- Abramson AS, Delagi EF. 1961. Influence of weight-bearing and muscle contraction on disuse osteoporosis. *Archives of physical medicine and rehabilitation* 42:147-151.
- Abu Khamidakh AE, Juuti-Uusitalo K, Larsson K, Skottman H, Hyttinen J. 2013. Intercellular Ca(2+) wave propagation in human retinal pigment epithelium cells induced by mechanical stimulation. *Exp Eye Res* 108:129-139.
- Alevriadou BR, Shanmughapriya S, Patel A, Stathopoulos PB, Madesh M. 2017. Mitochondrial Ca(2+) transport in the endothelium: regulation by ions, redox signalling and mechanical forces. *Journal of the Royal Society, Interface* 14(137).
- Alford AI, Jacobs CR, Donahue HJ. 2003. Oscillating fluid flow regulates gap junction communication in osteocytic MLO-Y4 cells by an ERK1/2 MAP kinase-dependent mechanism *small star, filled*. *Bone* 33(1):64-70.
- Ando J, Yamamoto K. 2009. Vascular mechanobiology: endothelial cell responses to fluid shear stress. *Circulation journal : official journal of the Japanese Circulation Society* 73(11):1983-1992.
- Back M, Gasser TC, Michel JB, Caligiuri G. 2013. Biomechanical factors in the biology of aortic wall and aortic valve diseases. *Cardiovascular research* 99(2):232-241.
- Bakker AD, Soejima K, Klein-Nulend J, Burger EH. 2001. The production of nitric oxide and prostaglandin E(2) by primary bone cells is shear stress dependent. *Journal of biomechanics* 34(5):671-677.
- Barczyk M, Carracedo S, Gullberg D. 2010. Integrins. *Cell and tissue research* 339(1):269-280.
- Benirschke SK, Mirels H, Jones D, Tencer AF. 1993. The use of resonant frequency measurements for the noninvasive assessment of mechanical stiffness of the healing tibia. *Journal of orthopaedic trauma* 7(1):64-71.
- Berk BC. 2008. Atheroprotective signaling mechanisms activated by steady laminar flow in endothelial cells. *Circulation* 117(8):1082-1089.
- Berridge MJ, Bootman MD, Lipp P. 1998. Calcium - a life and death signal. *Nature* 395(6703):645-648.
- Berridge MJ, Dupont G. 1994. Spatial and temporal signalling by calcium. *Current Opinion in Cell Biology* 6(2):267-274.

- Berridge MJ, Lipp P, Bootman MD. 2000. The versatility and universality of calcium signalling. *Nat Rev Mol Cell Biol* 1(1):11-21.
- Berthier E, Young EW, Beebe D. 2012. Engineers are from PDMS-land, Biologists are from Polystyrenia. *Lab on a chip* 12(7):1224-1237.
- Bloomfield SA. 2006. Does altered blood flow to bone in microgravity impact on mechanotransduction? *J Musculoskelet Neuronal Interact* 6(4):324-326.
- Blount P, Sukharev SI, Moe PC, Nagle SK, Kung C. 1996. Towards an understanding of the structural and functional properties of MscL, a mechanosensitive channel in bacteria. *Biology of the cell* 87(1-2):1-8.
- Boeynaems JM, Communi D, Gonzalez NS, Robaye B. 2005. Overview of the P2 receptors. *Seminars in thrombosis and hemostasis* 31(2):139-149.
- Bonewald LF. 2011. The amazing osteocyte. *J Bone Miner Res* 26(2):229-238.
- Bryan NS, Bian K, Murad F. 2009. Discovery of the nitric oxide signaling pathway and targets for drug development. *Frontiers in bioscience (Landmark edition)* 14:1-18.
- Burger EH, Klein-Nulend J. 1998. Microgravity and bone cell mechanosensitivity. *Bone* 22(5 Suppl):127S-130S.
- Burnstock G. 1972. Purinergic nerves. *Pharmacological reviews* 24(3):509-581.
- Burnstock G. 2016. Purinergic Signalling and Endothelium. *Current vascular pharmacology* 14(2):130-145.
- Burnstock G. 2017. Purinergic Signalling: Therapeutic Developments. *Frontiers in pharmacology* 8:661.
- Burnstock G, Verkhratsky A. 2009. Evolutionary origins of the purinergic signalling system. *Acta physiologica (Oxford, England)* 195(4):415-447.
- Callister WD. 2001. *Fundamentals of materials science and engineering : an interactive e.text*. New York: Wiley.
- Carafoli E, Krebs J. 2016. Why Calcium? How Calcium Became the Best Communicator. *The Journal of biological chemistry* 291(40):20849-20857.
- Cardinale M, Pope MH. 2003. The effects of whole body vibration on humans: dangerous or advantageous? *Acta Physiol Hung* 90(3):195-206.
- Cardinale M, Wakeling J. 2005. Whole body vibration exercise: are vibrations good for you? *Br J Sports Med* 39(9):585-589; discussion 589.

- Castillo AB, Alam I, Tanaka SM, Levenda J, Li J, Warden SJ, Turner CH. 2006. Low-amplitude, broad-frequency vibration effects on cortical bone formation in mice. *Bone* 39(5):1087-1096.
- Celil Aydemir AB, Minematsu H, Gardner TR, Kim KO, Ahn JM, Lee FY. 2010. Nuclear factor of activated T cells mediates fluid shear stress- and tensile strain-induced Cox2 in human and murine bone cells. *Bone* 46(1):167-175.
- Cengel YA, Cimbala JM. 2018. *Fluid mechanics : fundamentals and applications*.
- Charles LE, Ma CC, Burchfiel CM, Dong RG. 2018. Vibration and Ergonomic Exposures Associated With Musculoskeletal Disorders of the Shoulder and Neck. *Safety and health at work* 9(2):125-132.
- Chen H, Cornwell J, Zhang H, Lim T, Resurreccion R, Port T, Rosengarten G, Nordon RE. 2013. Cardiac-like flow generator for long-term imaging of endothelial cell responses to circulatory pulsatile flow at microscale. *Lab on a chip* 13(15):2999-3007.
- Collaborators GDaIaP. 2017. Global, regional, and national incidence, prevalence, and years lived with disability for 328 diseases and injuries for 195 countries, 1990-2016: a systematic analysis for the Global Burden of Disease Study 2016. *Lancet* (London, England) 390(10100):1211-1259.
- Conklin DJ. 2014. Recent developments in vascular biology. *Circulation research* 115(12):e79-82.
- Corrigan MA, Johnson GP, Stavenschi E, Riffault M, Labour MN, Hoey DA. 2018. TRPV4-mediates oscillatory fluid shear mechanotransduction in mesenchymal stem cells in part via the primary cilium. *Scientific reports* 8(1):3824.
- Davies PF. 1995. Flow-mediated endothelial mechanotransduction. *Physiological reviews* 75(3):519-560.
- Davies PF, Mundel T, Barbee KA. 1995. A mechanism for heterogeneous endothelial responses to flow in vivo and in vitro. *Journal of biomechanics* 28(12):1553-1560.
- Deliot N, Constantin B. 2015. Plasma membrane calcium channels in cancer: Alterations and consequences for cell proliferation and migration. *Biochimica et biophysica acta* 1848(10 Pt B):2512-2522.
- Delling M, DeCaen PG, Doerner JF, Febvay S, Clapham DE. 2013. Primary cilia are specialized calcium signalling organelles. *Nature* 504(7479):311-314.
- Delling M, Indzhykulian AA, Liu X, Li Y, Xie T, Corey DP, Clapham DE. 2016. Primary cilia are not calcium-responsive mechanosensors. *Nature* 531(7596):656-660.

- Diao X, Li Z, An B, Xin H, Wu Y, Li K, Feng F, Dou C. 2017. The Microdamage and Expression of Sclerostin in Peri-implant Bone under One-time Shock Force Generated by Impact. *Scientific reports* 7(1):6508.
- DiCarlo AL, Holdsworth DW, Poepping TL. 2019. Study of the effect of stenosis severity and non-Newtonian viscosity on multidirectional wall shear stress and flow disturbances in the carotid artery using particle image velocimetry. *Medical engineering & physics* 65:8-23.
- Dixon SJ, Sims SM. 2000. P2 purinergic receptors on osteoblasts and osteoclasts: Potential targets for drug development. *Drug Dev Res* 49(3):187-200.
- Erb L, Liao Z, Seye CI, Weisman GA. 2006. P2 receptors: intracellular signaling. *Pflügers Archiv : European journal of physiology* 452(5):552-562.
- Ergin FG, Watz BB, Gade-Nielsen NF. 2018. A Review of Planar PIV Systems and Image Processing Tools for Lab-On-Chip Microfluidics. *Sensors (Basel, Switzerland)* 18(9).
- Fritton JC, Rubin CT, Qin YX, McLeod KJ. 1997. Whole-body vibration in the skeleton: development of a resonance-based testing device. *Annals of biomedical engineering* 25(5):831-839.
- Fritton SP, Weinbaum S. 2009. Fluid and Solute Transport in Bone: Flow-Induced Mechanotransduction. *Annual review of fluid mechanics* 41:347-374.
- Fukumoto S, Martin TJ. 2009. Bone as an endocrine organ. *Trends in endocrinology and metabolism: TEM* 20(5):230-236.
- Gale KB, Jafek RA, Lambert JC, Goenner LB, Moghimifam H, Nze CU, Kamarapu KS. 2018. A Review of Current Methods in Microfluidic Device Fabrication and Future Commercialization Prospects. *Inventions* 3(3).
- Genetos DC, Geist DJ, Liu D, Donahue HJ, Duncan RL. 2005. Fluid shear-induced ATP secretion mediates prostaglandin release in MC3T3-E1 osteoblasts. *J Bone Miner Res* 20(1):41-49.
- Gerlach H, Rossaint R, Pappert D, Falke KJ. 1993. Time-course and dose-response of nitric oxide inhalation for systemic oxygenation and pulmonary hypertension in patients with adult respiratory distress syndrome. *European Journal of Clinical Investigation* 23(8):499-502.
- Gifford JL, Walsh MP, Vogel HJ. 2007. Structures and metal-ion-binding properties of the Ca²⁺-binding helix-loop-helix EF-hand motifs. *The Biochemical journal* 405(2):199-221.

- Gilsanz V, Wren TA, Sanchez M, Dorey F, Judex S, Rubin C. 2006. Low-level, high-frequency mechanical signals enhance musculoskeletal development of young women with low BMD. *J Bone Miner Res* 21(9):1464-1474.
- Gimbrone MA, Jr., Nagel T, Topper JN. 1997. Biomechanical activation: an emerging paradigm in endothelial adhesion biology. *The Journal of clinical investigation* 99(8):1809-1813.
- Grimm D, Grosse J, Wehland M, Mann V, Reseland JE, Sundaresan A, Corydon TJ. 2016. The impact of microgravity on bone in humans. *Bone* 87:44-56.
- Guharay F, Sachs F. 1984. Stretch-activated single ion channel currents in tissue-cultured embryonic chick skeletal muscle. *The Journal of physiology* 352:685-701.
- Guntur AR, Rosen CJ. 2012. Bone as an endocrine organ. *Endocrine practice : official journal of the American College of Endocrinology and the American Association of Clinical Endocrinologists* 18(5):758-762.
- Guo LX, Teo EC. 2005. Prediction of the modal characteristics of the human spine at resonant frequency using finite element models. *Proc Inst Mech Eng [H]* 219(4):277-284.
- Hahn C, Schwartz MA. 2009. Mechanotransduction in vascular physiology and atherogenesis. *Nature reviews Molecular cell biology* 10(1):53-62.
- Halldorsson S, Lucumi E, Gómez-Sjöberg R, Fleming RMT. 2015. Advantages and challenges of microfluidic cell culture in polydimethylsiloxane devices. *Biosensors and Bioelectronics* 63:218-231.
- Halliday D, Resnick R, Walker J. 2005. *Fundamentals of physics, extended*. New York; Chichester: Wiley.
- Helmlinger G, Geiger RV, Schreck S, Nerem RM. 1991. Effects of pulsatile flow on cultured vascular endothelial cell morphology. *Journal of biomechanical engineering* 113(2):123-131.
- Holdsworth DW, Rickey DW, Drangova M, Miller DJ, Fenster A. 1991. Computer-controlled positive displacement pump for physiological flow simulation. *Medical & biological engineering & computing* 29(6):565-570.
- Hou WW, Zhu ZL, Zhou Y, Zhang CX, Yu HY. 2011. Involvement of Wnt activation in the micromechanical vibration-enhanced osteogenic response of osteoblasts. *Journal of orthopaedic science : official journal of the Japanese Orthopaedic Association* 16(5):598-605.
- Hu Z, Welch I, Yuan X, Pollmann SI, Nikolov HN, Holdsworth DW. 2015. Quantification of mouse in vivo whole-body vibration amplitude from motion-blur using x-ray imaging. *Physics in medicine and biology* 60(16):6423-6439.

- Hung CT, Pollack SR, Reilly TM, Brighton CT. 1995. Real-time calcium response of cultured bone cells to fluid flow. *Clinical orthopaedics and related research*(313):256-269.
- Huo B, Lu XL, Costa KD, Xu Q, Guo XE. 2010. An ATP-dependent mechanism mediates intercellular calcium signaling in bone cell network under single cell nanoindentation. *Cell Calcium* 47(3):234-241.
- Huxley H, Hanson J. 1954. Changes in the cross-striations of muscle during contraction and stretch and their structural interpretation. *Nature* 173(4412):973-976.
- Ingber DE. 1997. Tensegrity: the architectural basis of cellular mechanotransduction. *Annual review of physiology* 59:575-599.
- Ingber DE. 2008. Tensegrity and mechanotransduction. *Journal of bodywork and movement therapies* 12(3):198-200.
- Iwamoto J, Takeda T, Sato Y, Uzawa M. 2005. Effect of whole-body vibration exercise on lumbar bone mineral density, bone turnover, and chronic back pain in postmenopausal osteoporotic women treated with alendronate. *Aging Clin Exp Res* 17(2):157-163.
- Jaalouk DE, Lammerding J. 2009. Mechanotransduction gone awry. *Nat Rev Mol Cell Biol* 10(1):63-73.
- Janmey PA, McCulloch CA. 2007. Cell mechanics: Integrating cell responses to mechanical stimuli. *Annual Review of Biomedical Engineering*. Palo Alto: Annual Reviews. p 1-34.
- Jing D, Lu XL, Luo E, Sajda P, Leong PL, Guo XE. 2013. Spatiotemporal properties of intracellular calcium signaling in osteocytic and osteoblastic cell networks under fluid flow. *Bone* 53(2):531-540.
- Johnson DL, McAllister TN, Frangos JA. 1996. Fluid flow stimulates rapid and continuous release of nitric oxide in osteoblasts. *Am J Physiol* 271(1 Pt 1):E205-208.
- Joiner DM, Tayim RJ, Kadado A, Goldstein SA. 2012. Bone marrow stromal cells from aged male rats have delayed mineralization and reduced response to mechanical stimulation through nitric oxide and ERK1/2 signaling during osteogenic differentiation. *Biogerontology* 13(5):467-478.
- Jorgensen NR, Geist ST, Civitelli R, Steinberg TH. 1997. ATP- and gap junction-dependent intercellular calcium signaling in osteoblastic cells. *The Journal of cell biology* 139(2):497-506.

- Judex S, Boyd S, Qin YX, Turner S, Ye K, Muller R, Rubin C. 2003. Adaptations of trabecular bone to low magnitude vibrations result in more uniform stress and strain under load. *Annals of biomedical engineering* 31(1):12-20.
- Judex S, Donahue LR, Rubin C. 2002. Genetic predisposition to low bone mass is paralleled by an enhanced sensitivity to signals anabolic to the skeleton. *FASEB J* 16(10):1280-1282.
- Katz AM. 2002. Ernest Henry Starling, his predecessors, and the "Law of the Heart". *Circulation* 106(23):2986-2992.
- Kiiski J, Heinonen A, Jarvinen TL, Kannus P, Sievanen H. 2008. Transmission of vertical whole body vibration to the human body. *J Bone Miner Res* 23(8):1318-1325.
- Kim IS, Song YM, Lee B, Hwang SJ. 2012. Human mesenchymal stromal cells are mechanosensitive to vibration stimuli. *Journal of dental research* 91(12):1135-1140.
- Klein-Nulend J, Bacabac RG, Mullender MG. 2005. Mechanobiology of bone tissue. *Pathol Biol (Paris)* 53(10):576-580.
- Kloda A, Martinac B. 2001. Mechanosensitive channel of *Thermoplasma*, the cell wall-less archaea: cloning and molecular characterization. *Cell biochemistry and biophysics* 34(3):321-347.
- Kloda A, Martinac B. 2002. Mechanosensitive channels of bacteria and archaea share a common ancestral origin. *European Biophysics Journal* 31(1):14-25.
- Koga T, Matsui Y, Asagiri M, Kodama T, de Crombrughe B, Nakashima K, Takayanagi H. 2005. NFAT and Osterix cooperatively regulate bone formation. *Nat Med* 11(8):880-885.
- Kumaran V, Bandaru P. 2016. Ultra-fast microfluidic mixing by soft-wall turbulence. *Chemical Engineering Science* 149:156-168.
- Kwaku Essien S, Trask C, Khan M, Boden C, Bath B. 2018. Association Between Whole-Body Vibration and Low-Back Disorders in Farmers: A Scoping Review. *Journal of agromedicine* 23(1):105-120.
- Le Dain AC, Saint N, Kloda A, Ghazi A, Martinac B. 1998. Mechanosensitive ion channels of the archaeon *Haloferax volcanii*. *The Journal of biological chemistry* 273(20):12116-12119.
- Lee CY, Chang CL, Wang YN, Fu LM. 2011. Microfluidic mixing: a review. *International journal of molecular sciences* 12(5):3263-3287.

- Li J, Liu D, Ke HZ, Duncan RL, Turner CH. 2005. The P2X7 nucleotide receptor mediates skeletal mechanotransduction. *The Journal of biological chemistry* 280(52):42952-42959.
- Liao JK. 2013. Linking endothelial dysfunction with endothelial cell activation. *The Journal of clinical investigation* 123(2):540-541.
- Liu M, Tanswell AK, Post M. 1999. Mechanical force-induced signal transduction in lung cells. *Am J Physiol* 277(4 Pt 1):L667-683.
- Liu Y, Olsen MG, Fox RO. 2009. Turbulence in a microscale planar confined impinging-jets reactor. *Lab on a chip* 9(8):1110-1118.
- Lorusso D, Nikolov HN, Milner JS, Ochotny NM, Sims SM, Dixon SJ, Holdsworth DW. 2016. Practical fabrication of microfluidic platforms for live-cell microscopy. *Biomedical microdevices* 18(5):78.
- Loukin S, Zhou X, Su Z, Saimi Y, Kung C. 2010. Wild-type and brachyolmia-causing mutant TRPV4 channels respond directly to stretch force. *The Journal of biological chemistry* 285(35):27176-27181.
- Lynch MA, Brodt MD, Silva MJ. 2010. Skeletal effects of whole-body vibration in adult and aged mice. *Journal of orthopaedic research : official publication of the Orthopaedic Research Society* 28(2):241-247.
- Macek Jilkova Z, Lisowska J, Manet S, Verdier C, Deplano V, Geindreau C, Faurobert E, Albiges-Rizo C, Duperray A. 2014. CCM proteins control endothelial beta1 integrin dependent response to shear stress. *Biology open*.
- Mahto SK, Tenenbaum-Katan J, Greenblum A, Rothen-Rutishauser B, Sznitman J. 2014. Microfluidic shear stress-regulated surfactant secretion in alveolar epithelial type II cells in vitro. *American journal of physiology Lung cellular and molecular physiology* 306(7):L672-683.
- Malachanne E, Dureisseix D, Jourdan F. 2011. Numerical model of bone remodeling sensitive to loading frequency through a poroelastic behavior and internal fluid movements. *Journal of the mechanical behavior of biomedical materials* 4(6):849-857.
- Malone AM, Anderson CT, Tummala P, Kwon RY, Johnston TR, Stearns T, Jacobs CR. 2007. Primary cilia mediate mechanosensing in bone cells by a calcium-independent mechanism. *Proceedings of the National Academy of Sciences of the United States of America* 104(33):13325-13330.
- Martinac B. 2001. Mechanosensitive channels in prokaryotes. *Cellular physiology and biochemistry : international journal of experimental cellular physiology, biochemistry, and pharmacology* 11(2):61-76.

- Mc Namara K, Alzubaidi H, Jackson JK. 2019. Cardiovascular disease as a leading cause of death: how are pharmacists getting involved? *Integrated pharmacy research & practice* 8:1-11.
- McCann MR, Veras MA, Yeung C, Lalli G, Patel P, Leitch KM, Holdsworth DW, Dixon SJ, Seguin CA. 2017. Whole-body vibration of mice induces progressive degeneration of intervertebral discs associated with increased expression of IL-1beta and multiple matrix degrading enzymes. *Osteoarthritis and cartilage* 25(5):779-789.
- McCormick ME, Tzima E. 2016. Pulling on my heartstrings: mechanotransduction in cardiac development and function. *Current opinion in hematology* 23(3):235-242.
- Merriman H, Jackson K. 2009. The effects of whole-body vibration training in aging adults: a systematic review. *J Geriatr Phys Ther* 32(3):134-145.
- Meusch J, Rahmatalla S. 2014. Whole-body vibration transmissibility in supine humans: effects of board litter and neck collar. *Applied ergonomics* 45(3):677-685.
- Michael Delaine-Smith R, Javaheri B, Helen Edwards J, Vazquez M, Rumney RM. 2015. Preclinical models for in vitro mechanical loading of bone-derived cells. *BoneKEY reports* 4:728.
- Michel CC. 1988. Capillary permeability and how it may change. *The Journal of physiology* 404:1-29.
- Mikolajewicz N, Zimmermann EA, Willie BM, Komarova SV. 2018. Mechanically stimulated ATP release from murine bone cells is regulated by a balance of injury and repair. *eLife* 7:e37812.
- Miller RT. 2017. Mechanical properties of basement membrane in health and disease. *Matrix biology : journal of the International Society for Matrix Biology* 57-58:366-373.
- Mohrman DE, Heller LJ, Mohrman DE. 2018. *Cardiovascular physiology*.
- Morey-Holton ER. 2003. The impact of gravity on life. In: Rothschild LJ, Lister AM, editors. *Evolution on Planet Earth*. London: Academic Press. p 143-159.
- Murthy SE, Dubin AE, Patapoutian A. 2017. Piezos thrive under pressure: mechanically activated ion channels in health and disease. *Nature reviews Molecular cell biology* 18(12):771-783.
- Nabavi N, Khandani A, Camirand A, Harrison RE. 2011. Effects of microgravity on osteoclast bone resorption and osteoblast cytoskeletal organization and adhesion. *Bone* 49(5):965-974.

- Nag S, Resnick A. 2017. Biophysics and biofluid dynamics of primary cilia: evidence for and against the flow-sensing function. *Am J Physiol Renal Physiol* 313(3):F706-f720.
- Nauli SM, Alenghat FJ, Luo Y, Williams E, Vassilev P, Li X, Elia AE, Lu W, Brown EM, Quinn SJ, Ingber DE, Zhou J. 2003. Polycystins 1 and 2 mediate mechanosensation in the primary cilium of kidney cells. *Nature genetics* 33(2):129-137.
- Nauli SM, Zhou J. 2004. Polycystins and mechanosensation in renal and nodal cilia. *Bioessays* 26(8):844-856.
- Nauman EA, Risic KJ, Keaveny TM, Satcher RL. 1999. Quantitative assessment of steady and pulsatile flow fields in a parallel plate flow chamber. *Annals of biomedical engineering* 27(2):194-199.
- Negoro H, Urban-Maldonado M, Liou LS, Spray DC, Thi MM, Suadicani SO. 2014. Pannexin 1 channels play essential roles in urothelial mechanotransduction and intercellular signaling. *PLoS One* 9(8):e106269.
- Nguyen AM, Jacobs CR. 2013. Emerging role of primary cilia as mechanosensors in osteocytes. *Bone* 54(2):196-204.
- Nguyen HT, Thach H, Roy E, Huynh K, Perrault CM. 2018. Low-Cost, Accessible Fabrication Methods for Microfluidics Research in Low-Resource Settings. *Micromachines* 9(9).
- Nilsson T, Wahlstrom J, Burstrom L. 2017. Hand-arm vibration and the risk of vascular and neurological diseases-A systematic review and meta-analysis. *PLoS One* 12(7):e0180795.
- Nishitani WS, Alencar AM, Wang Y. 2015. Rapid and Localized Mechanical Stimulation and Adhesion Assay: TRPM7 Involvement in Calcium Signaling and Cell Adhesion. *PLOS ONE* 10(5):e0126440.
- Ohyama M, Mizushige K, Ohyama H, Takahashi T, Hosomi N, Ichihara S, Kohno M. 2002. Carotid turbulent flow observed by convergent color Doppler flowmetry in silent cerebral infarction. *The international journal of cardiovascular imaging* 18(2):119-124.
- Orrenius S, Zhivotovsky B, Nicotera P. 2003. Regulation of cell death: the calcium-apoptosis link. *Nature reviews Molecular cell biology* 4(7):552-565.
- Orriss IR. 2015. The role of purinergic signalling in the musculoskeletal system. *Autonomic neuroscience : basic & clinical* 191:124-134.
- Ozkaya N, Willems B, Goldsheyder D. 1994. Whole-body vibration exposure: a comprehensive field study. *Am Ind Hyg Assoc J* 55(12):1164-1171.

- Pankratov Y, Lalo U, Verkhatsky A, North RA. 2006. Vesicular release of ATP at central synapses. *Pflugers Archiv : European journal of physiology* 452(5):589-597.
- Papaioannou TG, Stefanadis C. 2005. Vascular wall shear stress: basic principles and methods. *Hellenic journal of cardiology : HJC = Hellenike kardiologike epitheorese* 46(1):9-15.
- Park JY, Pillinger MH, Abramson SB. 2006. Prostaglandin E2 synthesis and secretion: the role of PGE2 synthases. *Clinical immunology (Orlando, Fla)* 119(3):229-240.
- Pastor-Anglada M, Perez-Torras S. 2018. Who Is Who in Adenosine Transport. *Frontiers in pharmacology* 9:627.
- Pead MJ, Suswillo R, Skerry TM, VEDI S, Lanyon LE. 1988. Increased 3H-uridine levels in osteocytes following a single short period of dynamic bone loading in vivo. *Calcified tissue international* 43(2):92-96.
- Pemberton GD, Childs P, Reid S, Nikukar H, Tsimbouri PM, Gadegaard N, Curtis AS, Dalby MJ. 2015. Nanoscale stimulation of osteoblastogenesis from mesenchymal stem cells: nanotopography and nanokicking. *Nanomedicine (London, England)* 10(4):547-560.
- Penley NJ, Schafer CP, Bartoe JD. 2002. The International Space Station as a microgravity research platform. *Acta Astronaut* 50(11):691-696.
- Pitts KL, Fenech M. 2013. Micro-particle image velocimetry for velocity profile measurements of micro blood flows. *Journal of visualized experiments : JoVE*(74):e50314.
- Poepping TL, Rankin RN, Holdsworth DW. 2010. Flow patterns in carotid bifurcation models using pulsed Doppler ultrasound: effect of concentric vs. eccentric stenosis on turbulence and recirculation. *Ultrasound in medicine & biology* 36(7):1125-1134.
- Polacheck WJ, Li R, Uzel SG, Kamm RD. 2013. Microfluidic platforms for mechanobiology. *Lab on a chip* 13(12):2252-2267.
- Pope MH, Magnusson M, Hansson T. 1997. The upper extremity attenuates intermediate frequency vibrations. *Journal of biomechanics* 30(2):103-108.
- Praetorius HA, Spring KR. 2001. Bending the MDCK cell primary cilium increases intracellular calcium. *The Journal of membrane biology* 184(1):71-79.
- Praetorius HA, Spring KR. 2003. Removal of the MDCK cell primary cilium abolishes flow sensing. *The Journal of membrane biology* 191(1):69-76.

- Putney JW. 2018. Forms and functions of store-operated calcium entry mediators, STIM and Orai. *Advances in biological regulation* 68:88-96.
- Rafieian-Kopaei M, Setorki M, Douidi M, Baradaran A, Nasri H. 2014. Atherosclerosis: process, indicators, risk factors and new hopes. *International journal of preventive medicine* 5(8):927-946.
- Raghavan V, Weisz OA. 2016. Discerning the role of mechanosensors in regulating proximal tubule function. *Am J Physiol Renal Physiol* 310(1):F1-5.
- Ralevic V, Burnstock G. 1998. Receptors for purines and pyrimidines. *Pharmacological reviews* 50(3):413-492.
- Ramanadham S, Ali T, Ashley JW, Bone RN, Hancock WD, Lei X. 2015. Calcium-independent phospholipases A2 and their roles in biological processes and diseases. *Journal of lipid research* 56(9):1643-1668.
- Ramasamy SK. 2017. Structure and Functions of Blood Vessels and Vascular Niches in Bone. *Stem Cells International* 2017:10.
- Ramasamy SK, Kusumbe AP, Adams RH. 2015. Regulation of tissue morphogenesis by endothelial cell-derived signals. *Trends in cell biology* 25(3):148-157.
- Randall JM, Matthews RT, Stiles MA. 1997. Resonant frequencies of standing humans. *Ergonomics* 40(9):879-886.
- Rao P, Knaus EE. 2008. Evolution of nonsteroidal anti-inflammatory drugs (NSAIDs): cyclooxygenase (COX) inhibition and beyond. (1482-1826 (Electronic)).
- Redford GI, Majumdar ZK, Sutin JDB, Clegg RM. 2005. Properties of microfluidic turbulent mixing revealed by fluorescence lifetime imaging. *The Journal of Chemical Physics* 123(22):224504.
- Reed A, Kohl P, Peyronnet R. 2014. Molecular candidates for cardiac stretch-activated ion channels. *Global cardiology science & practice* 2014(2):9-25.
- Robertson SN, Campsie P, Childs PG, Madsen F, Donnelly H, Henriquez FL, Mackay WG, Salmerón-Sánchez M, Tsimbouri MP, Williams C, Dalby MJ, Reid S. 2018. Control of cell behaviour through nanovibrational stimulation: nanokicking. *Philos Trans A Math Phys Eng Sci* 376(2120).
- Robling AG, Bellido T, Turner CH. 2006. Mechanical stimulation in vivo reduces osteocyte expression of sclerostin. *J Musculoskelet Neuronal Interact* 6(4):354.
- Rodat-Despoix L, Hao J, Dandonneau M, Delmas P. 2013. Shear stress-induced Ca mobilization in MDCK cells is ATP dependent, no matter the primary cilium. *Cell Calcium*.

- Roelants M, Delecluse C, Goris M, Verschueren S. 2004. Effects of 24 weeks of whole body vibration training on body composition and muscle strength in untrained females. *Int J Sports Med* 25(1):1-5.
- Rogers MJ, Hrovat K, Moskowitz ME. 1999. Effects of exercise equipment on the microgravity environment. *Adv Space Res* 24(10):1283-1287.
- Ross TD, Coon BG, Yun S, Baeyens N, Tanaka K, Ouyang M, Schwartz MA. 2013. Integrins in mechanotransduction. *Curr Opin Cell Biol* 25(5):613-618.
- Rubin C, Pope M, Fritton JC, Magnusson M, Hansson T, McLeod K. 2003. Transmissibility of 15-hertz to 35-hertz vibrations to the human hip and lumbar spine: determining the physiologic feasibility of delivering low-level anabolic mechanical stimuli to skeletal regions at greatest risk of fracture because of osteoporosis. *Spine* 28(23):2621-2627.
- Rubin C, Turner AS, Bain S, Mallinckrodt C, McLeod K. 2001. Anabolism. Low mechanical signals strengthen long bones. *Nature* 412(6847):603-604.
- Rubin C, Turner AS, Muller R, Mittra E, McLeod K, Lin W, Qin YX. 2002. Quantity and quality of trabecular bone in the femur are enhanced by a strongly anabolic, noninvasive mechanical intervention. *J Bone Miner Res* 17(2):349-357.
- Rubin CT, Capilla E, Luu YK, Busa B, Crawford H, Nolan DJ, Mittal V, Rosen CJ, Pessin JE, Judex S. 2007. Adipogenesis is inhibited by brief, daily exposure to high-frequency, extremely low-magnitude mechanical signals. *Proceedings of the National Academy of Sciences of the United States of America* 104(45):17879-17884.
- Sachs F. 2010. Stretch-activated ion channels: what are they? *Physiology (Bethesda, Md)* 25(1):50-56.
- Satir P, Pedersen LB, Christensen ST. 2010. The primary cilium at a glance. *Journal of cell science* 123(Pt 4):499-503.
- Schmid R, Evans RJ. 2019. ATP-Gated P2X Receptor Channels: Molecular Insights into Functional Roles. *Annual review of physiology* 81:43-62.
- Scott A, Khan KM, Duronio V, Hart DA. 2008. Mechanotransduction in human bone in vitro cellular physiology that underpins bone changes with exercise. *Sports Med* 38(2):139-160.
- Seidel H, Bluthner R, Hinz B. 2001. Application of finite-element models to predict forces acting on the lumbar spine during whole-body vibration. *Clinical biomechanics (Bristol, Avon)* 16 Suppl 1:S57-63.

- Shen SC, House RA. 2017. Hand-arm vibration syndrome: What family physicians should know. *Canadian family physician Medecin de famille canadien* 63(3):206-210.
- Sia SK, Whitesides GM. 2003. Microfluidic devices fabricated in poly(dimethylsiloxane) for biological studies. *Electrophoresis* 24(21):3563-3576.
- Sirois E, Charara J, Ruel J, Dussault JC, Gagnon P, Doillon CJ. 1998. Endothelial cells exposed to erythrocytes under shear stress: an in vitro study. *Biomaterials* 19(21):1925-1934.
- Slatkowska L, Alibhai SM, Beyene J, Hu H, Demaras A, Cheung AM. 2011. Effect of 12 months of whole-body vibration therapy on bone density and structure in postmenopausal women: a randomized trial. *Ann Intern Med* 155(10):668-679.
- Sousa PC, Pinho FT, Alves MA. 2018. Purely-elastic flow instabilities and elastic turbulence in microfluidic cross-slot devices. *Soft Matter* 14(8):1344-1354.
- Spasic M, Jacobs CR. 2017. Primary cilia: Cell and molecular mechanosensors directing whole tissue function. *Seminars in cell & developmental biology* 71:42-52.
- Sprague B, Chesler NC, Magness RR. 2010. Shear stress regulation of nitric oxide production in uterine and placental artery endothelial cells: experimental studies and hemodynamic models of shear stresses on endothelial cells. *The International journal of developmental biology* 54(2-3):331-339.
- Spyropoulou A, Karamesinis K, Basdra EK. 2015. Mechanotransduction pathways in bone pathobiology. *Biochimica et biophysica acta* 1852(9):1700-1708.
- Suadicani SO, Brosnan CF, Scemes E. 2006. P2X7 receptors mediate ATP release and amplification of astrocytic intercellular Ca²⁺ signaling. *The Journal of neuroscience : the official journal of the Society for Neuroscience* 26(5):1378-1385.
- Sugimoto A, Miyazaki A, Kawarabayashi K, Shono M, Akazawa Y, Hasegawa T, Ueda-Yamaguchi K, Kitamura T, Yoshizaki K, Fukumoto S, Iwamoto T. 2017. Piezo type mechanosensitive ion channel component 1 functions as a regulator of the cell fate determination of mesenchymal stem cells. *Scientific reports* 7(1):17696.
- Sun Z, Guo SS, Fassler R. 2016. Integrin-mediated mechanotransduction. *The Journal of cell biology* 215(4):445-456.
- Takahara N, Ito S, Furuya K, Naruse K, Aso H, Kondo M, Sokabe M, Hasegawa Y. 2014. Real-time imaging of ATP release induced by mechanical stretch in human airway smooth muscle cells. *Am J Respir Cell Mol Biol* 51(6):772-782.
- Takahashi K, Kakimoto Y, Toda K, Naruse K. 2013. Mechanobiology in cardiac physiology and diseases. *J Cell Mol Med* 17(2):225-232.

- Takata S, Yasui N. 2001. Disuse osteoporosis. *The journal of medical investigation : JMI* 48(3-4):147-156.
- Tkachenko E, Gutierrez E, Ginsberg MH, Groisman A. 2009. An easy to assemble microfluidic perfusion device with a magnetic clamp. *Lab on a chip* 9(8):1085-1095.
- Tovar-Lopez F, Thurgood P, Gilliam C, Nguyen N, Pirogova E, Khoshmanesh K, Baratchi S. 2019. A Microfluidic System for Studying the Effects of Disturbed Flow on Endothelial Cells. *Frontiers in bioengineering and biotechnology* 7:81.
- Ulbrich C, Wehland M, Pietsch J, Aleshcheva G, Wise P, van Loon J, Magnusson N, Infanger M, Grosse J, Eilles C, Sundaresan A, Grimm D. 2014. The impact of simulated and real microgravity on bone cells and mesenchymal stem cells. *BioMed research international* 2014:928507.
- van Overbrüggen T, Klaas M, Soria J, Schröder W. 2016. Experimental analysis of particle sizes for PIV measurements. *Measurement Science and Technology* 27(9):094009.
- Volonte C, Amadio S, D'Ambrosi N, Colpi M, Burnstock G. 2006. P2 receptor web: complexity and fine-tuning. *Pharmacology & therapeutics* 112(1):264-280.
- Voyvodic PL, Min D, Baker AB. 2012. A multichannel dampened flow system for studies on shear stress-mediated mechanotransduction. *Lab on a chip* 12(18):3322-3330.
- Wall M, Butler D, Haj AE, Bodle JC, Lobo EG, Banes AJ. 2017. Key developments that impacted the field of mechanobiology and mechanotransduction. *Journal of orthopaedic research : official publication of the Orthopaedic Research Society* 36:605-619.
- Walsh MP. 1983. Calmodulin and its roles in skeletal muscle function. *Canadian Anaesthetists' Society journal* 30(4):390-398.
- Wang G, Yang F, Zhao W. 2016. Microelectrokinetic turbulence in microfluidics at low Reynolds number. *Physical Review E* 93(1):013106.
- Wang GR, Yang F, Zhao W. 2014. There can be turbulence in microfluidics at low Reynolds number. *Lab on a chip* 14(8):1452-1458.
- Watanabe H, Vriens J, Prenen J, Droogmans G, Voets T, Nilius B. 2003. Anandamide and arachidonic acid use epoxyeicosatrienoic acids to activate TRPV4 channels. *Nature* 424(6947):434-438.
- Weinbaum S, Cowin SC, Zeng Y. 1994. A model for the excitation of osteocytes by mechanical loading-induced bone fluid shear stresses. *Journal of biomechanics* 27(3):339-360.

- Weinbaum S, Duan Y, Satlin LM, Wang T, Weinstein AM. 2010. Mechanotransduction in the renal tubule. *Am J Physiol Renal Physiol* 299(6):F1220-1236.
- Westerweel J, Elsinga GE, Adrian RJ. 2013. Particle Image Velocimetry for Complex and Turbulent Flows. *Annual review of fluid mechanics* 45(1):409-436.
- Winslow MM, Pan M, Starbuck M, Gallo EM, Deng L, Karsenty G, Crabtree GR. 2006. Calcineurin/NFAT signaling in osteoblasts regulates bone mass. *Dev Cell* 10(6):771-782.
- Wolff J. 2010a. The classic: on the inner architecture of bones and its importance for bone growth. 1870. *Clinical orthopaedics and related research* 468(4):1056-1065.
- Wolff J. 2010b. The classic: on the theory of fracture healing. 1873. *Clinical orthopaedics and related research* 468(4):1052-1055.
- Wolff J. 2011. The classic: On the significance of the architecture of the spongy substance for the question of bone growth: a preliminary publication. 1869. *Clinical orthopaedics and related research* 469(11):3077-3078.
- Wolff J, Maquet P, Furlong R. 1986. *The law of bone remodelling*: Springer-Verlag.
- Wragg JW, Durant S, McGettrick HM, Sample KM, Egginton S, Bicknell R. 2014. Shear stress regulated gene expression and angiogenesis in vascular endothelium. *Microcirculation (New York, NY : 1994)* 21(4):290-300.
- Wu XT, Sun LW, Qi HY, Shi H, Fan YB. 2016. The bio-response of osteocytes and its regulation on osteoblasts under vibration. *Cell biology international* 40(4):397-406.
- Yamazaki S, Weinhold PS, Graff RD, Tsuzaki M, Kawakami M, Minchew JT, Banes AJ. 2003. Annulus cells release ATP in response to vibratory loading in vitro. *Journal of cellular biochemistry* 90(4):812-818.
- Yellowley CE, Jacobs CR, Li Z, Zhou Z, Donahue HJ. 1997. Effects of fluid flow on intracellular calcium in bovine articular chondrocytes. *Am J Physiol* 273(1 Pt 1):C30-36.
- Yin J, Kuebler WM. 2010. Mechanotransduction by TRP channels: general concepts and specific role in the vasculature. *Cell biochemistry and biophysics* 56(1):1-18.
- Yu HS, Kim JJ, Kim HW, Lewis MP, Wall I. 2015. Impact of mechanical stretch on the cell behaviors of bone and surrounding tissues. *Journal of tissue engineering* 6:2041731415618342.
- Yurdagul A, Jr., Finney AC, Woolard MD, Orr AW. 2016. The arterial microenvironment: the where and why of atherosclerosis. *The Biochemical journal* 473(10):1281-1295.

- Zamponi GW, Striessnig J, Koschak A, Dolphin AC. 2015. The Physiology, Pathology, and Pharmacology of Voltage-Gated Calcium Channels and Their Future Therapeutic Potential. *Pharmacological reviews* 67(4):821-870.
- Zhou J, Li YS, Chien S. 2014a. Shear stress-initiated signaling and its regulation of endothelial function. *Arteriosclerosis, thrombosis, and vascular biology* 34(10):2191-2198.
- Zhou Y, Guan X, Liu T, Wang X, Yu M, Yang G, Wang H. 2014b. Whole body vibration improves osseointegration by up-regulating osteoblastic activity but down-regulating osteoblast-mediated osteoclastogenesis via ERK1/2 pathway. *Bone* 71:17-24.

Chapter 2

Vibration of osteoblastic cells using a novel motion-control platform does not acutely alter cytosolic calcium, but desensitizes subsequent responses to extracellular ATP¹

¹ Modified from a manuscript in revision for the *Journal of Cellular Physiology*: Lorusso, D., Nikolov, H.N., Holdsworth, D.W., and Dixon, S.J. (2019) Vibration of osteoblastic cells using a novel motion-control platform does not acutely alter cytosolic calcium, but desensitizes subsequent responses to extracellular ATP.

2.1 Chapter summary

Low-magnitude high-frequency mechanical vibration induces biological responses in many tissues. Like many cell types, osteoblasts respond rapidly to certain forms of mechanostimulation, such as fluid shear, with transient elevation in the concentration of cytosolic free calcium ($[Ca^{2+}]_i$). However, it is not known whether vibration of osteoblastic cells also induces acute elevation in $[Ca^{2+}]_i$. To address this question, we built a platform for vibrating live cells that is compatible with microscopy and microspectrofluorimetry, enabling us to observe immediate responses of cells to low-magnitude high-frequency vibrations. The horizontal vibration system was mounted on an inverted microscope, and its mechanical performance was evaluated using optical tracking and accelerometry. The platform was driven by a sinusoidal signal at 20 – 500 Hz, producing peak accelerations from 0.1 to 1 g. Accelerometer-derived displacements matched those observed optically within 10%. We then used this system to investigate the effect of acceleration on $[Ca^{2+}]_i$ in rodent osteoblastic cells. Cells were loaded with fura-2, and $[Ca^{2+}]_i$ was monitored using microspectrofluorimetry and fluorescence ratio imaging. No acute changes in $[Ca^{2+}]_i$ or cell morphology were detected in response to vibration over the range of frequencies and accelerations studied. However, vibration did attenuate Ca^{2+} transients generated subsequently by extracellular ATP, which activates P2 purinoceptors and has been implicated in mechanical signaling in bone. In summary, we developed and validated a motion-control system capable of precisely delivering vibrations to live cells during real-time microscopy. Vibration did not elicit acute elevation of $[Ca^{2+}]_i$, but did desensitize responses to later stimulation with ATP

2.2 Introduction

Many tissues have the ability to sense and respond to their local mechanical environment. This phenomenon is known as mechanotransduction, and is the process by which cells sense a mechanical stimulus and translate it into biochemical signals (Orr et al., 2006). In skeletal tissues, mechanotransduction plays a critical role in development (Xiao and Quarles, 2010), modeling (Robling and Turner, 2009), and remodeling (Turner and Pavalko, 1998). Moreover, lack of adequate mechanical stimulation can lead to osteoporosis (Alexandre and Vico, 2011).

Cells are capable of responding to a number of different modes of mechanical stimulation, including fluid shear, strain due to membrane stretching, and vibration (Pham et al., 2017). A number of specialized sensory cells transduce mechanical vibrations, including cells involved in hearing, balance, proprioception, and cutaneous sensation. Interestingly, low-magnitude high-frequency (LMHF) vibrations have been shown to influence skeletal tissues (Thompson et al., 2014). The term LMHF vibration is generally used to refer to time varying displacements when the magnitude of the peak acceleration is 1 g (where 1 g is equal to the acceleration due to gravity, i.e. 9.8 m/s^2) or less, and the frequency is greater than 15 Hz. Devices have been developed to apply such vibrations clinically and in animal models – a process known as “whole body vibration” (WBV). These studies have generated divergent results. Some authors found that vibration is a promising therapeutic approach, in that it can lead to increased bone mass in animals (Judex et al., 2007) and humans (Marin-Cascales et al., 2018). In contrast, other investigators have found that WBV is not a useful treatment for the patient

population most in need (Slatkowska et al., 2011). Additionally, some studies have shown that there are potential risks to WBV (Cardinale and Pope, 2003; McCann et al., 2015).

The biological mechanisms underlying mechanotransduction are areas of intense study (Wall et al., 2017). In cells of the osteoblast lineage, early signaling events activated by mechanical stimuli such as fluid flow and membrane stretch include transient elevation in the concentration of cytosolic free calcium ($[Ca^{2+}]_i$) (Jing et al., 2014; Lorusso et al., 2016; Mikolajewicz et al., 2018; Thi et al., 2013). Furthermore, such responses have been shown to be dependent on the release of nucleotides, such as ATP, that act in an autocrine/paracrine manner on Ca^{2+} -mobilizing P2 receptors on the cell surface (Riddle et al., 2007). In this regard, biosensors have been used to monitor ATP release in response to the mechanical stimulation of osteoblastic cells (Hecht et al., 2013; Mikolajewicz et al., 2018).

Despite a wealth of information on signaling initiated by fluid flow and membrane stretch, relatively little is known about the early mechanotransduction events stimulated by vibration. One challenge in vibration research has been the inability to analyze real-time responses of live cells to stimuli. A second challenge has been to devise a system that allows pure vibrational stimuli without simultaneous fluid shear, which would otherwise confound our ability to identify mechanisms specific to vibrational stimuli. To address this challenge, we developed a system to study the immediate responses of cells to LMHF vibrations using real-time optical approaches. We then validated the precise control of displacement, acceleration and frequency by the system. Using the system, we found that vibration did not induce acute elevation of $[Ca^{2+}]_i$ in osteoblastic cells. However, vibration did desensitize the ability of extracellular ATP to subsequently

induce P2 receptor-mediated elevation of $[Ca^{2+}]_i$. Thus, although incapable of inducing Ca^{2+} signaling itself, vibration did diminish sensitivity to other factors, indicating that cells had indeed responded to the vibrational stimuli applied. Moreover, desensitization to the effects of extracellular ATP would be predicted to make cells less responsive to other forms of mechanical stimuli *in vivo*.

2.3 Materials and methods

2.3.1 Motion control platform for horizontal vibration of live cells during microscopy

Development of a suitable device for vibrating live cells during real-time microscopy depended on meeting several design criteria. The ability to vibrate a cell culture dish over a range of accelerations and frequencies requires that the moving components of the device have minimal mass and also be suspended with minimal friction. Another criterion is that the device must hold the cells within the focal plane of the microscope objective during vibrational displacement; therefore, we designed the platform to vibrate cells horizontally, parallel to the plane of the microscope stage. Culture dishes were suspended so that the distance from the cell monolayer to the objective remained unchanged during vibration.

The vibration device was mounted on the stage of an inverted microscope to permit the use of conventional microscopy techniques (Fig. 2.1). The base of the device was precision machined on a standard 3-axis CNC mill (Trak K3SX-3 with ProTrak SMX

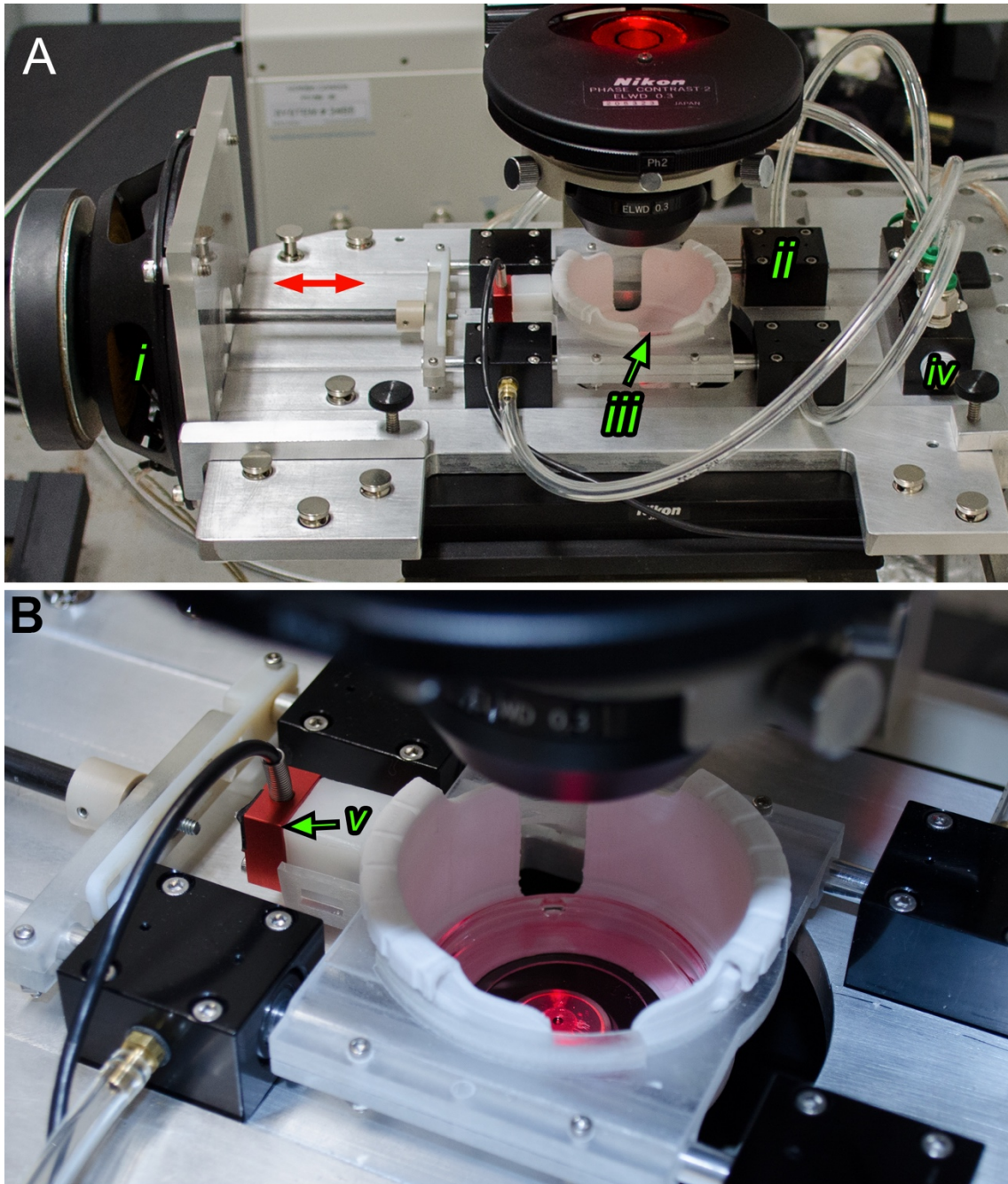


Figure 2.1 The motion-control platform mounted on an inverted microscope. (A) The vibration system was assembled on a solid aluminum plate to provide rigidity. A signal from a waveform generator is sent to the electromagnetic actuator (i) that drives a rod coupled to two aluminum support rails. These rails are suspended by four air bushings, each contained within a black pillow-block housing unit (ii). The rails support an acrylic carriage, coupled to the cell culture dish holder (iii). Compressed air from the manifold (iv) generates the pressure required for the air bushings. The system generates uniaxial horizontal displacements parallel to the plane of the microscope stage, as indicated by the red double-headed arrow. (B) Image shows a close-up view of cell culture dish (50 mm diameter) inserted in the vibration platform. An on-board accelerometer (v) monitors motion continuously during experimentation. The platform is compatible with microscopy techniques involving both trans- and epi-illumination.

control module; Southwestern Industries Inc., Rancho-Dominguez, CA) from aluminum cast plate (MIC-6, which is stress relieved to prevent potential long term distortions). A 150-W, 4- Ω commercial speaker (Pyramid, Brooklyn, NY) was used to actuate the moving parts of the device. A 6.4-mm outer diameter (OD) carbon fiber tube was fixed to the center of the speaker diaphragm with quick-setting epoxy (Speed Set Professional Epoxy, LePage, Mississauga, Canada). Two neodymium magnets were used to couple the actuator rod to a custom-designed adapter 3D-printed from acrylic. This adapter attached to two support rails (aluminum tubes, nominally 6.4 mm OD), which had been polished to a mirror-like finish to reduce friction. The aluminum tubes were each suspended by two low-friction air bushings (NewWay, Aston, PA), with 6.4 mm inner diameter (ID). These steps to reduce friction were required to ensure accurate reproduction of input motion waveforms. A 3D-printed acrylic carriage was mounted between the two aluminum tubes. This carriage was designed to couple to a cell culture dish holder (3D-printed from polylactic acid) that secured a 50-mm diameter cell culture dish with a 30-mm diameter glass bottom of approximately 100 μm thickness (MatTek Corp., Ashland, MA).

Culture dishes could be inserted and removed from the culture dish holder. This allows cell preparations to be taken from the incubator and placed in the system to study acute effects of vibration. Moreover, cell preparations could be vibrated and then returned to the incubator to permit multiple applications of vibrational stimuli, or to assess of long-term biological changes.

A waveform generator (182A; Wavetek, San Diego, CA) produced a signal at a specified frequency (nominal frequency). The signal was split in two; one used to drive the speaker

and one recorded using PowerLab and LabChart (ADInstruments, Dunedin, New Zealand). Data from LabChart were used to determine the actual frequency of the sinusoidal signal (input frequency). The signal to drive the speaker was amplified with a power amplifier (P-906MK2; TOA Electronics, Burlingame, CA). We tested the device with simple harmonic signals, i.e. sinusoids, of various frequencies and peak accelerations.

In all experiments, motion was measured with an on-board, factory-calibrated accelerometer (7521A1; Dytran Instruments, Chatsworth, CA) that was fastened to the 3D-printed carriage. The accelerometer bandwidth was 0 to 1500 Hz with a range of ± 2 g. Its output was displayed on an oscilloscope (PM 3350A; Philips, Amsterdam, Netherlands) and digital multimeter (115 True-RMS; Fluke Corp., Everett, WA), and was recorded with LabChart. Nominal accelerations were set by manually adjusting the gain on the power amplifier, using feedback from the signal on the multimeter.

2.3.2 Characterization of motion using high-speed imaging and micro-particle tracking

To validate motion of the platform and accelerometer output, we created a spatial distribution of fiducial particles, which were individually tracked using high-speed optical imaging. Black-dyed polystyrene microspheres (diameter 6 μm ; Polysciences, Warrington, PA) were suspended in distilled water at 2.1×10^8 particles per mL. The particle suspension was added to a 50-mm glass-bottomed cell culture dish and allowed to dry. Once the water had evaporated, the particles remained adherent on the surface of the glass. To preserve this distribution of fiducial particles, we embedded them in

polydimethylsiloxane (PDMS, Sylgard 184; Dow Corning, Midland, MI). PDMS elastomer and curing agent were mixed in a ratio of 10:1 (wt:wt), vacuum degassed, and 200 μ L were applied to the center of the dish and spun for 60 s at 3000 RPM. The PDMS layer was then allowed to cure over the next 48 h. This created an optically clear coating of PDMS of approximately 20- μ m thickness over the beads. The dish was then placed in the motion-control platform, with 3.5 mL of water added to mimic the mass of fluid present in live-cell experiments. In some experiments designed to assess the possibility of fluid motion relative to the dish, we also introduced fiducial particles suspended in distilled water that were allowed to settle onto the PDMS layer containing fixed particles. These unfixed particles (Fluostar, EBM; Tokyo, Japan) were 15 μ m in diameter, a size selected to be at least that of the thickness of an adherent osteoblastic cell.

In all experiments, vibration parameters (20 – 500 Hz, 0.1 – 1.0 g) were monitored with the on-board accelerometer. To validate the output of the accelerometer, we imaged fiducial particles during vibration at 30, 45, and 90 Hz, with peak accelerations of 0.1, 0.2, and 0.3 g. Imaging and tracking of fiducial particles was performed as described previously (Lorusso et al., 2016). Briefly, we imaged the motion of particles on an inverted microscope (Diaphot, Splan4 4x objective, NA 0.25; Nikon, Tokyo, Japan) using a high-speed camera (Exilim Ex-F1; Casio, Tokyo, Japan) at 1200 frames per second. Digital video image sequences were then analyzed frame-by-frame to track the position of individual particles over time (Image J, Particle Track and Analysis PTA v 1.1, developed by Yoshiyuki Arai, Osaka University, Japan). We quantified positions, frequency, and peak acceleration of individual particles as described in section 3.1 below.

Data were fit using GraphPad Prism (San Diego, CA) software by nonlinear least-squares regression.

2.3.3 Culture and transfection of osteoblastic cell lines

We studied two rodent cell lines, rat osteoblast-like cells UMR-106 and mouse preosteoblastic MC3T3-E1, both of which are known to be mechanically sensitive (Kim et al., 2018; Lorusso et al., 2017b; Lorusso et al., 2016; Lyons et al., 2016). Both cell lines were cultured at 37°C, 5% CO₂ with α -MEM medium (buffered with HCO₃⁻, 26 mM), 10% fetal bovine serum (FBS) and antibiotics (supplemented α -MEM), as previously described (Grol et al., 2013). Where indicated, we monitored organization of actin within live MC3T3-E1 cells. Cells were transfected with pEGFP-actin vector (catalog #6116-1, Clontech Laboratories/Takara Bio USA, Mountain View, CA) in α -MEM using X-tremeGENE 9 Transfection Reagent (Sigma-Aldrich Canada, Oakville, ON) according to the manufacturer's recommendation. Cells were then incubated for 18-24 h prior to live cell imaging.

2.3.4 Isolation and culture of rat osteoclasts

Osteoclasts were isolated from neonatal Wistar rats as described previously (Tanabe et al., 2011) using a protocol approved by the Council on Animal Care of the University of Western Ontario and in accord with the guidelines of the Canadian Council on Animal Care. Briefly, long bones were minced with a scalpel in M199 buffered with HCO₃⁻ and supplemented with 15% FBS and antibiotics. Cells were suspended by repeated passage through a glass pipette and plated on 50-mm glass-bottom dishes (MatTek). Dishes were

incubated at 37°C in 5% CO₂ for 1 h, gently washed with phosphate-buffered saline to remove non-adherent cells, and incubated in M199 buffered with HCO₃⁻ and supplemented with 15% FBS and antibiotics for 1–2 h before experiments.

2.3.5 Spectrofluorometric measurement of [Ca²⁺]_i

Spectrofluorimetry was used to characterize the elevation of [Ca²⁺]_i induced by ATP in suspensions of MC3T3-E1 cells (not subjected to vibration) as described previously (Grol et al., 2012). Cells were grown on Falcon® 100 mm TC-treated culture dishes in supplemented α-MEM. On the day of the experiment, cells were loaded with indo-1 by incubation with indo-1-AM (3 μM) for 30 min at 37°C. Cells were then washed with phosphate-buffered saline and harvested by trypsinization. Supplemented α-MEM was added to neutralize trypsin, and cells were sedimented and resuspended in MEM (HEPES-buffered). For measurement of [Ca²⁺]_i, aliquots were sedimented and resuspended in 3 mL of HEPES buffer in a fluorometric cuvette at room temperature. HEPES buffer contained (in mM): 135 NaCl, 5 KCl, 1 MgCl₂, 1 CaCl₂, 10 glucose, and 20 HEPES (nominally Ca²⁺-free buffer contained no added CaCl₂), adjusted to 290 ± 5 mOsm/L and pH 7.30 ± 0.02. Samples were excited at 355 nm and emission was monitored simultaneously at 405 and 485 nm using a dual emission QuantaMaster fluorometer (Horiba - Photon Technology International, Birmingham, NJ). Test substances were added directly to the cuvette. Ratios of fluorescence intensities at 405/485 nm reflect [Ca²⁺]_i (Grynkiewicz et al., 1985). Data were analyzed using FelixGX software from Horiba - Photon Technology International.

2.3.6 Microspectrofluorimetry and fluorescence ratio imaging of $[Ca^{2+}]_i$

For vibration studies, $[Ca^{2+}]_i$ levels were monitored by microspectrofluorimetry and fluorescence ratio imaging. For such studies, osteoblastic cells or osteoclasts were plated on 50-mm glass-bottom dishes (MatTek). Unless otherwise specified, osteoblastic cells were plated at a density of approximately 2×10^4 cells/cm². Cultures were then incubated for 24-72 h (in some cases, the medium was changed to serum-free α -MEM for the final 24 h of incubation). Prior to imaging, osteoblastic cells or osteoclasts were loaded with calcium-sensitive fluorescent dye fura-2 by incubation with fura-2-AM (1.5 μ M) in α -MEM at 37°C in 5% CO₂ for 30 min. Medium was then replaced 3.5 mL of fresh α -MEM or M199 [buffered with HEPES (25 mM)] to maintain physiological pH during extended experimentation in room air. In osteoblast experiments, cells were imaged in α -MEM with or without FBS. Osteoclasts were imaged in M199 supplemented with FBS.

Microspectrofluorimetry permitted us to measure $[Ca^{2+}]_i$ of cells when the culture dish was mounted in the motion-control platform. The average $[Ca^{2+}]_i$ of a field of cells could be monitored continuously throughout an experiment (before, during, and after vibrational stimuli were applied). Studies were performed using an inverted microscope (Nikon Eclipse TE2000-U) with a Plan Fluor 40X/1.3 NA oil/water immersion objective. Cells loaded with fura-2 were excited with alternating wavelengths of 345 and 380 nm using a DeltaRam X illuminator (Horiba - Photon Technology International) and the emission signal was filtered at 510 nm, as described previously (Pereverzev et al., 2008). Ratios of fluorescence intensities at 345/380 nm were acquired at 200 ms intervals with a

D-104 Microscope Photometer (Horiba - Photon Technology International) and analyzed using FelixGX software.

Fluorescence ratio imaging was also used to obtain real-time $[Ca^{2+}]_i$ measurements from cells in dishes mounted in the motion-control platform. This technique provided the opportunity to visualize $[Ca^{2+}]_i$ with powerful spatial resolution before and after vibration. However, during vibration, images were blurred due to the associated motion. Ratio imaging was performed with an inverted microscope (Nikon Diaphot) using a Plan Fluor 40X/1.3 NA oil/water immersion objective. Again, cell samples were again excited with alternating wavelengths of 345 and 380 nm using a DeltaRam X illuminator and the emission signal was filtered at 510 ± 20 nm, as described previously (Wheal et al., 2014). Ratio images were acquired at 1 s intervals with a sCMOS camera (pco.edge 4.2 LT, 2048 x 2048 pixels; PCO AG, Kelheim, Germany) and EasyRatioPro 2.3 Software (Horiba- Photon Technology International) (Lorusso et al., 2016). The ratio of fluorescence intensities at 345/380 nm gives an index of $[Ca^{2+}]_i$ independent of cell thickness or dye leakage. All experiments were performed at room temperature.

2.3.7 Fluorescence imaging of actin dynamics and time-lapse phase-contrast microscopy

Actin organization in live MC3T3-E1 cells expressing EGFP-actin was monitored using an inverted microscope (Nikon Diaphot) using a Plan Fluor 40X/1.3 NA oil/water immersion objective. Samples were excited at 470 nm using the DeltaRam X illuminator and the emission signal was filtered at 500-550 nm. Images were acquired with the sCMOS camera and EasyRatioPro 2.3 Software. Time-lapse, phase-contrast imaging of

osteoclasts was performed using the same microscope with a Plan Fluor ELWD 40X/0.6 NA Ph2 objective. Experiments were performed at room temperature. Actin experiments were performed in phenol red-free medium.

2.3.8 Statistical analyses

For motion characterization studies, curves were fit to data using GraphPad Prism 7 software (San Diego, CA) software by nonlinear least-squares regression. For the $[Ca^{2+}]_i$ studies, data are ratios of fluorescence intensities, normalized as a percentage of the baseline ratio using the formula $(100R/R_0)-100$, where R was the fluorescence ratio and R_0 was the baseline ratio. Data shown are means \pm SEM or medians \pm 95% confidence intervals as indicated. Data were analyzed by the Mann-Whitney test, Welch's t-test, Fisher's exact test, or two-way analysis of variance (ANOVA) using GraphPad Prism 7. Differences were accepted as statistically significant at $p < 0.05$.

2.4 Results

2.4.1 Accuracy and precision of the motion-control platform

For studies of cellular responses to vibrations, it is essential to not only have the capability to control the magnitude and frequency of vibrations delivered, but also to be able to monitor them in real-time as they are applied to live cells or tissues. To validate this ability, we operated the vibration platform over a range of sinusoidal frequencies (nominally 20 – 500 Hz) and peak accelerations (nominally 0.1 – 1 g). Acceleration was monitored with the on-board accelerometer fixed to the platform (Fig. 2.1B), while simultaneously imaging fiducial particles fixed to the glass surface of the cell culture

dish. We first plotted the instantaneous accelerations recorded using the accelerometer as a function of time at nominal frequencies of 30, 45, and 90 Hz and nominal peak accelerations of 0.1, 0.2, and 0.3 g (Fig. 2.2). Using least-squares regression, a sine function was fit to these data:

$$y = \text{baseline} + \text{amplitude} * \sin(2\pi * \text{frequency} * x + \text{phase shift}) \quad (\text{Equation 3.1})$$

where A is the sinusoidal amplitude and f is the frequency in Hz. The accelerations recorded using the accelerometer faithfully yielded sinusoidal patterns with $R^2 \geq 0.99$ in each case.

We then used imaging data, which were acquired concurrently, to validate the frequency and peak acceleration as recorded by the on-board accelerometer. Using particle tracking methods, we determined the position of marker beads over time at nominal sinusoidal frequencies of 30, 45 and 90 Hz and nominal peak accelerations 0.1, 0.2 and 0.3 g (Fig. 2.3A and Video 2.1). At 0.5 g, we were unable to image particles over the full range of frequencies and these data were not included. A sine function was then fit to the position *versus* time data (Equation 1, Fig. 2.3B), with excellent goodness of fit (R^2 ranged from 0.96 to 0.99).

We next compared the frequency obtained from curve fits to the accelerometer data (recorded frequency, accelerometer) to the frequency of the signal from the waveform generator (input frequency, Table 2.1). The mean of the difference between these two values (error) was 0.13%, with no error greater than 0.38%. We then compared the frequencies obtained from the optical tracking data to those recorded using the accelerometer. In this case, percent differences ranged from only 0.17 to 0.54%

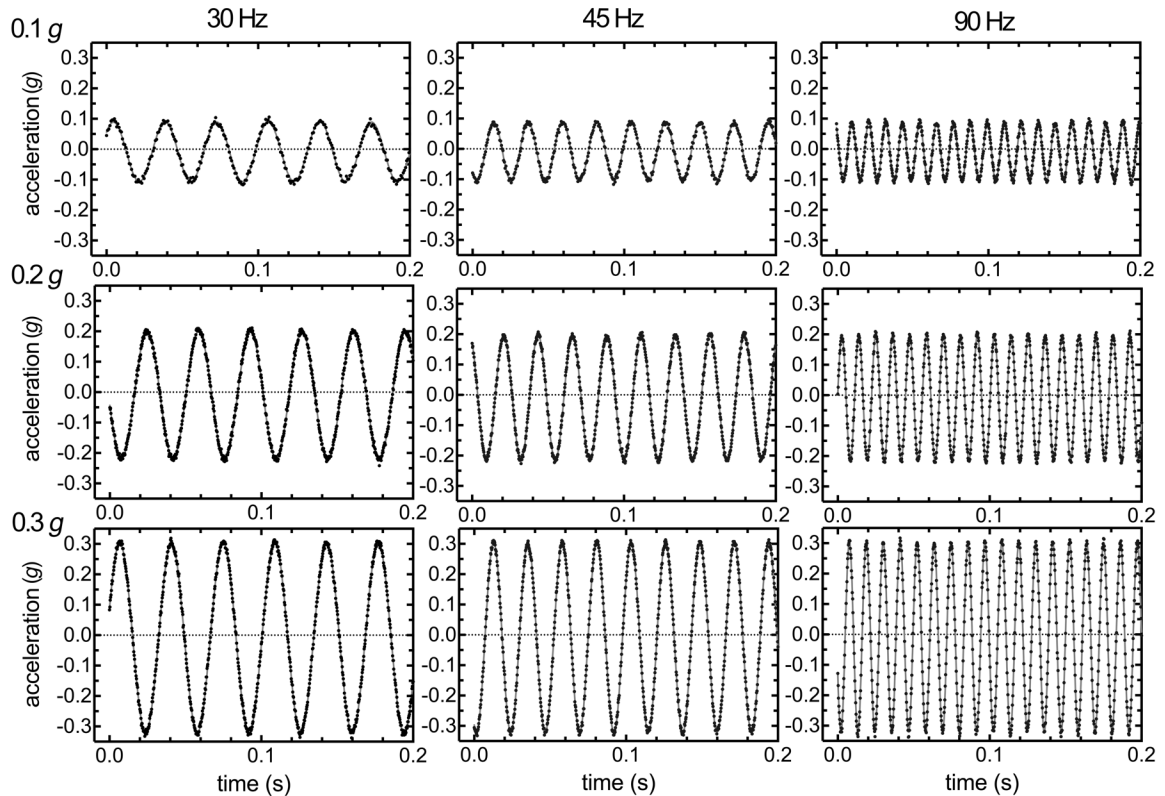


Figure 2.2 Accelerations monitored using on-board accelerometer. Representative data show magnitude of accelerations when the platform was vibrated at nominal peak accelerations of 0.1, 0.2, or 0.3 g and frequencies of 30, 45, or 90 Hz. Data points are instantaneous accelerations from the accelerometer as a function of time recorded on LabChart at sampling rates of at least 4×10^3 points/s. Data were fit to a sine function (Equation 1) and are representative of 40 determinations in which frequency ranged from 20 to 500 Hz and nominal peak accelerations from 0.1 to 1 g . Goodness of fit (R^2) was 0.99 or above in all cases. The time periods of 0.2 s that are shown were selected randomly from the entire data set. For the 0.1 g at 30 Hz dataset, 2 rows of data were skipped for every row graphed. For the 0.1 g at 45 Hz dataset, 1 row of data was skipped for every row graphed. All lines on the graph are best fits, while points are actual data.

Table 2.1 Peak accelerations recorded using the on-board accelerometer or optical tracking at various nominal frequencies and accelerations

Nominal input freq (Hz)	Nominal accel (g)	Recorded peak acceleration (g) (accelerometry)		Recorded acceleration (g) (optical tracking)		Acceleration difference (%) (accelerometer vs optical)
		Value	SE	Value	SE	
30	0.1	0.098	<0.001	0.104	0.001	6.62
	0.2	0.209	<0.001	0.228	0.001	8.86
	0.3	0.311	<0.001	0.336	0.007	7.69
45	0.1	0.096	<0.001	0.103	0.004	6.91
	0.2	0.206	<0.001	0.222	0.004	7.56
	0.3	0.312	<0.001	0.334	0.012	6.61
90	0.1	0.096	<0.001	0.101	0.003	5.67
	0.2	0.207	<0.001	0.215	0.022	3.58
	0.3	0.313	<0.001	0.321	0.037	2.51

The nominal input frequency (column 1) was selected on the waveform generator. The nominal peak acceleration (column 2) was set using the accelerometer output. To validate acceleration measurements, we monitored motion simultaneously by accelerometry and optical particle tracking. The best-fit peak acceleration values from accelerometry are shown in column 3. For the optical data, the best-fit value for amplitude of vibration was used to calculate the acceleration (column 4), using the expression for simple harmonic motion (Equation 2). Standard errors (SE) indicate precision over the duration (0.5 s) of the sampled data (10^3 points). The acceleration difference (column 5) is the difference between the accelerations derived using the two methods and is expressed as a percentage of the average value.

(Table 2.1). Finally, it should be noted that the frequency data obtained from curve fits to both the accelerometer and optical tracking data exhibited relatively small standard errors, indicating that the frequency of platform motion remained stable over time. Thus, data obtained using the accelerometer appeared to be valid, and the platform moved at a stable frequency that accurately reproduced the input signal.

To validate the peak acceleration reported by accelerometry, the sinusoidal amplitude (maximal displacement from baseline) reported by particle tracking was used to calculate peak acceleration using the equation governing simple harmonic motion:

$$a_{peak} = A(2\pi f)^2 \quad (\text{Equation 2})$$

where a_{peak} is the peak acceleration in m/s^2 , A is the sinusoidal amplitude in meters, and f is the frequency of vibration in Hz. We found a mean difference of $\sim 6\%$ between the accelerations derived from optical tracking and those recorded using the accelerometer, with no difference greater than 8.86% (Table 2.1).

Finally, we plotted the relationship between amplitude and frequency for both the accelerometer and optical tracking data (Fig. 2.3C). To calculate maximal displacements (amplitude) from the accelerometer measurements, we used the peak acceleration values from curve fits with sine functions (*e.g.* Fig. 2.2) and, using Equation 2, solved for A :

$$A = a_{peak}/(2\pi f)^2 \quad (\text{Equation 3})$$

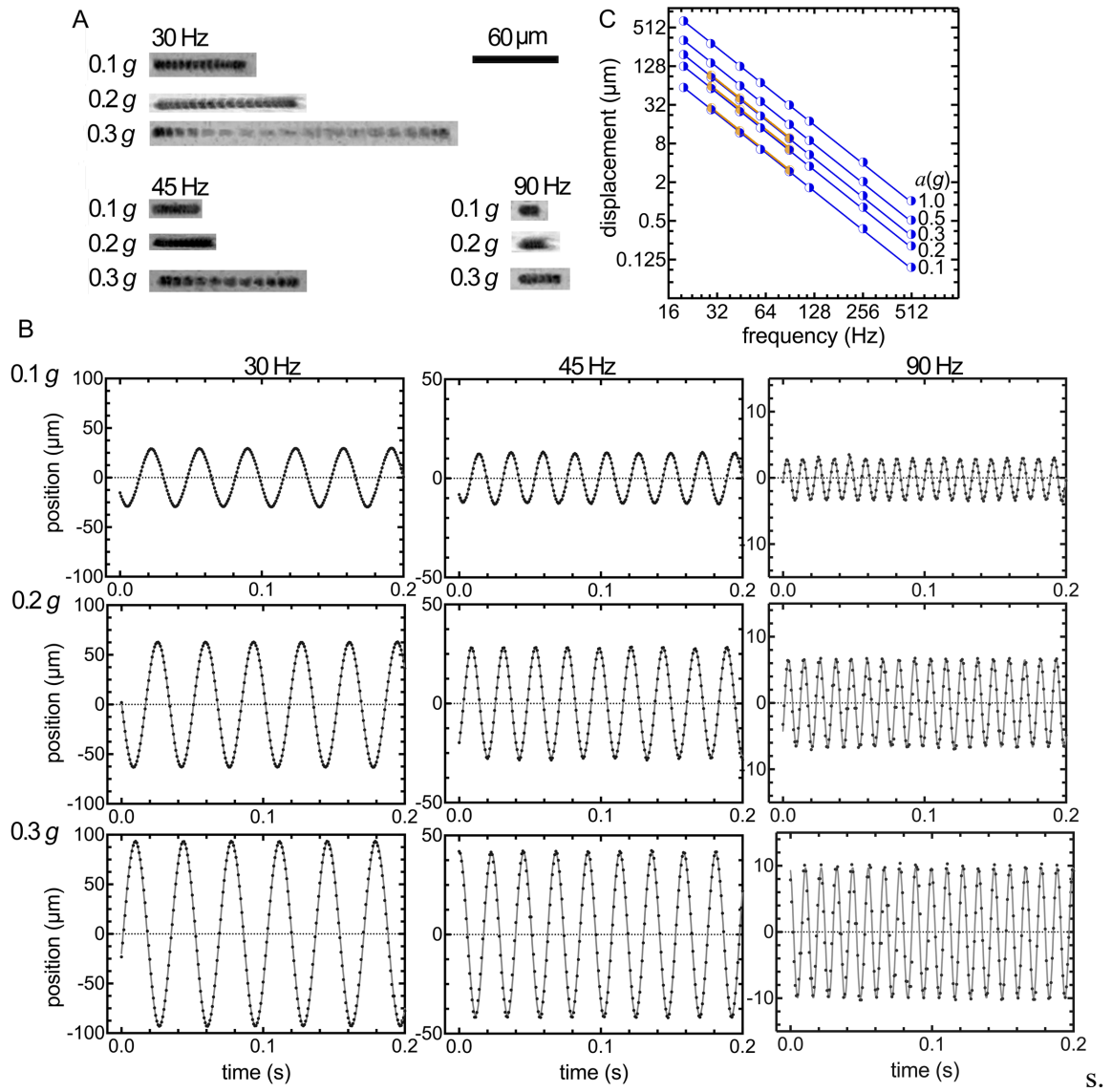


Figure 2.3 Direct observation of vibrational displacement with optical particle tracking. (A) Maximum intensity projection of vibrated fiducial marker particles. To validate the accelerations reported by the on-board accelerometer, a subset of frequencies (nominally 30, 45, and 90 Hz) and magnitudes of peak acceleration (nominally 0.1, 0.2, and 0.3 g) were simultaneously monitored with optical particle tracking. A dish seeded with fiducial marker particles was vibrated under an inverted microscope. The markers were imaged at 1200 frames per second using a high-speed camera. Videos were then cut and cropped, and one cycle of each bead's motion was projected onto a single image, allowing visualization of particle motion over time. Movies from this experiment are provided as Video 2.1. (B) Fiducial marker particles imaged in panel A were analyzed using particle-tracking software to determine the displacement of vibration. A sine function (Equation 1) was fit to the data. Goodness of fit (R^2) was an average of > 0.99 at 30 and 45 Hz, and 0.96 at 90 Hz. The time periods of 0.2 s that are shown were selected randomly from the entire data set. (C) Graph shows displacement of simple harmonic vibration (as recorded *via* accelerometry and particle tracking) over a range of frequencies and peak accelerations (20 to 500 Hz and 0.1 to 1 g , respectively). Motion was monitored using the accelerometer (blue, as described in Figure 2.2) and validated with optical microscopy (orange). Resulting maximum displacements were plotted and fit with the function describing simple harmonic motion (Equation 3). From the accelerometer data, best-fit values for a_{peak} were $0.095 \pm 0.001 g$, $0.199 \pm 0.001 g$, $0.302 \pm 0.001 g$, $0.502 \pm 0.001 g$, and $1.005 \pm 0.002 g$ (means \pm SE, corresponding to nominal peak accelerations of 0.1, 0.2, 0.3, 0.5, and 1.0 g , respectively). From the optical tracking data, best-fit values for a_{peak} were $0.100 \pm 0.001 g$, $0.216 \pm 0.002 g$, and $0.317 \pm 0.005 g$ (means \pm SE, corresponding to nominal peak accelerations of 0.1, 0.2, and 0.3 g , respectively). All lines on the graph are best fits, while points are actual data.

Table 2.2 Peak accelerations recorded using the on-board accelerometer or optical tracking at various nominal frequencies and accelerations

Nominal input freq (Hz)	Nominal accel (g)	Recorded peak acceleration (g) (accelerometry)		Recorded acceleration (g) (optical tracking)		Acceleration difference (%) (accelerometer vs optical)
		Value	SE	Value	SE	
30	0.1	0.098	<0.001	0.104	0.001	6.62
	0.2	0.209	<0.001	0.228	0.001	8.86
	0.3	0.311	<0.001	0.336	0.007	7.69
45	0.1	0.096	<0.001	0.103	0.004	6.91
	0.2	0.206	<0.001	0.222	0.004	7.56
	0.3	0.312	<0.001	0.334	0.012	6.61
90	0.1	0.096	<0.001	0.101	0.003	5.67
	0.2	0.207	<0.001	0.215	0.022	3.58
	0.3	0.313	<0.001	0.321	0.037	2.51

The nominal input frequency (column 1) was selected on the waveform generator. The nominal peak acceleration (column 2) was set using the accelerometer output. To validate acceleration measurements, we monitored motion simultaneously by accelerometry and optical particle-tracking. The best-fit peak acceleration values from accelerometry are shown in column 3. For the optical data, the best-fit value for amplitude of vibration was used to calculate the acceleration (column 4), using the expression for simple harmonic motion (Equation 2). Standard errors (SE) indicate precision over the duration (0.5 s) of the sampled data (10^3 points). The acceleration difference (column 5) is the difference between the accelerations derived using the two methods and is expressed as a percentage of the average value.

Displacement data from the tracking measurements were obtained directly from curve fits with sine functions (e.g. Fig. 2.3B). We then fit the displacement versus frequency data obtained using both methods with Equation 3, which yielded excellent agreement between the peak accelerations from the accelerometer and optical tracking data (Fig. 2.3C). R^2 values were greater than 0.98 in all cases.

2.4.2 Assessment of fluid motion using microscope-based particle tracking

We investigated whether, during vibration, there was motion of the fluid relative to the dish, during vibration with our device. To determine this, we used the optical particle tracking method described above. In this case, in addition to the 6- μm particles fixed to the bottom of the dish, 15- μm fiducial particles suspended in distilled water were allowed to settle (unfixed particles, Fig. 2.4A, left panel). The size of these particles simulated that of a cell on the dish. Sinusoidal vibrations were delivered to the dish (nominally 45 Hz with peak acceleration of 0.3 g, Fig. 2.4A, middle panel). Particle motion was tracked, and positions of the fixed and unfixed particles were fit to a sine function and plotted over time (Fig. 2.4B). The similarity between the two motion waveforms indicates that there was minimal relative motion between the fluid and the dish. Following the cessation of vibration, distilled water was puffed into the cell culture dish to demonstrate that the unfixed particle was in fact non-adherent (Fig. 2.4A, right panel). Based on these findings, we were confident that our device would induce vibrational stimuli to cells without confounding responses arising from fluid flow.

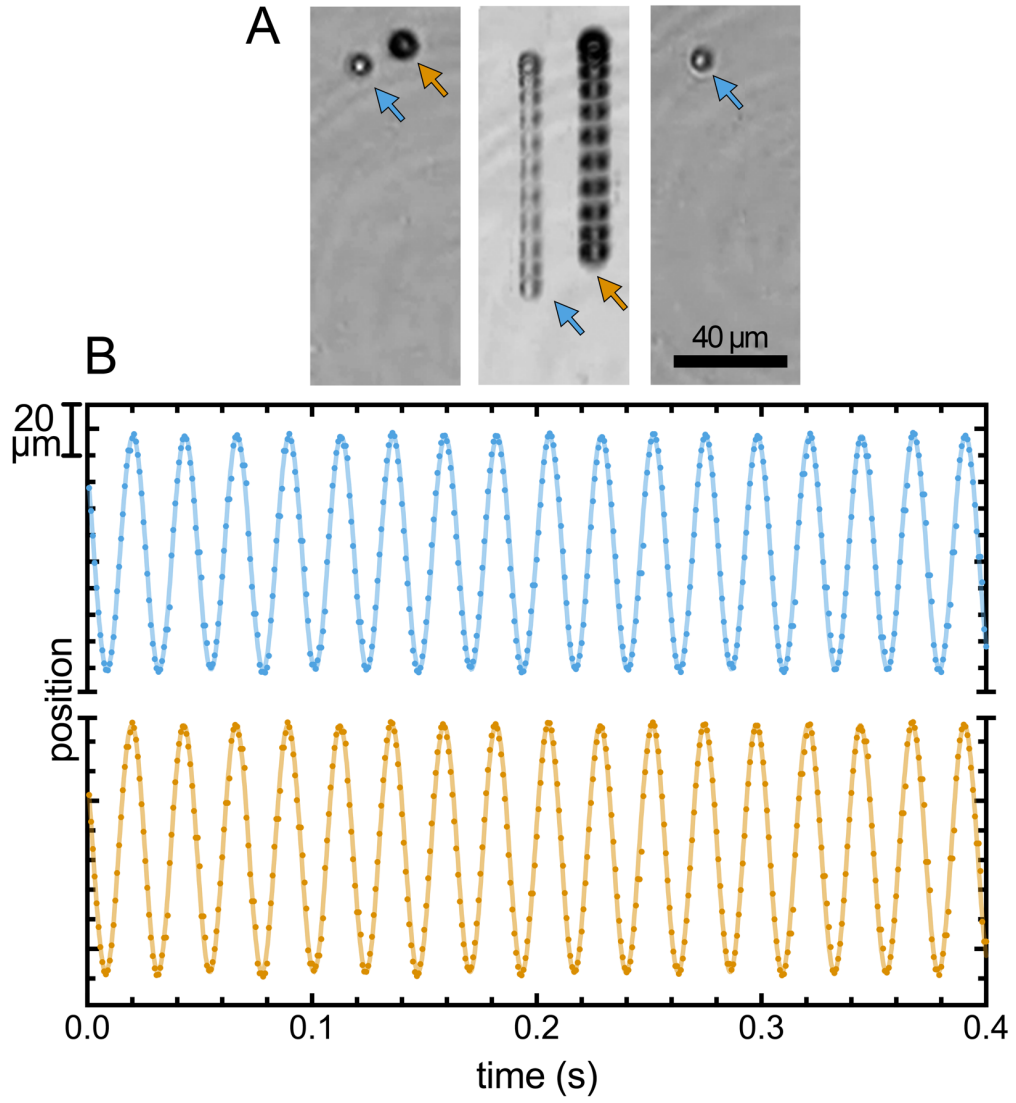


Figure 2.4 Tracking of fixed and unfixed particles to evaluate the possibility of flow between the fluid and the culture dish. Particles (15 μm diameter, unfixed) suspended in water were added to a culture dish with fixed fiducial particles (6 μm diameter). (A) After suspended particles had settled, an unfixed particle (orange arrow) was identified in the same focal plane as a fixed particle (blue arrow, left panel). The dish was then vibrated (nominally 45 Hz and 0.3 g peak acceleration). The particles were imaged at high speed and tracked frame by frame (middle panel), as described in the legend for Figure 2.3A. Following vibration, the fluid in the dish was agitated to confirm that the unfixed particle was free to move relative to the culture dish (right panel). Scale bar represents 40 μm . (B) Positions of the fixed (blue, upper data set) and unfixed (orange, lower data set) particles during vibration were fit with a sine function (Equation 1). Frequency of the fixed particle was 43.18 Hz, while that of the unfixed particle was 43.19 Hz. The sinusoidal amplitude of the fixed particle was 43.8 μm , while that of the unfixed particle was 41.6 μm . Data indicate little discrepancy in the relative motion of the fluid and the dish.

2.4.3 LMHF vibration of live UMR-106 rat osteoblast-like cells while monitoring $[Ca^{2+}]_i$ using microspectrofluorimetry

Having validated that we can precisely apply accelerations at specific frequencies with our platform, we examined the effects of LMHF vibration on live-cells. Based on previous reports that other forms of mechanical stimuli (e.g. fluid shear) induce calcium signaling in osteoblastic cells (Donahue et al., 2001; Lorusso et al., 2016), we anticipated that vibration might also induce acute elevation of $[Ca^{2+}]_i$. To investigate this possibility, we first loaded UMR-106 rat osteoblastic cells with fura-2, placed them in the device, and monitored $[Ca^{2+}]_i$ levels using microspectrofluorimetry (Fig. 2.5). Baseline values were observed to be stable. When vibrated with a sinusoidal waveform (nominally 45 Hz and 0.3 g), some noise was evident in fluorescence intensities at 345 and 380 nm. However, there was virtually no change in their ratio, indicating no alteration in $[Ca^{2+}]_i$. As a positive control, we added exogenous ATP, which is known to activate Ca^{2+} mobilizing P2Y receptors on these cells (Jorgensen et al., 1997; Reimer and Dixon, 1992). As expected, ATP induced transient elevation in fluorescence intensity at 345 nm and simultaneous reduction of signal at 380 nm. These changes are consistent with an authentic elevation of $[Ca^{2+}]_i$, which is reflected by the transient increase in fluorescence ratio.

We next assessed whether UMR-106 cells might respond when vibrated under different conditions. Cultures were subjected to nominal frequencies of 30 to 90 Hz, nominal accelerations of 0.3 and 1.0 g, and durations of vibration ranging from 0.5 to 15

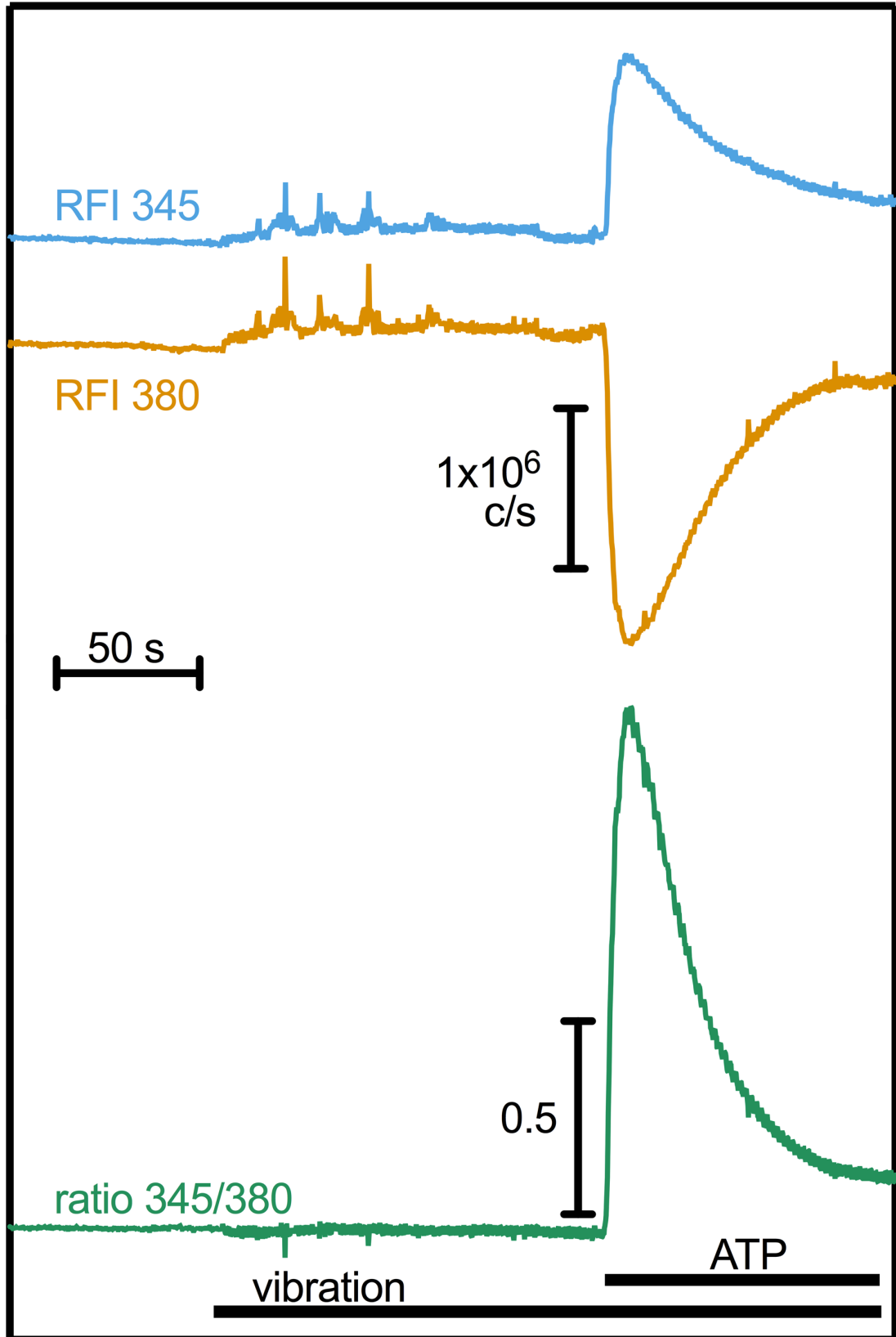


Figure 2.5 LMHF vibration of rat osteoblastic cells while monitoring $[Ca^{2+}]_i$ by microspectrofluorimetry. UMR-106 cells were loaded with calcium-sensitive dye fura-2 and placed in the vibration device on the microscope. Data illustrate relative fluorescence intensities (RFIs) and ratio from the entire field of cells (~20 to 50 cells per field). Background signal was monitored and then vibration was applied to the cells at 45 Hz and 0.3 g peak acceleration. Where indicated, ATP was added to the cell culture dish (100 μ M final). ATP induced a transient increase in $[Ca^{2+}]_i$ as indicated by a concomitant rise in RFI at 345 nm and drop at 380 nm (units are counts per second, c/s). The ratio of fluorescence intensities at 345 and 380 nm reflects the time course of the change in $[Ca^{2+}]_i$. Vibration had no detectable effect on $[Ca^{2+}]_i$; however, a robust response was induced by the purinergic agonist ATP (positive control). Data are representative of 10 dishes in 6 independent experiments.

min. Cells were also tested at different densities (initial plating density ranging from 5 to 20×10^3 cells/cm²), and with or without pre-incubation in serum-free medium. Under no condition did we observe any elevation of $[Ca^{2+}]_i$ in response to vibration, including during the onset and termination of the mechanical stimulus. Findings were based on whole-field measurements using microspectrofluorimetry on a total of 16 dishes of cells from 6 independent experiments².

2.4.4 LMHF vibration of live MC3T3-E1 murine osteoblast-like cells while monitoring $[Ca^{2+}]_i$ by fluorescence ratio imaging

We next investigated whether other cell types could respond to LMHF vibration with elevation of $[Ca^{2+}]_i$. We loaded murine preosteoblastic MC3T3-E1 cells with fura-2, placed them in the device, and monitored $[Ca^{2+}]_i$ using fluorescence ratio imaging. In this series of experiments, we first monitored fluorescence intensity at 345 and 380 nm from the entire field of view. Although it is not technically feasible to resolve images of individual cells during vibration due to blurring, we were able to obtain a meaningful signal from the entire field of cells (Fig 2.6A). Once the vibration had ceased, it was then possible to image individual cells (Fig. 2.6B), enabling us to quantify responses of single cells to the subsequent addition of ATP (Fig. 2.6C).

Like UMR-106 cells, MC3T3-E1 cells did not display acute change in $[Ca^{2+}]_i$ in response to vibration (Fig. 2.6A, nominally 45 Hz and 0.3 g). Similarly, responses were not

² It should also be noted that mechanical vibration did not induce any apparent cell damage or detachment from the substratum. Following vibration, cells remained loaded with fura-2 and maintained baseline levels $[Ca^{2+}]_i$, arguing against loss of membrane integrity.

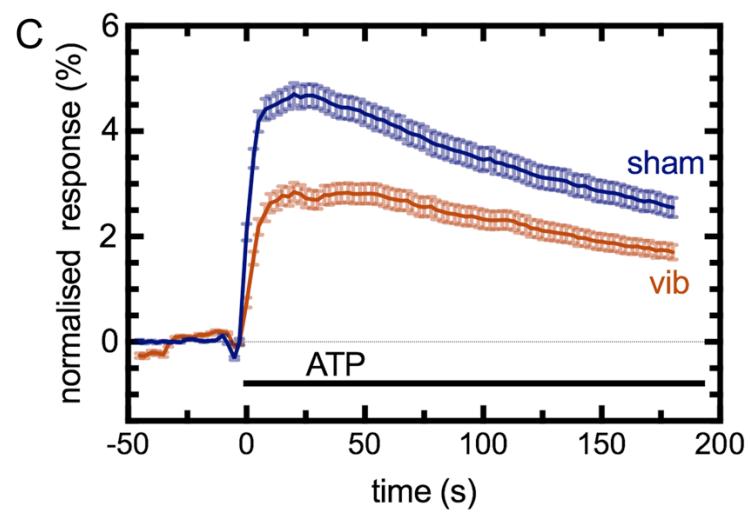
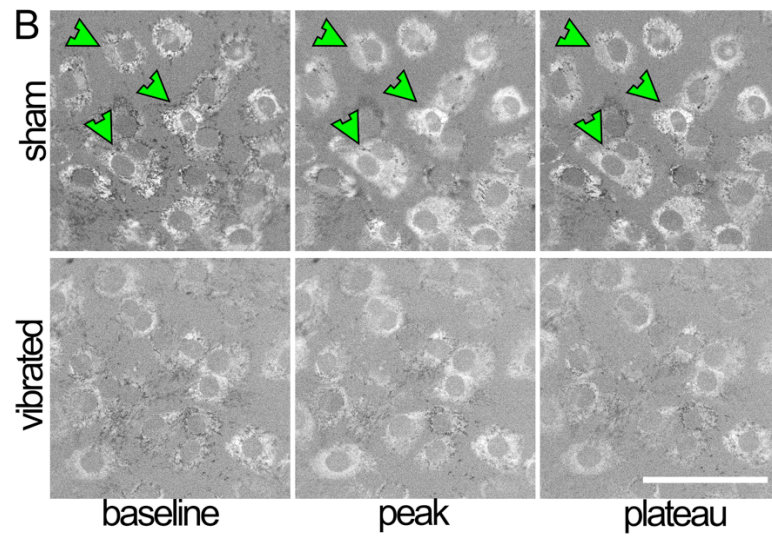
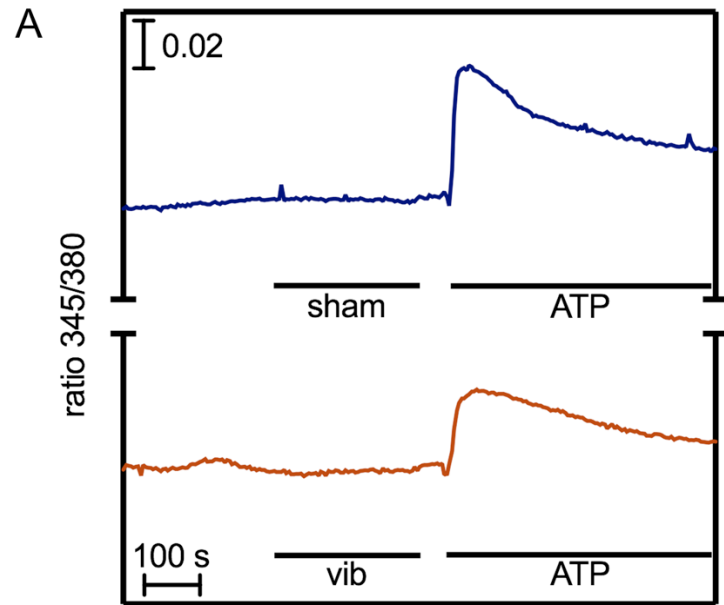


Figure 2.6 LMHF vibration of murine osteoblastic cells during real-time fluorescence ratio imaging of $[Ca^{2+}]_i$. MC3T3-E1 cells were loaded with fura-2 and placed in the vibration device on the microscope. (A) Representative time courses of the ratio of fluorescence intensities at 345 and 380 nm from entire fields of cells (~20 to 50 cells per field). Parallel samples of cells were treated without (sham) or with vibration (vib) at 45 Hz and 0.3 g peak acceleration. Where indicated, ATP (100 μ M final) was added to the culture dish as a positive control. On its own, vibration had no detectable effect on $[Ca^{2+}]_i$. However, the subsequent response to ATP appeared diminished following vibration. (B) Representative ratio images showing the responses of MC3T3-E1 cells to extracellular ATP following pretreatment with sham (upper row) or vibration (lower row) as described above for panel A. Images at left are immediately prior ATP addition, middle images are at the peak elevation of $[Ca^{2+}]_i$, and images at right are during the plateau phase (approximately 5 min following the addition of ATP). Increased brightness of the image, reflects an increased ratio and hence elevation of $[Ca^{2+}]_i$. Green arrowheads indicate individual cells that display robust elevation of $[Ca^{2+}]_i$ in response to ATP. Scale bar represents 100 μ m. Movies corresponding to these particular images are provided as Videos 2.2 and 2.3. (C) Time-course of responses of individual cells to ATP following treatment with vibration or sham. Regions of interest containing individual cells (or small numbers of contiguous cells) were selected from full-field images described above for panel A. Time 0 represents the time of addition of ATP. Fluorescence intensity ratios were normalized as a percentage of baseline (where baseline was defined as the mean ratio value for the 45 s prior to addition of ATP). Data indicate changes in ratios, with baseline set at 0%, and are the mean \pm SEM of n = 236 cells for sham and 253 cells for vibration. The experiment was performed using 9 dishes of cells under each condition, in 3 independent experiments. The response of vibrated cells to ATP was significantly less than the response of sham control cells, $p < 0.0001$, based on two-way ANOVA.

observed when MC3T3-E1 cells were vibrated at 1 g. Moreover, in additional experiments not shown, we did not observe $[Ca^{2+}]_i$ changes in primary rat osteoclasts subjected to vibrational stimuli (based on a total of 5 cells from 3 independent experiments). Although failing to respond to vibration, both MC3T3-E1 cells and osteoclasts responded to the positive control agonist ATP with elevation of $[Ca^{2+}]_i$.

To determine the source of Ca^{2+} underlying this response to ATP in MC3T3-E1 cells, we quantified the elevation of $[Ca^{2+}]_i$ in the presence and absence of extracellular Ca^{2+} , and following depletion of intracellular Ca^{2+} stores using thapsigargin. The response to ATP was still robust in the absence of extracellular Ca^{2+} (Fig. 2.7). Moreover, pretreatment with thapsigargin markedly diminished the response to ATP (Fig. 2.8). Taken together, these findings establish that most, if not all, of the ATP-induced elevation of $[Ca^{2+}]_i$ is due to P2Y receptor-mediated release of Ca^{2+} from intracellular stores.

Following vibration of MC3T3-E1 cells, we noticed that the subsequent response to ATP appeared to be suppressed compared to that in non-vibrated (sham-treated) cells. To quantify this phenomenon, we monitored the responses to ATP of multiple individual cells following pretreatment with vibration or sham. Ratio images of fura-2-loaded MC3T3-E1 cells revealed that the majority of sham-treated cells responded to ATP with transient elevation in $[Ca^{2+}]_i$; whereas responses in cells pretreated with vibration were muted (Fig. 2.6B and Videos 2.2 and 2.3). We then averaged the time course data for individual cells pretreated with vibration ($n = 253$) or without vibration ($n = 236$). These data clearly show that vibration pretreatment attenuated the Ca^{2+} transient generated by

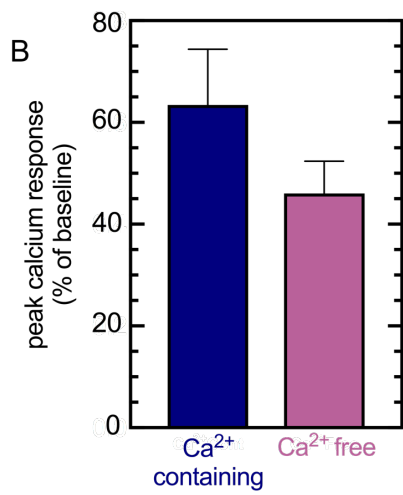
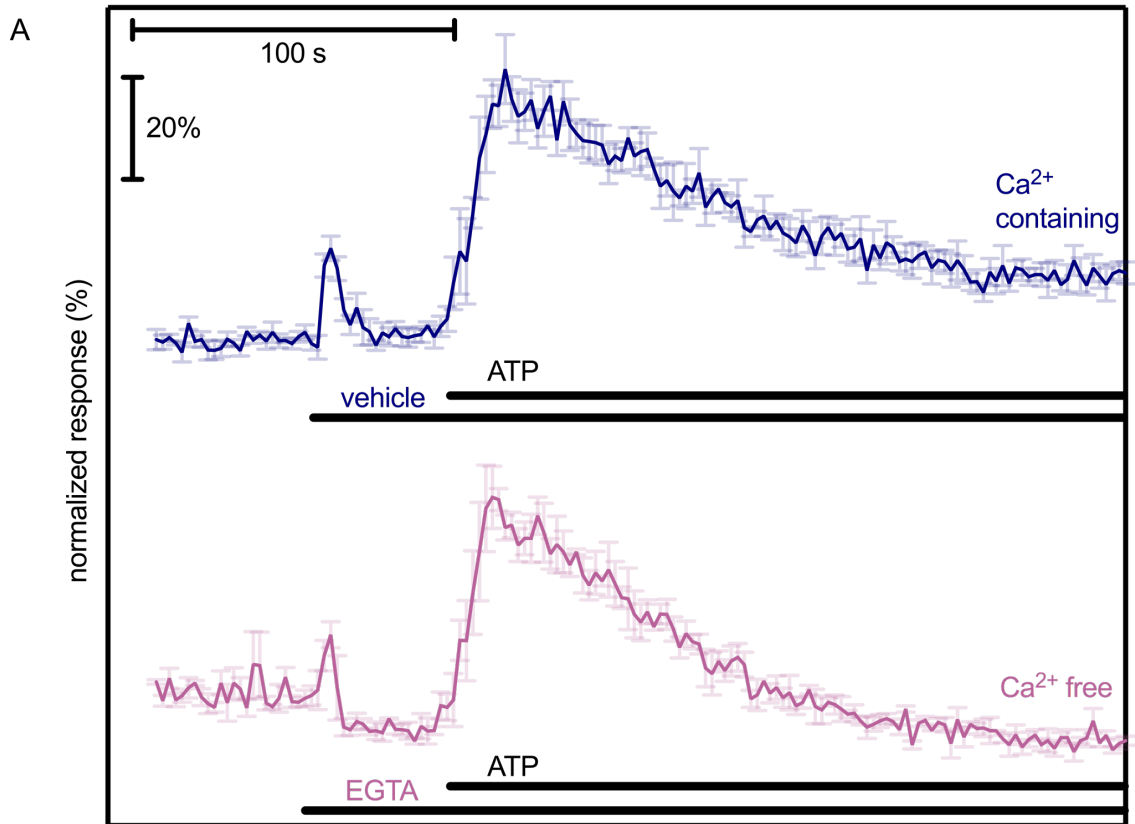


Figure 2.7 Spectrofluorimetric measurement of ATP-induced elevation of $[Ca^{2+}]_i$ in MC3T3-E1 cells suspended in Ca^{2+} -containing and Ca^{2+} -free buffer. MC3T3-E1 cells (not subjected to vibration) were loaded with calcium-sensitive fluorescent dye indo-1 and $[Ca^{2+}]_i$ was monitored with a cuvette-based spectrofluorimeter. (A) Upper trace: In calcium-containing medium, vehicle (for EGTA) was added to the cell suspension where indicated by the black horizontal bar below the trace. ATP (100 μ M) was then added to the cell suspension where indicated, inducing transient elevation in $[Ca^{2+}]_i$. Lower trace: Parallel samples of MC3T3-E1 cells were suspended in nominally calcium-free medium and treated with EGTA (1 mM final) to chelate residual extracellular free Ca^{2+} . ATP (100 μ M final) was added to the cell suspension, again yielding a $[Ca^{2+}]_i$ transient. Fluorescence intensity ratios were normalized as a percentage of baseline (where baseline was defined as the mean ratio value for the 15 s prior to addition of vehicle/EGTA). Data were captured every 100 ms, and for every data point plotted, 19 were not displayed (to improve visual clarity). Data are the mean \pm SEM from 4 samples in calcium-containing medium and 3 samples in calcium-free medium from 3 independent experiments. (B) The peak value of fluorescence intensity ratio above baseline was determined for each sample. Bars on the graph are the means \pm SEM. Responses of cells in calcium-free medium were not significantly different than those of cells in calcium-containing medium ($p = 0.1$ assessed using Welch's *t*-test). These data are consistent with ATP-induced elevation of $[Ca^{2+}]_i$ arising primarily by release from intracellular stores. A small addition artifact occurred during addition of test substances to the cuvette.

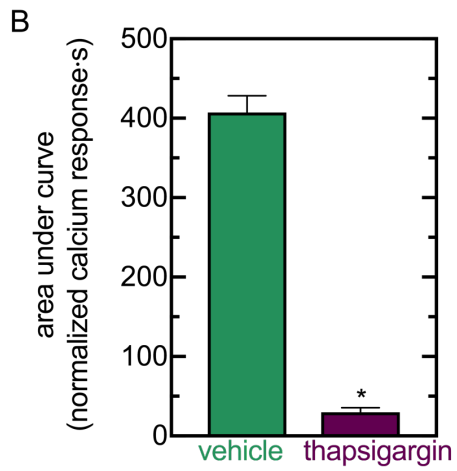
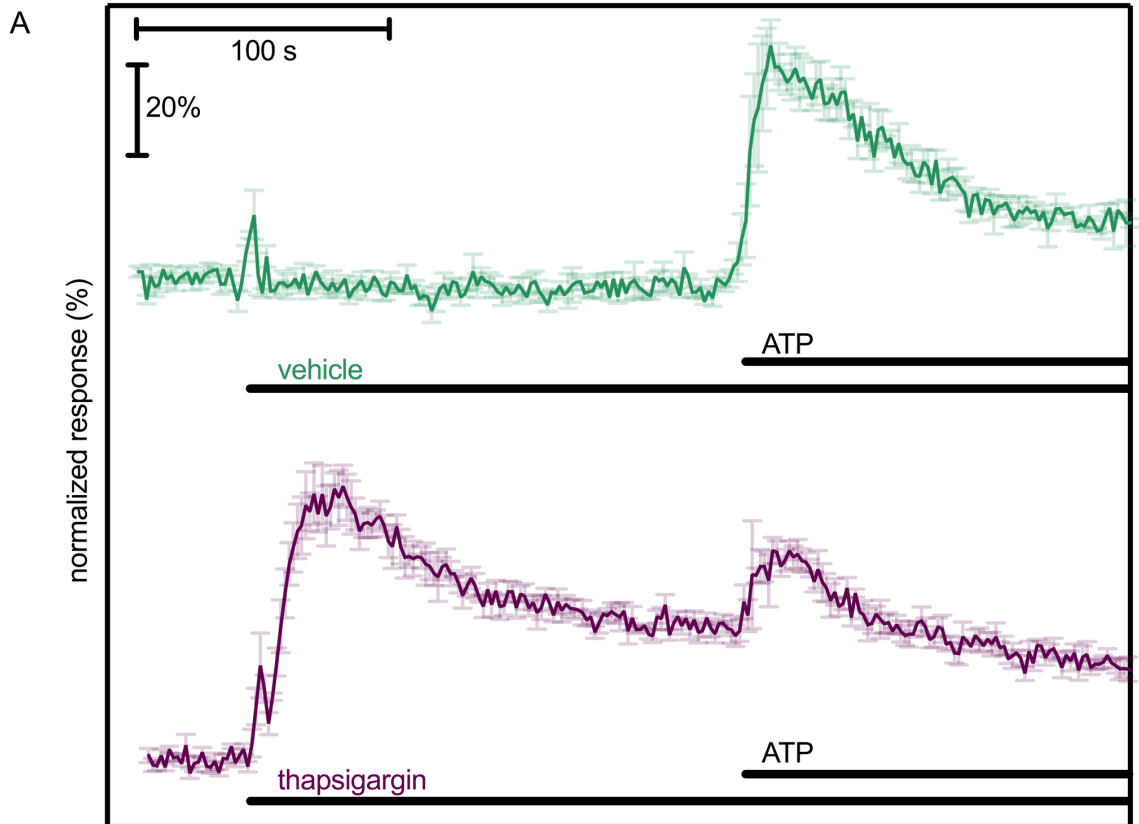


Figure 2.8 Spectrofluorometric measurement of ATP-induced elevation of $[Ca^{2+}]_i$ in MC3T3-E1 cells following depletion of intracellular Ca^{2+} stores.

subsequent addition of ATP (Fig. 2.6C, the effect of vibration compared to sham was significant at $p < 0.0001$, based on two-way ANOVA). We further analyzed the responses of the same individual cells described in Figure 6C. The magnitude of the peak elevation of $[Ca^{2+}]_i$ induced by ATP was plotted for cells subjected to pretreatment under sham conditions or vibration (Fig. 2.9). Vibration was found to significantly suppress the median peak Ca^{2+} response by 38% ($p < 0.0001$, based on a Mann-Whitney test). We also evaluated the percentage of cells responding to ATP under both conditions. Responding cells were defined as those in which elevation of $[Ca^{2+}]_i$ was greater than 2% of baseline. We found that, for sham pretreatment, 197 out of 236 cells responded (83%). In contrast, following pretreatment with vibration, 171 out of 253 cells responded (68%), significantly fewer than following sham ($p < 0.0001$, Fisher's exact test). We next investigated whether the effect of vibration could be explained by this increase in the proportion of non-responsive cells. When data from non-responders were excluded, vibration was still found to significantly suppress the peak elevation of $[Ca^{2+}]_i$ induced by ATP (Fig. 2.10, $p = 0.0017$, based on a Mann-Whitney test). Taken together, our findings established that vibration diminished the sensitivity of cells to the purinergic agonist ATP. Therefore, even though vibration on its own did not produce a Ca^{2+} signal, it did elicit a biological response in these cells.

2.4.5 Cell morphology and actin dynamics in cells exposed to LMHF vibration

Others have reported effects of chronic vibration on cytoskeletal organization of primary osteoblasts (Jing et al., 2015). Therefore, we considered the possibility that LMHF

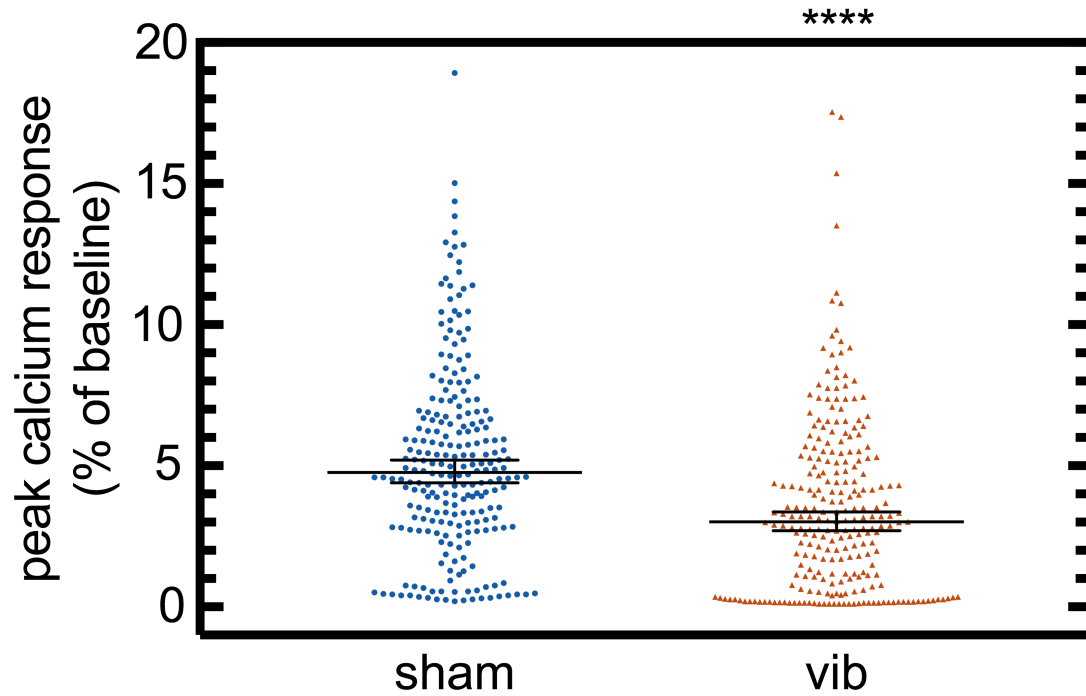


Figure 2.9 Magnitude of the peak elevation of $[Ca^{2+}]_i$ induced by ATP in MC3T3-E1 cells pretreated with vibration or sham. From the data described in the legend to Figure 2.6C, we determined the peak value of fluorescence intensity ratio above baseline for each individual cell region of interest. Each point represents a value for a single cell. Indicated are medians \pm 95% confidence intervals for $n = 236$ sham cells and 253 vibrated cells. Responses of vibrated cells to ATP were less than those of sham control cells (distributions were significantly different, $p < 0.0001$, based on a Mann-Whitney test).

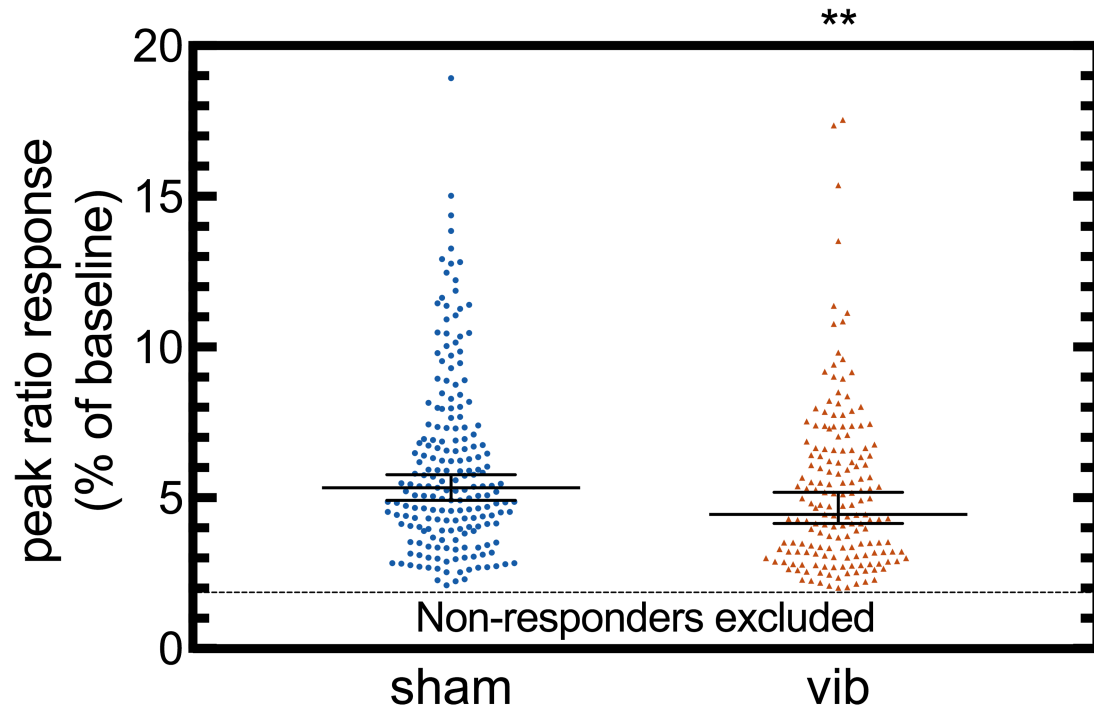


Figure 2.10 Magnitude of the peak elevation of $[Ca^{2+}]_i$ induced by ATP in MC3T3-E1 cells pretreated with vibration or sham, with non-responding cells excluded. As described in the legend to Figure 2.9, the peak value of fluorescence intensity ratio above baseline was determined for each individual cell region of interest. Each point represents a value for a single cell. Non-responding cells (defined as those in which elevation of $[Ca^{2+}]_i$ was less than 2% of baseline) were excluded from this analysis. Indicated are medians \pm 95% confidence intervals for $n = 197$ responding sham cells and 171 responding vibrated cells. Responses of vibrated cells to ATP were still less than those of sham control cells (distributions were significantly different, $p = 0.002$, based on a Mann-Whitney test).

vibration might induce acute changes in cell morphology or cytoskeletal organization. We first monitored actin organization in live MC3T3-E1 cells. Cells were transfected with EGFP-tagged actin and imaged before and immediately after vibration. MC3T3-E1 cells exhibited well-developed stress fibers and dynamic membrane ruffling; however, there were no acute changes in actin distribution that could be attributed to vibration (Fig. 2.10). Moreover, we monitored the morphology of live rat osteoclasts using time-lapse phase-contrast imaging. As previously described (Lapierre et al., 2010), osteoclasts were found to be highly-motile, extending and retracting lamellipodia. However, vibration had no marked effect on osteoclast morphology or motility (Video 2.4).

2.5 Discussion

2.5.1 Novel motion-control platform for application of vibrational stimuli

We developed a platform for the vibration of live cells and tissues at 20 – 500 Hz, and 0.1 – 1 g that is compatible with microscopy techniques including fluorescence microscopy. The frequency and magnitude of vibration are monitored in real time using the on-board accelerometer and were found to be accurate and precise.

A subset of the accelerometry measurements was validated using optical particle tracking and there was excellent agreement between the two methods. However, it was not feasible to use optical particle tracking for the entire acceleration range and frequency bandwidth of the accelerometer. This is due to the limitations in frame rate (resolving high-velocity motion), field of view (< 500 μm), and optical resolution of our imaging

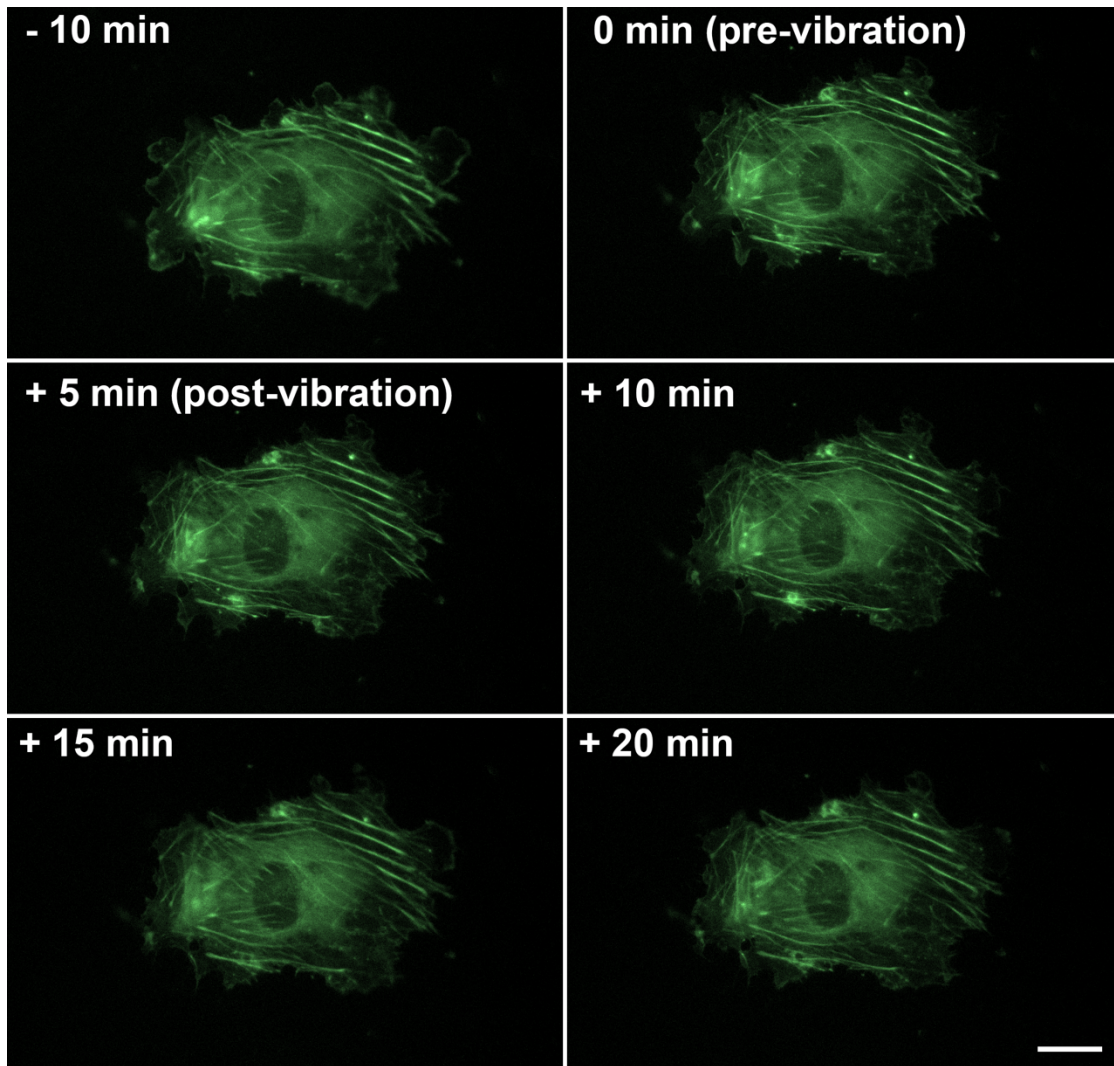


Figure 2.11 Live-cell imaging of actin dynamics showed no acute changes in actin distribution induced by vibration. MC3T3-E1 cells were transfected with pEGFP-actin and placed into the vibration device mounted on an inverted microscope. The cells were imaged for 10 minutes to monitor basal activity, and then vibrated for 5 minutes at 45 Hz and 1 g peak acceleration. The cells were then imaged again immediately following vibration and for 15 minutes following vibration. The cells remained adherent and viable following vibration, and did not show any apparent reorganization of actin filaments in response to vibration. This figure is a series of images from a single cell, representative of 11 cells from 3 independent experiments. Scale bar represents 20 μm .

system. For the same peak acceleration, the displacement caused by vibration at low frequencies (< 30 Hz) is larger (in the range of hundreds of microns) than that at higher frequencies. Due to particles moving out of the microscope field of view, it was therefore not always feasible to image particles at low frequencies. On the other hand, at higher frequencies (> 90 Hz), two limitations arise. First, at high accelerations, high velocity particles become difficult to image due to limitations in acquisition frame rate and signal detection. Second, at low accelerations, the small displacements (< 10 μm) become difficult to image. For example, at 250 Hz and 0.1 g, the theoretical amplitude of vibration is less than 400 nm, a value that is not easily resolved with conventional imaging techniques. This underscores the strength of using the accelerometer to evaluate motion of the device across a range of parameters that would otherwise not be feasible to monitor by traditional methods.

The device is controlled using an open-loop system, where the nominal frequency and acceleration are manually selected with control knobs on the function generator and amplifier, respectively. On occasion, this leads to a slight discrepancy between the nominal and actual values, which are recorded continuously during experimentation. The control system could be improved upon with a closed-loop proportional-integral-derivative system. Such a system would automatically monitor the frequency and magnitude of acceleration delivered by the device, compare them to set target values, and iteratively adjust settings until they match the target values. However, the open-loop device was found to be extremely stable (i.e. once set, the parameters of vibration did not drift over time), making a closed-loop system unnecessary for our purposes.

A key component of the system was the linear air bushing suspension system. It provided a low friction interface that contributed to the high degree of stability over a wide range of vibrational parameters. A prototype system previously described by our lab used bearings (Holdsworth et al., 2012). Using this prototype system, friction produced during vibration led to mechanical instabilities (including unwanted resonances), which led to instability in the vibration parameters. In contrast, the current device allows investigators to study cellular responses to vibrational stimuli over a range of frequencies and accelerations. Additional future improvements to the system could include features to facilitate exact alignment of the air bushings and the suspended tubes, and to improve the ease of insertion and removal of the culture dish.

In the present study, sinusoidal signals were used for validation and cell experimentation because sinusoids are monoharmonic (i.e. one frequency). There are several advantages of using this approach. First, sinusoidal signals enhance our ability to detect potential artifacts (e.g. the presence of mechanical resonances). Second, they conform to a simple mathematical relationship among peak acceleration, sinusoidal amplitude, and frequency (Equation 2). Third, sinusoidal signals facilitate investigation of the possible frequency dependence of biological responses to vibration. Finally, use of sinusoidal vibration allows comparison of findings with the results of previous studies of vibration in a variety of biological systems.

2.5.2 Vibration of osteoblastic cells does not acutely alter cytosolic calcium

We first used the custom motion-control platform to investigate whether vibration

induces transient changes in $[Ca^{2+}]_i$ similar to those induced by other mechanical stimuli such as fluid shear, membrane stretch and deformation (Adachi et al., 2009; Donahue et al., 2001; Hung et al., 1995; Lorusso et al., 2016; Mikolajewicz et al., 2018; Nishitani et al., 2011; Thompson et al., 2014; Wu et al., 1999). Under the conditions tested, changes in $[Ca^{2+}]_i$ were not observed in response to mechanical vibration of UMR-106 cells, MC3T3-E1 cells, or primary rat osteoclasts.

The range of vibration frequencies and acceleration magnitudes we chose to examine was based on work described in the literature. Previous studies have reported biological effects resulting from LMHF vibrations (usually accelerations ~ 1 g or less, and frequencies from 15 to 90 Hz). For example, several studies have shown effects of 45 Hz vibrations in a variety of systems (McCann et al., 2013; McCann et al., 2015; Murfee et al., 2005; Runge et al., 2018). However, these findings do not preclude the possibility that other frequencies and accelerations have significant biological effects as well. For example, some studies indicate that 20 and 60 Hz vibrations differ in their effects on cell growth and metabolism (Rosenberg et al., 2002) and others have shown changes in differentiation of osteosarcoma cells at 30 Hz (Pre et al., 2009). Therefore, our motion-control platform was designed to operate over a range of relevant frequencies and accelerations. Nevertheless, no changes in $[Ca^{2+}]_i$ were observed in response to vibration at any of the frequencies and accelerations tested. We also examined the effects of different durations and repeated applications of vibrational stimuli; however, in no case did we observe an elevation in $[Ca^{2+}]_i$. It is possible that cells would respond to vibration differently if cultured on biological substrata or in a 3D culture system (McClarren and Olabisi, 2018). These possibilities will form the basis of future studies.

In the present study, we observed that there is minimal motion of fluid at the surface of the dish (relative to the dish itself). As force is applied to accelerate the culture dish, the dish moves, and fluid in contact with the dish follows its motion, as is predicted with a no-slip condition. This was confirmed in Figure 2.4 with our observation that a suspended particle close to the surface of the dish closely matches the motion of the dish (embedded particle). In this situation, shear stress results from viscous drag in the fluid boundary layer above the dish. In Figure 2.4, we observed that the conditions generated during vibration matched those of the Stokes oscillatory boundary layer problem (Kundu and Cohen, 2010). Thus, the fluid shear stress at the dish surface can be solved using the Navier-Stokes equation. Based on the conditions present in Figures 4-7, the maximal shear stress at the wall was calculated to be ~ 0.03 Pa, approximately an order of magnitude less than that used to stimulate $[Ca^{2+}]_i$ transients in osteoblasts and other cell types (Hung et al., 1996; Kamioka et al., 2006; Lorusso et al., 2017a; Lorusso et al., 2016; Masyuk et al., 2006). Indeed, in the present study, we observed that the resultant fluid shear due to vibration of the dish is insufficient to generate calcium transients in osteoblastic cells (Figures 5-7). The prototype system developed previously by our lab was found to induce $[Ca^{2+}]_i$ transients in osteoblastic cells (Holdsworth et al., 2012). This may have been due to mechanical instabilities in the system leading to resonances, which would have increased the magnitude of fluid shear.

2.5.3 Vibration of osteoblastic cells desensitizes subsequent responses to extracellular ATP

Extracellular ATP is known to cause transient increases in $[Ca^{2+}]_i$ similar to those observed upon the initiation of fluid shear stress. ATP is an agonist of cell surface P2 receptors, which mobilize intracellular calcium in many cell types including osteoblasts (Burnstock et al., 2013; Dixon and Sims, 2000). Moreover, release of endogenous ATP has been shown to mediate fluid flow-induced $[Ca^{2+}]_i$ elevations in osteoblastic cells (Li et al., 2005; You et al., 2002). Although we found that vibration itself did not elicit elevation of $[Ca^{2+}]_i$, pretreatment with vibration desensitized the subsequent calcium response to exogenous ATP. This observation shows the fact that cells had indeed responded to the vibrational stimulus applied.

The mechanism underlying the ability of vibration to desensitize ATP-induced calcium signaling is not clear. Moreover, the initial mechanosensor that detects accelerations is not known. It is suggested that vibration exposes cells to cyclic compressive and tensile forces. Possible sensors that detect the resulting strains include extracellular matrix (ECM) binding proteins, stretch-activated ion channels, and the cytoskeleton (Robertson et al., 2018). For example, integrins, which couple the cell to the surrounding ECM, detect and transduce mechanical forces through associated focal adhesion complexes to downstream effectors (Sun et al., 2016). As well, LINC (linker of nucleoskeleton and cytoskeleton) complexes have been shown to be critical for mesenchymal stem cells to sense LMHF vibrations (Touchstone et al., 2019; Uzer et al., 2015). It is possible that these or other pathways suppress calcium signaling in osteoblasts.

Inhibition of calcium signaling would be predicted to have major effects on cell function. In general, cytosolic calcium contributes to the control of a number of processes, including secretion, metabolism, gene expression, proliferation, and cell death (Berridge, 2016; Berridge et al., 1998). In osteoblasts, ATP-induced elevation of $[Ca^{2+}]_i$ activates NFATc1 (Grol et al., 2013), a transcription factor which has been shown to regulate osteoblast differentiation (Koga et al., 2005; Winslow et al., 2006). Similarly, the calcium/calmodulin-activated kinase calmodulin kinase II plays an important role in the control of osteoblast differentiation (Zayzafoon, 2006).

It is unlikely that desensitization of the response to extracellular ATP arises from suppression of the transcription or translation of P2 receptors, as the effect of vibration is relatively rapid. On the other hand, desensitization of P2 receptors by vibration could involve phosphorylation and/or internalization of these receptors. One possibility is that vibration induces the release of small amounts of endogenous ATP from the cell. This ATP may be sufficient to desensitize cells to exogenous ATP, but insufficient to reach the concentration required to trigger a global calcium response. Nevertheless, vibration-induced desensitization of P2 receptors would be expected to suppress the response of osteoblasts to other forms of mechanical stimulation, in particular, those whose mechanotransduction pathways involve P2 receptor signaling (e.g. fluid flow and membrane deformation). Hence, *in vivo* vibration may counteract the physiological effects of other forms of mechanical stimulation.

In conclusion, we have developed a novel system capable of real-time microscopy of live cells during LMHF vibrations. Acceleration and frequency were precisely controlled and could be accurately monitored during experimentation. Under the conditions studied,

acceleration did not induce detectable changes in $[Ca^{2+}]_i$, but did desensitize cells to the effect of exogenous ATP. Our motion-control platform may facilitate future investigations of the early responses of osteoblasts, and other cell types and tissues to vibrational stimuli *in vitro*.

2.6 References

- Adachi T, Aonuma Y, Tanaka M, Hojo M, Takano-Yamamoto T, Kamioka H. 2009. Calcium response in single osteocytes to locally applied mechanical stimulus: differences in cell process and cell body. *Journal of biomechanics* 42(12):1989-1995.
- Alexandre C, Vico L. 2011. Pathophysiology of bone loss in disuse osteoporosis. *Joint, bone, spine : revue du rhumatisme* 78(6):572-576.
- Berridge MJ. 2016. The inositol trisphosphate/calcium signaling pathway in health and disease. *Physiological reviews* 96(4):1261-1296.
- Berridge MJ, Bootman MD, Lipp P. 1998. Calcium - a life and death signal. *Nature* 395(6703):645-648.
- Burnstock G, Arnett TR, Orriss IR. 2013. Purinergic signalling in the musculoskeletal system. *Purinergic Signal* 9(4):541-572.
- Cardinale M, Pope MH. 2003. The effects of whole body vibration on humans: dangerous or advantageous? *Acta Physiol Hung* 90(3):195-206.
- Dixon SJ, Sims SM. 2000. P2 purinergic receptors on osteoblasts and osteoclasts: Potential targets for drug development. *Drug Dev Res* 49(3):187-200.
- Donahue SW, Jacobs CR, Donahue HJ. 2001. Flow-induced calcium oscillations in rat osteoblasts are age, loading frequency, and shear stress dependent. *American journal of physiology Cell physiology* 281(5):C1635-1641.
- Grol MW, Pereverzev A, Sims SM, Dixon SJ. 2013. P2 receptor networks regulate signaling duration over a wide dynamic range of ATP concentrations. *Journal of cell science* 126(Pt 16):3615-3626.
- Grol MW, Zelner I, Dixon SJ. 2012. P2X(7)-mediated calcium influx triggers a sustained, PI3K-dependent increase in metabolic acid production by osteoblast-like cells. *American journal of physiology Endocrinology and metabolism* 302(5):E561-575.
- Hecht E, Liedert A, Ignatius A, Mizaikoff B, Kranz C. 2013. Local detection of mechanically induced ATP release from bone cells with ATP biosensors. *Biosensors & bioelectronics* 44:27-33.
- Holdsworth DW, Nikolov H, Au JL, Beaucage K, Kishimoto J, Dixon SJ. Simultaneous vibration and high-speed microscopy to study mechanotransduction in living

- cells. Proceedings of SPIE - The International Society for Optical Engineering; 2012; San Diego, CA, United states. SPIE. p 831715.
- Hung CT, Allen FD, Pollack SR, Brighton CT. 1996. Intracellular Ca^{2+} stores and extracellular Ca^{2+} are required in the real-time Ca^{2+} response of bone cells experiencing fluid flow. *J Biomech* 29(11):1411-1417.
- Hung CT, Pollack SR, Reilly TM, Brighton CT. 1995. Real-time calcium response of cultured bone cells to fluid flow. *Clinical orthopaedics and related research*(313):256-269.
- Jing D, Baik AD, Lu XL, Zhou B, Lai X, Wang L, Luo E, Guo XE. 2014. In situ intracellular calcium oscillations in osteocytes in intact mouse long bones under dynamic mechanical loading. *FASEB J* 28(4):1582-1592.
- Jing D, Tong S, Zhai M, Li X, Cai J, Wu Y, Shen G, Zhang X, Xu Q, Guo Z, Luo E. 2015. Effect of low-level mechanical vibration on osteogenesis and osseointegration of porous titanium implants in the repair of long bone defects. *Scientific reports* 5:17134.
- Jorgensen NR, Geist ST, Civitelli R, Steinberg TH. 1997. ATP- and gap junction-dependent intercellular calcium signaling in osteoblastic cells. *The Journal of cell biology* 139(2):497-506.
- Judex S, Lei X, Han D, Rubin C. 2007. Low-magnitude mechanical signals that stimulate bone formation in the ovariectomized rat are dependent on the applied frequency but not on the strain magnitude. *Journal of biomechanics* 40(6):1333-1339.
- Kamioka H, Sugawara Y, Murshid SA, Ishihara Y, Honjo T, Takano-Yamamoto T. 2006. Fluid shear stress induces less calcium response in a single primary osteocyte than in a single osteoblast: implication of different focal adhesion formation. *J Bone Miner Res* 21(7):1012-1021.
- Kim CH, Jeung EB, Yoo YM. 2018. Combined Fluid Shear Stress and Melatonin Enhances the ERK/Akt/mTOR Signal in Cilia-Less MC3T3-E1 Preosteoblast Cells. *International journal of molecular sciences* 19(10).
- Koga T, Matsui Y, Asagiri M, Kodama T, de Crombrughe B, Nakashima K, Takayanagi H. 2005. NFAT and Osterix cooperatively regulate bone formation. *Nat Med* 11(8):880-885.
- Kundu PK, Cohen IM. 2010. *Fluid Mechanics*. Amsterdam: Elsevier Science.
- Lapierre DM, Tanabe N, Pereverzev A, Spencer M, Shugg RP, Dixon SJ, Sims SM. 2010. Lysophosphatidic acid signals through multiple receptors in osteoclasts to elevate cytosolic calcium concentration, evoke retraction, and promote cell survival. *The Journal of biological chemistry* 285(33):25792-25801.

- Li J, Liu D, Ke HZ, Duncan RL, Turner CH. 2005. The P2X7 nucleotide receptor mediates skeletal mechanotransduction. *The Journal of biological chemistry* 280(52):42952-42959.
- Lorusso D, Nikolov HN, Chmiel T, Beach RJ, Sims SM, Dixon SJ, Holdsworth DW. A device for real-time live-cell microscopy during dynamic dual-modal mechanostimulation. *Proceedings of SPIE*; 2017a; Bellingham. Spie-Int Soc Optical Engineering. p 101370F.
- Lorusso D, Nikolov HN, Chmiel T, Beach RJ, Sims SM, Dixon SJ, Holdsworth DW. 2017b. A device for real-time live-cell microscopy during dynamic dual-modal mechanostimulation. *Medical Imaging 2017: Biomedical Applications in Molecular, Structural, and Functional Imaging*. Bellingham: Spie-Int Soc Optical Engineering.
- Lorusso D, Nikolov HN, Milner JS, Ochotny NM, Sims SM, Dixon SJ, Holdsworth DW. 2016. Practical fabrication of microfluidic platforms for live-cell microscopy. *Biomed Microdevices* 18(5):78.
- Lyons JS, Iyer SR, Lovering RM, Ward CW, Stains JP. 2016. Novel multi-functional fluid flow device for studying cellular mechanotransduction. *Journal of biomechanics* 49(16):4173-4179.
- Marin-Cascales E, Alcaraz PE, Ramos-Campo DJ, Martinez-Rodriguez A, Chung LH, Rubio-Arias JA. 2018. Whole-body vibration training and bone health in postmenopausal women: A systematic review and meta-analysis. *Medicine* 97(34):e11918.
- Masyuk AI, Masyuk TV, Splinter PL, Huang BQ, Stroope AJ, LaRusso NF. 2006. Cholangiocyte cilia detect changes in luminal fluid flow and transmit them into intracellular Ca^{2+} and cAMP signaling. *Gastroenterology* 131(3):911-920.
- McCann MR, Patel P, Beaucage KL, Xiao Y, Bacher C, Siqueira WL, Holdsworth DW, Dixon SJ, Seguin CA. 2013. Acute vibration induces transient expression of anabolic genes in the murine intervertebral disc. *Arthritis and rheumatism* 65(7):1853-1864.
- McCann MR, Patel P, Pest MA, Ratneswaran A, Lalli G, Beaucage KL, Backler GB, Kamphuis MP, Esmail Z, Lee J, Barbalinardo M, Mort JS, Holdsworth DW, Beier F, Dixon SJ, Seguin CA. 2015. Repeated exposure to high-frequency low-amplitude vibration induces degeneration of murine intervertebral discs and knee joints. *Arthritis & rheumatology (Hoboken, NJ)* 67(8):2164-2175.
- McClarren B, Olabisi R. 2018. Strain and Vibration in Mesenchymal Stem Cells. *Int J Biomater* 2018:8686794.

- Mikolajewicz N, Zimmermann EA, Willie BM, Komarova SV. 2018. Mechanically stimulated ATP release from murine bone cells is regulated by a balance of injury and repair. *eLife* 7:e37812.
- Murfee WL, Hammett LA, Evans C, Xie L, Squire M, Rubin C, Judex S, Skalak TC. 2005. High-frequency, low-magnitude vibrations suppress the number of blood vessels per muscle fiber in mouse soleus muscle. *J Appl Physiol* (1985) 98(6):2376-2380.
- Nishitani WS, Saif TA, Wang Y. 2011. Calcium signaling in live cells on elastic gels under mechanical vibration at subcellular levels. *PLoS One* 6(10):e26181.
- Orr AW, Helmke BP, Blackman BR, Schwartz MA. 2006. Mechanisms of mechanotransduction. *Dev Cell* 10(1):11-20.
- Pereverzev A, Komarova SV, Korcok J, Armstrong S, Tremblay GB, Dixon SJ, Sims SM. 2008. Extracellular acidification enhances osteoclast survival through an NFAT-independent, protein kinase C-dependent pathway. *Bone* 42(1):150-161.
- Pham MH, Buser Z, Wang JC, Acosta FL. 2017. Low-magnitude mechanical signals and the spine: A review of current and future applications. *Journal of clinical neuroscience : official journal of the Neurosurgical Society of Australasia* 40:18-23.
- Pre D, Ceccarelli G, Benedetti L, Magenes G, Cusella De Angelis MG. 2009. Effects of Low Amplitude, High Frequency Vibrations on Proliferation and Differentiation of SAOS-2 Human Osteogenic cell line. *Tissue Eng Part C Methods* 15:669-679.
- Reimer WJ, Dixon SJ. 1992. Extracellular nucleotides elevate $[Ca^{2+}]_i$ in rat osteoblastic cells by interaction with two receptor subtypes. *Am J Physiol* 263(5 Pt 1):C1040-1048.
- Riddle RC, Taylor AF, Rogers JR, Donahue HJ. 2007. ATP release mediates fluid flow-induced proliferation of human bone marrow stromal cells. *J Bone Miner Res* 22(4):589-600.
- Robertson SN, Campsie P, Childs PG, Madsen F, Donnelly H, Henriquez FL, Mackay WG, Salmerón-Sánchez M, Tsimbouri MP, Williams C, Dalby MJ, Reid S. 2018. Control of cell behaviour through nanovibrational stimulation: nanokicking. *Philos Trans A Math Phys Eng Sci* 376(2120).
- Robling AG, Turner CH. 2009. Mechanical signaling for bone modeling and remodeling. *Critical reviews in eukaryotic gene expression* 19(4):319-338.
- Rosenberg N, Levy M, Francis M. 2002. Experimental model for stimulation of cultured human osteoblast-like cells by high frequency vibration. *Cytotechnology* 39(3):125-130.

- Runge WO, Ruppert DS, Marcellin-Little DJ, Dahners LE, Harrysson O, Weinhold PS. 2018. Bone changes after short-term whole body vibration are confined to cancellous bone. *J Musculoskelet Neuronal Interact* 18(4):485-492.
- Slatkovska L, Alibhai SM, Beyene J, Hu H, Demaras A, Cheung AM. 2011. Effect of 12 months of whole-body vibration therapy on bone density and structure in postmenopausal women: a randomized trial. *Ann Intern Med* 155(10):668-679.
- Sun Z, Guo SS, Fassler R. 2016. Integrin-mediated mechanotransduction. *The Journal of cell biology* 215(4):445-456.
- Tanabe N, Wheal BD, Kwon J, Chen HH, Shugg RP, Sims SM, Goldberg HA, Dixon SJ. 2011. Osteopontin signals through calcium and nuclear factor of activated T cells (NFAT) in osteoclasts: a novel RGD-dependent pathway promoting cell survival. *The Journal of biological chemistry* 286(46):39871-39881.
- Thi MM, Suadican SO, Schaffler MB, Weinbaum S, Spray DC. 2013. Mechanosensory responses of osteocytes to physiological forces occur along processes and not cell body and require alphaVbeta3 integrin. *Proceedings of the National Academy of Sciences of the United States of America* 110(52):21012-21017.
- Thompson WR, Yen SS, Rubin J. 2014. Vibration therapy: clinical applications in bone. *Current opinion in endocrinology, diabetes, and obesity* 21(6):447-453.
- Touchstone H, Bryd R, Loiate S, Thompson M, Kim S, Puranam K, Senthilnathan AN, Pu X, Beard R, Rubin J, Alwood J, Oxford JT, Uzer G. 2019. Recovery of stem cell proliferation by low intensity vibration under simulated microgravity requires LINC complex. *NPJ Microgravity* 5:11.
- Turner CH, Pavalko FM. 1998. Mechanotransduction and functional response of the skeleton to physical stress: the mechanisms and mechanics of bone adaptation. *Journal of orthopaedic science : official journal of the Japanese Orthopaedic Association* 3(6):346-355.
- Uzer G, Thompson WR, Sen B, Xie Z, Yen SS, Miller S, Bas G, Styner M, Rubin CT, Judex S, Burrige K, Rubin J. 2015. Cell Mechanosensitivity to Extremely Low-Magnitude Signals Is Enabled by a LINCed Nucleus. *Stem Cells* 33(6):2063-2076.
- Wall M, Butler D, Haj AE, Bodle JC, Loba EG, Banes AJ. 2017. Key developments that impacted the field of mechanobiology and mechanotransduction. *Journal of orthopaedic research : official publication of the Orthopaedic Research Society* 36:605-619.
- Wheal BD, Beach RJ, Tanabe N, Dixon SJ, Sims SM. 2014. Subcellular elevation of cytosolic free calcium is required for osteoclast migration. *J Bone Miner Res* 29(3):725-734.

- Winslow MM, Pan M, Starbuck M, Gallo EM, Deng L, Karsenty G, Crabtree GR. 2006. Calcineurin/NFAT signaling in osteoblasts regulates bone mass. *Dev Cell* 10(6):771-782.
- Wu Z, Wong K, Glogauer M, Ellen RP, McCulloch CA. 1999. Regulation of stretch-activated intracellular calcium transients by actin filaments. *Biochemical and biophysical research communications* 261(2):419-425.
- Xiao ZS, Quarles LD. 2010. Role of the polycystin-primary cilia complex in bone development and mechanosensing. *Annals of the New York Academy of Sciences* 1192:410-421.
- You J, Jacobs CR, Steinberg TH, Donahue HJ. 2002. P2Y purinoceptors are responsible for oscillatory fluid flow-induced intracellular calcium mobilization in osteoblastic cells. *The Journal of biological chemistry* 277(50):48724-48729.
- Zayzafoon M. 2006. Calcium/calmodulin signaling controls osteoblast growth and differentiation. *Journal of cellular biochemistry* 97(1):56-70.

Chapter 3

Practical fabrication of microfluidic platforms for live-cell microscopy³

³ Modified from publication: Lorusso D, Nikolov HN, Milner JS, Ochotny NM, Sims SM, Dixon SJ, Holdsworth DW. (2016). Practical fabrication of microfluidic platforms for live-cell microscopy. *Biomedical Microdevices*, **18**, 78.

3.1 Chapter summary

We describe a simple fabrication technique – targeted towards non-specialists – that allows for the production of leak-proof polydimethylsiloxane (PDMS) microfluidic devices that are compatible with live-cell microscopy. Thin PDMS base membranes were spin-coated onto a glass-bottom cell culture dish and then partially cured *via* microwave irradiation. PDMS chips were generated using a replica molding technique, and then sealed to the PDMS base membrane by microwave irradiation. Once a mold was generated, devices could be rapidly fabricated within hours. Fibronectin pre-treatment of the PDMS improved cell attachment. Coupling the device to programmable pumps allowed application of precise fluid flow rates through the channels. The transparency and minimal thickness of the device enabled compatibility with inverted light microscopy techniques (*e.g.* phase-contrast, fluorescence imaging, *etc.*). The key benefits of this technique are the use of standard laboratory equipment during fabrication and ease of implementation, helping to extend applications in live-cell microfluidics for scientists outside the engineering and core microdevice communities.

3.2 Introduction

Recent advances in polydimethylsiloxane (PDMS) microfluidics have facilitated biocompatible microdevices for precise experimentation, with the potential for a paradigm shift in the modern study of biology. Replica-molding techniques are a simple and affordable method for the production of custom PDMS devices. The investigation of cells in microfluidic environments is a topic of great interest (Ertel et al., 1994; Gross et al., 2007; Lee et al., 2015b; Loutharback et al., 2015; Meyvantsson and Beebe, 2008;

Miller and Anderson, 1988), and continues to provide constructive insights in many fields (Leclerc et al., 2006; Lee et al., 2015a; Moraes et al., 2013; Polacheck et al., 2013; Yasotharan et al., 2015; Young and Beebe, 2010).

Much work has been done to increase the accessibility of micro-device fabrication, including microwave plasma treatments (Ginn and Steinbock; Hui et al., 2005) and coronal discharge systems (Haubert et al., 2006). However, despite the relative simplicity of PDMS microdevice fabrication techniques, the barrier to entry remains high. Lithography techniques typically require specialized expertise and can take days to produce a device. Irreversible and semi-reversible fixation of PDMS by bonding methods, such as oxygen plasma, coronal discharge, or chemical gluing, can also require long fabrication times and dedicated equipment. Additionally, oxygen plasma techniques display relatively low bond strengths (maximally 0.5 MPa) (Beh et al., 2012) and thus are not ideal for applications where higher chamber pressures could cause leaking.

Here, we present a low-cost, readily accessible technique for the irreversible fixation of PDMS layers to one another in microdevice fabrication by the partial curing of PDMS with microwave irradiation. This approach, related to previously developed multilayer fixation techniques (Unger et al., 2000), utilizes replica-molding to allow the fabrication of several devices in a single day from a single mold. Additionally, the achieved bond strength likely approaches the maximum possible for PDMS – once sealed, the layers cannot be separated without tearing the PDMS itself. Although this method was developed for the study of live cells under steady-flow fluid shear during real-time microscopy, it can be easily extended to a wide range of applications. A low-cost, easily fabricated microfluidic flow chamber will have multiple applications in biomedical

research, including cardiovascular research, regulation of flow in the kidneys, and musculoskeletal regulation. We modeled the PDMS flow system using computational fluid dynamics (CFD) to calculate the velocity distribution across the lumen (at three different widths), from which the resultant wall shear stress was derived. This CFD model was validated using micro-particle image velocimetry (micro-PIV) to compare predicted maximum velocities to measured maximum velocities. One of the advantages of the microfluidic device that we describe is that it presents an opportunity to lower the barrier of entry into microfluidics for non-experts, e.g. cell and molecular biologists. We believe that this system can bring powerful microfluidic techniques to the bench top of researchers who are not expert developers of microfluidic devices.

3.3 Methods

3.3.1 Microfluidic device fabrication

In this investigation, we used custom-designed and fabricated molds to produce a microfluidic chamber. Replica molds were designed using 3D CAD software (SolidWorks; Dassault Systèmes, Velizy-Villacoublay, France), with specified channel dimensions of 100 μm in height and a graduated width paradigm, providing three widths (*i.e.* 500, 750, and 1500 μm nominal width) over a total path length of approximately 10 cm (Fig. 3.1a). The path of the channel winds several times between straight sections to maximize functional surface area for cell growth. Once designed, the CAD file was uploaded using tool-path generating software (Mastercam, CNC Software Inc., Tolland CT) to a standard 3-axis CNC mill (Trak K3SX-3 with ProTrak SMX control module;

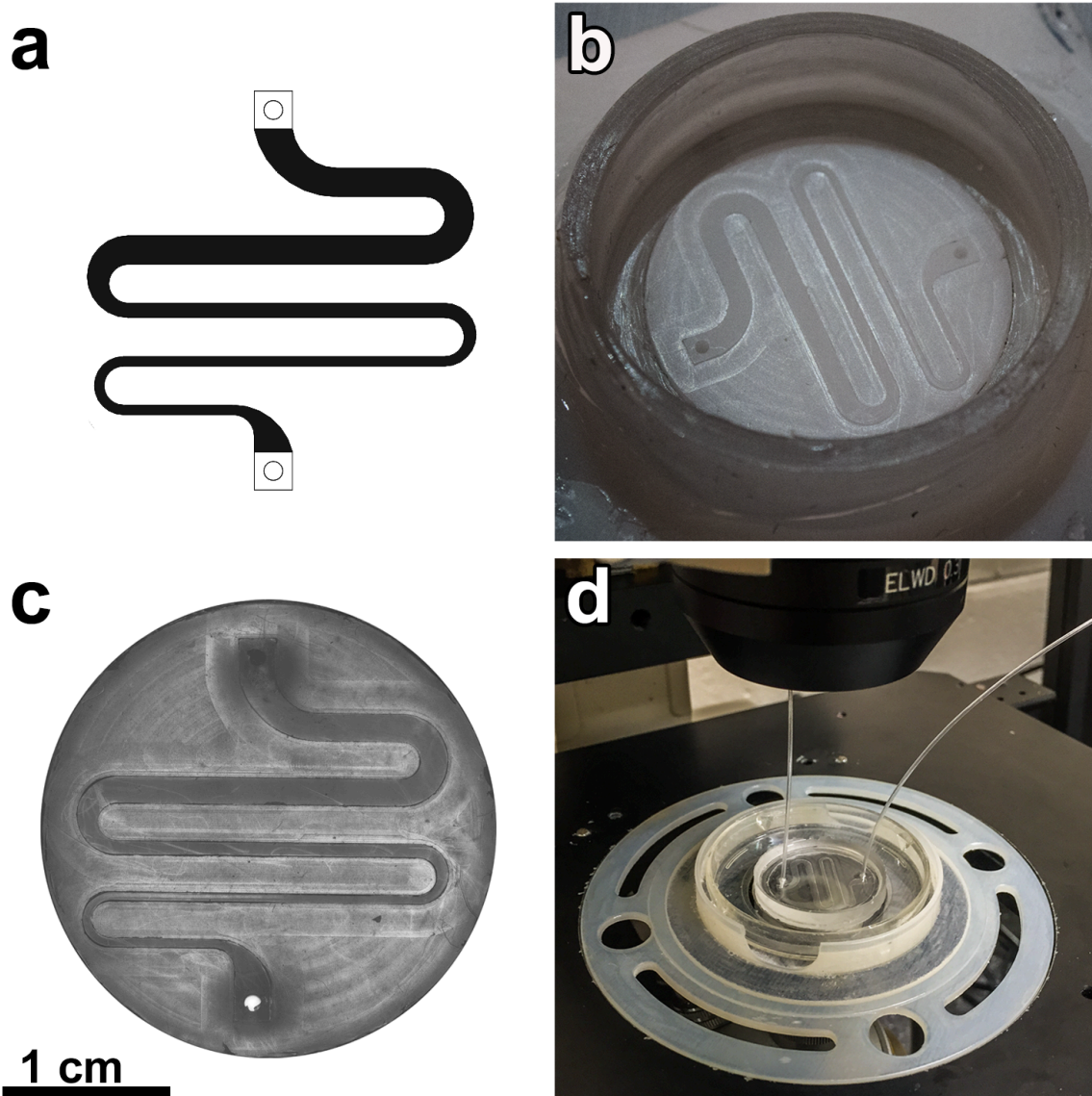


Figure 3.1 Microfluidic device fabrication. (a) CAD software was used to create a plan for a positive replica mold of the channel that was machined using a CNC mill. (b) The replica mold used to cast a PDMS model of the micro-channel. (c) A micrograph of the cast microfluidic chip, prior to fabrication of the device. This chamber was irreversibly sealed to a partially cured, thin base membrane of PDMS that was spin coated onto a glass bottom cell culture dish. (d) The completed device as seen on the microscope stage, housed in a custom stage ring.

Southwestern Industries Inc., Rancho-Dominguez CA) and machined from a piece of acrylic (Fig. 3.1b).

Once the mold was completed, vacuum-degassed Sylgard 184 (10:1 base: cross-linker, Dow Corning, Midland MI) was cast into the mold and allowed to cure fully before it was removed from the mold (Fig. 3.1c). A custom-built spin coater was constructed from a servo motor and a motor controller (Galil DM710 Motion Controller; Galil Motion Control, Rocklin CA), and then used (60 s at 3000 RPM) to spin a thin (~20 μm) layer of PDMS on the surface of a glass-bottomed cell-culture dish 30 mm in diameter (MatTek Corp., Ashland MA). Microwave irradiation (*i.e.* full power at 1000 W) in a conventional microwave oven was used to cure three different aspects of the assembly. First, the aforementioned cast chamber was microwave cured fully in 20 minutes. Next, the thin PDMS base membrane was partially cured to achieve an adhesive-like consistency. This requires several important considerations: first, microwave cure time must be determined empirically (15 minutes in our case, which can be raised or lowered by changing the volume of water in the accompanying heat sink), and second, thermal consistency between runs must be maintained. The time between initial mixing of base and cross-linker and microwaving also affects results. We recommend using the microwave at full power to enable more effective approximation of the wattage being utilized.

Following microwave curing of the base membrane, the fully cured PDMS chamber was carefully pressed into place on top of the partially cured membrane (making sure to avoid trapped air bubbles), and the full assembly was then microwaved for 6 minutes until the two layers were irreversibly bonded (Fig. 3.1d). Note that to protect the magnetron from overheating we included additional water as a heat sink (300 mL). To complete the

device, inlet and outlet polyethylene tubes with a 0.58 mm inner diameter (Becton-Dickinson, Mississauga ON) were bonded to their respective ports using Speed Set Professional Epoxy (LePage).

3.3.2 Measurement of channel dimensions

Our microfluidic chamber is intended for the controlled application of fluid shear to cell monolayers within it, therefore it was necessary to validate the geometry of the device channels to ensure the accurate prediction of experimental shear stress. Channels were directly measured using an AxioImager Z1 light microscope (Carl Zeiss, Jena, Germany) with a calibrated Z-axis (Zeiss EC Epiplan 20x/0.4, $\infty/0$) and a three-axis measuring microscope (3x) (STM6, Olympus, Tokyo, Japan).

3.3.3 Computational fluid dynamics

The accuracy of our wall-shear calculations was integral to the success of this project, and CFD was used to compute the velocity fields and wall shear stress within the microfluidic chambers. Commercially available software Abaqus CFD (Dassault Systèmes, Velizy-Villacoublay, France) was used to model fluid flow within the channels. Three geometric configurations were investigated (height x width): 90 μm x 522 μm , 90 μm x 770 μm , and 90 μm x 1517 μm . Channel dimensions used in the model were derived from microscopy measurements. Channel length in all cases was 1200 μm . Uniform velocity profiles were prescribed at the inlet and calculated for each case using cross-sectional area and volumetric flow rates (ranging from 15 $\mu\text{L min}^{-1}$ to 125 $\mu\text{L min}^{-1}$). Fully developed flow was achieved in the highest Reynolds number case

($Re = 6.78$, $90\ \mu\text{m} \times 522\ \mu\text{m}$ geometry at $125\ \mu\text{L}\ \text{min}^{-1}$) within $600\ \mu\text{m}$ downstream of the inlet. A zero-pressure boundary condition was prescribed at the outlet and walls were prescribed as no-slip. Each model was meshed using linear (first-order) hexahedral elements using a uniform (isotropic) node spacing of $5\ \mu\text{m}$. Total numbers of nodes for each model were: 480,795 ($90\ \mu\text{m} \times 522\ \mu\text{m}$), 709,745 ($90\ \mu\text{m} \times 770\ \mu\text{m}$) and 1,308,960 ($90\ \mu\text{m} \times 1517\ \mu\text{m}$). Solutions were generated through an adaptive time-stepping scheme using an initial step size of 10^{-4} seconds, maximum CFL number of 0.45 and a growth scale factor of 0.025. Final time-step size was approximately 3.05×10^{-5} seconds. Steady state was achieved in the highest Reynolds number case (see above for description) after 0.0045 seconds. All subsequent simulations were run for 0.005 seconds to ensure a stabilized solution. The modeled fluid was α -MEM cell culture medium at room temperature ($20\ ^\circ\text{C}$). The density and viscosity of the medium approximated that of water, $0.998\ \text{g}\cdot\text{mL}^{-1}$ and $1.011\ \text{mPa}\cdot\text{s}$, respectively (Hinderliter et al., 2010).

3.3.4 Particle image velocimetry

Validation of the CFD model was required to verify our predicted velocities. A micro-particle image velocimetry (micro-PIV) method was used, in which $6\ \mu\text{m}$ black polystyrene beads (Polysciences, Warrington, PA) were diluted 1:75 in neutral-density saline (*i.e.* 6.8% w/v) and pumped through the channel with a syringe pump (NE-1000, New Era Pump Systems, Farmingdale, NY) over a range of flow rates ($5 - 10\ \mu\text{L}\cdot\text{min}^{-1}$). The beads were visualized under flow on an inverted microscope (Diaphot, Splan4 4x objective, N.A. 0.25, Nikon, Tokyo, Japan) and imaged with a consumer grade high-speed digital camera (Casio Exilim Ex-F1, Tokyo Japan) at up to 1200 frames per second

(FPS). The field of view during video capture at 1200 FPS was 100 μm by 400 μm , with an estimated depth of field of 60 μm . Captured videos (approximately 30 seconds long each) were then uploaded to a consumer-grade personal computer and processed in ImageJ (NIH, Bethesda, Maryland) to remove background structures. An ImageJ software plugin (Particle Track and Analysis PTA v 1.1, Yoshiyuki Arai) was then used to analyze the videos frame-by-frame and automatically determine the velocities of individual particles within the channels by measuring the displacement in pixels per frame and then converting this to millimeters per second. Every particle in the video excerpt (at minimum 40 particle) were measured per flow rate per channel width, yielding a distribution of velocities. Therefore, particles of random position were measured, and there was no bias in particle selection. From this velocity distribution, the peak velocity, i.e. the maximum observed instantaneous velocity for a particle at any given frame, was selected. Particles showing the peak velocity will necessarily travel upon the centerline of the channel by virtue of the natural velocity profile. Peak velocities as a function of flow rate, for both predicted and observed velocities, were plotted and linear regression was performed to determine the slope. Slopes were compared using a commercial data analysis software package (Prism, GraphPad Software Inc., La Jolla, CA).

3.3.5 Cell culture and imaging

To verify biocompatibility and ability to image cells, channels were disinfected by perfusing with 70% ethanol, followed by exposure to the culture hood UV lamp for 15 minutes. Prior to seeding of cells, fibronectin (FN, F1141 Sigma-Aldrich, St. Louis, MO)

at $20 \mu\text{g}\cdot\text{mL}^{-1}$ in PBS was circulated through the channels and allowed to incubate at 37°C , 5% CO_2 for 1 hour. Osteoblast-like MC3T3-E1 cells were grown to confluence in α -MEM, 10% fetal bovine serum (FBS) and antibiotics as previously described (Grol et al., 2013). Cells were then harvested, seeded into the microfluidic chambers at a density of $30,000 \text{ cells}\cdot\text{cm}^{-2}$, and allowed to adhere for 1-2 hours. Cells were then imaged using phase-contrast microscopy (Nikon Eclipse; 20x Plan Fluor Objective, N.A 0.45) or fluorescence microscopy (as described below).

Following adhesion within the channels, cells were loaded with the Ca^{2+} -sensitive probe fura-2, by incubation with fura-2 AM ($1.5 \mu\text{M}$) in α -MEM supplemented with 10% FBS and antibiotics at 37°C in 5% CO_2 for 30 min. Cells in the $522 \mu\text{m}$ channel were then imaged with an inverted Nikon microscope (Nikon Eclipse TE2000-U, Tokyo, Japan). Cells were imaged using a Plan Fluor 40X/1.3 NA oil/water immersion objective. Cell samples were excited with alternating wavelengths of 345/380 nm using a DeltaRAM™ X illuminator (Horiba - Photon Technology International (PTI), Birmingham, NJ, USA) and the emission signal was filtered at $(510 \pm 20 \text{ nm})$ (Wheal et al., 2014). Ratio images were acquired every 10 seconds with a pco.edge 4.2 LT sCMOS camera (2048 x 2048 pixels; PCO AG, Kelheim, Germany) and EasyRatioPro 2.3 Software (Horiba-PTI). Cells were initially superfused at low-shear flow ($10 \mu\text{L}\cdot\text{min}^{-1}$) with M199 [buffered with HEPES (25 mM) and HCO_3^- (4 mM) with supplemented with 10% FBS and antibiotics]. After approximately 5 min, the flow rate was increased to $40 \mu\text{L}\cdot\text{min}^{-1}$, corresponding to approximately 1 Pa of wall shear. Measurement of cytosolic free Ca^{2+} ($[\text{Ca}^{2+}]_i$) is technically challenging because of the variable thickness of cells. For fura-2, the ratio of

fluorescence intensity at 345/380 nm gives an index of $[Ca^{2+}]_i$ independent of cell thickness and reliably reports the frequency and time-course of $[Ca^{2+}]_i$ transients.

3.4 Results

3.4.1 Device measurements

Accurate and reproducible dimensions within the microfluidic channels are essential to the resultant fluid shear imposed on cells, therefore channel dimensions were evaluated non-destructively using microscopic imaging. The mean height was 90 μm with a standard deviation (SD) of 0.8 μm (Table 3.1). The mean width of each channel was determined to be $522 \pm 5.7 \mu\text{m}$, $770 \pm 4.8 \mu\text{m}$, and $1517 \pm 17.8 \mu\text{m}$. Thus, channel heights and widths had an error in precision of up to 1% about the mean, and derived cross-sectional area had an error in precision of approximately 2% about the mean, leading to potential errors in the calculation of velocity of approximately 2%.

3.4.2 Computational fluid dynamics

CFD was used to calculate the fluid velocities and resultant wall shear. Using the boundaries described above, fully developed velocity profiles were generated for flow rates from 5 – 15 $\mu\text{L} \cdot \text{min}^{-1}$, and resultant peak-velocity values were plotted against corresponding flow rates. Linear regression was performed yielding regression lines for each channel width. CFD-derived peak wall-shear stress values along the top and bottom surfaces of the channel ranged between 1 – 3 Pa midway across the width at 125 $\mu\text{L} \cdot \text{min}^{-1}$ (Fig. 3.2). Reynolds numbers were 6.8, 4.8, and 2.6 for channel widths of 522 μm , 770 μm , and 1517 μm , respectively.

Table 3.1 Precision of micro-channel height and width dimensions.

	Height (μm)	Width 1 (μm)	Width 2 (μm)	Width 3 (μm)
Mean	90.0	522.2	770.0	1517.2
SD	0.8	5.7	4.8	17.8

Measurements were taken directly from microscopic analysis of five different devices, each measured multiple times at a minimum of 9 different locations along their respective channel.

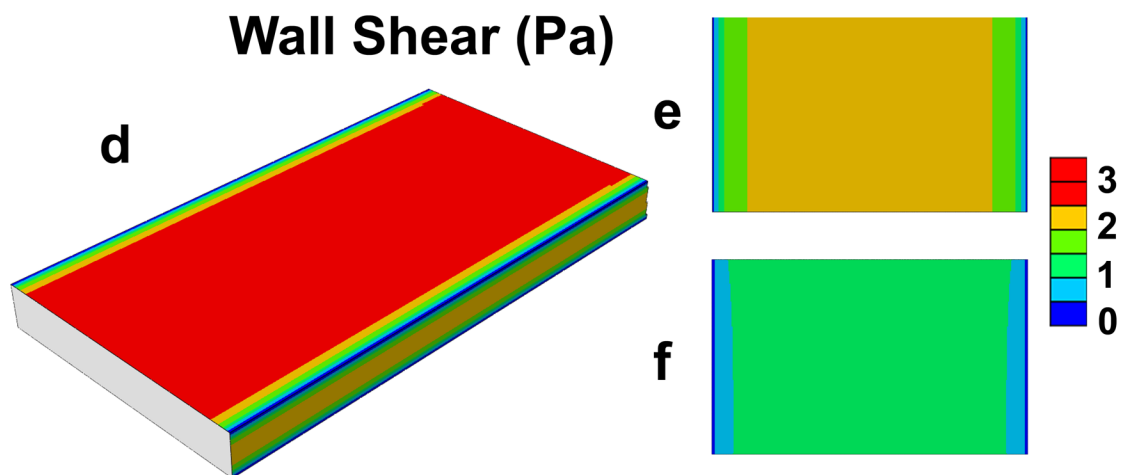
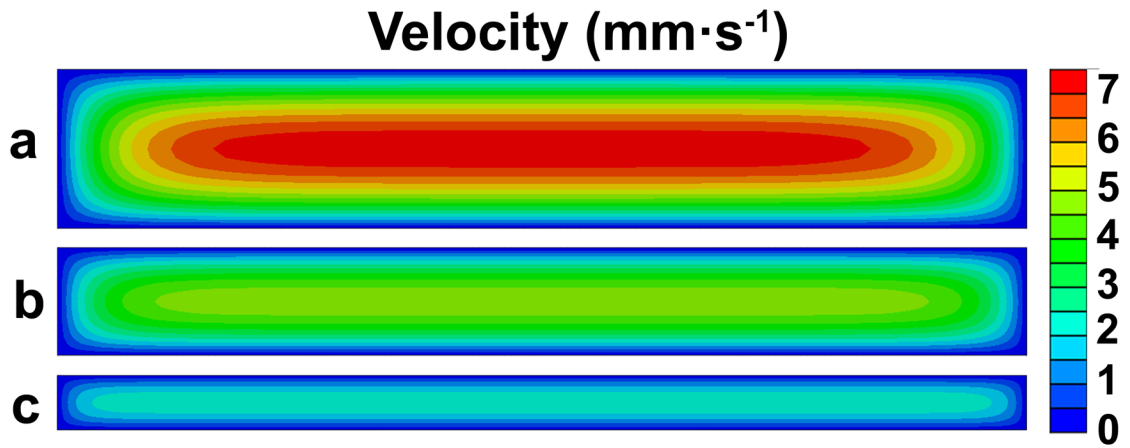


Figure 3.2 A 3D visualization of the computational fluid dynamics (CFD)-generated velocity profiles and derived wall shear rates. Abaqus CFD was used to predictively model the fluid flow within geometries matching that of our channels and then calculate the resultant wall shear profile of cell culture medium at room temperature (density = $0.9982 \text{ g}\cdot\text{mL}^{-1}$, viscosity = $1.002\text{E-}3 \text{ Pa}\cdot\text{s}$) pumped through channels at $125 \text{ }\mu\text{L}\cdot\text{min}^{-1}$. a-c represent the velocity profiles through the cross-section for the 522, 770, and 1517 μm channel widths, respectively. For a-c, scale at right represents fluid velocity in $\text{mm}\cdot\text{s}^{-1}$. d-f represent the developed shear stress at the wall for the 522, 770, and 1517 μm channel widths, respectively, in isometric projection (d) and top-down views (e, f) views (normalized for channel width). Peak developed shear rate (at the center of the top/bottom wall) ranged from approximately 1-3 Pa from the widest channel to the narrowest, respectively. For d-f, scale at right represents wall shear in Pa.

3.4.3 Particle velocimetry

Micro-PIV was performed to validate the predicted CFD velocities. Six-micrometer polystyrene beads were imaged at 1200 frames per second on an inverted microscope (Fig. 3.3), and their velocities are subsequently calculated. The peak velocity recorded was measured for flow rates up to $10 \mu\text{L}\cdot\text{min}^{-1}$ (Fig. 3.4) and results were plotted against flow rate. Linear regression was performed for the results of each channel width, yielding a significantly non-zero curve for all cases, where $p \leq 0.0001$ for width of $522 \mu\text{m}$; $p = 0.0003$ for width of $770 \mu\text{m}$; and $p = 0.0017$ for width of $1517 \mu\text{m}$. Comparing these slopes to our CFD-generated data using ANCOVA, there was no significant difference with the observed micro-PIV-derived data in any channel width; $p = 0.99$ ($F = 2.59\text{E-}4$) for $522 \mu\text{m}$ width, $p = 0.99$ ($F = 2.49\text{E-}4$) for $770 \mu\text{m}$ width, and $p = 0.84$ ($F = 0.04$) for $1517 \mu\text{m}$ width.

3.4.4 Validation of biocompatibility & $[\text{Ca}^{2+}]_i$ imaging

Biocompatibility is essential for future implementations of our platform. To investigate biocompatibility, osteoblast-like MC3T3-E1 cells were seeded into chambers at $30,000 \text{ cells cm}^{-2}$ and incubated without flow for approximately two hours to allow the cells to adhere. Images were captured between 2-4 hours after initial seeding (Fig. 3.5). Cells adhered and survived with a normal morphology within the channels.

Following cell seeding within the channels, the channels were also tested for compatibility with fluorescence imaging using UV excitation wavelengths. For these proof-of-concept studies, MC3T3-E1 cells were loaded with ratiometric calcium dye

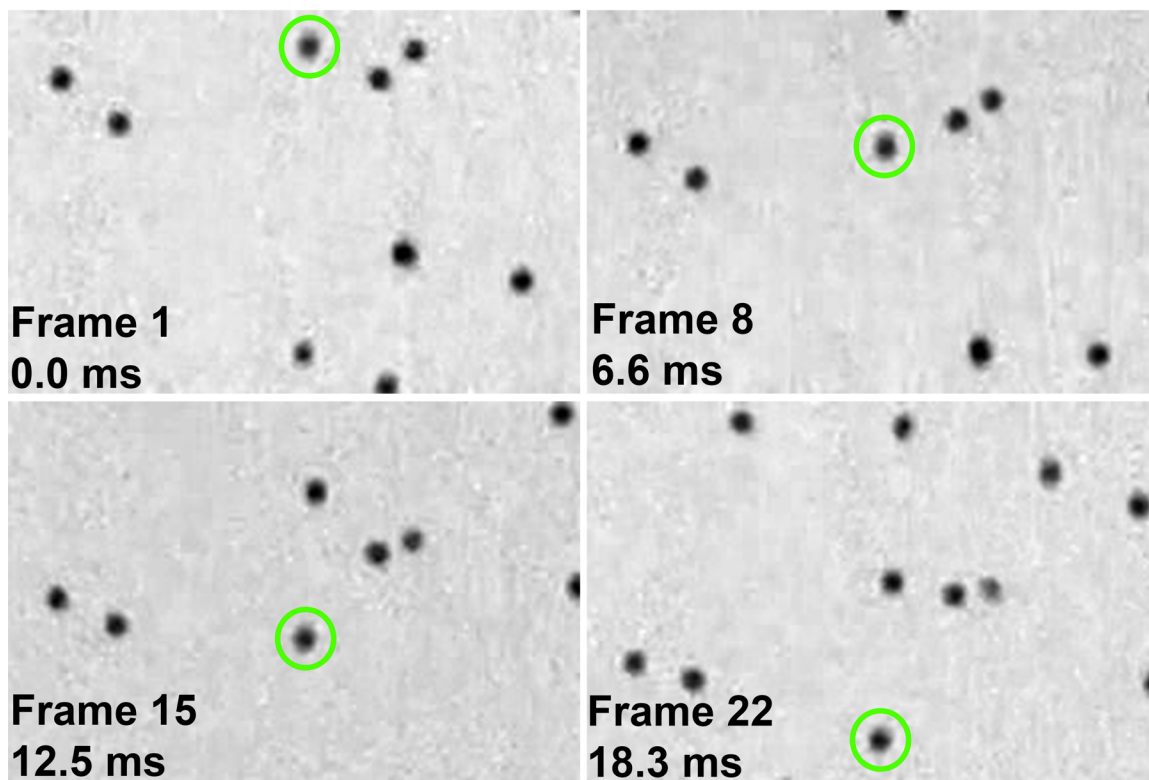


Figure 3.3 High-speed imaging of micro-particle flow within microfluidic channels. Polystyrene microspheres were loaded within the microfluidic channels at neutral density in a 6.8% w/v saline solution. Flow was established with a programmable syringe pump at a range of flow rates. Illustrated are representative images from a single video obtained at $10 \mu\text{L}\cdot\text{min}^{-1}$ in the $522 \mu\text{m}$ wide channel. Frames were captured 1200 times per second (every 0.83 ms) with a consumer high-speed camera on an inverted microscope (10x objective). By tracking the displacement of individual particles between frames, particle velocities can be calculated. Green circles highlight the position of the same individual particle in each frame. The direction of flow is from top to bottom in this example. For such particle imaging velocimetry (PIV) experiments, at least 40 particles were tracked per flow rate at each channel width. From the velocity distributions, peak velocities were obtained.

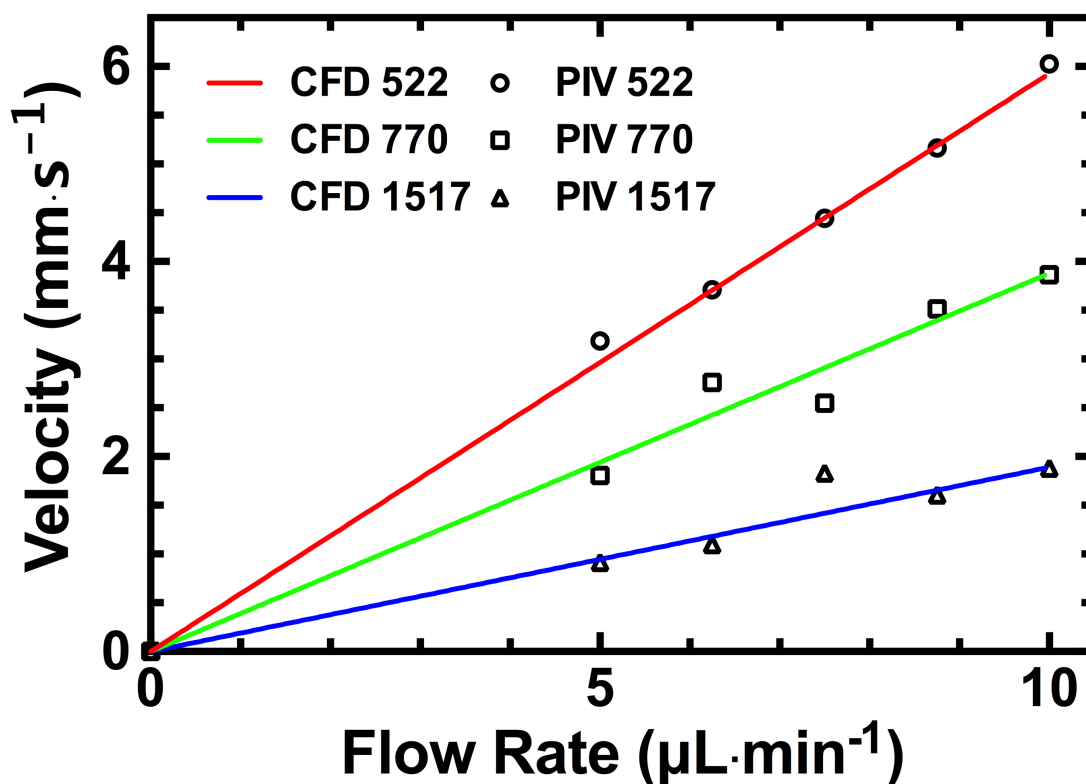


Figure 3.4 Peak-velocity from CFD and PIV over a range of steady flow rates.

Coloured lines represent the CFD-generated peak velocities over a range of flow rates. Numerical calculations were performed for a channel of 90 μm height with widths of 522 μm , 770 μm or 1517 μm , at flow rates from 0 – 15 $\mu\text{L}\cdot\text{min}^{-1}$. Peak velocity was linearly related to flow rate ($y = 0.5929x$, $y = 0.3878x$, $y = 0.1891x$ for narrowest to widest channels, respectively). Open symbols represent data obtained by particle imaging velocimetry. Beads were pumped through channels at a range of flow rates (5 - 10 $\mu\text{L}\cdot\text{min}^{-1}$) and imaged using a high-speed digital camera on an inverted phase-contrast microscope. Images were then processed and resultant peak velocities were plotted versus flow rates. Linear regression was performed on these data ($y = 0.5934x$, $y = 0.3872x$, and $y = 0.1955x$, for narrowest to widest channels, respectively), revealing excellent agreement with the CFD data (slopes were not significantly different based on ANCOVA)

fura-2, then monitored for $[Ca^{2+}]_i$ changes in response to alterations in fluid flow (Fig. 3.6a). Ratio imaging of fura-2-loaded cells showed prompt calcium elevation in response to a change in fluid flow from 10 to 40 $\mu\text{L}\cdot\text{min}^{-1}$ (corresponding to approximately 0.25 to 1.0 Pa of wall shear). Responses consisted of transient elevations of $[Ca^{2+}]_i$ lasting approximately 1 min (Fig. 3.6b). In summary, our preliminary phase and fluorescence experiments illustrate that this device could be easily applied to real-time imaging of cellular responses to stimuli applied using microfluidics.

3.5 Discussion & conclusions

We have successfully developed a technique for the fabrication of microfluidic systems capable of accurately delivering steady-flow fluid shear to live cells during real-time microscopy. We have done so using an innovative and low-cost approach for microdevice fabrication, which has minimal equipment and expertise requirements that would typically be available to most non-specialist labs. The fabrication process necessitates access to a standard milling machine to produce a mold, a simple spin-coater to distribute a thin bonding layer of PDMS to the substrate, and a conventional microwave oven to partially cure a thin PDMS layer. An advantage to this technique is that exact replication of nominally prescribed dimensions is not necessary in most cases; a more typical requirement is that the dimensions of the fabricated structures be known accurately after the fact, and that the technique is reproducible. With knowledge of the observed dimensions, commercially available finite-element modeling software can be used to numerically calculate the resultant wall shear, a quantity that is difficult to measure empirically. Computational fluid dynamic predictions can then be verified by

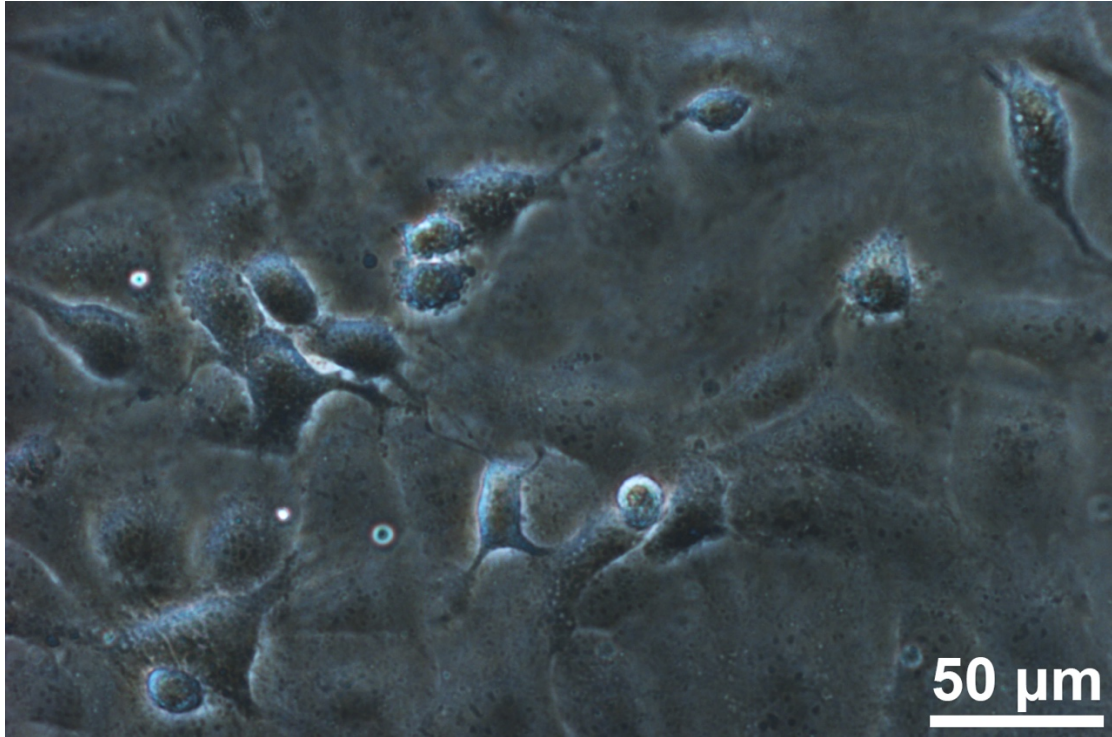


Figure 3.5 Osteoblast-like cells imaged inside a prototype microfluidic channel.

MC3T3-E1 cells cultured in α -MEM with 10% FBS were seeded into the channel at $30,000 \text{ cells}\cdot\text{cm}^{-2}$. Images were taken approximately 4 hours after seeding, using an inverted phase-contrast microscope with 20x PlanFluor objective. This image is representative of cells seeded in our microfluidic environment across at 3 devices in at least 5 independent experiments. These data provide proof-of-concept for biocompatibility and imaging compatibility of our microfluidic devices.

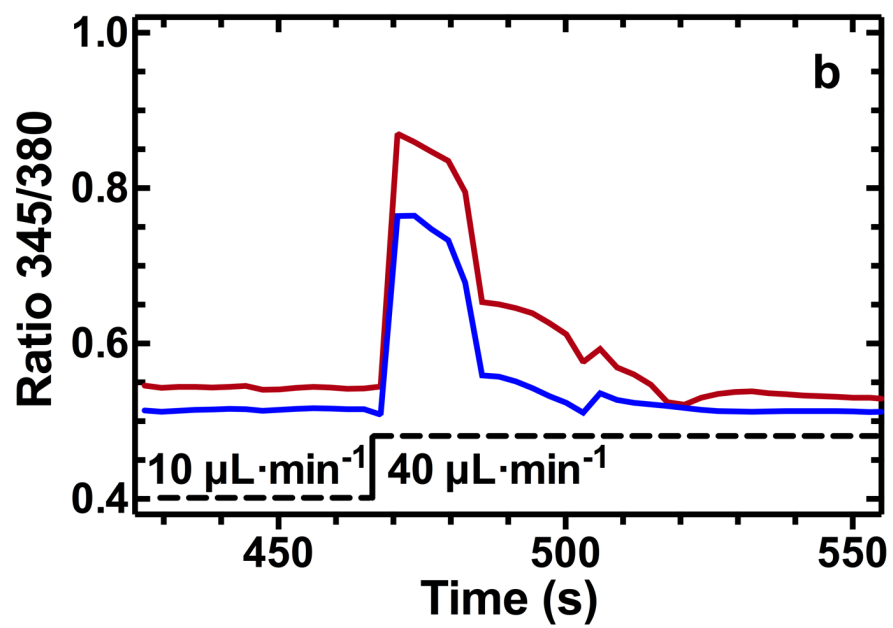
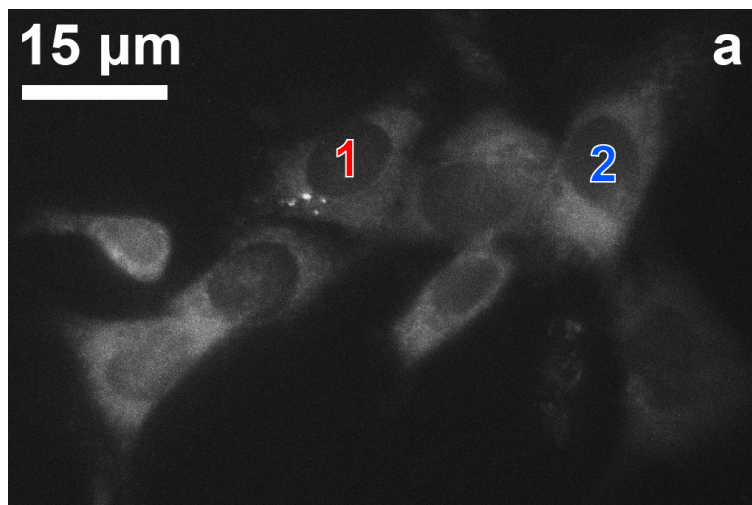


Figure 3.6 Device compatibility with live-cell fluorescence imaging of cytosolic free calcium. MC3T3-E1 cells were seeded within the microfluidic channels at $30,000 \text{ cells}\cdot\text{cm}^{-2}$ and allowed to adhere. Following adhesion, the cells were loaded with fura-2 and imaged on a Nikon inverted microscope. An illustration of a representative field of fura-2-loaded cells imaged at 345 nm excitation. b Cytosolic free calcium ($[\text{Ca}^{2+}]_i$) was monitored as the ratio of fluorescence intensity at 345/380 nm. Initially, cell culture medium was pumped through the channels at $10 \mu\text{L}\cdot\text{min}^{-1}$ (corresponding to approximately 0.25 Pa of fluid shear). At 464 seconds, flow was increased to $40 \mu\text{L}\cdot\text{min}^{-1}$ (corresponding to approximately 1 Pa). Most, if not all, cells tested responded to the change in shear with transient elevation of $[\text{Ca}^{2+}]_i$. Red and blue traces illustrate the responses of cells labelled 1 and 2 respectively in panel a. Data are representative of 3 independent experiments.

comparison with observed peak velocities, which are relatively straightforward to measure with a laboratory inverted microscope and consumer-grade high-speed camera.

This approach is straightforward, robust, and affordable; it results in irreversibly bonded chambers that are leak-tight to pressures in excess of 1.5 MPa. While partial curing of PDMS has been discussed in the literature (Yu et al., 2011), our microwave method is at minimum six-fold faster and is one aspect of our accessible approach to microfluidic fabrication. The method presented here results in irreversibly sealed devices, but reversibly sealed PDMS devices are also employed extensively in the literature (Chen et al., 2014; Konda et al., 2015). While reversible seals are generally unable to withstand pressures required in our experimental studies, they also have many advantages over irreversible seals. Due to their ability to be disassembled, reversibly sealed PDMS devices can be disassembled and cleaned for reuse, or even salvaged for *post facto* analysis. This ability to disassemble reversibly sealed devices can be used to increase the lifespan of devices, however, we maintain the ability to clean and reuse our devices several times. Additionally, while devices made with our technique last for many uses, when they reach the end of their lifespan they are cheap, easy, and efficient to replace.

Our platform technology could serve to extend the accessibility of microfluidics to future studies of the real-time effects of fluid shear on live cells. Additionally, our fabrication techniques may facilitate the development of microdevices for routine live-cell imaging applications, using similar fabrication methods.

3.6 References

- Beh CW, Zhou W, Wang TH. 2012. PDMS-glass bonding using grafted polymeric adhesive--alternative process flow for compatibility with patterned biological molecules. *Lab on a chip* 12(20):4120-4127.
- Chen Q, Li G, Nie Y, Yao S, Zhao J. 2014. Investigation and improvement of reversible microfluidic devices based on glass-PDMS-glass sandwich configuration. *Microfluidics and Nanofluidics* 16(1):83-90.
- Ertel SI, Ratner BD, Kaul A, Schway MB, Horbett TA. 1994. In vitro study of the intrinsic toxicity of synthetic surfaces to cells. *Journal of biomedical materials research* 28(6):667-675.
- Ginn BT, Steinbock O. 2003. Polymer Surface Modification Using Microwave-Oven-Generated Plasma. *Langmuir* 19(19):8117-8118.
- Grol MW, Pereverzev A, Sims SM, Dixon SJ. 2013. P2 receptor networks regulate signaling duration over a wide dynamic range of ATP concentrations. *Journal of cell science* 126(Pt 16):3615-3626.
- Gross PG, Kartalov EP, Scherer A, Weiner LP. 2007. Applications of microfluidics for neuronal studies. *Journal of the neurological sciences* 252(2):135-143.
- Haubert K, Drier T, Beebe D. 2006. PDMS bonding by means of a portable, low-cost corona system. *Lab on a chip* 6(12):1548-1549.
- Hinderliter PM, Minard KR, Orr G, Chrisler WB, Thrall BD, Pounds JG, Teeguarden JG. 2010. ISDD: A computational model of particle sedimentation, diffusion and target cell dosimetry for in vitro toxicity studies. *Part Fibre Toxicol* 7(1):36.
- Hui AY, Wang G, Lin B, Chan WT. 2005. Microwave plasma treatment of polymer surface for irreversible sealing of microfluidic devices. *Lab on a chip* 5(10):1173-1177.
- Konda A, Taylor JM, Stoller MA, Morin SA. 2015. Reconfigurable microfluidic systems with reversible seals compatible with 2D and 3D surfaces of arbitrary chemical composition. *Lab on a chip* 15(9):2009-2017.
- Leclerc E, David B, Griscom L, Lepioufle B, Fujii T, Layrolle P, Legallais C. 2006. Study of osteoblastic cells in a microfluidic environment. *Biomaterials* 27(4):586-595.
- Lee GH, Lee JS, Wang X, Hoon Lee S. 2015a. Bottom-Up Engineering of Well-Defined 3D Microtissues Using Microplatforms and Biomedical Applications. *Advanced healthcare materials* 5:56-74.

- Lee Y, Lee JM, Bae PK, Chung IY, Chung BH, Chung BG. 2015b. Photo-crosslinkable hydrogel-based 3D microfluidic culture device. *Electrophoresis* 36(7-8):Na.
- Loutherback K, Chen L, Holman HY. 2015. An open-channel microfluidic membrane device for long-term FTIR spectromicroscopy of live adherent cells. *Analytical chemistry* 87(9):4601-4606.
- Meyvantsson I, Beebe DJ. 2008. Cell culture models in microfluidic systems. *Annual review of analytical chemistry (Palo Alto, Calif)* 1:423-449.
- Miller KM, Anderson JM. 1988. Human monocyte/macrophage activation and interleukin 1 generation by biomedical polymers. *Journal of biomedical materials research* 22(8):713-731.
- Moraes C, Likhitpanichkul M, Lam CJ, Beca BM, Sun Y, Simmons CA. 2013. Microdevice array-based identification of distinct mechanobiological response profiles in layer-specific valve interstitial cells. *Integrative Biology* 5(4):673-680.
- Polacheck WJ, Li R, Uzel SG, Kamm RD. 2013. Microfluidic platforms for mechanobiology. *Lab on a chip* 13(12):2252-2267.
- Unger MA, Chou H-P, Thorsen T, Scherer A, Quake SR. 2000. Monolithic Microfabricated Valves and Pumps by Multilayer Soft Lithography. *Science* 288(5463):113-116.
- Wheal BD, Beach RJ, Tanabe N, Dixon SJ, Sims SM. 2014. Subcellular elevation of cytosolic free calcium is required for osteoclast migration. *J Bone Miner Res* 29(3):725-734.
- Yasocharan S, Pinto S, Sled JG, Bolz S-S, Gunther A. 2015. Artery-on-a-chip platform for automated, multimodal assessment of cerebral blood vessel structure and function. *Lab on a chip* 15(12):2660-2669.
- Young EW, Beebe DJ. 2010. Fundamentals of microfluidic cell culture in controlled microenvironments. *Chem Soc Rev* 39(3):1036-1048.
- Yu H, Zhou G, Chau F, Sinha S. 2011. Soft lithography replication based on PDMS partial curing. *Microsystem Technologies* 17(3):443-449.

Chapter 4

A microfluidic system for real-time microscopic imaging of
endothelial cell responses to laminar and disturbed fluid
flow⁴

⁴ Manuscript in preparation for submission: Lorusso, D., Soon, K., Sacoransky, E., Nikolov, H.N., deBruyn, J.R., Pickering, J.G., Dixon, S.J., Holdsworth, D.W., Poepping, T.L.. A microfluidic system for real-time microscopic imaging of endothelial cell responses to laminar and disturbed fluid flow.

4.1 Chapter summary

Blood flow dynamics play a critical role in health and disease of the human vasculature. Endothelial cells (ECs) lining these vessels are mechanosensitive and are able to discern between unidirectional laminar flow and multi-directional disturbed flow – a pathological stimulus that is associated with the initiation and progression of atherosclerosis. The immediate mechanotransductive response of ECs exposed to disturbed flow is not well understood. Here, a microfluidic device is presented that is able to generate laminar and disturbed flow regimens at physiologically relevant wall shear magnitudes, and is also compatible with real-time live-cell imaging. The device was used to observe immediate responses of ECs to disturbed flow. The custom-designed device was fabricated from polydimethylsiloxane using a replica molding technique. Flow within the channels was evaluated experimentally using micro-particle image velocimetry. Human umbilical vein endothelial cells were seeded within the channels, loaded with a calcium-sensitive fluorescent probe, and changes in the concentration of cytosolic free calcium elicited by laminar and disturbed flow were monitored. Repeatable and physiologically relevant levels of uni- and multi-directional wall shear stress (0-5 Pa) were generated. This device will enable further studies into the understanding of the responses of ECs to flow dynamics and their relevance to vascular health and disease.

4.2 Introduction

The human vasculature is a mechanically sensitive organ, and fluid shear stress due to blood flow is a key regulator of health and disease. Vascular endothelial cells (ECs) play a major role in sensing and responding to mechanical loads and forces. Vascular EC dysfunction has been identified as a key contributor to vascular pathologies (Castellon and Bogdanova, 2016), such as atherosclerosis (Grassi et al., 2011), a disease that is known to have high rates of associated morbidity and mortality worldwide (Herrington et al., 2016). Researchers have shown that not just biochemical signals, but also mechanical blood-flow dynamics play an important role in EC dysfunction (Gimbrone, 1999). Both the initiation and progression of atherosclerosis have been found to result from pathological blood-flow dynamics (Gimbrone and Garcia-Cardena, 2013). ECs themselves are capable of sensing and discriminating different flow paradigms (Nakajima and Mochizuki, 2017), such as laminar uni-directional flow versus turbulent-like multi-directional flow. What is not well understood is the mechanotransductive mechanisms by which VECs might differentiate between these different forms of fluid shear stress stimuli and how they signal differentially downstream following such stimuli.

EC mechanotransduction has been a primary focus for vascular biologists in recent decades, and the response to fluid flow has been studied extensively (Ando and Yamamoto, 2009; Chistiakov et al., 2017; Davies, 1995; Wang et al., 2013). *In vivo*, atheroprone and atheroprotective regions of the human vasculature have been identified, where specific areas have been found to be more or less susceptible to the initiation and progression of atherosclerotic lesions. Atheroprone regions, which present as bifurcations

and curved areas of the vasculature, are determined by the flow dynamics resulting from the geometries of these regions (Heo et al., 2014). One key mechanism used by ECs in the immediate response to fluid flow is cytosolic calcium signaling (Ando and Yamamoto, 2013). In response to extracellular fluid flow exerting wall shear stresses on the cell, ATP is released by the cell to signal through cell-surface nucleotide receptors (P2X and P2Y purinoceptors), which in many cases signal in part through transient increase in the concentration of cytosolic free calcium. Cellular responses to laminar (Berk, 2008), pulsatile (Uzarski et al., 2013), and low-frequency oscillatory (Heckel et al., 2015) flows have been studied, and cells have been shown to display distinct behaviour in response to these different forms of fluid flow. This is consistent with the ability of cells to discriminate between different flow patterns *in vivo*. Studies have investigated long-term downstream cell responses to turbulent flow (Kutikhin et al., 2018), however there is a lack of research surrounding the short-term (second to minutes time scale) response of cells to disturbed flow (i.e. time-dependent, multi-directional fluid flow) (Baeyens, 2018). A key reason for this lack of research is that tools do not exist to apply time-dependent, multi-directional fluid flow to live-cells during real-time microscopy.

Microfluidics is a modern, established approach to study cells during fluid flow stimuli (Shemesh et al., 2015; Sia and Whitesides, 2003; Zhang and van Noort, 2011). Devices exist to create high Reynolds number (Re) turbulent flow (Kathuria et al., 2013; Liu et al., 2009) in micromixers, but they are not compatible with either live-cell cultures or real-time microscopic monitoring. Similarly, many devices exist for studying EC physiology and mechanotransduction (Chen et al., 2013; Fiddes et al., 2010; van der

Meer et al., 2010), but are typically only compatible with uni-directional laminar flow regimes (Young and Simmons, 2010). Critically, it is difficult to generate high-Re flow in microfluidic environments. Geometric scale and velocity are two defining factors of Re and are part of the reason for this difficulty. First, decreasing the size of channels to the sub-millimetre scale of micro-scale fluidic devices to increase compatibility with microscopy lowers the Re of the fluid, and second, increasing velocity will increase the Re, but will also increase the wall shear stress (WSS) on cells – making such strategies inappropriate for live-cell real-time microscopic experimentation. However, disturbed flow patterns similar to turbulence, but at low Re, can be generated in microfluidic devices.

Here, we report the development and validation of a microfluidic device that can generate multi-directional flow disturbances. Impinging high-velocity jets were used to generate flow disturbances in an adjacent cell imaging region of a microfluidic flow chamber. This creates time-dependent, multi-directional fluid shear stress within the imaging chamber of the device at magnitudes of wall shear (0 – 5 Pa). This range of wall shear stress magnitude is suitable for live-cell cultures and relevant to the magnitudes of stress experienced by endothelial cells *in vivo* (Baeyens et al., 2016). Laminar and disturbed flow patterns were characterized as a function of inlet flow rates. Reproducibility of disturbed flow stimulus both within one device and between different devices was evaluated. Compatibility with real-time microscopic observation allowed direct evaluation of fluid velocities over time, which could then be used to accurately predict wall shear at given inlet flow rates. The device was then used to monitor cytosolic free calcium in human VECs exposed to laminar (unidirectional shear) and disturbed (multi-

directional shear) flow at comparable magnitudes of wall shear stress. Thus, a microfluidic device was developed to apply controlled, multi-directional shear to live-cell cultures during real-time microscopy. This tool will enable studies of the role of disturbed flow in the pathogenesis endothelial dysfunction.

4.3 Methods

4.3.1 Microfluidic device fabrication

A device to investigate the real-time response of endothelial cells to multi-directional disturbed flow requires several capabilities. These include the ability to generate this stimulus at a relevant wall shear range, while also being compatible with real-time microscopy, as well as live-cell cultures. To the best of our knowledge, a device meeting these requirements is not currently described in the literature, and therefore, a custom device was required to meet these criteria. This challenge was approached using polydimethylsiloxane (PDMS)-based microfluidic devices. The techniques described in Chapter 3 (Lorusso et al., 2016), based on PDMS replica-molding methods, were used to build this device. Briefly, a negative of the device was planned with computer-assisted design software (Fig. 4.1a) and machined into a negative mold from acrylic on a three-axis CNC mill (Fig. 4.1b). PDMS (Sylgard 184, Dow Corning, Midland MI) was prepared in a 10:1 base:elastomer ratio, mixed, and vacuum degassed to remove bubbles. PDMS was poured into the negative mold that, when fully cured and hardened, produced a positive replica of the chip. An ultra-thin layer of PDMS was then spin-coated onto a glass-bottom cell culture dish (MatTek Corp., Ashland MA), and partially cured with

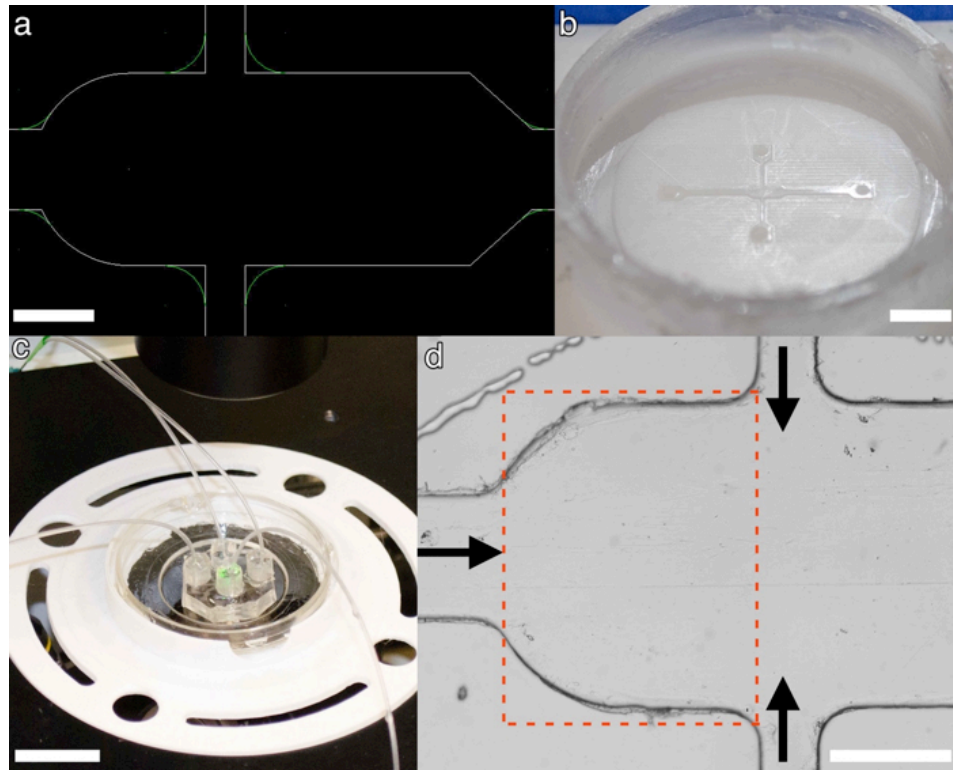


Figure 4.1 Microfluidic device design and fabrication. a) CAD of the disturbed flow microfluidic chip mold. A geometry of the mold for the disturbed flow chip was drawn with CAD, and the toolpath was generated in MasterCAM. The white lines represent the drawn geometry, while the green accents indicate rounding due to the diameter of the mill cutter. White bar represents 500 μm . b) Photograph of the disturbed flow microfluidic device mold. The positive mold used to cast negative replicas of the disturbed flow microfluidic chip. White bar represents 25 mm. c) A photograph of the completed device, pictured on the microscope stage. A thin bonding layer of PDMS was spun onto a glass-bottomed cell-culture dish, and a replica chip was irreversibly sealed to this bonding layer. Miniature tubing was added to allow the introduction of flow to the device, and inlets were sealed to prevent leakage. White bar represents 50 mm. d) A micrograph of the disturbed flow microfluidic device. Outlined in red is the cell-culture imaging region used in the present study. Black arrows represent the three inlets. The large main inlet (left) was used to create laminar flow in the imaging region, while the two opposing inlets to the right were used to create disturbed flow. White bar represents 500 μm .

heat until it was tacky. The fully cured PDMS positive replica of the chip was then gently placed against the partially cured PDMS layer. The bottom layer of the device was then fully cured by further application of heat. Following the addition of miniature tubing (PE-50, BD Canada; Mississauga ON) and sealing of inlets, the device was ready to use on the microscope (Fig. 4.1c). Some key advantages of this approach were: 1) straightforward design and fabrication of custom devices, 2) leak-proof seals achieved by irreversible PDMS-PDMS bonding, 3) optical clarity with minimal device thickness to optimize quality and compatibility with microscope objectives, and 4) biocompatibility with live-cell cultures.

To generate the multi-directional disturbed flow, at physiologically relevant wall shear ranges compatible with live-cells, a design was used with impinging high-velocity jets (Liu et al., 2009). The microfluidic path consisted of three narrow inlet channels and one outlet channel with a common, relatively larger central flow chamber where cells could be seeded (Figure 4.1). One axial inlet was used to apply laminar flow to the cells. The remaining two smaller inlets were directly opposite to one another. Given sufficient flow rates (4 mL/min) in opposing inlets, these created high-velocity jets that impinged on one another, resulting in multi-directional flow disturbances in the critical zone of the cell chamber, adjacent to the opposing inlets (Figure 4.1d).

4.3.2 Micro-particle image velocimetry

Micro-PIV was performed to evaluate the direction, velocity, and wall shear stress produced by flow within the device. PIV fluid was prepared by diluting 0.5 μm fluorescent microspheres (R500; Thermo Fisher Scientific, Waltham, MA) in distilled

water to achieve a final seeding density of approximately 30 particles per $100 \times 100 \mu\text{m}^2$ area. Experiments were performed on two different microfluidic devices of the same design to evaluate inter-device variability. The microfluidic device was mounted on an inverted microscope (Olympus IX71; Tokyo, Japan). Fluid was delivered over a range of flow rates, from 100 – 250 $\mu\text{L}/\text{min}$ from the main inlet, or 4 mL/min from the opposing inlets. Fluorescent particles suspended in the fluid were pumped into the device and excited (Fig. 4.2a,b) with an Nd:YLF laser (20 W, 532 nm), and imaged using a 10x objective (NA 0.3). Emission was filtered at $610 \pm 37 \text{ nm}$, and detected using a high-speed CMOS camera with its frame rate synchronized to the laser pulse repetition frequency (2.557 kHz, $1300 \times 1024 \text{ pixels}^2$). For laminar flow, this process was repeated at 5 vertical increments to establish velocity profiles along the height axis (z) of the channel. This was performed by focusing the microscope on the bottom wall (floor) of the channel, then the top wall (ceiling) of the channel, and recording the stage position at both heights. The z-positions of the top and bottom of the channel were used to determine the central plane of the device. From this central plane, the top half and bottom half were again split by 2 more planes, each towards both horizontal walls (flow channel ceiling and floor); thus comprising the 5 planes total used in these experiments. For disturbed flow, data was captured at only one height per experiment, either close to the floor of the flow channel, or along the central plane. A vertical stack could not be assembled from the

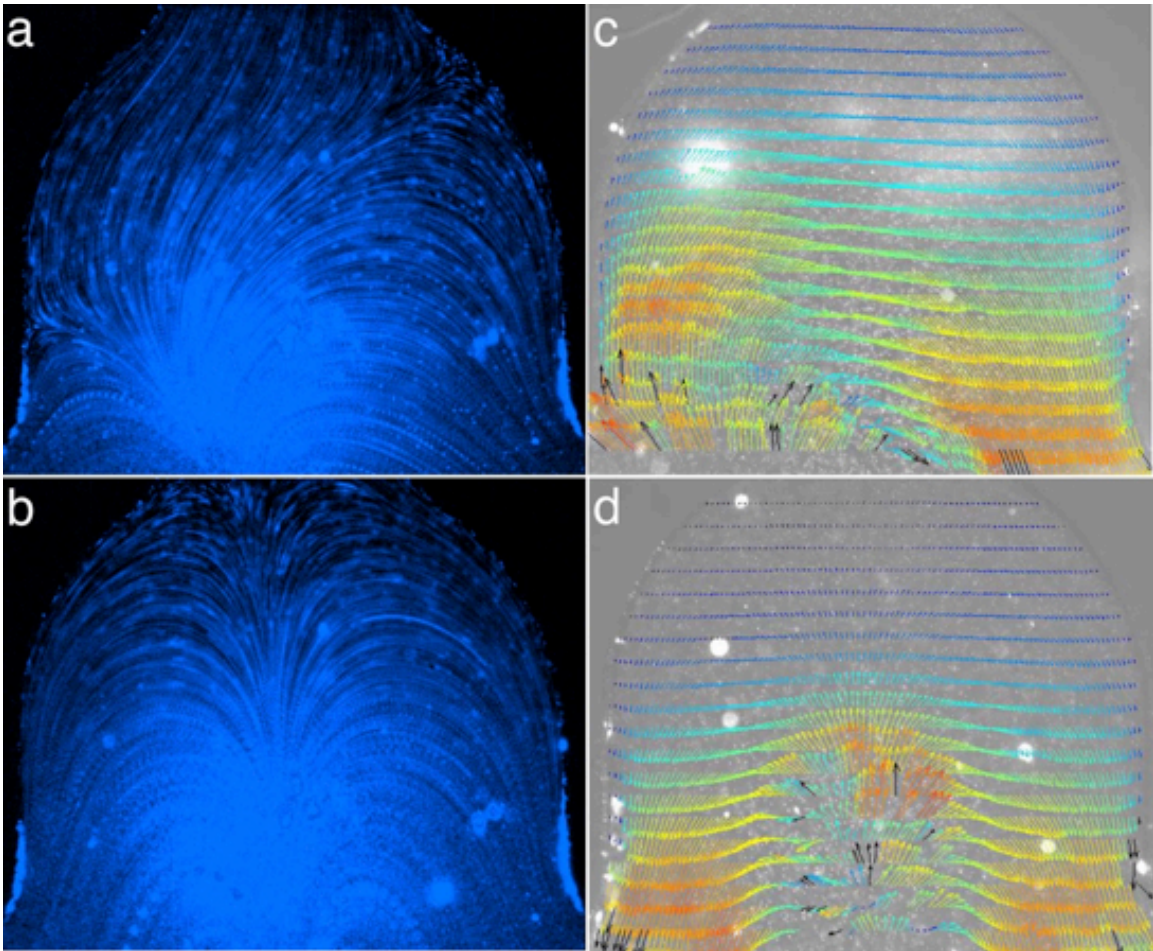


Figure 4.2 Imaging of micro-particles and resultant velocity vector fields. Micro-particles were pumped through the device with steady flow (4 mL/min) from both side inlets and imaged using the micro-PIV system. a), b) Multi-exposure images visualizing particle motion streamlines. Images represent the sum of 100 images captured over 50 ms real-time, with a frame rate of 2.557 kHz. Images were modified with a colour mixer to create a monochromatic image. Red and green signal were removed from their respective output channels, and the green signal was reconstituted in the blue output channel. c), d) Velocity vector maps, each resulting from two consecutive frames of particle images (~ 0.4 ms gap), representing velocity fields captured over the course of 30-60 s. This demonstrates the fluctuations in velocity fields determined by the micro-PIV method employed within our device.

disturbed flow data, as the time-dependent nature of the flow would result in asynchronicity of the z-increments. All data acquisition and cross-correlation analysis were performed using commercial PIV software (DaVis 8.3, LaVision, Inc.). To evaluate the data, an initial interrogation window of 128×128 pixels was applied with a 50% overlap between fast-Fourier-transform-based cross-correlations, and reduced to a final window of 32×32 pixels with a 75% overlap, leading to velocity vectors spaced $8 \mu\text{m}$ apart in each x-y plane collected (Fig. 4.2c,d). Velocity maps captured throughout the height of the device were stacked to construct the 3D velocity datasets. The imaging region studied during experimentation was a pixel matrix spanning 0.943 mm long (x-dimension) 1.340 mm wide (y-dimension).

4.3.3 Micro-PIV data processing and analysis

Shear stress (τ) parameters were calculated as follows, building off existing metrics described in the literature (DiCarlo et al., 2019). Wall shear stress ($\vec{\tau}_w$) was evaluated based on the slope of the velocity at the wall:

$$\vec{\tau}_w = \mu \left(\frac{dv}{dz} \right)_{z=floor}$$

where v is velocity (m/s) and μ is viscosity (Pa s). The mean wall shear stress was then defined as the mean wall shear stress vector over time:

$$\vec{\tau}_{mean} = \frac{1}{T} \int_0^T \vec{\tau}_w dt$$

Time-averaged wall shear stress, indicating mean of the wall shear stress magnitude, was calculated as:

$$TAWSS = \frac{1}{T} \int_0^T |\vec{\tau}_w|$$

And the oscillatory shear index (OSI) (Ku et al., 1985), which represents the fraction of WSS in the reverse direction relative to the average WSS direction, was calculated as:

$$OSI = 0.5 \left[1 - \left(\frac{|\vec{\tau}_{mean}|}{TAWSS} \right) \right]$$

where a maximum value of 0.5 indicates equal forward and reverse WSS. A modified version of Transverse WSS (TransWSS) was employed in this study. The TransWSS metric is used to determine the components of wall shear that occur perpendicular to the mean shear vector. This is a useful descriptor in many cases, but in our case we felt it did not adequately describe the flow disturbance that might be felt by cells in in our channels. We wished to describe the flow perpendicular not to the mean shear vector during disturbed flow, but rather compared to the mean shear vector of our laminar flow case. As the mean laminar shear vector is the flow paradigm experienced by the cells for over 24 hours during incubation, and therefore is the axis of cell polarity or alignment. Therefore TransWSS was modified to define a new Transverse to Laminar WSS (TLWSS), and this was used to characterize disturbed flow regimen in our devices:

$$TLWSS = \frac{1}{T} \int_0^T \left| \vec{\tau}_w \cdot \left(\vec{n} \times \frac{\int_0^T \vec{\tau}_w \text{ lam} dt}{\left| \int_0^T \vec{\tau}_w \text{ lam} dt \right|} \right) \right|$$

where numerator and denominator arise from mean WSS and TAWSS during laminar flow regimen using the main inlet. This effectively represents the average magnitude of the WSS that is perpendicular to the expected direction of cellular alignment. All calculations were performed in MATLAB (MathWorks; Natick, MA) and Excel (Microsoft; Redmond, WA).

4.3.4 Cell culture and live-cell imaging

Human umbilical vein endothelial cells (HUVEC, CRL-1730™; ATCC, Manassas, VA) were subcultured to passage 4 or 5 and grown to confluence. Primary human aortic endothelial cells (HAEC, CC-2535; Lonza, Rochester, NY) were subcultured to passage 10 to 20. Cells were incubated in Endothelial Growth Medium-2 (EGM-2) Bulletkit (CC-3162; Lonza) at 37°C and 5% CO₂, with regular medium changes every other day. According to the method described in Chapter 3 (Lorusso et al., 2016), cells were grown in the device as follows. A microfluidic device was pre-treated with 20-μg/mL fibronectin (F1411, MilliporeSigma) for at least 1 hour. Cells were then trypsinized and seeded into the microfluidic device at a density of 2-3x10⁶ cells/mL. Devices were incubated statically at 37°C and 5% CO₂ for approximately 3 hours (to allow the cells to attach). Devices were then perfused with EGM-2 at a rate of 10 μL/h with a programmable syringe pump (NE-1000 or NE-100; New Era Pump Systems, Farmingdale, NY) for a minimum of 48 h (37°C and 5% CO₂) prior to live-cell imaging experiments.

Imaging of cytosolic free calcium followed the method described previously in Chapters 2 and 3 (Lorusso et al., 2016), where cells were loaded with the calcium-sensitive

fluorescent probe fura-2 by incubation with 1.5 μM fura-2-AM for 30 min. Unloaded dye was flushed from the channels, and the device was mounted on an inverted microscope (Nikon Eclipse TE2000-U, Tokyo, Japan) equipped with a ratio-illuminator (DeltaRam X; Horiba – Photon Technology International, Birmingham, NJ). Samples were excited with 500 ms exposures of alternating wavelength 345 nm and 380 nm light, and emission signal was filtered at 510 ± 20 nm. Ratio images were acquired every second with a 4.2 LT sCMOS camera (2048 x 2048 pixels pco.edge; PCO AG, Kelheim, Germany) and image capture software (EasyRatioPro 2.3; Horiba-PTI). Background signal was collected for a minimum of 10 min as cells were perfused using a syringe pump with 10 $\mu\text{L}/\text{min}$ of unsupplemented α -MEM medium to prevent depletion of nutrients or build-up of waste. The $[\text{Ca}^{2+}]_i$ responses of cells were then monitored over time in response to laminar or disturbed flow stimuli.

4.4 Results

4.4.1 Laminar flow characterization measurements

First, a series of experiments were performed to determine the laminar flow patterns within our device. Steady-state flow allows us to measure different depths sequentially and assess accuracy of estimating WSS from a single velocity plane near the wall, as would be required during disturbed flow. Additionally, the laminar flow regimen must be characterized as it is used not only during cell culture to establish a healthy VEC phenotype, but also during $[\text{Ca}^{2+}]_i$ imaging experiments as a control mechanostimulus. To achieve the laminar flow regimen, the micro-PIV method described above in Section 4.3.2 was used. PIV fluid containing micro-particles was pumped through the device over

a range of flow rates. Resulting particle motion was imaged at 5 heights within the channels to build a 3D velocity profile. Velocity vector fields were generated (Fig. 4.3a) to determine the magnitude and direction of flow throughout the channel. A 3D drawing of the device illustrates the orientation of Cartesian axes within the device (Fig. 4.3b), specifically, channel length (x), channel width (y), and channel height (z).

Velocity magnitude was then determined as a function of length (x) through the channel (Fig. 4.4a). As expected, as the inlet laminar flow channel opened into the central imaging flow chamber, the velocity profile developed and decreased with increasing channel width. Using velocity fields generated at each of the 5 heights, the velocity profile along the height (z) of the channel was determined and fitted to a second-order polynomial (Fig. 4.4b).

From the velocity profiles along the height of the channel, an average height dimension for the channel ($106 \pm 6 \mu\text{m}$, mean \pm SD) was determined by averaging the intercept of each curve fit, for 20 x-y positions repeated at 4 different flow rates in 1 device ($n = 80$). From this, the actual height difference between the lowest z-plane measured in our flow channel and the floor of the flow channel itself was determined ($\Delta z = 11 \mu\text{m}$). This parameter was used for empirical determination of the wall shear stress.

The wall shear stress generated at the channel floor during flow was then determined given the velocity measurements made in Fig. 4.3 and 4.4. This displays the pattern of wall shear stress across the entire segment of the flow channel studied. Two different methods of calculating wall shear stress (τ_w) were compared (Fig 4.5a). The first method (τ_{fit}) used the fitted quadratic velocity profile based on measurements at 5 depths, and

then finding the slope of the fit at $0.1 \mu\text{m}$ above the channel floor, as described above. The second method ($\tau_{\Delta z}$) estimated the WSS based on the linear slope extending from the velocity measurement nearest to the wall (Δz from the floor) and presuming zero velocity at the wall (no-slip). This method only requires velocity measurement at one depth along with an accurate estimation of Δz , such as is feasible with disturbed flow when limited by asynchronous data for planes of different depths. These methods were found to differ up to $\sim 0.3 \text{ Pa}$. As expected, the wall shear stress follows the same pattern as the velocity profile along the channel length (Fig. 4.5a). A 2D colour map of time-averaged wall shear stress is shown for $250 \mu\text{L}/\text{min}$ flow rate (Fig. 4.5b). Wall shear stress as a function of flow rate was then plotted for each position x_{1-4} , and fitted by linear regression (Fig. 4.6). As expected, wall shear was found to increase in a linear relationship with flow rate within our channel. Within the imaging region of our device, the wall shear stress generated at flow rates of $Q = 100 - 250 \mu\text{L}/\text{min}$ ranged between $\tau_w = 0.64 - 2.3 \text{ Pa} \pm 21.5\%$.

4.4.1 Disturbed flow analysis

Having characterized the microfluidic device for laminar flow cases, the disturbed flow patterns were then evaluated. The same micro-PIV methods established in the laminar flow studies were used. For laminar flow cases, the wall shear stress was adequately described with TAWSS, as the velocity vectors were not time-dependent. However, during disturbed flow, the flow velocity magnitudes and directions vary as a function of time. Therefore, to fully characterize disturbed flow patterns, quiver plots were used to display velocity vectors overlaid on colour-encoded parametric maps (Fig. 4.7). Briefly,

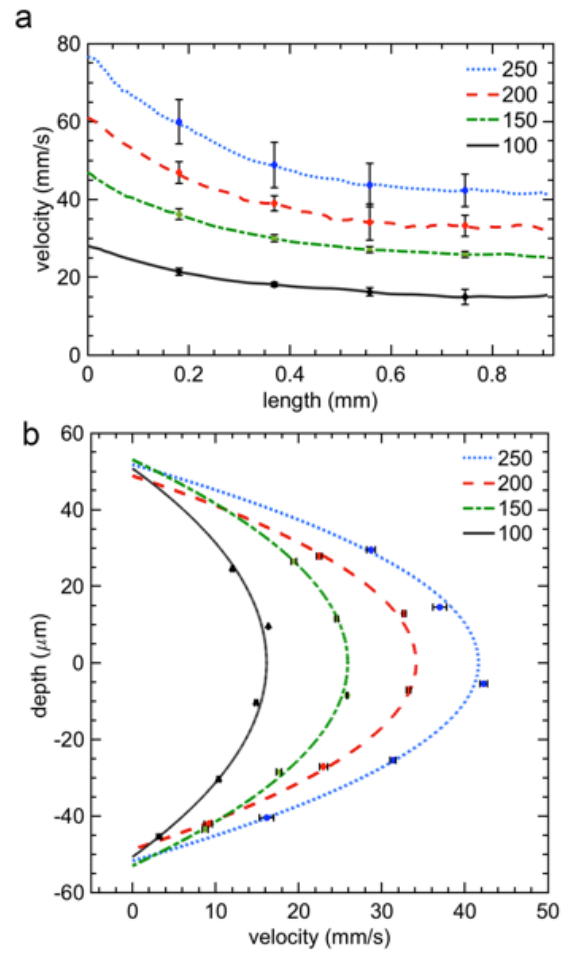


Figure 4.3 Laminar flow characterization plots from micro-PIV. a) Velocity magnitudes were experimentally determined by micro-PIV at four different flow rates (100 – 250 $\mu\text{L}/\text{min}$) and plotted as a function of channel length along the centreline ($y = 0$) for central plane ($z = 0$). Lines and data points both represent discrete data points, with standard deviations shown over $1/5^{\text{th}}$, $2/5^{\text{th}}$, $3/5^{\text{th}}$, and $4/5^{\text{th}}$ of the channel length. Flow profile appears to develop by approximately 0.5 mm along the channel length evaluated. Figure annotations show the flow rate in $\mu\text{L}/\text{min}$. b) Plot of velocity profile along the depth of the device. Velocity vectors were recorded at 4 different flow rates along 5 different depths. Plot represents the velocity profile at one x-y position within the flow chamber. Data points indicate discrete velocity measurements, while lines indicate second-order polynomial curve fits to the data. Error bars are standard error of the mean velocity magnitude. Direction of flow from left to right. Data are representative of one device, with one 40 ms recording (99 vector fields each) taken at each of four different flow rates.

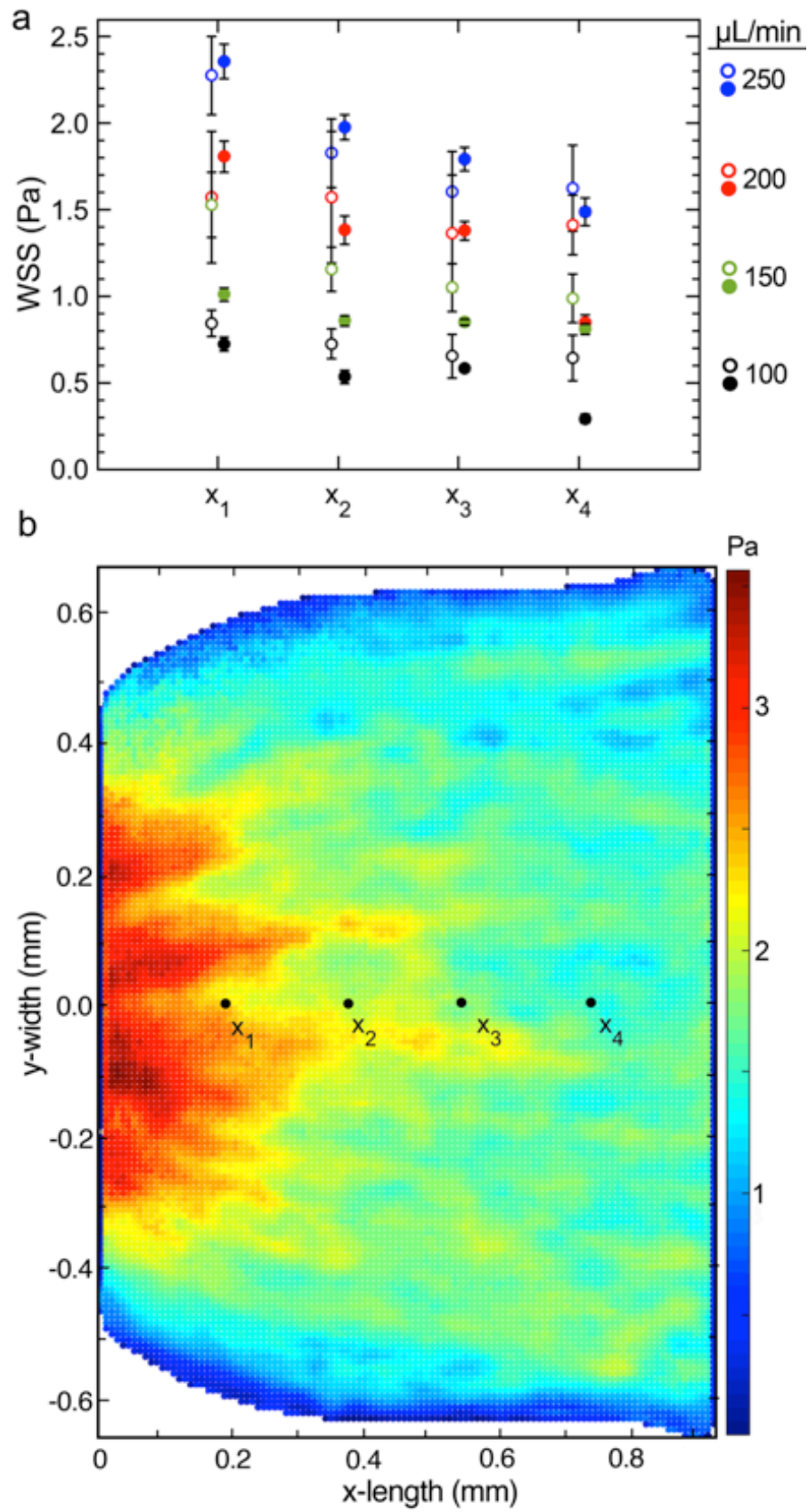


Figure 4.4 Wall shear stress resulting from laminar flow in the microfluidic device. a) Comparison of two methods of calculating wall shear stress magnitude. Mean velocity maps were derived for 5 planes for each flow rate. WSS was then calculated using two different methods at the locations indicated in the bottom panel. Open data points indicate TAWSS \pm 95% confidence interval calculated by the τ_{fit} method, which uses the curve fit in the velocity profile to estimate shear stress at the wall. Filled data points indicate TAWSS \pm SEM calculated by the $\tau_{\Delta z}$ method, which uses velocities at the closest recorded channel depth to estimate shear stress ($n = 99$ time points). b) Colour-encoded 2D map of τ_{mean} . TAWSS based on $\tau_{\Delta z}$ method for 250 $\mu\text{L}/\text{min}$ flow rate. Points along the channel indicate the same x-y positions used in (a). Data are representative of one device, with one recording of 99 vector fields at each of the four flow rates.

velocity vectors from different time points are overlaid on their respective x-y coordinates to generate a cumulative representation of the velocity flow fields.

To evaluate disturbed flow patterns in our device, flow was monitored at the Δz height and used to determine the wall shear stress. Magnitude of the average wall shear stress vector, with quiver plots overlaid, is shown (Fig. 4.8a). At flow rates of 4 mL/min per side-inlet, average wall shear magnitudes of 0-8 Pa TAWSS (Fig. 4.8b) were observed (depending on position within the channel). Shear directions were highly variable as intended by the design, and dependent upon the x-y position within the device. To estimate the directional changes, OSI maps were then generated (Fig. 4.8c). The centre of the channel exhibited the highest proportion of flow reversal (high OSI). Quiver plots revealed that flow varied over the region of observation, from side to side oscillations, to wholly multidirectional flows. OSI was not fully descriptive of variability in directionality when compared with quiver plots, as it does not discern well between bi-directional and multi-directional flow. Next, TLWSS, a customized form of a common metric (i.e. transverse WSS) was used to determine the mean wall shear occurring orthogonal to the mean shear direction over time during laminar flow (Fig. 4.8d). Again this indicated transverse components of wall shear stress, but as is revealed by the overlaid quiver plots, this metric does not fully distinguish different forms of disturbed flow, as previously discussed in large artery models (DiCarlo et al., 2019). Shear components observed transverse to the mean direction of laminar flow were maximal along the centreline of the device, and range from approximately 2 – 4 Pa, in the central region away from the walls and jets (maximum values lie in the jets, however we do not consider these areas during cell studies and therefore are not relevant).

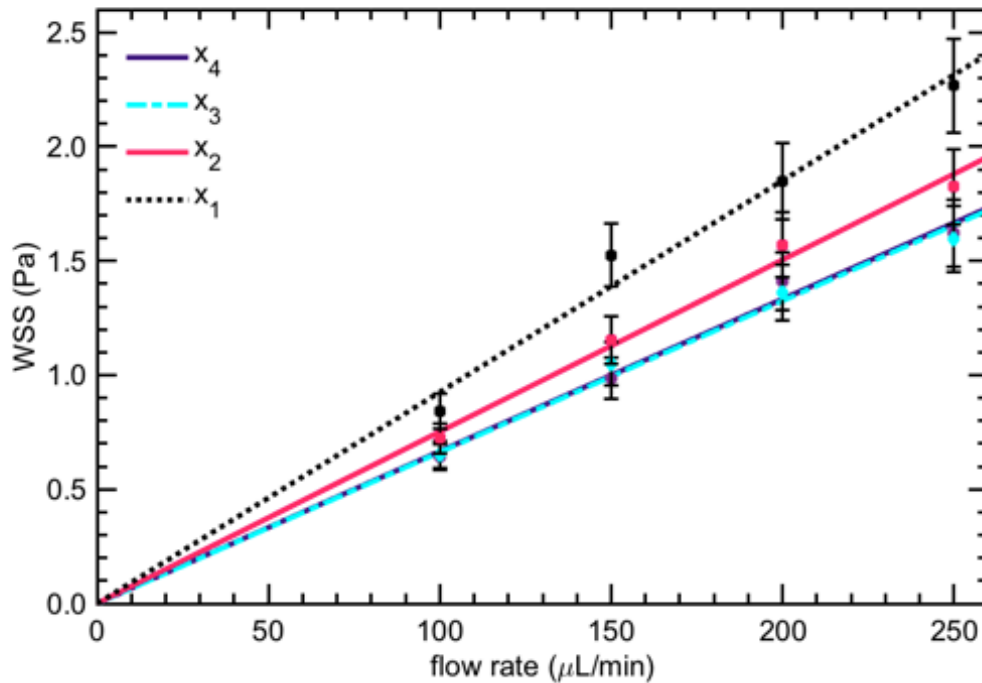


Figure 4.5 Wall shear stress as a function of flow rate over a range of channel positions. Using micro-PIV experimentally derived velocity vectors, WSS was estimated at 4 channel positions with the τ_{fit} method at four input flow rates ranging from 100 – 250 $\mu\text{L}/\text{min}$. Data points represent discrete WSS estimates, while lines indicate linear fits to the data. Data are representative of one device, with one 40 ms recording of 99 vector fields, repeated for each of the four flow rates. Convergence of the values with increasing length along the channel is consistent with development of the flow along the channel as walls become parallel.

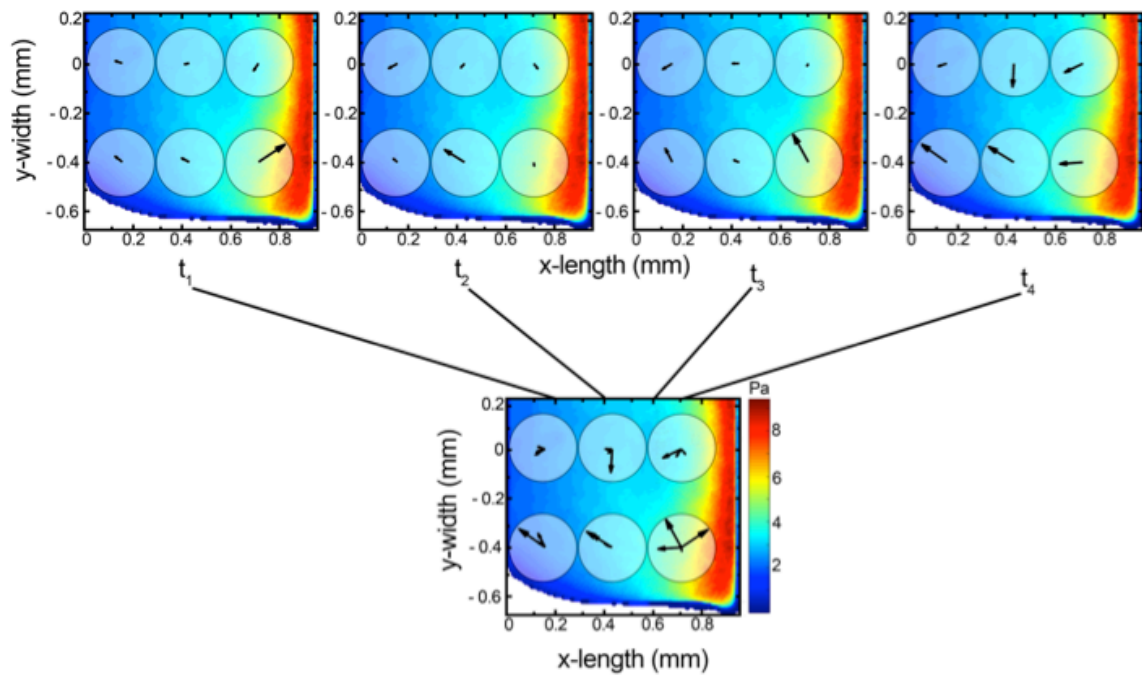


Figure 4.6 WSS vector maps were combined to generate x-y positional quiver plots. Demonstration of the method for constructing vector quiver plots, where vectors indicating direction over an ensemble of time points are superimposed at selected sites onto a 2D color-encoded parametric map of TAWSS. Here, a cropped view of the channel resulting from 4 mL/min side inlet flow rates was recorded for the central plane of the device. Four time-points taken 15 frames (5 ms) apart are shown from left to right along the top of the figure. Quiver plots represent the magnitude (arrow length) and direction of velocity vectors at 6 positions in the channel. Quiver plots at the different time-points are combined into one image to show the variation in velocity vectors over the length of the experiment. The full radius of the circular compass containing the vector direction arrows is equivalent to ~ 6 Pa.

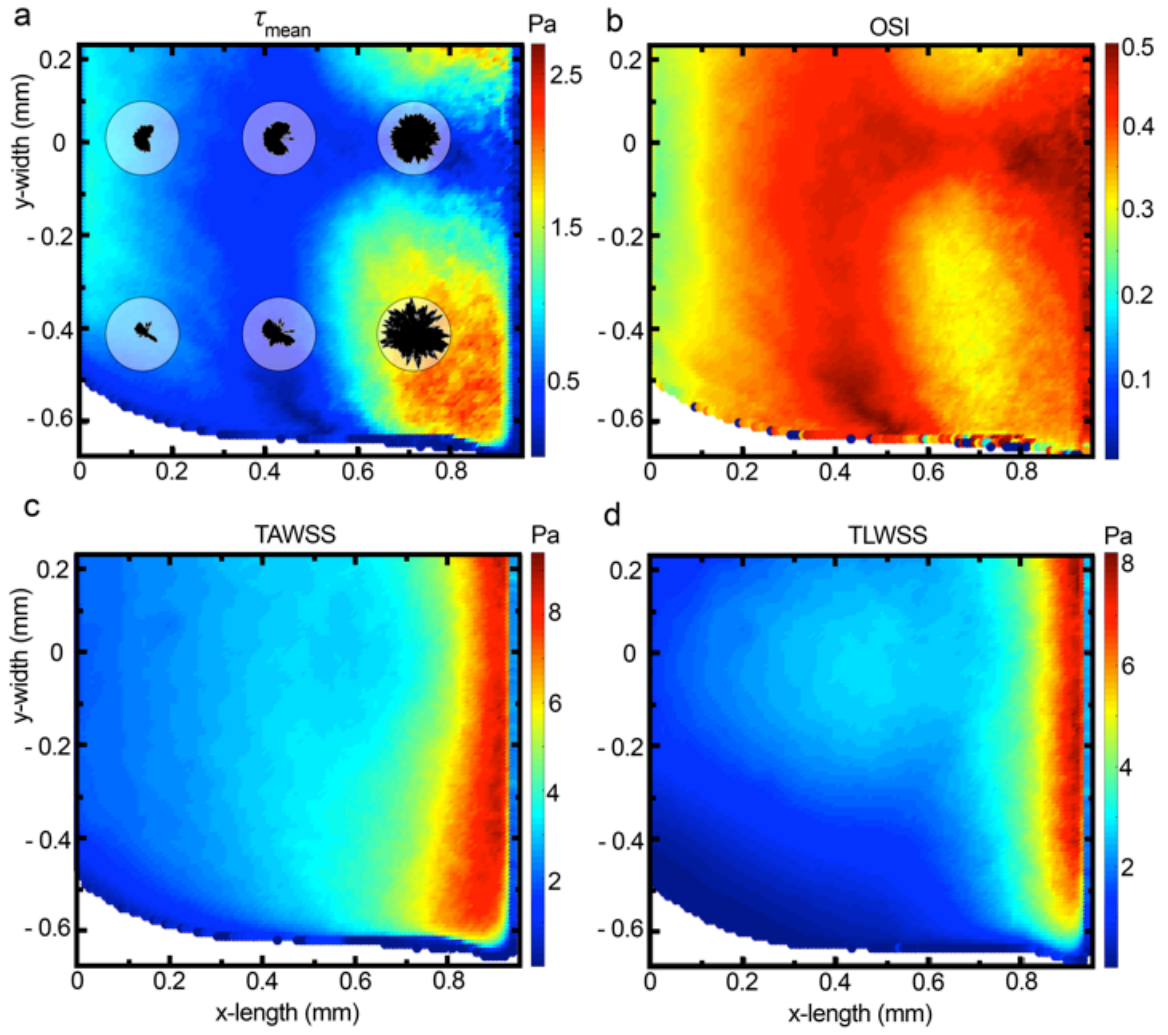


Figure 4.7 2D colour-encoded maps of wall shear stress metrics derived from micro-PIV during disturbed flow in the microfluidic device. Velocities resulting from 4 mL/min per side inlet were recorded for a plane approximately 11 μm above the channel floor. The quality of particle images was compromised in the upper region, so the field of view has been truncated to approximately 60% of the total imaging area. a) Map of magnitude of the mean vector, $|\tau_{\text{mean}}|$, with direction quiver plots overlaid, where compass radii is equal to ~ 10 Pa. Vector quiver plot reveals a high degree of multi-directional flow, dependent upon position within the channel, ranging from bi-directional fluctuations to nearly uniform directional changes. b) Map of OSI demonstrating the component of reversed flow, where 0.5 indicates that 50% of flow is in the reverse direction, with the highest reverse flow observed along the channel centreline. c) Map of TAWSS demonstrating the mean WSS magnitude over time. Wall shear stresses observed range from about 2 – 4 Pa for central region away from the vertical walls and the jets. d) Map of TLWSS demonstrating the shear components transverse to the site-specific axis of laminar flow applied during cell incubation. Representative of 19 recordings of 99 vector fields each ($n = 1881$) in one device, spanning ~ 10 min. For visual clarity, vector arrows above one standard deviation of the mean shear vector were filtered from the display.

The repeatability of the metrics evaluated both within a device (intradvice variability), and between two different devices (interdevice variability) was then evaluated. Across 5 trials in two devices, flow was monitored at the centreline ($y = 0$) over 61 recordings each (6039 vector fields). For each trial, the above metrics were calculated to describe the flow in 3 positions in our channel and compared across trials and devices. Again, we determined the variability of the time-average of the vector magnitude (Fig. 4.9a), and the OSI (Fig. 4.9b), and finally the TLWSS (4.9c). Comparing these plots, it is clear that we consistently have generated time-dependent, multi-directional disturbed flow using 4 mL/min per side inlet.

4.4.2 Imaging $[Ca^{2+}]_i$ during disturbed flow

With an understanding of the disturbed flow profiles within our channels, the $[Ca^{2+}]_i$ responses of VEC cells within our channels was evaluated in response to laminar and disturbed flow. This was intended to determine the feasibility of biological experiments within the device. First, HAEC were seeded inside the channels, loaded with calcium-sensitive fluorescent dye fura-2, and imaged (Fig. 4.10). A field of cells was selected near (above) the impinging jets, and exposed to increasing elevations of shear stress. Flow was applied through the side inlets. As flow rate was increased, flow transitioned from laminar to disturbed flow. Cellular changes in $[Ca^{2+}]_i$ were observed. Laminar flow yielded a sharp calcium transient for approximately a minute and a half. Disturbed flow was then applied, yielding a more sustained calcium response, lasting approximately twice as long. Next, HUVECs were tested using a similar protocol. HUVECs were again seeded into the device and loaded with fura-2. Cells were then imaged on the microscope

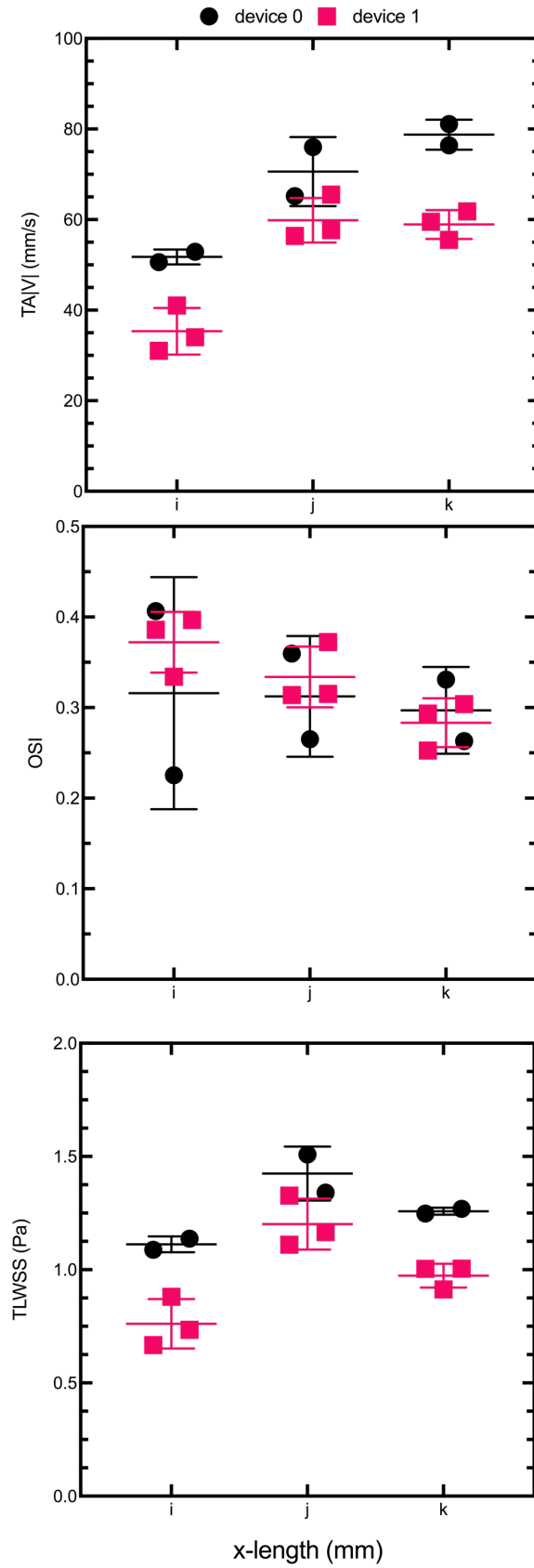


Figure 4.8 Repeatability of disturbed flow metrics determined by micro-PIV.

Results for the central plane disturbed flow at 4mL/min from 5 trials in 2 devices were plotted and compared as a function of three x-y positions approximately along the channel centre-line ($y = 0$). a) The time-average of the mean velocity magnitude b) The OSI, representing the fraction of WSS in the reverse direction, relative to mean WSS direction. c) The TLWSS, representing the wall shear component transverse to the local directional axis of laminar flow. Plots show the mean \pm SD of values in each device at each location. Representative of five independent trials, from two separate devices (black circles, red squares), with 61 recordings of 99 (6039) vector fields for each data point. The ability to generate multi-directional disturbed flow is consistent between trials and devices, although magnitudes appear to vary, indicating a systematic bias between devices. Differences likely result from variability in position of device in the field of view, as well as selection of the z-plane in the device. Small differences due to variability in the device fabrication could also contribute. Excellent intradevice repeatability, and good interdevice variability were observed.

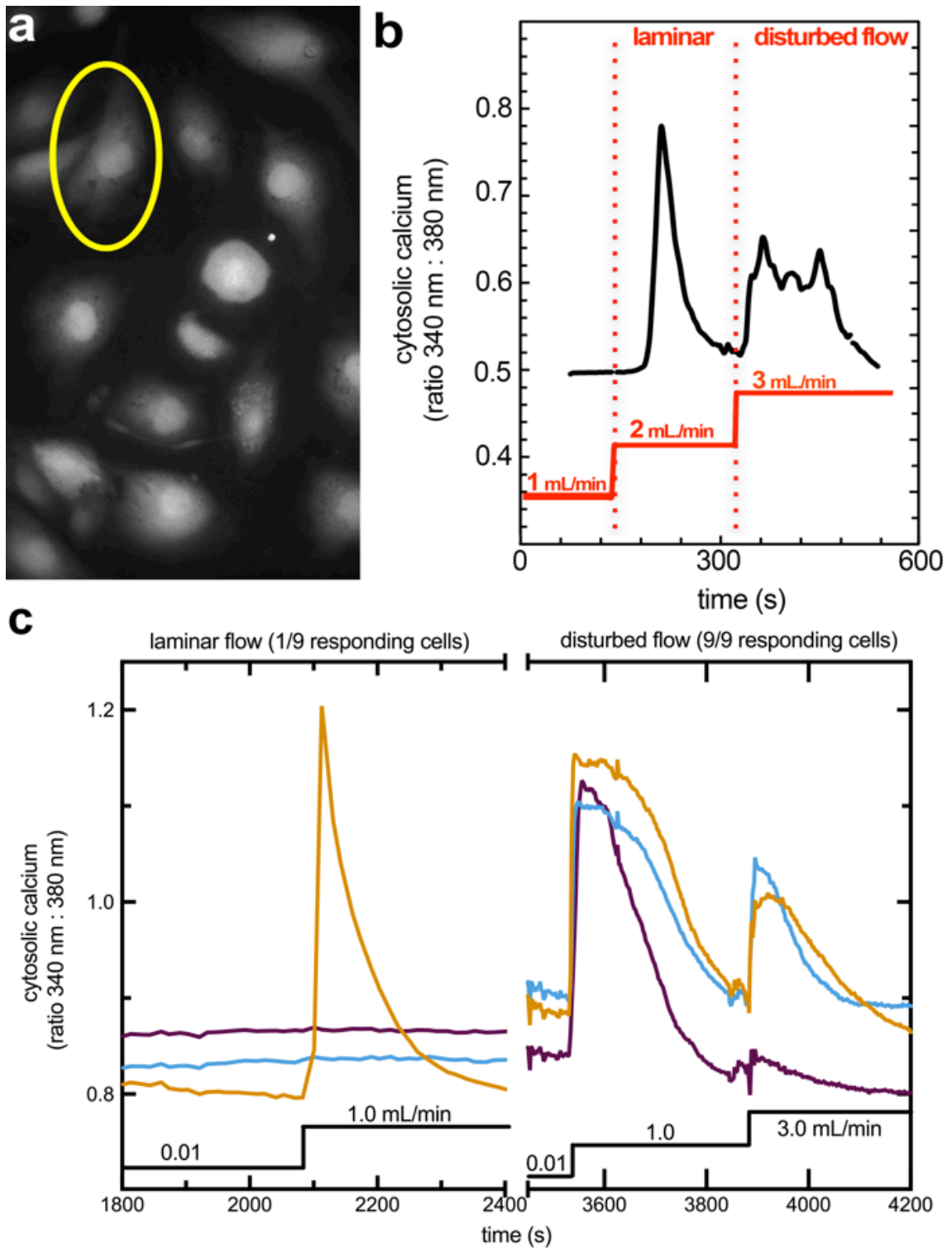


Figure 4.9 $[Ca^{2+}]_i$ imaging in VECs during disturbed flow. a) Representative field of fura-2-loaded cells imaged with an excitation wavelength of 345 nm. HAECs were seeded within the microfluidic device and allowed to adhere. Following 48h of incubation and laminar flow (10 μ L/h), cells were loaded with the calcium-sensitive fluorescent dye fura-2 and imaged on an inverted microscope. Polarization of the cells along the axis of laminar flow was not observed at a flow rate of 10 μ L/h. b) Monitoring of $[Ca^{2+}]_i$ in response to flow stimuli. $[Ca^{2+}]_i$ is represented as the ratio of fluorescence intensity at 345 : 380 nm. Background flow rate of 1 mL/min was applied through both the side inlets. When flow was increased to 2 mL/min, a sharp $[Ca^{2+}]_i$ transient was observed. When flow rate was further increased to 3 mL/min, creating disturbed flow, a muted but temporally sustained $[Ca^{2+}]_i$ transient was observed. c) Using the same protocol as b, HUVECs were loaded with fura-2 and imaged. $[Ca^{2+}]_i$ was monitored over time in response to flow stimuli. Background flow rate of 0.01 mL/min was applied through the top (laminar) inlet. Laminar flow was increased to 1 mL/min, and a sharp $[Ca^{2+}]_i$ transient was observed in 1/9 cells. After a ~15 min recovery period, flow was pumped through side inlets at 1 mL/min, applying flow transverse to the axis of laminar flow, and a sustained $[Ca^{2+}]_i$ transient was observed. This 1 mL/min flow rate from the side inlets would not develop disturbed flow, as determined in experiments not shown. When side inlet flow was increased to 3 mL/min to generate disturbed flow, a muted but temporally sustained $[Ca^{2+}]_i$ transient was observed in 9/9 cells. The different lines on the plot are 3 individual cell $[Ca^{2+}]_i$ ratio measurements. Data are representative of 10 cells total, from two independent experiments in two different cell types.

to observe changes in $[Ca^{2+}]_i$ in response to laminar and disturbed flow (Fig. 4.10c). Cells were initially exposed to background flow (0.01 mL/min) from the larger laminar flow inlet. The flow rate was then increased to 1 mL/min to expose cells to laminar WSS, and a sharp calcium transient was observed in 1 of 9 cells monitored. The cells were then allowed a period of approximately 15 minutes to recover at a flow rate of 0.01 mL/min. At this point, background flow from the top inlet was paused. Flow at the side inlets was then applied at 1 mL/min, inducing flow transverse to the axis of laminar flow. Again a transient increase in $[Ca^{2+}]_i$ was observed, this time in all 9 of 9 cells monitored. The flow rate was increased to 3 mL/min from the side inlets, again stimulating all 9 cells.

4.5 Discussion & conclusions

We have successfully developed a method for applying disturbed flows to live-cells during real-time monitoring. The technique is compatible with fluorescence microscopy techniques, including micro-PIV and calcium ratio imaging. The shear vectors during both laminar and disturbed flow were determined experimentally with micro-PIV and were found to be repeatable and within the range set out to be achieved. Human VECs were found to be viable in our device, displaying variable responses dependent on the flow regimen. The device was designed and built using an established technique that is straightforward and accessible with minimal investment. The device design was adapted from a micromixer previously published in the literature (Liu et al., 2009), and modified to suit our purposes. We added an additional inlet to enable laminar flow in the cell-imaging region of the device, allowing the establishment of cellular alignment and normal VEC morphology. Our device was fabricated from PDMS, which enables ease of

biocompatibility with live-cells, allowing for cell adhesion (with fibronectin pre-treatment), while maintaining optical clarity for compatibility with established imaging techniques. PDMS microfluidic devices have the additional benefit that once a mold is constructed, several devices can be rapidly produced, enabling ease of device manufacturing for experimentation. PDMS microchannels may expand their dimensions under flow, depending on conditions and thus create uncertainty in the device dimensions, leading to erroneous wall shear stress calculations. However, the channel dimensions were determined experimentally using fits to the velocity profile in the height dimension of our cell, under similar flow conditions used during cell experimentation. This alleviates this potential confounding factor and gives us confidence that the shear stress vectors predicted during calibration should be comparable to the conditions experienced by the cells.

During laminar flow, two different methods of estimating wall shear from observed velocity vectors were investigated. These two methods were found to differ by up to ~ 0.3 Pa. Method 1 involved taking the slope at the wall of the curve fit, while method 2 involved estimating the magnitude by taking the slope at Δz . Therefore, as we could not use Method 1 during disturbed flow (as we cannot generate a coherent z-profile due to the time-dependent asynchronicity of disturbed flow), our shear stress magnitudes could potentially deviate from those expected by up to the same amount. We do not believe this to be a major consideration as we are mostly concerned with the direction and directional changes of the shear vectors, which are still assessed accurately by our method.

Shear stress vectors were compared over several independent trials, including complete disassembly and reassembly. Excellent intradevice variability and good interdevice

variability was observed for all the parameters measured. Highly multidirectional flow was generated in all cases as observed by quiver plots, and supported by OSI no less than 0.2 for every trial (though commonly much higher). Shear stress cannot be monitored by micro-PIV during cell experimentation, but the ability to calibrate several devices yields predictable shear stresses during cellular experiments. Shear stress vectors determined have a degree of uncertainty to their magnitude. It was found that the TLWSS range observed (52%, 30%, 32% at positions i,j,k – see Fig. 4.9) during disturbed flow was acceptable for the objectives of the present study and future directions. A key factor to note, is that while this range may impede the power of our ability to compare shear stress magnitudes within the range observed, we still maintain the capability to apply predictable magnitudes of wall shear, comparable to those applied during laminar flow. Additionally, shear stress directions were highly repeatable, given a sufficient time scale (~5 min) similar to those used within cell studies. This time scale was found to be suitable in comparison to the time-scale of cell experimentation. Although instantaneous shear vectors cannot be predicted, this is a necessary by-product of our goal to generate disturbed flow within our device. In fact, the unpredictable nature of the instantaneous flow is evidence of the successful generation of the disturbed flow paradigm.

The minimum wall shear that can be applied is determined by the ability of the pump to deliver low flow rates. Similarly, the maximal wall shear generated within the channels at laminar flow is determined by the maximal flow rate provided by the pump, and also by the pressure of the system. As flow rate is increased, pressure also increases within the device, and beyond a certain point either the pump will stall due to back-pressure, or the device will fail due to rupturing of the PDMS or inlet seals.

The endothelial cells lining human vasculature are key to vascular health and disease (McCarron et al., 2019; Rajendran et al., 2013). The vasculature is known to be mechanically sensitive and VECs are thought to be the mechanosensors (Liu et al., 2013; Zaragoza et al., 2012). Fluid shear stress arising from blood flow is a key regulator of VEC outcomes (Chistiakov et al., 2017). Aside from fluid shear, blood triggers vascular EC responses in a variety of other ways, including but not limited to pressurization of the vessels causing mechanical stretch of the vessel wall (Anwar et al., 2012; Liu et al., 2013); delivering growth factors, nutrients and other soluble factors to the ECs (Godoy et al., 2013; Harjes et al., 2012); and interactions of circulating blood cells and their products with ECs (Colin et al., 2014; Said et al., 2017; Schmidt et al., 2013; Voisin and Nourshargh, 2013). Notwithstanding these other important players, it has been established that shear stress due to blood flow is critical for the initiation and progression of atherosclerosis (Gimbrone and Garcia-Cardena, 2013; Heo et al., 2014; Le et al., 2017) and other vascular diseases including hypertension (Goto et al., 2018), thrombosis (Ascutto et al., 2017), and aneurysms (Geers et al., 2017).

Endothelial dysfunction has been identified as a key mediator of many disease states, including and extending beyond that just of the vasculature (Castellon and Bogdanova, 2016; Coco et al., 2019; Echeverria et al., 2019; Konukoglu and Uzun, 2017; Losinska et al., 2019; Premer et al., 2019; Randi, 2016; Viridis et al., 2019). It has also been found that endothelial dysfunction itself is significantly mediated by fluid shear stress due to blood flow (Gimbrone et al., 2000). Interestingly, it is not just the magnitude, but the directions and time-dependent nature of fluid shear stress vectors that contribute to endothelial dysfunction (Lee et al., 2015). Fluid dynamics are often disturbed *in vivo*,

leading to endothelial dysfunction and disease (Heo et al., 2016; Heo et al., 2011). This sensitivity of VECs to variable flow direction, while critical, is not fully understood. It has been suggested that VECs respond to atheroprone flow with calcium-dependent mechanisms (Green et al., 2018). Indeed, it appears that cells are able to align to the axis of flow, and initiate distinct patterns of Ca^{2+} signaling when exposed to flow orthogonal to that alignment (Lafaurie-Janvore et al., 2016). Further studies have been performed in an attempt to elucidate mechanisms by which Ca^{2+} signaling may be altered in response to disturbed flow (Melchior and Frangos, 2010; Melchior and Frangos, 2012). Generally, our goal was to facilitate the further study of vascular ECs exposed to more pathologically relevant forms of disturbed flow. Vascular ECs tended to have more sustained $[\text{Ca}^{2+}]_i$ elevations in response to disturbed flow. As well, cells appeared less sensitive to laminar flow than to disturbed flow. However, these results must be confirmed with additional experiments. It is plausible that modified $[\text{Ca}^{2+}]_i$ dynamics could have consequences for VEC-mediated diseases associated with disturbed flow.

In conclusion, we have developed and validated a microfluidic system for applying disturbed flow to live-cells during real-time microscopy. The device has been shown to be compatible with real-time monitoring of $[\text{Ca}^{2+}]_i$ in cells exposed to laminar and disturbed flow paradigms. This device will facilitate studies into the early responses of VECs to disturbed flow.

4.6 References

- Ando J, Yamamoto K. 2009. Vascular mechanobiology: endothelial cell responses to fluid shear stress. *Circulation journal : official journal of the Japanese Circulation Society* 73(11):1983-1992.
- Ando J, Yamamoto K. 2013. Flow detection and calcium signaling in vascular endothelial cells. *Cardiovascular research* 99(2):260-268.
- Anwar MA, Shalhoub J, Lim CS, Gohel MS, Davies AH. 2012. The effect of pressure-induced mechanical stretch on vascular wall differential gene expression. *Journal of vascular research* 49(6):463-478.
- Ascutto R, Ross-Ascutto N, Guillot M, Celestin C. 2017. Computational fluid dynamics characterization of pulsatile flow in central and Sano shunts connected to the pulmonary arteries: importance of graft angulation on shear stress-induced, platelet-mediated thrombosis. *Interactive cardiovascular and thoracic surgery* 25(3):414-421.
- Baeyens N. 2018. Fluid shear stress sensing in vascular homeostasis and remodeling: Towards the development of innovative pharmacological approaches to treat vascular dysfunction. *Biochemical pharmacology* 158:185-191.
- Baeyens N, Bandyopadhyay C, Coon BG, Yun S, Schwartz MA. 2016. Endothelial fluid shear stress sensing in vascular health and disease. *The Journal of clinical investigation* 126(3):821-828.
- Berk BC. 2008. Atheroprotective signaling mechanisms activated by steady laminar flow in endothelial cells. *Circulation* 117(8):1082-1089.
- Castellon X, Bogdanova V. 2016. Chronic Inflammatory Diseases and Endothelial Dysfunction. *Aging and disease* 7(1):81-89.
- Chen H, Cornwell J, Zhang H, Lim T, Resurreccion R, Port T, Rosengarten G, Nordon RE. 2013. Cardiac-like flow generator for long-term imaging of endothelial cell responses to circulatory pulsatile flow at microscale. *Lab on a chip* 13(15):2999-3007.
- Chistiakov DA, Orekhov AN, Bobryshev YV. 2017. Effects of shear stress on endothelial cells: go with the flow. *Acta physiologica (Oxford, England)* 219(2):382-408.
- Coco C, Sgarra L, Potenza MA, Nacci C, Pasculli B, Barbano R, Parrella P, Montagnani M. 2019. Can Epigenetics of Endothelial Dysfunction Represent the Key to Precision Medicine in Type 2 Diabetes Mellitus? *International journal of molecular sciences* 20(12).

- Colin Y, Le Van Kim C, El Nemer W. 2014. Red cell adhesion in human diseases. *Current opinion in hematology* 21(3):186-192.
- Davies PF. 1995. Flow-mediated endothelial mechanotransduction. *Physiological reviews* 75(3):519-560.
- DiCarlo AL, Holdsworth DW, Poepping TL. 2019. Study of the effect of stenosis severity and non-Newtonian viscosity on multidirectional wall shear stress and flow disturbances in the carotid artery using particle image velocimetry. *Medical engineering & physics* 65:8-23.
- Echeverria C, Eltit F, Santibanez JF, Gatica S, Cabello-Verrugio C, Simon F. 2019. Endothelial dysfunction in pregnancy metabolic disorders. *Biochimica et biophysica acta Molecular basis of disease*.
- Fiddes LK, Raz N, Srigunapalan S, Tumarkan E, Simmons CA, Wheeler AR, Kumacheva E. 2010. A circular cross-section PDMS microfluidics system for replication of cardiovascular flow conditions. *Biomaterials* 31(13):3459-3464.
- Geers AJ, Morales HG, Larrabide I, Butakoff C, Bijlenga P, Frangi AF. 2017. Wall shear stress at the initiation site of cerebral aneurysms. *Biomechanics and modeling in mechanobiology* 16(1):97-115.
- Gimbrone MA, Jr. 1999. Endothelial dysfunction, hemodynamic forces, and atherosclerosis. *Thrombosis and haemostasis* 82(2):722-726.
- Gimbrone MA, Jr., Garcia-Cardena G. 2013. Vascular endothelium, hemodynamics, and the pathobiology of atherosclerosis. *Cardiovascular pathology : the official journal of the Society for Cardiovascular Pathology* 22(1):9-15.
- Gimbrone MA, Jr., Topper JN, Nagel T, Anderson KR, Garcia-Cardena G. 2000. Endothelial dysfunction, hemodynamic forces, and atherogenesis. *Annals of the New York Academy of Sciences* 902:230-239; discussion 239-240.
- Godoy AS, Chung I, Montecinos VP, Buttyan R, Johnson CS, Smith GJ. 2013. Role of androgen and vitamin D receptors in endothelial cells from benign and malignant human prostate. *American journal of physiology Endocrinology and metabolism* 304(11):E1131-1139.
- Goto K, Ohtsubo T, Kitazono T. 2018. Endothelium-Dependent Hyperpolarization (EDH) in Hypertension: The Role of Endothelial Ion Channels. *International journal of molecular sciences* 19(1).
- Grassi D, Desideri G, Ferri C. 2011. Cardiovascular risk and endothelial dysfunction: the preferential route for atherosclerosis. *Current pharmaceutical biotechnology* 12(9):1343-1353.

- Green JP, Souilhol C, Xanthis I, Martinez-Campesino L, Bowden NP, Evans PC, Wilson HL. 2018. Atheroprone flow activates inflammation via endothelial ATP-dependent P2X7-p38 signalling. *Cardiovascular research* 114(2):324-335.
- Harjes U, Bensaad K, Harris AL. 2012. Endothelial cell metabolism and implications for cancer therapy. *British journal of cancer* 107(8):1207-1212.
- Heckel E, Boselli F, Roth S, Krudewig A, Belting HG, Charvin G, Vermot J. 2015. Oscillatory Flow Modulates Mechanosensitive *klf2a* Expression through *trpv4* and *trpp2* during Heart Valve Development. *Curr Biol* 25(10):1354-1361.
- Heo KS, Berk BC, Abe J. 2016. Disturbed Flow-Induced Endothelial Proatherogenic Signaling Via Regulating Post-Translational Modifications and Epigenetic Events. *Antioxidants & redox signaling* 25(7):435-450.
- Heo KS, Fujiwara K, Abe J. 2011. Disturbed-flow-mediated vascular reactive oxygen species induce endothelial dysfunction. *Circulation journal : official journal of the Japanese Circulation Society* 75(12):2722-2730.
- Heo KS, Fujiwara K, Abe J. 2014. Shear stress and atherosclerosis. *Molecules and cells* 37(6):435-440.
- Herrington W, Lacey B, Sherliker P, Armitage J, Lewington S. 2016. Epidemiology of Atherosclerosis and the Potential to Reduce the Global Burden of Atherothrombotic Disease. *Circulation research* 118(4):535-546.
- Kathuria SV, Chan A, Graceffa R, Paul Nobrega R, Robert Matthews C, Irving TC, Perot B, Bilsel O. 2013. Advances in turbulent mixing techniques to study microsecond protein folding reactions. *Biopolymers* 99(11):888-896.
- Konukoglu D, Uzun H. 2017. Endothelial Dysfunction and Hypertension. *Advances in experimental medicine and biology* 956:511-540.
- Ku DN, Giddens DP, Zarins CK, Glagov S. 1985. Pulsatile flow and atherosclerosis in the human carotid bifurcation. Positive correlation between plaque location and low oscillating shear stress. *Arteriosclerosis (Dallas, Tex)* 5(3):293-302.
- Kutikhin AG, Sinitsky MY, Yuzhalin AE, Velikanova EA. 2018. Whole-Transcriptome Sequencing: a Powerful Tool for Vascular Tissue Engineering and Endothelial Mechanobiology. *High-throughput* 7(1).
- Lafaurie-Janvore J, Antoine EE, Perkins SJ, Babataheri A, Barakat AI. 2016. A simple microfluidic device to study cell-scale endothelial mechanotransduction. *Biomedical microdevices* 18(4):63.
- Le NT, Sandhu UG, Quintana-Quezada RA, Hoang NM, Fujiwara K, Abe JI. 2017. Flow signaling and atherosclerosis. *Cellular and molecular life sciences : CMLS* 74(10):1835-1858.

- Lee J, Packard RR, Hsiai TK. 2015. Blood flow modulation of vascular dynamics. *Current opinion in lipidology* 26(5):376-383.
- Liu HB, Zhang J, Xin SY, Liu C, Wang CY, Zhao D, Zhang ZR. 2013. Mechanosensitive properties in endothelium and their roles in regulation of endothelial function. *Journal of cardiovascular pharmacology* 61(6):461-470.
- Liu Y, Olsen MG, Fox RO. 2009. Turbulence in a microscale planar confined impinging-jets reactor. *Lab on a chip* 9(8):1110-1118.
- Lorusso D, Nikolov HN, Milner JS, Ochotny NM, Sims SM, Dixon SJ, Holdsworth DW. 2016. Practical fabrication of microfluidic platforms for live-cell microscopy. *Biomedical microdevices* 18(5):78.
- Losinska K, Korkosz M, Kwasny-Krochin B. 2019. Endothelial dysfunction in patients with ankylosing spondylitis. *Reumatologia* 57(2):100-105.
- McCarron JG, Wilson C, Heathcote HR, Zhang X, Buckley C, Lee MD. 2019. Heterogeneity and emergent behaviour in the vascular endothelium. *Current opinion in pharmacology* 45:23-32.
- Melchior B, Frangos JA. 2010. Shear-induced endothelial cell-cell junction inclination. *American journal of physiology Cell physiology* 299(3):C621-629.
- Melchior B, Frangos JA. 2012. Galphaq/11-mediated intracellular calcium responses to retrograde flow in endothelial cells. *American journal of physiology Cell physiology* 303(4):C467-473.
- Nakajima H, Mochizuki N. 2017. Flow pattern-dependent endothelial cell responses through transcriptional regulation. *Cell cycle (Georgetown, Tex)* 16(20):1893-1901.
- Premer C, Kanelidis AJ, Hare JM, Schulman IH. 2019. Rethinking Endothelial Dysfunction as a Crucial Target in Fighting Heart Failure. *Mayo Clinic proceedings Innovations, quality & outcomes* 3(1):1-13.
- Rajendran P, Rengarajan T, Thangavel J, Nishigaki Y, Sakthisekaran D, Sethi G, Nishigaki I. 2013. The vascular endothelium and human diseases. *International journal of biological sciences* 9(10):1057-1069.
- Randi AM. 2016. Endothelial dysfunction in von Willebrand disease: angiogenesis and angiodyplasia. *Thrombosis research* 141 Suppl 2:S55-58.
- Said AS, Rogers SC, Doctor A. 2017. Physiologic Impact of Circulating RBC Microparticles upon Blood-Vascular Interactions. *Frontiers in physiology* 8:1120.
- Schmidt S, Moser M, Sperandio M. 2013. The molecular basis of leukocyte recruitment and its deficiencies. *Molecular immunology* 55(1):49-58.

- Shemesh J, Jalilian I, Shi A, Heng Yeoh G, Knothe Tate ML, Ebrahimi Warkiani M. 2015. Flow-induced stress on adherent cells in microfluidic devices. *Lab on a chip* 15(21):4114-4127.
- Sia SK, Whitesides GM. 2003. Microfluidic devices fabricated in poly(dimethylsiloxane) for biological studies. *Electrophoresis* 24(21):3563-3576.
- Uzarski JS, Scott EW, McFetridge PS. 2013. Adaptation of endothelial cells to physiologically-modeled, variable shear stress. *PLoS One* 8(2):e57004.
- van der Meer AD, Poot AA, Feijen J, Vermes I. 2010. Analyzing shear stress-induced alignment of actin filaments in endothelial cells with a microfluidic assay. *Biomicrofluidics* 4(1):11103.
- Virdis A, Masi S, Colucci R, Chiriaco M, Uliana M, Puxeddu I, Bernardini N, Blandizzi C, Taddei S. 2019. Microvascular Endothelial Dysfunction in Patients with Obesity. *Current hypertension reports* 21(4):32.
- Voisin MB, Nourshargh S. 2013. Neutrophil transmigration: emergence of an adhesive cascade within venular walls. *Journal of innate immunity* 5(4):336-347.
- Wang C, Baker BM, Chen CS, Schwartz MA. 2013. Endothelial cell sensing of flow direction. *Arteriosclerosis, thrombosis, and vascular biology* 33(9):2130-2136.
- Young EW, Simmons CA. 2010. Macro- and microscale fluid flow systems for endothelial cell biology. *Lab on a chip* 10(2):143-160.
- Zaragoza C, Marquez S, Saura M. 2012. Endothelial mechanosensors of shear stress as regulators of atherogenesis. *Current opinion in lipidology* 23(5):446-452.
- Zhang C, van Noort D. 2011. Cells in microfluidics. *Top Curr Chem* 304:295-321.

Chapter 5

General discussion & conclusions

5.1 Summary & future directions

Human tissues possess the ability to sense and respond to mechanical loads and forces. This ability is known as mechanotransduction, and it functions to convert mechanical stimuli to biochemical signals – the native language of the cell. Interest in the phenomenon of mechanotransduction is more than a curiosity; mechanical loading plays an essential role in the physiology and pathology of most human tissue systems. The molecular signaling pathways underlying mechanotransduction are not fully understood. One reason for this knowledge gap has been the lack of technology. The mechanical stimuli that cells respond to require specialized equipment to generate for *in vitro* studies. The mechanical signals that are especially relevant to cells *in vivo* are dynamic, time-dependent loads and forces. Additionally, the transient nature of the initial mechanotransductive biochemical signals necessitates the use of real-time monitoring for their detection. Although scientists have a plethora of tools at their disposal, existing systems do not have the ability to provide relevant mechanical stimuli while allowing observation of early responses in live cells.

In this thesis, the development and utilization of new technologies have been presented. These tools are intended to “open the door” for future investigations of the cellular mechanisms of mechanotransduction. My studies, at the interface between cell biology and engineering, addressed the following three discrete deficiencies in the field.

Objective 1 – To develop and validate a system for high-frequency vibration of live cells during real-time microscopy

There existed a deficiency in available technologies for the application of low-magnitude high-frequency vibrations to live-cells during real-time microscopy. LMHF stimuli have been shown to be relevant to human health and disease. Most studies into the effects of vibration involve the whole-body vibration of animals, and then assay the downstream biological effects. While the literature reports existing methods to vibrate cells, these methods are not compatible with simultaneous microscopic monitoring.

Therefore, in Chapter 2, we described the development of a device for the application of LMHF stimuli to live-cells during real-time microscopic monitoring. The platform has been validated at frequencies up to 500 Hz, and magnitudes of up to 1 g peak acceleration. Two methods were used to evaluate the vibrations produced by the device, and were found to agree within 10%. The device has been used in a series of experiments to demonstrate that osteoblastic cells did not respond with $[Ca^{2+}]_i$ to vibrational parameters previously identified in the literature as having biological effects on whole animal and cell culture models. It was then demonstrated that, while the cells studied did not respond to the vibrations delivered with $[Ca^{2+}]_i$, they did become desensitized to subsequent additions of exogenous ATP. With the development of this technology, researchers can begin to attempt unravelling the molecular mechanisms of cellular mechanotransduction. This work has also presented results with potential implications in the purinergic signaling pathways involved in osteoblastic mechanotransduction of LMHF vibration.

Objective 2 – To develop validate a microfluidics fabrication technique for devices compatible with live-cell microscopy

There exists a deficiency of readily-accessible techniques for the simple and affordable fabrication of microfluidic devices compatible with live-cell microscopy. Investigations utilizing microfluidics have already offered novel insights into biology, and has promising future as a platform for routine wet-lab use. However, current methods may require specialized equipment or expertise in engineering, raising the barrier to entry above that which biologists feel comfortable approaching.

Therefore, in Chapter 3 we described the development of an accessible method for the practical fabrication of microfluidic devices, geared towards non-specialists. The system is capable of accurately and precisely delivering steady-flow fluid shear to live cells during real-time microscopy. A PDMS-based replica molding fabrication technique was developed that produces leak-proof microfluidic devices. The reproducibility of this technique was then evaluated. The fabrication technique produced channel dimensions with precision in the estimated cross-sectional areas of up to 2%. The flow characteristics generated in our device were determined using both computational and experimental techniques. Wall shear stresses ranged between 1-3 Pa at the flow rates studied, and our CFD and PIV results were found to not deviate significantly from one another. Finally, the compatibility of the device with live cell cultures, and fluorescence based imaging systems, was demonstrated. The calcium responses of cells to laminar fluid flow were also demonstrated. We have improved the accessibility for biological applications of microfluidics. This has the potential to increase the breadth and impact of cell studies, in the short and long term, by enabling biologists to generate customized research tools relevant to their topic of interest.

Objective 3 – To develop and validate a system to study the real-time responses of live cells to disturbed fluid flow

There existed a deficiency in the available techniques for the application of multi-directional, disturbed fluid shear stress to live cells during real-time microscopic monitoring. Disturbed flow has long been implicated in the pathogenesis of vascular endothelial cell activation, and consequently dysfunction. This pathological state disrupts not only the vessel wall, but has also been associated with a host of systemic disease states. There exists a substantial understanding into the downstream signals and effects of endothelial dysfunction. However, the knowledge of the fast-acting, transient signals that underlie endothelial mechanobiology is comparatively meagre. A major reason for this lack of knowledge is a lack of technology to facilitate the relevant biological investigations.

Therefore, in Chapter 4 we described the development of a microfluidic device to apply disturbed flow to live cells during real-time microscopic monitoring. The device was determined to repeatably deliver time-dependent, multidirectional wall shears. The flow was found to be highly multi-directional, as demonstrated by OSI of no less than 0.2, supported by vector quiver plots to visualize flow directions. The device maintains the ability to apply laminar flows to cells as well, an important consideration for experimental control, as well as the establishment of physiological endothelial cell behavior. Microfabrication techniques established in Chapter 3 were used to achieve this goal. A series of sophisticated micro-particle imaging studies were then performed to experimentally determine fluid behaviour of disturbed flow within the device. Following this, the reproducibility of disturbed flow generation in this device was demonstrated

both within the same device, and between different devices. Flow parameters were found to have excellent agreement when evaluated within the same device, and good agreement when evaluated between different devices. We then demonstrated the compatibility of our device and the disturbed flow stimulus with live endothelial cells, and observed responses of cells to laminar and disturbed flows. With this technology, researchers can investigate the spatiotemporal dynamics of key signaling molecules such as $[Ca^{2+}]_i$ in the early steps of disturbed flow mechanotransduction.

Taken all together, this thesis describes the development a suite of tools that facilitate the investigation of signaling pathways activated during cellular mechanotransduction. These tools accurately and precisely generate specific, dynamic forms of mechanical stimuli that are relevant to human physiology and pathology. The ability to deliver mechanical loads isolated from other modes of mechanical stimuli will be key in future studies aimed at unraveling the cellular mechanisms of mechanotransduction.

5.2 General significance

Despite the fact these tools load cells with different modes of mechanical stimuli, the forces applied share many similarities. For example, they hold in common their time-dependent nature, and their potential to converge on specific aspects of the mechanotransductive machinery. Equally interesting is the potential for divergence within the mechanisms of cellular mechanotransduction. In fact, we have identified examples of such convergence and divergence. Following, is an example of divergence in mechanotransduction signaling demonstrated in this thesis.

We (and others) have shown that osteoblastic cells respond to fluid shear stress with transient elevations in $[Ca^{2+}]_i$. We have also shown, for the first time, that contrary to this, osteoblastic cells do not respond to LMHF vibrational stimuli with acute changes in $[Ca^{2+}]_i$. To the best of our knowledge, this is the first time this divergence has been demonstrated. Although it only holds over the range of vibrational parameters investigated (frequency, magnitude, loading period), and specific cell types interrogated (mouse and rat osteoblasts, rat osteoclasts), this is an important contribution to the mechanotransduction knowledge-base. This implies the potential for differential regulation of cell signaling pathways in response to different mechanical stimuli. It also raises potential questions for mechanical loading *in vivo*.

As previously discussed, loading *in vivo* is thought to influence the cell through multiple modes of mechanical stimulation simultaneously. For example, during peak systole, an endothelial cell lining an artery will experience not only fluid shear due to blood flow, but also tensile strain as the vessel expands (due to increased hydrostatic pressure), stretching the cell. Or, during locomotion, bone cells are vibrated at both low (Wang et al., 2016) and high (Beck, 2015; Nagaraja and Jo, 2014) frequencies, while simultaneously being sheared by interstitial fluid displaced during loading. So, how then does the cell respond to these differential stimuli? Our results suggest that these diverging effects of different mechanical loads on mechanotransduction can converge at different steps in the molecular machinery. Following, is a possible example of such convergence.

Although fluid shear and vibration were shown to diverge in their effects on $[Ca^{2+}]_i$ (with fluid shear stimulating elevations $[Ca^{2+}]_i$ and vibration having no apparent effect on $[Ca^{2+}]_i$), they may have had a common effect (upstream of Ca^{2+}_i) on purinergic signaling.

It has been shown in the literature that the mechanism underlying the calcium response to fluid flow is mediated by the release of ATP and subsequent activation of cell-surface P2 receptors (Genetos et al., 2005; Riddle et al., 2007; You et al., 2002). Therefore, the finding in Chapter 2 that LMHF vibration desensitized ATP-induced $[Ca^{2+}]_i$ signaling implies some commonality in the signaling mechanisms involved in the response to both forms of mechanical stimulation. Whether the desensitization we observed *in vitro* is recapitulated *in vivo* is not clear. It is conceivable that a small amount of ATP release *in vitro* was sufficient to induce desensitisation, but insufficient to trigger a global elevation in $[Ca^{2+}]_i$. On the other hand, *in vivo*, that small amount of ATP release might be sufficient to trigger a global elevation in $[Ca^{2+}]_i$ due to relatively small volume of extracellular fluid present between cells *in vivo*. This is in contrast to the relatively large volume of medium bathing the cells *in vitro*, which would rapidly dilute any released ATP to subthreshold concentrations.

5.3 Limitations of the research and suggestions for future studies

It is not clear if responses to mechanical stimuli observed separately *in vitro*, are indicative of what happens *in vivo* during simultaneous loading (e.g. vibration and fluid shear). Leading from this thought, one key feature of the vibration device from Chapter 2 is that it is compatible with microfluidic devices fabricated using the methods described in Chapter 3. In another study, we have demonstrated the feasibility of combining these two methods to simultaneously apply vibration and fluid shear stress, each of which can be independently configured and controlled (Lorusso et al., 2017). Thus, there is potential

to investigate the biological effects of combining both stimuli, and evaluating their synergy (or lack thereof).

This dual-modal approach could have implications for the conclusions made regarding the vibration device in Chapter 2. The mechanism of P2 desensitization by LMHF vibration is unclear. It appears that it is predominantly P2Y receptors experiencing desensitization during vibrational pretreatment. In other cell systems, P2Y receptors have been reported to desensitize within minutes, likely *via* MAPK-mediated phosphorylation, followed by receptor internalization (Liu et al., 2002). As mentioned above, it is possible that the vibrational stimulus causes release of ATP at concentrations sufficient to desensitize P2Y, but insufficient to induced a global Ca^{2+} response. ATP release could be mediated by an active vesicular exocytotic mechanism or by passive, membrane-damage-related leak or rupture.

A future study leading from this would be to investigate the effect of increasing the cell surface area to extracellular fluid volume ratio in the device. An established method for increasing this ratio is with microfluidics. Therefore, one could repeat these experiments in a microfluidic device with a higher surface area to volume ratio, and investigating whether the resulting increase in concentration of extracellular ATP is now enough to trigger elevation of $[\text{Ca}^{2+}]_i$ in response to vibration. This would be a challenging experiment, but technically feasible.

Another future study would be to determine if the lack of $[\text{Ca}^{2+}]_i$ transients resulting from LMHF vibration holds true for different experimental systems and conditions. For example, high frequency vibrations have been linked to endothelial dysfunction (Cho et

al., 2011). Therefore, it may be fruitful to investigate whether non-bone cells respond to LMHF vibration with elevation of $[Ca^{2+}]_i$. Aside from testing different cell types or vibrational parameters, the nature of the dish substrate could be a key variable. It has already been determined that vibration effects can be affected by extracellular adhesion (Kim et al., 2012). Thus, it could be fruitful to establish the effects of modifying the elastic modulus of the substratum (e.g. using something softer than glass, such as PDMS), the type of cell culture (e.g. 3D instead of 2D), and the biochemical properties of the substratum (protein surface coatings such as fibronectin, vitronectin, laminin, collagen, etc.).

The device described in Chapter 4 generates disturbed flow during real-time microscopy. We demonstrated that the device was compatible with live cell culture and imaging. During these experiments, we observed that cells were more likely to display temporally sustained elevations in $[Ca^{2+}]_i$ in response to disturbed flow, compared to the laminar flow. Future studies characterizing these differences may be useful in evaluating the initiation of endothelial cell pathogenesis. Prolonged $[Ca^{2+}]_i$ elevation has been shown to be aberrant signal, for example, in the cardiomyocytes of uraemic rats (McMahon et al., 2002) and in human iPSCs modelling cardiac arrhythmia (Spencer et al., 2014). Prolonged calcium transients have also been observed in endothelial cells responding to electrical fields (Takahashi et al., 2005) and experiencing diabetes-associated endothelial dysfunction (Sheikh et al., 2012). Clearly, altered calcium dynamics can be associated with disease. Recently it has been shown that spatiotemporal dynamics of Ca^{2+} transients are key to controlling endothelial physiology, and that pathological low shear flows could disrupt these dynamics, similar to what we are suggesting here (Taylor et al., 2017).

I posit that researchers interested in recreating these technologies can utilize the methods described in this thesis to identify specific mechanical loading regimens relevant to human physiology and pathology. One specific long-term goal for mechanotransduction research is understanding the mechanosensors responsible for the initial detection of a mechanical load. While many such mechanisms have been identified (Jansen et al., 2015), the cooperation of these different pathways in the orchestration of mechanotransduction is not well understood. Additionally, how signaling is modulated depending upon the time-dependent dynamics of the load is unclear. For example, the primary cilium is a physical structure and, as such, will have mechanical resonances determined by its mechanical properties. Indeed, researchers have already made attempts to evaluate these characteristics (Resnick, 2015). As the cilium is loaded mechanically, it is thought to deflect. Therefore, it is reasonable to assume that the deflections of the cilium will be a function not only of the magnitude of the load, but the frequency content as well. Specific frequencies of mechanical loading could even stimulate resonances within the ciliary structure, amplifying the deformation of the cilium.

Mechanotransduction appears to be a physiological function that is highly conserved between cell types and organisms, and thus has applications in a range of research fields. In fact, Chapter 4 is the culmination of a collaboration with physicist Dr. Tamie Poepping. Similarly, our practical fabrication technique described in Chapter 3 is currently being utilized in ongoing studies with vascular biology collaborators at Western. Additionally, it has led to a successful collaboration with physicist Dr. John de Bruyn (Liu et al., 2018). I believe that what we have learned and developed here will be

readily transferrable, fostering future scientific inquiry into mechanotransduction and other fields of research.

5.4 Concluding remarks

This thesis has described the development and implementation of a suite of platforms for the dynamic mechanostimulation of live cells during real-time microscopic monitoring. These devices can deliver precise and biologically relevant dynamic loads to cell cultures during simultaneous microscopic analysis. The vibration and fluid flow platforms provide powerful tools for future research investigating cellular mechanotransduction mechanisms. Discoveries made using these platforms may eventually contribute to the development of therapeutic medical interventions (pharmacological or non-pharmacological) for pathologies of the skeleton, vasculature, and other human tissues.

5.5 References

- Beck BR. 2015. Vibration Therapy to Prevent Bone Loss and Falls: Mechanisms and Efficacy. *Current osteoporosis reports* 13(6):381-389.
- Cho JG, Witting PK, Verma M, Wu BJ, Shanu A, Kairaitis K, Amis TC, Wheatley JR. 2011. Tissue vibration induces carotid artery endothelial dysfunction: a mechanism linking snoring and carotid atherosclerosis? *Sleep* 34(6):751-757.
- Genetos DC, Geist DJ, Liu D, Donahue HJ, Duncan RL. 2005. Fluid shear-induced ATP secretion mediates prostaglandin release in MC3T3-E1 osteoblasts. *J Bone Miner Res* 20(1):41-49.
- Jansen KA, Donato DM, Balcioglu HE, Schmidt T, Danen EHJ, Koenderink GH. 2015. A guide to mechanobiology: Where biology and physics meet. *Biochimica et Biophysica Acta (BBA) - Molecular Cell Research* 1853(11, Part B):3043-3052.
- Kim IS, Song YM, Lee B, Hwang SJ. 2012. Human mesenchymal stromal cells are mechanosensitive to vibration stimuli. *Journal of dental research* 91(12):1135-1140.
- Liu R, Gutiérrez AM, Ring A, Persson AEG. 2002. Nitric Oxide Induces Resensitization of P2Y Nucleotide Receptors in Cultured Rat Mesangial Cells. *Journal of the American Society of Nephrology* 13(2):313.
- Liu Y, Lorusso D, Holdsworth DW, Poepping TL, de Bruyn JR. 2018. Effect of confinement on the rheology of a yield-stress fluid. *Journal of Non-Newtonian Fluid Mechanics* 261:25-32.
- Lorusso D, Nikolov HN, Chmiel T, Beach RJ, Sims SM, Dixon SJ, Holdsworth DW. A device for real-time live-cell microscopy during dynamic dual-modal mechanostimulation. *Proceedings of SPIE; 2017; Bellingham. Spie-Int Soc Optical Engineering.* p 101370F.
- McMahon AC, Greenwald SE, Dodd SM, Hurst MJ, Raine AEG. 2002. Prolonged calcium transients and myocardial remodelling in early experimental uraemia. *Nephrology Dialysis Transplantation* 17(5):759-764.
- Nagaraja PM, Jo H. 2014. The Role of Mechanical Stimulation in Recovery of Bone Loss—High versus Low Magnitude and Frequency of Force. *Life* 4(2).
- Resnick A. 2015. Mechanical properties of a primary cilium as measured by resonant oscillation. *Biophysical journal* 109(1):18-25.

- Riddle RC, Taylor AF, Rogers JR, Donahue HJ. 2007. ATP release mediates fluid flow-induced proliferation of human bone marrow stromal cells. *J Bone Miner Res* 22(4):589-600.
- Sheikh AQ, Hurley JR, Huang W, Taghian T, Kogan A, Cho H, Wang Y, Narmoneva DA. 2012. Diabetes Alters Intracellular Calcium Transients in Cardiac Endothelial Cells. *PLOS ONE* 7(5):e36840.
- Spencer CI, Baba S, Nakamura K, Hua EA, Sears MA, Fu CC, Zhang J, Balijepalli S, Tomoda K, Hayashi Y, Lizarraga P, Wojciak J, Scheinman MM, Aalto-Setälä K, Makielski JC, January CT, Healy KE, Kamp TJ, Yamanaka S, Conklin BR. 2014. Calcium transients closely reflect prolonged action potentials in iPSC models of inherited cardiac arrhythmia. *Stem cell reports* 3(2):269-281.
- Takahashi K, Doge F, Yoshioka M. 2005. Prolonged Ca²⁺ transients in ATP-stimulated endothelial cells exposed to 50 Hz electric fields. *Cell biology international* 29(3):237-243.
- Taylor MS, Choi CS, Bayazid L, Glosemeyer KE, Baker CCP, Weber DS. 2017. Changes in vascular reactivity and endothelial Ca(2+) dynamics with chronic low flow. *Microcirculation (New York, NY : 1994)* 24(3).
- Wang L, Hsu H-Y, Li X, Xian CJ. 2016. Effects of Frequency and Acceleration Amplitude on Osteoblast Mechanical Vibration Responses: A Finite Element Study. *BioMed research international* 2016:16.
- You J, Jacobs CR, Steinberg TH, Donahue HJ. 2002. P2Y purinoceptors are responsible for oscillatory fluid flow-induced intracellular calcium mobilization in osteoblastic cells. *The Journal of biological chemistry* 277(50):48724-48729.

Appendices

Appendix A: Legends for movie files

Video 2.1 Direct high-speed imaging of fiducial particles undergoing vibrational displacement. Polystyrene fiducial marker particles (6 μm diameter) were embedded in polydimethylsiloxane (PDMS). The dish was filled with 3.5 mL of water, to emulate the mass of a dish with medium and cells. The dish was then vibrated at the indicated frequencies and magnitudes of peak acceleration, under an inverted microscope. Images were acquired at 1200 frames per second using a high-speed camera. Videos were cut and cropped, and several full cycles of each bead's motion are shown. Images are shown at 30 frames per second (i.e. slowed down 40x). Selected images from this experiment are provided in Figure 3A.

Video 2.2 Ratio imaging of ATP-induced $[\text{Ca}^{2+}]_i$ elevation in MC3T3-E1 cells following sham pretreatment (non-vibrated). As described in the legend for Figure 6, cells were loaded with the calcium-sensitive dye fura-2 and placed in the vibration device on the microscope. Cells were not pretreated with vibration (sham). Video begins following sham pretreatment. ATP (100 μM final) was added to the culture dish at the time indicated on the video. Images are ratios of fluorescence intensities at 345 and 380 nm from an entire field of cells. Increased brightness reflects an increased ratio and hence elevation of $[\text{Ca}^{2+}]_i$. ATP induced transient elevation of $[\text{Ca}^{2+}]_i$ in the majority of cells. Frames were acquired at 1 frame per second (500 ms exposure for each wavelength), and are shown at 15 frames per second (sped up 15x). Selected images from this experiment are provided in Figure 6B. Representative of a total of 9 dishes of cells from 3 independent experiments.

Video 2.3 Ratio imaging of ATP-induced $[\text{Ca}^{2+}]_i$ elevation in MC3T3-E1 cells following pretreatment with vibration. A parallel sample of cells (from the same experiment illustrated in Supporting Video S2) were loaded with fura-2 and placed in the vibration device. Cells were treated with vibration for 5 min at 45 Hz and 0.3 g peak acceleration. The first 2 seconds of video correspond to the final 30 seconds of real-time experimental

vibration, during which images are motion blurred. Vibration was then discontinued and ATP (100 μ M final) was added to the culture dish at the time indicated on the video. Images are ratios of fluorescence intensities at 345 and 380 nm from an entire field of cells. Increased brightness reflects an increased ratio and hence elevation of $[Ca^{2+}]_i$. ATP-induced transient elevation of $[Ca^{2+}]_i$ was suppressed compared to that of sham-pretreated cells shown in Supporting Video S2. Frames were acquired at 1 frame per second (500 ms exposure for each wavelength), and are shown at 15 frames per second (sped up 15x). Selected images from this experiment are provided in Figure 6B. Representative of a total of 9 dishes of cells from 3 independent experiments.

Video 2.4 Phase-contrast imaging of cell morphology in primary rat osteoclasts before and after vibration. A sample of cells isolated from neonatal Wister rats were isolated in the morning and plated with HEPES-buffered M199. Later that day, dishes were placed in the vibration device. Cells were observed for ~12.5 minutes, vibrated for ~5 min at 45 Hz and 1 g peak acceleration, and then observed again for another ~12.5 minutes. During vibration images captured are motion blurred. Two osteoclasts (large multi-nucleated cells near the centre of the field of view) were located in this field of view and their morphology was observed. No marked changes in behavior or appearance were noted following vibration when compared to the same cell's behavior prior to vibration. Cell motility, size, and shape appeared to remain constant regardless of the vibrational stimulus. Satellite cells of indeterminate lineage were also found in the culture dish and did not appear to noticeably respond to vibration. Video is 30 minutes and 7 seconds in real-time, played back in 18 seconds (sped up ~100x). Video is representative of 16 osteoclasts in 8 dishes from 3 independent experiments.

Appendix B: Animal use protocol

AUP Number: 2016-100

PI Name: Sims, Stephen M

AUP Title: Role Of Cytosolic Calcium In The Regulation Of Osteoclasts And Bone Resorption// Ion Transport And Signalling In Skeletal Cells: P2 Nucleotide Receptor Function In Bone

Approval Date: 12/07/2016

Official Notice of Animal Use Subcommittee (AUS) Approval: Your new Animal Use Protocol (AUP) entitled "Role Of Cytosolic Calcium In The Regulation Of Osteoclasts And Bone Resorption// Ion Transport And Signalling In Skeletal Cells: P2 Nucleotide Receptor Function In Bone

" has been APPROVED by the Animal Use Subcommittee of the University Council on Animal Care. This approval, although valid for four years, and is subject to annual Protocol Renewal.2016-100::1

This AUP number must be indicated when ordering animals for this project.

Animals for other projects may not be ordered under this AUP number.

Purchases of animals other than through this system must be cleared through the ACVS office. Health certificates will be required.

The holder of this Animal Use Protocol is responsible to ensure that all associated safety components (biosafety, radiation safety, general laboratory safety) comply with institutional safety standards and have received all necessary approvals. Please consult directly with your institutional safety officers.

Submitted by: Copeman, Laura
on behalf of the Animal Use Subcommittee
University Council on Animal Care

Appendix C: Copyright permissions

Creative Commons — Attribution 4.0 International — CC BY 4.0

<https://creativecommons.org/licenses/by/4.0/legalcode>

Help us build a vibrant, collaborative global commons

[Donate Now](#)

This page is available in the following languages:



Creative Commons Legal Code

Attribution 4.0 International

Official translations of this license are available [in other languages](#).

Creative Commons Corporation (“Creative Commons”) is not a law firm and does not provide legal services or legal advice. Distribution of Creative Commons public licenses does not create a lawyer-client or other relationship. Creative Commons makes its licenses and related information available on an “as-is” basis. Creative Commons gives no warranties regarding its licenses, any material licensed under their terms and conditions, or any related information. Creative Commons disclaims all liability for damages resulting from their use to the fullest extent possible.

Using Creative Commons Public Licenses

Creative Commons public licenses provide a standard set of terms and conditions that creators and other rights holders may use to share original works of authorship and other material subject to copyright and certain other rights specified in the public license below. The following considerations are for informational purposes only, are not exhaustive, and do not form part of our licenses.

Considerations for licensors: Our public licenses are intended for use by those authorized to give the public permission to use material in ways otherwise restricted by copyright and certain other rights. Our licenses are irrevocable. Licensors should read and understand the terms and conditions of the license they choose before applying it. Licensors should also secure all rights necessary before applying our licenses so that the public can reuse the material as expected. Licensors should clearly mark any material not subject to the license. This includes other CC-licensed material, or material used under an exception or limitation to copyright. [More considerations for licensors.](#)▼

Considerations for the public: By using one of our public licenses, a licensor grants the public permission to use the licensed material under specified terms and conditions. If the licensor’s permission is not necessary for any reason—for example, because of any applicable exception or limitation to copyright—then that use is not regulated by the license. Our licenses grant only permissions under copyright and certain other rights that a licensor has authority to grant. Use of the licensed material may still be restricted for other reasons, including because others have copyright or other rights in the material. A licensor may make special requests, such as asking that all changes be marked or described. Although not required by our licenses, you are encouraged to respect those requests where reasonable. [More considerations for the public.](#)▼

Creative Commons Attribution 4.0 International Public License

By exercising the Licensed Rights (defined below), You accept and agree to be bound by the terms and conditions of this Creative Commons Attribution 4.0 International Public License (“Public License”). To the extent this Public License may be interpreted as a contract, You are granted the Licensed Rights in consideration of Your acceptance

of these terms and conditions, and the Licensor grants You such rights in consideration of benefits the Licensor receives from making the Licensed Material available under these terms and conditions.

Section 1 – Definitions.

- a. **Adapted Material** means material subject to Copyright and Similar Rights that is derived from or based upon the Licensed Material and in which the Licensed Material is translated, altered, arranged, transformed, or otherwise modified in a manner requiring permission under the Copyright and Similar Rights held by the Licensor. For purposes of this Public License, where the Licensed Material is a musical work, performance, or sound recording, Adapted Material is always produced where the Licensed Material is synched in timed relation with a moving image.
- b. **Adapter's License** means the license You apply to Your Copyright and Similar Rights in Your contributions to Adapted Material in accordance with the terms and conditions of this Public License.
- c. **Copyright and Similar Rights** means copyright and/or similar rights closely related to copyright including, without limitation, performance, broadcast, sound recording, and Sui Generis Database Rights, without regard to how the rights are labeled or categorized. For purposes of this Public License, the rights specified in Section 2(b)(1)-(2) are not Copyright and Similar Rights.
- d. **Effective Technological Measures** means those measures that, in the absence of proper authority, may not be circumvented under laws fulfilling obligations under Article 11 of the WIPO Copyright Treaty adopted on December 20, 1996, and/or similar international agreements.
- e. **Exceptions and Limitations** means fair use, fair dealing, and/or any other exception or limitation to Copyright and Similar Rights that applies to Your use of the Licensed Material.
- f. **Licensed Material** means the artistic or literary work, database, or other material to which the Licensor applied this Public License.
- g. **Licensed Rights** means the rights granted to You subject to the terms and conditions of this Public License, which are limited to all Copyright and Similar Rights that apply to Your use of the Licensed Material and that the Licensor has authority to license.
- h. **Licensor** means the individual(s) or entity(ies) granting rights under this Public License.
- i. **Share** means to provide material to the public by any means or process that requires permission under the Licensed Rights, such as reproduction, public display, public performance, distribution, dissemination, communication, or importation, and to make material available to the public including in ways that members of the public may access the material from a place and at a time individually chosen by them.
- j. **Sui Generis Database Rights** means rights other than copyright resulting from Directive 96/9/EC of the European Parliament and of the Council of 11 March 1996 on the legal protection of databases, as amended and/or succeeded, as well as other essentially equivalent rights anywhere in the world.
- k. **You** means the individual or entity exercising the Licensed Rights under this Public License. **Your** has a corresponding meaning.

Section 2 – Scope.

- a. **License grant.**
 1. Subject to the terms and conditions of this Public License, the Licensor hereby grants You a worldwide, royalty-free, non-sublicensable, non-exclusive, irrevocable license to exercise the Licensed Rights in the Licensed Material to:
 - A. reproduce and Share the Licensed Material, in whole or in part; and
 - B. produce, reproduce, and Share Adapted Material.
 2. Exceptions and Limitations. For the avoidance of doubt, where Exceptions and Limitations apply to Your use, this Public License does not apply, and You do not need to comply with its terms and conditions.
 3. Term. The term of this Public License is specified in Section 6(a).

4. **Media and formats; technical modifications allowed.** The Licensor authorizes You to exercise the Licensed Rights in all media and formats whether now known or hereafter created, and to make technical modifications necessary to do so. The Licensor waives and/or agrees not to assert any right or authority to forbid You from making technical modifications necessary to exercise the Licensed Rights, including technical modifications necessary to circumvent Effective Technological Measures. For purposes of this Public License, simply making modifications authorized by this Section 2(a)(4) never produces Adapted Material.
 5. **Downstream recipients.**
 - A. **Offer from the Licensor – Licensed Material.** Every recipient of the Licensed Material automatically receives an offer from the Licensor to exercise the Licensed Rights under the terms and conditions of this Public License.
 - B. **No downstream restrictions.** You may not offer or impose any additional or different terms or conditions on, or apply any Effective Technological Measures to, the Licensed Material if doing so restricts exercise of the Licensed Rights by any recipient of the Licensed Material.
 6. **No endorsement.** Nothing in this Public License constitutes or may be construed as permission to assert or imply that You are, or that Your use of the Licensed Material is, connected with, or sponsored, endorsed, or granted official status by, the Licensor or others designated to receive attribution as provided in Section 3(a)(1)(A)(i).
- b. Other rights.**
1. Moral rights, such as the right of integrity, are not licensed under this Public License, nor are publicity, privacy, and/or other similar personality rights; however, to the extent possible, the Licensor waives and/or agrees not to assert any such rights held by the Licensor to the limited extent necessary to allow You to exercise the Licensed Rights, but not otherwise.
 2. Patent and trademark rights are not licensed under this Public License.
 3. To the extent possible, the Licensor waives any right to collect royalties from You for the exercise of the Licensed Rights, whether directly or through a collecting society under any voluntary or waivable statutory or compulsory licensing scheme. In all other cases the Licensor expressly reserves any right to collect such royalties.

Section 3 – License Conditions.

Your exercise of the Licensed Rights is expressly made subject to the following conditions.

a. Attribution.

1. If You Share the Licensed Material (including in modified form), You must:
 - A. retain the following if it is supplied by the Licensor with the Licensed Material:
 - i. identification of the creator(s) of the Licensed Material and any others designated to receive attribution, in any reasonable manner requested by the Licensor (including by pseudonym if designated);
 - ii. a copyright notice;
 - iii. a notice that refers to this Public License;
 - iv. a notice that refers to the disclaimer of warranties;
 - v. a URI or hyperlink to the Licensed Material to the extent reasonably practicable;
 - B. indicate if You modified the Licensed Material and retain an indication of any previous modifications; and
 - C. indicate the Licensed Material is licensed under this Public License, and include the text of, or the URI or hyperlink to, this Public License.

2. You may satisfy the conditions in Section 3(a)(1) in any reasonable manner based on the medium, means, and context in which You Share the Licensed Material. For example, it may be reasonable to satisfy the conditions by providing a URI or hyperlink to a resource that includes the required information.
3. If requested by the Licensor, You must remove any of the information required by Section 3(a)(1)(A) to the extent reasonably practicable.
4. If You Share Adapted Material You produce, the Adapter's License You apply must not prevent recipients of the Adapted Material from complying with this Public License.

Section 4 – Sui Generis Database Rights.

Where the Licensed Rights include Sui Generis Database Rights that apply to Your use of the Licensed Material:

- a. for the avoidance of doubt, Section 2(a)(1) grants You the right to extract, reuse, reproduce, and Share all or a substantial portion of the contents of the database;
- b. if You include all or a substantial portion of the database contents in a database in which You have Sui Generis Database Rights, then the database in which You have Sui Generis Database Rights (but not its individual contents) is Adapted Material; and
- c. You must comply with the conditions in Section 3(a) if You Share all or a substantial portion of the contents of the database.

For the avoidance of doubt, this Section 4 supplements and does not replace Your obligations under this Public License where the Licensed Rights include other Copyright and Similar Rights.

Section 5 – Disclaimer of Warranties and Limitation of Liability.

- a. **Unless otherwise separately undertaken by the Licensor, to the extent possible, the Licensor offers the Licensed Material as-is and as-available, and makes no representations or warranties of any kind concerning the Licensed Material, whether express, implied, statutory, or other. This includes, without limitation, warranties of title, merchantability, fitness for a particular purpose, non-infringement, absence of latent or other defects, accuracy, or the presence or absence of errors, whether or not known or discoverable. Where disclaimers of warranties are not allowed in full or in part, this disclaimer may not apply to You.**
- b. **To the extent possible, in no event will the Licensor be liable to You on any legal theory (including, without limitation, negligence) or otherwise for any direct, special, indirect, incidental, consequential, punitive, exemplary, or other losses, costs, expenses, or damages arising out of this Public License or use of the Licensed Material, even if the Licensor has been advised of the possibility of such losses, costs, expenses, or damages. Where a limitation of liability is not allowed in full or in part, this limitation may not apply to You.**
- c. The disclaimer of warranties and limitation of liability provided above shall be interpreted in a manner that, to the extent possible, most closely approximates an absolute disclaimer and waiver of all liability.

Section 6 – Term and Termination.

- a. This Public License applies for the term of the Copyright and Similar Rights licensed here. However, if You fail to comply with this Public License, then Your rights under this Public License terminate automatically.
- b. Where Your right to use the Licensed Material has terminated under Section 6(a), it reinstates:
 1. automatically as of the date the violation is cured, provided it is cured within 30 days of Your discovery of the violation; or

2. upon express reinstatement by the Licensor.

For the avoidance of doubt, this Section 6(b) does not affect any right the Licensor may have to seek remedies for Your violations of this Public License.

- c. For the avoidance of doubt, the Licensor may also offer the Licensed Material under separate terms or conditions or stop distributing the Licensed Material at any time; however, doing so will not terminate this Public License.
- d. Sections 1, 5, 6, 7, and 8 survive termination of this Public License.

Section 7 – Other Terms and Conditions.

- a. The Licensor shall not be bound by any additional or different terms or conditions communicated by You unless expressly agreed.
- b. Any arrangements, understandings, or agreements regarding the Licensed Material not stated herein are separate from and independent of the terms and conditions of this Public License.


Section 8 – Interpretation.

- a. For the avoidance of doubt, this Public License does not, and shall not be interpreted to, reduce, limit, restrict, or impose conditions on any use of the Licensed Material that could lawfully be made without permission under this Public License.
- b. To the extent possible, if any provision of this Public License is deemed unenforceable, it shall be automatically reformed to the minimum extent necessary to make it enforceable. If the provision cannot be reformed, it shall be severed from this Public License without affecting the enforceability of the remaining terms and conditions.
- c. No term or condition of this Public License will be waived and no failure to comply consented to unless expressly agreed to by the Licensor.
- d. Nothing in this Public License constitutes or may be interpreted as a limitation upon, or waiver of, any privileges and immunities that apply to the Licensor or You, including from the legal processes of any jurisdiction or authority.

Creative Commons is not a party to its public licenses. Notwithstanding, Creative Commons may elect to apply one of its public licenses to material it publishes and in those instances will be considered the "Licensor." The text of the Creative Commons public licenses is dedicated to the public domain under the [CC0 Public Domain Dedication](#). Except for the limited purpose of indicating that material is shared under a Creative Commons public license or as otherwise permitted by the Creative Commons policies published at creativecommons.org/policies, Creative Commons does not authorize the use of the trademark "Creative Commons" or any other trademark or logo of Creative Commons without its prior written consent including, without limitation, in connection with any unauthorized modifications to any of its public licenses or any other arrangements, understandings, or agreements concerning use of licensed material. For the avoidance of doubt, this paragraph does not form part of the public licenses.

Creative Commons may be contacted at creativecommons.org.

Additional languages available: [Bahasa Indonesia](#), [Español](#), [euskara](#), [Deutsch](#), [Español](#), [français](#), [hrvatski](#), [italiano](#), [latviski](#), [Lietuvių](#), [Nederlands](#), [norsk](#), [polski](#), [português](#), [suomeksi](#), [svenska](#), [te reo Māori](#), [Türkçe](#), [čeština](#), [Ελληνικό](#), [русский](#), [українська](#), [العربية](#), [日本語](#). Please read the [FAQ](#) for more information about official translations.



Confirmation Number: 11819152

Citation Information

Order Detail ID: 71911160

Annual review of fluid mechanics by ANNUAL REVIEWS. Reproduced with permission of ANNUAL REVIEWS in the format Thesis/Dissertation via Copyright Clearance Center.

Close


SPRINGER NATURE LICENSE TERMS AND CONDITIONS	
Jul 09, 2019	
<p>This Agreement between Daniel Lorusso ("You") and Springer Nature ("Springer Nature") consists of your license details and the terms and conditions provided by Springer Nature and Copyright Clearance Center.</p>	
License Number	4624630934085
License date	Jul 09, 2019
Licensed Content Publisher	Springer Nature
Licensed Content Publication	Medical & Biological Engineering & Computing
Licensed Content Title	Computer-controlled positive displacement pump for physiological flow simulation
Licensed Content Author	D. W. Holdsworth, D. W. Rickey, M. Drangova et al
Licensed Content Date	Jan 1, 1991
Licensed Content Volume	29
Licensed Content Issue	6
Type of Use	Thesis/Dissertation
Requestor type	academic/university or research institute
Format	print and electronic
Portion	figures/tables/illustrations
Number of figures/tables/illustrations	1
Will you be translating?	no
Circulation/distribution	<501
Author of this Springer Nature content	no
Title	Dynamic mechanostimulation of live cells during real-time microscopy
Institution name	The University of Western Ontario
Expected presentation date	Aug 2019
Portions	Figure 7
Requestor Location	Daniel Lorusso 1151 Richmond St. N.

**JOHN WILEY AND SONS LICENSE
TERMS AND CONDITIONS**

Jul 09, 2019

This Agreement between Daniel Lorusso ("You") and John Wiley and Sons ("John Wiley and Sons") consists of your license details and the terms and conditions provided by John Wiley and Sons and Copyright Clearance Center.

License Number	4624660910371
License date	Jul 09, 2019
Licensed Content Publisher	John Wiley and Sons
Licensed Content Publication	Drug Development Research
Licensed Content Title	P2 purinergic receptors on osteoblasts and osteoclasts: Potential targets for drug development
Licensed Content Author	S. Jeffrey Dixon, Stephen M. Sims
Licensed Content Date	Apr 27, 2000
Licensed Content Volume	49
Licensed Content Issue	3
Licensed Content Pages	14
Type of use	Dissertation/Thesis
Requestor type	University/Academic
Format	Print and electronic
Portion	Figure/table
Number of figures/tables	1
Original Wiley figure/table number(s)	Figure 2
Will you be translating?	No
Title of your thesis / dissertation	Dynamic mechanostimulation of live cells during real-time microscopy
Expected completion date	Aug 2019
Expected size (number of pages)	1
Requestor Location	Daniel Lorusso 1151 Richmond St. N. London, ON N6A 3K7 Canada Attn: Daniel Lorusso
Publisher Tax ID	EU826007151



Confirmation Number: 11830197

Citation Information

Order Detail ID: 71940788

The biochemical journal by JOHNSTON LABORATORIES ; BIOCHEMICAL SOCIETY (GREAT BRITAIN) Reproduced with permission of PORTLAND PRESS LTD. in the format Thesis/Dissertation via Copyright Clearance Center.

Close

SPRINGER NATURE LICENSE TERMS AND CONDITIONS	
Jul 08, 2019	
<p>This Agreement between Daniel Lorusso ("You") and Springer Nature ("Springer Nature") consists of your license details and the terms and conditions provided by Springer Nature and Copyright Clearance Center.</p>	
License Number	4624390985336
License date	Jul 08, 2019
Licensed Content Publisher	Springer Nature
Licensed Content Publication	Biomedical Microdevices
Licensed Content Title	Practical fabrication of microfluidic platforms for live-cell microscopy
Licensed Content Author	Daniel Lorusso, Hristo N. Nikolov, Jaques S. Milner et al
Licensed Content Date	Jan 1, 2016
Licensed Content Volume	18
Licensed Content Issue	5
Type of Use	Thesis/Dissertation
Requestor type	academic/university or research institute
Format	print and electronic
Portion	full article/chapter
Will you be translating?	no
Circulation/distribution	<501
Author of this Springer Nature content	yes
Title	Dynamic mechanostimulation of live cells during real-time microscopy
Institution name	The University of Western Ontario
Expected presentation date	Aug 2019
Requestor Location	Daniel Lorusso 1151 Richmond St. N. London, ON N6A 3K7 Canada Attn: Daniel Lorusso
Total	0.00 USD



Creative Commons Legal Code

Attribution-NonCommercial-NoDerivs 3.0 United States



CREATIVE COMMONS CORPORATION IS NOT A LAW FIRM AND DOES NOT PROVIDE LEGAL SERVICES. DISTRIBUTION OF THIS LICENSE DOES NOT CREATE AN ATTORNEY-CLIENT RELATIONSHIP. CREATIVE COMMONS PROVIDES THIS INFORMATION ON AN "AS-IS" BASIS. CREATIVE COMMONS MAKES NO WARRANTIES REGARDING THE INFORMATION PROVIDED, AND DISCLAIMS LIABILITY FOR DAMAGES RESULTING FROM ITS USE.

License

THE WORK (AS DEFINED BELOW) IS PROVIDED UNDER THE TERMS OF THIS CREATIVE COMMONS PUBLIC LICENSE ("CCPL" OR "LICENSE"). THE WORK IS PROTECTED BY COPYRIGHT AND/OR OTHER APPLICABLE LAW. ANY USE OF THE WORK OTHER THAN AS AUTHORIZED UNDER THIS LICENSE OR COPYRIGHT LAW IS PROHIBITED.

BY EXERCISING ANY RIGHTS TO THE WORK PROVIDED HERE, YOU ACCEPT AND AGREE TO BE BOUND BY THE TERMS OF THIS LICENSE. TO THE EXTENT THIS LICENSE MAY BE CONSIDERED TO BE A CONTRACT, THE LICENSOR GRANTS YOU THE RIGHTS CONTAINED HERE IN CONSIDERATION OF YOUR ACCEPTANCE OF SUCH TERMS AND CONDITIONS.

1. Definitions

- a. **"Collective Work"** means a work, such as a periodical issue, anthology or encyclopedia, in which the Work in its entirety in unmodified form, along with one or more other contributions, constituting separate and independent works in themselves, are assembled into a collective whole. A work that constitutes a Collective Work will not be considered a Derivative Work (as defined below) for the purposes of this License.
- b. **"Derivative Work"** means a work based upon the Work or upon the Work and other pre-existing works, such as a translation, musical arrangement, dramatization, fictionalization, motion picture version, sound recording, art reproduction, abridgment, condensation, or any other form in which the Work may be recast, transformed, or adapted, except that a work that constitutes a Collective Work will not be considered a Derivative Work for the purpose of this License. For the avoidance of doubt, where the Work is a musical composition or sound recording, the synchronization of the Work in timed-relation with a moving image ("synching") will be considered a Derivative Work for the purpose of this License.
- c. **"Licensor"** means the individual, individuals, entity or entities that offers the Work under the terms of this License.
- d. **"Original Author"** means the individual, individuals, entity or entities who created the Work.
- e. **"Work"** means the copyrightable work of authorship offered under the terms of this License.
- f. **"You"** means an individual or entity exercising rights under this License who has not previously violated the terms of this License with respect to the Work, or who has received express permission from the Licensor to exercise rights under this License despite a previous violation.

2. Fair Use Rights. Nothing in this license is intended to reduce, limit, or restrict any rights arising from fair use, first sale or other limitations on the exclusive rights of the copyright owner under copyright law or other applicable laws.

3. License Grant. Subject to the terms and conditions of this License, Licensor hereby grants You a worldwide, royalty-free, non-exclusive, perpetual (for the duration of the applicable copyright) license to exercise the rights in the Work as stated below:

- a. to reproduce the Work, to incorporate the Work into one or more Collective Works, and to reproduce the Work as incorporated in the Collective Works; and,
- b. to distribute copies or phonorecords of, display publicly, perform publicly, and perform publicly by means of a digital audio transmission the Work including as incorporated in Collective Works.

The above rights may be exercised in all media and formats whether now known or hereafter devised. The above rights include the right to make such modifications as are technically necessary to exercise the rights in other media and formats, but otherwise you have no rights to make Derivative Works. All rights not expressly granted by Licensor are hereby reserved, including but not limited to the rights set forth in Sections 4(d) and 4(e).

4. Restrictions. The license granted in Section 3 above is expressly made subject to and limited by the following restrictions:

- a. You may distribute, publicly display, publicly perform, or publicly digitally perform the Work only under the terms of this License, and You must include a copy of, or the Uniform Resource Identifier for, this License with every copy or phonorecord of the Work You distribute, publicly display, publicly perform, or publicly digitally perform. You may not offer or impose any terms on the Work that restrict the terms of this License or the ability of a recipient of the Work to exercise the rights granted to that recipient under the terms of the License. You may not sublicense the Work. You must keep intact all notices that refer to this License and to the disclaimer of warranties. When You distribute, publicly display, publicly perform, or publicly digitally perform the Work, You may not impose any technological measures on the Work that restrict the ability of a recipient of the Work from You to exercise the rights granted to that recipient under the terms of the License. This Section 4(a) applies to the Work as incorporated in a Collective Work, but this does not require the Collective Work apart from the Work itself to be made subject to the terms of this License. If You create a Collective Work, upon notice from any Licensor You must, to the extent practicable, remove from the Collective Work any credit as required by Section 4(c), as requested.
- b. You may not exercise any of the rights granted to You in Section 3 above in any manner that is primarily intended for or directed toward commercial advantage or private monetary compensation. The exchange of the Work for other copyrighted works by means of digital file-sharing or otherwise shall not be considered to be intended for or directed toward commercial advantage or private monetary compensation, provided there is no payment of any monetary compensation in connection with the exchange of copyrighted works.
- c. If You distribute, publicly display, publicly perform, or publicly digitally perform the Work (as defined in Section 1 above) or Collective Works (as defined in Section 1 above), You must, unless a request has been made pursuant to Section 4(a), keep intact all copyright notices for the Work and provide, reasonable to the medium or means You are utilizing: (i) the name of the Original Author (or pseudonym, if applicable) if supplied, and/or (ii) if the Original Author and/or Licensor designate another party or parties (e.g. a sponsor institute, publishing entity, journal) for attribution ("Attribution Parties") in Licensor's copyright notice, terms of service or by other reasonable means, the name of such party or parties; the title of the Work if supplied; to the extent reasonably practicable, the Uniform Resource Identifier, if any, that Licensor specifies to be associated with the Work, unless such URI does not refer to the copyright notice or licensing information for the Work. The credit required by this Section 4(c) may be implemented in any reasonable manner; provided, however, that in the case of a Collective Work, at a minimum such credit will appear, if a credit for all contributing authors of the Collective Work appears, then as part of these credits and in a manner at least as prominent as the credits for the other contributing authors. For the avoidance of doubt, You may only use the credit required by this clause for the purpose of attribution in the manner set out above and, by exercising Your rights under this License, You may not implicitly or explicitly assert or imply any connection with, sponsorship or endorsement by the Original Author, Licensor and/or Attribution Parties, as appropriate, of You or Your use of the Work, without the separate, express prior written permission of the Original Author, Licensor and/or Attribution Parties.

d. For the avoidance of doubt, where the Work is a musical composition:

- i. **Performance Royalties Under Blanket Licenses.** Licensor reserves the exclusive right to collect whether individually or, in the event that Licensor is a member of a performance rights society (e.g. ASCAP, BMI, SESAC), via that society, royalties for the public performance or public digital performance (e.g. webcast) of the Work if that performance is primarily intended for or directed toward commercial advantage or private monetary compensation.
- ii. **Mechanical Rights and Statutory Royalties.** Licensor reserves the exclusive right to collect, whether individually or via a music rights agency or designated agent (e.g. Harry Fox Agency), royalties for any phonorecord You create from the Work ("cover version") and distribute, subject to the compulsory license created by 17 USC Section 115 of the US Copyright Act (or the equivalent in other jurisdictions), if Your distribution of such cover version is primarily intended for or directed toward commercial advantage or private monetary compensation.
- e. **Webcasting Rights and Statutory Royalties.** For the avoidance of doubt, where the Work is a sound recording, Licensor reserves the exclusive right to collect, whether individually or via a performance-rights society (e.g. SoundExchange), royalties for the public digital performance (e.g. webcast) of the Work, subject to the compulsory license created by 17 USC Section 114 of the US Copyright Act (or the equivalent in other jurisdictions), if Your public digital performance is primarily intended for or directed toward commercial advantage or private monetary compensation.

5. Representations, Warranties and Disclaimer

UNLESS OTHERWISE MUTUALLY AGREED TO BY THE PARTIES IN WRITING, LICENSOR OFFERS THE WORK AS-IS AND ONLY TO THE EXTENT OF ANY RIGHTS HELD IN THE LICENSED WORK BY THE LICENSOR. THE LICENSOR MAKES NO REPRESENTATIONS OR WARRANTIES OF ANY KIND CONCERNING THE WORK, EXPRESS, IMPLIED, STATUTORY OR OTHERWISE, INCLUDING, WITHOUT LIMITATION, WARRANTIES OF TITLE, MARKETABILITY, MERCHANTABILITY, FITNESS FOR A PARTICULAR PURPOSE, NONINFRINGEMENT, OR THE ABSENCE OF LATENT OR OTHER DEFECTS, ACCURACY, OR THE PRESENCE OF ABSENCE OF ERRORS, WHETHER OR NOT DISCOVERABLE. SOME JURISDICTIONS DO NOT ALLOW THE EXCLUSION OF IMPLIED WARRANTIES, SO SUCH EXCLUSION MAY NOT APPLY TO YOU.

6. Limitation on Liability. EXCEPT TO THE EXTENT REQUIRED BY APPLICABLE LAW, IN NO EVENT WILL LICENSOR BE LIABLE TO YOU ON ANY LEGAL THEORY FOR ANY SPECIAL, INCIDENTAL, CONSEQUENTIAL, PUNITIVE OR EXEMPLARY DAMAGES ARISING OUT OF THIS LICENSE OR THE USE OF THE WORK, EVEN IF LICENSOR HAS BEEN ADVISED OF THE POSSIBILITY OF SUCH DAMAGES.

7. Termination

- a. This License and the rights granted hereunder will terminate automatically upon any breach by You of the terms of this License. Individuals or entities who have received Collective Works (as defined in Section 1 above) from You under this License, however, will not have their licenses terminated provided such individuals or entities remain in full compliance with those licenses. Sections 1, 2, 5, 6, 7, and 8 will survive any termination of this License.
- b. Subject to the above terms and conditions, the license granted here is perpetual (for the duration of the applicable copyright in the Work). Notwithstanding the above, Licensor reserves the right to release the Work under different license terms or to stop distributing the Work at any time; provided, however that any such election will not serve to withdraw this License (or any other license that has been, or is required to be, granted under the terms of this License), and this License will continue in full force and effect unless terminated as stated above.

8. Miscellaneous

- a. Each time You distribute or publicly digitally perform the Work (as defined in Section 1 above) or a Collective Work (as defined in Section 1 above), the Licensor offers to the recipient a license to the

- Work on the same terms and conditions as the license granted to You under this License.
- b. If any provision of this License is invalid or unenforceable under applicable law, it shall not affect the validity or enforceability of the remainder of the terms of this License, and without further action by the parties to this agreement, such provision shall be reformed to the minimum extent necessary to make such provision valid and enforceable.
 - c. No term or provision of this License shall be deemed waived and no breach consented to unless such waiver or consent shall be in writing and signed by the party to be charged with such waiver or consent.
 - d. This License constitutes the entire agreement between the parties with respect to the Work licensed here. There are no understandings, agreements or representations with respect to the Work not specified here. Licensor shall not be bound by any additional provisions that may appear in any communication from You. This License may not be modified without the mutual written agreement of the Licensor and You.

Creative Commons Notice

Creative Commons is not a party to this License, and makes no warranty whatsoever in connection with the Work. Creative Commons will not be liable to You or any party on any legal theory for any damages whatsoever, including without limitation any general, special, incidental or consequential damages arising in connection to this license. Notwithstanding the foregoing two (2) sentences, if Creative Commons has expressly identified itself as the Licensor hereunder, it shall have all rights and obligations of Licensor.

Except for the limited purpose of indicating to the public that the Work is licensed under the CCPL, Creative Commons does not authorize the use by either party of the trademark "Creative Commons" or any related trademark or logo of Creative Commons without the prior written consent of Creative Commons. Any permitted use will be in compliance with Creative Commons' then-current trademark usage guidelines, as may be published on its website or otherwise made available upon request from time to time. For the avoidance of doubt, this trademark restriction does not form part of this License.

Creative Commons may be contacted at <https://creativecommons.org/>.

Curriculum Vitae

Name: Daniel Lorusso

Post-secondary Education and Degrees: The University of Western Ontario
London, Ontario, Canada
2012-Present Ph.D Candidate
Physiology and Pharmacology,
Collaborative Specialization in Musculoskeletal Health Research

The University of Western Ontario
London, Ontario, Canada
2008-2012 B.M.Sc, Honors
Honors Specialization in Biochemistry & Cell Biology

Honours and Awards: Province of Ontario Graduate Scholarship
2015-2016

CMHR Transdisciplinary Bone & Joint Training Award
2015-2016

Canadian Institutes of Health Research (CIHR) Joint Motion Program (JuMP) Studentship
2013-2015

Dean's Honor List, The University of Western Ontario
2008-2012

The Western Scholarship of Distinction, The University of Western Ontario
2008

Related Work Experience: Teaching Assistant
Cell Physiology 3140A
The University of Western Ontario
2014, 2016

Research Assistant
Dr. Sandy Kirkley Centre for Musculoskeletal Health Research
The University of Western Ontario,
2012

Publications: Lorusso, D., Nikolov, H.N., Holdsworth, D.W., and Dixon, S.J. (2019) Vibration of osteoblastic cells using a novel motion-control platform does not acutely alter cytosolic calcium, but desensitizes subsequent responses to extracellular ATP. Submitted to the Journal of Cellular Physiology, in revision

D. R. Edey, S. I. Pollmann, D. Lorusso, M. Drangova, R. Flemming, D. W. Holdsworth. (2019) Extended dynamic range micro-computed tomography of geomaterials using a biomedical scanner. Journal of X-Ray Science and Technology, in press.

Liu, Y., Lorusso, D., Holdsworth, D.W., Poepping, T.L., de Bruyn, J.R. (2018) Effect of confinement on the rheology of a yield-stress fluid. Journal of Non-Newtonian Fluid Mechanics. 261: 25-32

Lorusso, D., Nikolov, H.N., Chmiel, T., Beach, R.J., Sims, S.M., Dixon, S.J., Holdsworth, D.W. (2017) A device for real-time live-cell microscopy during dynamic dual-modal mechanostimulation. Proc. SPIE 10137, Medical Imaging 2017: Biomedical Applications in Molecular, Structural, and Functional Imaging, 101370F.

Lorusso, D., Nikolov, H.N., Milner, J.S., Ochotny, N.M., Sims, S.M., Dixon, S.J., Holdsworth, D.W. (2016) Practical fabrication of microfluidic platforms for live-cell microscopy. Biomedical Microdevices. 18(5): 78

Lorusso, J., Fitzgeorge, L., Lorusso, D., and Lorusso, E. (2014) Examining practitioners' assessments of perceived aesthetic and diagnostic quality of high kVp-low mAs pelvis, chest, skull, and hand phantom radiographs. Journal of Medical Imaging and Radiation Sciences. 46, 162-173

Teeter, M.G., Milner, J.S., Au, J.L., Lorusso, D., Naudie, D.D., and Holdsworth, D.W. (2010) Regional measurements of surface deviation volume in worn polyethylene joint replacement components. J Long Term Eff Med Implants. 20(1): 49-56.